

Thèse

# INTEGRATION OF NANOMECHANICAL SENSORS ON CMOS BY NANOPATTERNING METHODS

présentée devant  
L'Institut National des Sciences Appliquées de Lyon  
et  
l'Universitat Autònoma de Barcelona

pour obtenir  
le grade de docteur

Ecole doctorale: EEA

par  
Julien ARCAMONE

Date de soutenance: 23 juillet 2007

## Jury

---

LORA TAMAYO D'OCÓN Emilio	Professeur d'université	Président
URANGA DEL MONTE Maria Aránzazu	Maître de Conférences	Rapporteuse
NICU Liviu	Chargé de recherche CNRS	
LOESCHNER Hans	Docteur	
PÉREZ-MURANO Francesc	Directeur de recherche CSIC	(Co-directeur de thèse)
BRÉMOND Georges	Professeur d'université	(Co-directeur de thèse)

à Charlotte, Gamin, Nelly et Jean

# ACKNOWLEDGEMENTS

Without the help and the intellectual, psychological and material support of many people, I could not have done this work. Therefore, I want to thank very gratefully everyone who has indirectly or directly participated to it.

I would like to thank very sincerely my two co-directors, Dr Francesc Pérez-Murano and Pr Georges Brémond, for their respective contribution.

I am also very grateful to all the other members of my committee who make me the honor to attend my PhD defense: Dra Arantxa Uranga, Pr Emilio Lora-Tamayo, Dr Hans Loeschner and Dr Liviu Nicu.

Querría agradecer ante todo a Francesc Pérez-Murano por haber dirigido ‘intensamente’ mi tesis y haberme animado continuamente. A nivel profesional, me ha transmitido mucho de su saber, en particular su capacidad de analizar los hechos con perspectiva y síntesis. Gracias por todo.

Quiero agradecer también al director del CNM, el profesor Francesc Serra Mestres, por haberme ofrecido la posibilidad de trabajar en su centro. Quiero dar todo mi sincero reconocimiento a los que han colaborado estrechamente conmigo: Ana Sánchez-Amores, Gemma Rius, Marta Duch, Marta Gerboles, Joseph Montserrat, Raquel Palencia, Josep Lorente, Guillermo Villanueva, Alberto Moreno y todos los otros, perdonadme por olvidarme. Sin la ayuda, el apoyo y los consejos de Bertrand Mishischi, el diseño del circuito hubiera sido imposible, muchísimas gracias a Paco Serra-Graells por su ayuda fundamental y su disponibilidad.

Muchas gracias también a todos los sucesivos miembros del despacho por los buenos momentos pasados: Gemma, Cristina, Olga, Guillermo, Andreu, Nadia, Iñigo, Irene, Giulio, Servane, Marc... Un saludo a todos los otros: Neus, Roger, Olivier, Pierre, Marcel, Nico, Roger, Jofre...

Querría dar un saludo especial y agradecer a los miembros del laboratorio ECAS de la ETSE-UAB: Pra Nuria Barniol, Dr Gabriel Abadal, Dra Arantxa Uranga, Dr Francesc Torres y Jordi Teva. Un saludo especial también a Mari-Carmen Mesas.

Quería también dar las gracias al Dr Jordi Fraxedas, del ICMAB-CSIC, por colaborar con nosotros y dejarnos usar su equipo de deposición de oro que nos permitió hacer uno de los experimentos claves de esta tesis.

De l'INSA Lyon et l'INL, je voudrais chaleureusement remercier mon second directeur de thèse, le Pr. Georges Brémond, pour son soutien et son aide notamment lors de mes passages à Lyon. J'ai une pensée particulière pour Pavel Budau qui nous a aidés avec enthousiasme et qui nous a quittés entre-temps dans des circonstances malheureuses. Merci aussi à Philippe Girard pour sa contribution à ce travail. Enfin, je tiens à remercier particulièrement le professeur Gérard Guillot de m'avoir accueilli au sein de l'INL, anciennement le LPM.

I will not forget my colleagues of EPFL: Dr Lianne Doeswijk and of course Pr Jürgen Brugger and Dr Marc van den Boogaart with whom we have been carrying out a very fruitful collaboration and with whom I also have spent friendly times.

Un grand merci aussi aux Dr Thierry Ondarçuhu et Erik Dujardin pour leur accueil lors de ma venue au CEMES-CNRS de Toulouse lors de notre fructueuse collaboration.

Je terminerai par mes proches. Charlotte, tu m'as supporté et encouragé constamment durant ces périodes intenses d'écriture: je ne sais comment te remercier pour ce que tu as fait pour moi. Je veux enfin exprimer toute ma gratitude envers mes parents pour tout leur soutien et tout ce qu'ils ont aussi fait pour moi jusqu'au jour d'aujourd'hui: c'est un peu pour vous que j'ai écrit ce manuscrit. Merci à toi aussi Benjamin pour ta fraternité, ainsi qu'à Manine et tous les autres que je n'oublie pas.



# INDEX

<b>THESIS PRESENTATION</b>	<b>PAGE 1</b>
----------------------------	---------------

<b>CHAPTER 1.</b>	<b>INTRODUCTION TO NANO/MICROMECHANICAL RESONATORS AND SYSTEMS</b>	<b>PAGE 5</b>
-------------------	--	---------------

I.	General Introduction .....	5
I.1.	MEMS overview .....	7
I.2.	NEMS: interest and features .....	9
II.	Nanopatterning techniques overview .....	11
III.	Nano/micromechanical resonators. Interest and physical features .....	14
III.1.	Types of nano/micromechanical resonators .....	14
III.2.	Mechanisms determining the quality factor and the noise .....	15
III.3.	Characterization techniques of frequency response .....	17
IV.	NEMS-based mass sensors .....	19
IV.1.	Quartz-crystal microbalances: applications and performance .....	19
IV.2.	State-of-the-art of mass sensors based on micro/nanomechanical resonators .....	19
	Bibliographical references .....	22

<b>CHAPTER 2.</b>	<b>CONCEPTS OF NANO/MICROMECHANICAL RESONATORS FOR MASS SENSING APPLICATIONS WITH ALL ELECTRIC ACTUATION AND DETECTION</b>	<b>PAGE 31</b>
-------------------	--	----------------

I.	Response of micro/nanomechanical resonators-based systems.....	34
I.1.	Equations of oscillating systems.....	34
I.1.a.	Harmonic (undamped non-driven) oscillators.....	34
I.1.b.	Damped non-driven oscillators. ....	35
I.1.c.	Driven damped oscillators .....	35
I.2.	Resonance frequency of nano/micromechanical resonators: Analytical modeling .....	37
I.2.a.	General equations.....	37
I.2.b.	Cantilever and bridge.....	40
I.2.b.i)	Cantilever.....	40
I.2.b.ii)	Bridge .....	42
I.2.c.	Quad-beams resonators.....	42
I.3.	Mass sensitivity of nano/micromechanical resonators .....	48
I.3.a.	Calculation of mass sensitivity.....	48
I.3.a.i)	Punctual mass sensitivity .....	48
I.3.a.ii)	Areal mass sensitivity .....	49
I.3.b.	Dynamic linear range.....	50
II.	Electrical response of electrostatically driven resonators .....	51
II.1.	Transduction principle: capacitive detection with electrostatic actuation.....	51
II.2.	Equivalent electrical modeling of a mechanical resonator.....	52
II.2.a.	Global equivalent electrical scheme.....	52
II.2.b.	RLC equivalent model of the motional impedance .....	54
II.2.b.i)	Phenomenological approach of a RLC oscillator .....	54
II.2.b.ii)	Parameters calculation .....	57
II.2.c.	Global response.....	59
II.3.	Response to electrostatic actuation.....	60
II.3.a.	Deflection and pull-in voltage related to electrostatic force.....	60
II.3.b.	Spring-softening effect.....	62
II.3.c.	Generalization .....	63
III.	Two approaches of flexural mode resonators: Out-of-plane and in-plane vibrating resonators.....	65
III.1.	Out-of-plane flexion mode resonators .....	65
III.1.a.	Comparison in terms of electrical response of three discrete devices with simplified RLC model .....	65
III.1.b.	Comparison in terms of mass sensitivity (punctual and distributed).....	67
III.1.b.i)	Punctual mass sensitivity .....	67
III.1.b.ii)	Distributed mass sensitivity.....	67
III.1.c.	Analysis of the quad-beams device.....	68
III.1.c.i)	Electromechanical modeling.....	68
III.1.c.ii)	Fabrication of discrete devices: e-beam lithography on SOI .....	70
III.1.c.iii)	Measurement of discrete devices .....	72
III.2.	In-plane flexion mode resonators. Cantilevers .....	74
	Conclusion of chapter 2 .....	76
	Bibliographical references .....	77

<b>CHAPTER 3.</b>	<b>DEVICE MODELING AND IC DESIGN OF NANO/MICROMECHANICAL RESONATORS ON CMOS CIRCUITRY</b>	<b>PAGE 81</b>
-------------------	---	----------------

I.	Interest of monolithic integration with CMOS.....	83
I.1.	Comparison integrated/discrete structures.....	83
I.2.	State-of-the-art of circuit topologies .....	84
II.	Integration of NEMS on CMOS.....	86
II.1.	Design of CMOS integrated NEMS resonators.....	86
II.1.a.	In-plane vibrating cantilevers.....	86
II.1.b.	Out-of-plane vibrating QB.....	86
II.2.	CCII CMOS circuit characteristics.....	87
II.2.a.	CCII Circuit topology.....	87
II.2.b.	CCII circuit performance .....	90
II.2.b.i)	Determination of operation points (DC) .....	91
II.2.b.ii)	AC response .....	92
II.2.b.iii)	Transient simulations .....	95
II.2.b.iv)	Conditions of saturation .....	97
II.2.b.v)	Linearity of the circuit response .....	97
II.2.b.vi)	Noise analysis.....	98
II.2.c.	CCII circuit performance with NEMS model at input .....	99
II.2.c.i)	Electrical simulations of cantilevers-CCII mixed circuit.....	99
II.2.c.ii)	Electrical simulations of QB-CCII mixed circuit .....	105
II.3.	NEMS/CMOS circuit layout.....	108
II.3.a.	CCII Circuit layout, integration areas layout.....	108
II.3.b.	Chip layout .....	111
	Conclusion of chapter 3.....	113
	Bibliographical references .....	114

<b>CHAPTER 4.</b>	<b>FABRICATION OF NANO/MICROMECHANICAL RESONATORS ON CMOS CIRCUITRY</b>	<b>PAGE 117</b>
-------------------	---	-----------------

I.	Lithography techniques for integration of NEMS on CMOS.....	120
I.1.	Nanostencil lithography, a full-wafer high-resolution technique .....	120
I.1.a.	State of the art, features and advantages of the technique .....	120
I.1.b.	Fundamental aspects of the fabrication of a full-wafer stencil by DUV.....	122
I.1.c.	Specific nanostencil layout for CNM CMOS wafer .....	125
I.2.	Electron beam lithography .....	127
II.	Fabrication of micro/nanomechanical resonators on CMOS by nanostencil lithography (nSL).....	128
II.1.	CNM CMOS technology .....	129
II.2.	Optimization of nSL process on CMOS: alignment and blurring corrections.....	131
II.2.a.	Alignment.....	131
II.2.b.	Blurring of Al patterns deposited by nSL.....	133
II.2.c.	Dummy wafers .....	139
II.3.	Post-processing of pre-fabricated CMOS wafers based on nSL.....	141
II.3.a.	<i>poly1</i> removal .....	141

II.3.b.	Alignment .....	142
II.3.c.	Al deposition.....	144
II.3.d.	Blurring correction.....	145
II.3.e.	Pattern transfer and release .....	145
II.3.f.	Test of CMOS compatibility of nSL.....	148
III.	Fabrication of nano/micromechanical resonators on CMOS by electron-beam lithography (eBL)	150
	Conclusion of chapter 4.....	151
	Bibliographical references .....	152

<b>CHAPTER 5.</b>	<b>EXPERIMENTAL CHARACTERIZATION OF NEMS/CMOS DEVICES</b>	<b>PAGE 155</b>
-------------------	---	-----------------

I.	Experimental procedure and measurement set-up.....	156
II.	CCH circuit characterization.....	158
III.	Electrical measurements of the frequency response of integrated resonators.....	159
III.1.	Electrical measurement of in-plane vibrating cantilevers.....	159
III.1.a.	Samples characteristics.....	159
III.1.b.	Experimental results.....	161
III.1.b.i)	Measurements in air with set-up 1 .....	161
III.1.b.ii)	Measurements in vacuum with set-up 2.....	162
III.1.b.iii)	Estimation of the Young modulus of the structural layer.....	163
III.1.b.iv)	Electrical results summary .....	164
III.1.c.	Analysis of results.....	165
III.1.c.i)	Estimation of the fringing field parasitic capacitance $C_{PA}$ .....	165
III.1.c.ii)	Driving voltage effect: spring-softening .....	165
III.1.c.iii)	Q factor evolution as a function of the pressure .....	167
III.1.c.iv)	Estimation of critical deflection .....	168
III.1.c.v)	Noise considerations.....	169
III.2.	Electrical measurement of out-of-plane vibrating quad-beams.....	171
III.2.a.	Samples characteristics.....	171
III.2.b.	Experimental results.....	171
III.2.b.i)	Measurements in air with set-up 1 .....	172
III.2.b.ii)	Measurements in vacuum with set-up 2.....	172
III.2.b.iii)	Electrical Results Summary .....	173
III.2.c.	Analysis of results.....	174
III.2.c.i)	Estimation of the fringing field parasitic capacitance $C_{PA}$ .....	174
III.2.c.ii)	Q factor evolution as a function of the pressure .....	174
III.2.c.iii)	Driving voltage effects.....	175
	Conclusion of chapter 5.....	177
	Bibliographical references .....	178

<b>CHAPTER 6.</b>	<b>FUNCTIONAL CHARACTERIZATION. IMPLEMENTATION OF NEMS/CMOS AS MASS SENSORS</b>	<b>PAGE 179</b>
I.	Punctual mass sensing.....	181
I.1.	Monitoring the evaporation of femtoliter droplets (exp. I).....	181
I.1.a.	Experimental set-up.....	182
I.1.b.	Results and analysis.....	186
I.2.	Double cantilever resonators (exp. II).....	189
I.2.a.	Features of double cantilever devices.....	189
I.2.b.	Results of mass sensing.....	195
II.	Distributed mass sensing experiments.....	200
II.1.	Monitoring the deposition of ultra-thin gold layers (exp. III).....	202
II.1.a.	Experimental set-up.....	202
II.1.b.	Nanomechanical sensor.....	206
II.1.c.	Results and analysis.....	207
II.2.	Application of NEMS/CMOS mass sensors as positioning sensors (exp. IV).....	216
II.2.a.	Quasi-dynamic approach.....	216
II.2.b.	System description.....	216
II.2.b.i)	Alignment procedure.....	218
II.2.b.ii)	Mass sensor requirements.....	220
	Conclusion of chapter 6.....	223
	Bibliographical references.....	224

<b>GENERAL CONCLUSION</b>	<b>PAGE 227</b>
---------------------------	-----------------

<b>ANNEX</b>	<b>PAGE 231</b>
--------------	-----------------

A1.	Resum en català.....	232
A2.	Resumen en castellano.....	234
A3.	Résumé en français.....	236
A4.	Zusammenfassung auf Deutsch.....	238
A5.	Glossary.....	239
A6.	Complete diagram of the CCII CMOS circuit.....	240
A7.	Technological processes.....	241
A7.1.	CNM CMOS process.....	241
A7.2.	Dummy wafers process.....	247
A7.3.	Post-processing based on eBL.....	250
A7.4.	Experimental results of pattern transfer of nanostencil lithography.....	251
A8.	QSD system: schematic of the mechanical holder of the sensor.....	253
A9.	AFM characterization of resonators: preliminary work.....	254
A10.	List of publications.....	257

# THESIS PRESENTATION

This PhD thesis has been mainly realized at the ‘Centro Nacional de Microelectrónica’ – ‘Instituto de Microelectrónica de Barcelona’ (CNM-IMB), that is part of the ‘Consejo Superior de Investigaciones Científicas’ (CSIC) (Spanish National Research Council), and directed there by Dr. Francesc Pérez-Murano. It has also been partly carried out at INSA Lyon, at the ‘Institut de Nanotechnologie de Lyon’ laboratory (INL), that is part of the ‘Centre National de la Recherche Scientifique’ (CNRS) (French National Research Center), and directed there by Pr. Georges Brémond.

This work must be placed in a context of rapid and growing expansion of the interest for the so-called ‘nanotechnologies’. This denomination actually covers an extremely wide range of applications which are related to very different scientific disciplines, like physics, chemistry, microelectronics, biology and biochemistry, materials science in general, etc...

Besides other research topics, like nano-materials (that find applications from metallurgy to medicine), the field of nanosensors is also extremely attractive because ultra-miniaturized sensing devices feature very high sensitivities to many different signal domains, like pressure, temperature, mass, mechanical stress, chemical adsorption, etc... Within this field, the scope of this thesis is related to resonant nanomechanical devices applied as ultra-sensitive mass sensors. A smart nanosystem has been developed based on a monolithic integration of a mechanical resonating device with CMOS.

At the beginning, this work partially relied on the previous experience of CNM acquired during its participation to the NANOMASS<sup>1</sup> project in which a similar approach was followed except for two major differences: a different interfacing CMOS circuit for the readout of the resonance

---

<sup>1</sup> Project funded by the European Commission within the FP5 (5<sup>th</sup> Framework Program), contract n° IST-1999-14053

signal and alternative nanolithography methods to define the nanodevices have been employed. In the NANOMASS project, the functionality of first prototypes was demonstrated. However, in the present work, the fabrication process has been improved in order to drastically increase the yield and a much better functionality of the devices has been demonstrated.

The work of this thesis has been carried out in the frame of the NaPa<sup>2</sup> project, whose objective is to develop emerging nanopatterning techniques which could be transferred to industry in short/medium terms. A complementary objective has been to promote possible applications, i.e. innovative nanodevices, using those techniques. Hence, the main goals of this thesis have been the simultaneous developments of (i) CMOS integrated nano (and micro) electromechanical systems (N-MEMS), and of (ii) an entire N-MEMS processing technology based on an advanced nanolithography technique named 'nanostencil', in order to fabricate monolithic systems with high yield and throughput.

This thesis features three well-distinct aspects: (i) the design of a nanodevice, (ii) its fabrication using nanofabrication techniques and (iii) its operation for sensing applications.

Concretely, it has consisted first in modeling and designing nano/micromechanical resonators, then the advantages and the feasibility of a monolithic integration on CMOS have been studied. Indeed, CMOS-NEMS are attractive systems which combine unprecedented sensing (and actuating) attributes originated by the mechanical part with the possibility of detecting the sensing signal in enhanced conditions (reducing parasitic loads) through the on-chip circuitry that can complementarily amplify and condition it.

These devices have been subsequently fabricated at full-wafer scale combining a standard CMOS technology with emerging nanolithography techniques, in particular with nanostencil lithography (nSL) whose practical implementation and patterning resolution have been optimized through a collaboration with EPFL (École Polytechnique Fédérale de Lausanne, Switzerland) in the frame of the NaPa project.

Then, the successful operation of the system has been demonstrated by characterizing precisely the frequency response of the micro/nanomechanical structure whose output signal is obtained under the form of an alternate electrical signal detected and amplified through a new specifically designed CMOS readout circuitry. Finally, this CMOS-NEMS resonator has been implemented as an ultra-sensitive mass sensor in four distinct experiments oriented to either scientific or technical purposes.

This PhD dissertation is structured in six chapters. Chapter 1 introduces the field of MEMS and their further evolution towards NEMS. With regard to this matter, an overview of modern nanopatterning techniques is given. Then, a survey of existing nano/micromechanical resonators is presented in terms of specific attributes and physical features: a special focus is given on the specific application of these resonating nano/micromechanical resonant structures as ultra-sensitive mass sensors.

---

<sup>2</sup> "Emerging Nanopatterning methods" project funded by the European Commission within FP6 (6<sup>th</sup> Framework Program), 31 (academic and industrial) partners from 14 countries (contract NMP4-CT-2003-500120)

In chapter 2, three types of nano/micromechanical resonators are analytically modeled in order to predict their mechanical frequency response. With the aim of electrically actuating and detecting the nanodevices, a capacitive detection scheme is adopted and an electromechanical model is followed to calculate their electrical response when mechanically resonating.

With regard to this matter, a specific low-power CMOS readout circuit has been designed. Its specifications have been defined according to theoretical predictions of resonance signal levels. Chapter 3 describes its topology and its operation principle. Its intrinsic behavior as well as its behavior when coupled to the electromechanically modeled nano/micromechanical resonator are fully analyzed based on simulations results.

Nevertheless, the practical realization of such CMOS integrated devices is challenging. In terms of fabrication, a full-wafer cost-effective integration of NEMS on CMOS still had to be demonstrated at this time. Because of this, a collaboration with EPFL (École Polytechnique Fédérale de Lausanne) was undertaken to further develop nanostencil lithography with the aim of integrating at full-wafer scale mesoscopic (nano and micro) structures on pre-fabricated CMOS circuitry. Chapter 4 describes the main initial issues that were identified and then solved. The successfully developed post-processing technology leading to the full-wafer integration of NEMS on CMOS in one single nSL step will be entirely detailed. In parallel, a second approach based on electron beam lithography with the aim to fabricate rapidly new prototypes of nanodevices on CMOS is also presented.

The complete characterization in air and vacuum of the obtained CMOS-NEMS is detailed in chapter 5. The main features of the frequency response, the experimental signal levels and the effect of the driving voltage on the mechanical frequency response are discussed.

Finally, chapter 6 focuses on the implementation of these CMOS-NEMS as ultra-sensitive mass sensors. This is currently one of the most explored applications of NEMS since nano/micromechanical resonators offer outstanding advantages in terms of sensitivity and integration compared to widely used quartz-crystal microbalances (QCM). Due to their small size, NEMS resonators inherently offer high mass sensing attributes together with a spatial resolution.

Four different experiments that have been designed and carried out are described in this chapter: (i) monitoring the evaporation of droplets to analyze wetting mechanisms at the femtoliter scale, (ii) a novel device is presented and tested that allows making reliable mass measurements in ambient conditions by directly providing the measurement uncertainty, (iii) monitoring in-situ the deposition of ultra-thin gold layers (sub-monolayer coverage). (iv) the very high areal mass sensitivity featured by the CMOS-NEMS has led us to implement it as a positioning sensor in a quasi-dynamic stencil lithography system, that is presently under development jointly with EPFL.

At the end, an annex section provides additional information: summaries in Catalan, Spanish, French and German, as well as technical data and schematics. Finally, a list of publications related to this thesis is presented.



# CHAPTER 1

## INTRODUCTION TO NANO/MICROMECHANICAL RESONATORS AND SYSTEMS

I.	General Introduction .....	5
I.1.	MEMS overview .....	7
I.2.	NEMS: interest and features .....	9
II.	Nanopatterning techniques overview .....	11
III.	Nano/micromechanical resonators. Interest and physical features .....	14
III.1.	Types of nano/micromechanical resonators .....	14
III.2.	Mechanisms determining the quality factor and the noise .....	15
III.3.	Characterization techniques of frequency response .....	17
IV.	NEMS-based mass sensors .....	19
IV.1.	Quartz-crystal microbalances: applications and performance .....	19
IV.2.	State-of-the-art of mass sensors based on micro/nanomechanical resonators .....	19
	Bibliographical references .....	22

### I. General Introduction

In the late 1970s, the semiconductor microelectronics industry gave rise to a new branch of science and technology referred to as microtechnology. Benefiting from the know-how in terms of materials and miniaturization processes acquired through the fabrication of silicon integrated circuits (IC), diverse types of mechanical devices with dimensions in the deep submillimeter range, typically 100 microns ( $\mu\text{m}$ ) or below, could be fabricated from then on.

In fact, for more than one hundred years already, the watchmaking industry mastered the fabrication of miniature mechanical pieces but the more recent booming of microtechnology comes from the coincidence that the silicon material used in IC also has outstanding mechanical properties [1], in particular a high Young modulus (around 160 GPa) and a wide and very linear elastic range. In parallel, the possibility to manufacture it under crystalline or polycrystalline

forms results in low dissipation layers. Another advantage comes from the fact that its processing is very well known and cost effective.

The outstanding electrical and mechanical properties of silicon allow designing smart mixed electro-mechanical monolithic components which involve on one hand a silicon micromechanical element for sensing (or actuating) purposes, and on another a microelectronics complementary-metal-oxide-semiconductor (CMOS) circuitry to control it.

Applicable to a broad range of sensing and actuating purposes, devices known as microelectromechanical systems (MEMS) provide enhanced sensitivity and resolution owing basically to their reduced size. Physically, they also access new interesting mechanisms that cannot be observed at macroscopic scales.

MEMS fabrication technology offers the possibility of very large scale integration (VLSI) of ultra-compact devices in a batch fabrication process. For this reason, a growing number of companies are already selling different types of MEMS-based products for clients coming from the automotive industry (the most famous is the accelerometer used in car airbags) until the biomedical sector (electronic blood pressure equipment, for instance).

Throughout the 80s and the 90s, MEMS have progressively been scaled down but not as fast as the Moore's law that guides the constant diminution of transistors size in IC. The obtained advantages when scaling down a mechanical element in the micron range and below are maybe not as straightforward as when a transistor is scaled down whereby faster and more complex functions per unit space are yielded. There is also maybe a cost reason as the MEMS market is not yet as profitable as the IC market although it also requires heavy investments in research and development.

However, jointly with the birth of the so-called 'nanotechnology' in the late 90s and the advances provided by novel deep-submicron CMOS processes, MEMS technology has recently derived towards a further miniaturization, under the form of so-called 'nanoelectromechanical systems' (NEMS). Indeed, a reduction of dimensions towards nanometer scale does not only represent a further and natural improvement: this leads not only to extremely high sensitivities and very high natural resonance frequencies but also new physical effects can be explored by the fact of getting closer to the atomic scale.

This global trend has created new needs in terms of lithography, and new versatile techniques are now required to scale down devices and thereby to reach nanometer resolution. Definitely, a certain number of nanopatterning techniques are already available like deep-ultra-violet lithography (DUV), immersion lithography (IL) or electron-beam lithography (eBL). The first two techniques represent a huge investment cost only affordable for large microelectronics foundries but prohibited de facto to research laboratories interested in the design of nanodevices. On the contrary, the use of eBL has democratized in the last few years as its use has spread among research laboratories. Its inherent low throughput arising from the serial operation does not constitute a limitation for research purposes but it does for industrial applications. Cheaper, parallel and 'clean' (resistless if possible) nanopatterning techniques are nowadays highly needed.

With regard to these matters, a short review of existing MEMS is going to be presented. Then, some interesting and specific features of NEMS considering them as further evolution of MEMS will be described. To fabricate NEMS, modern nanopatterning techniques are required: they will be briefly introduced. Finally, a short survey of existing nano/micromechanical resonators will be exposed insisting on the application as ultra-sensitive mass sensors.

## I.1. MEMS overview

Microelectromechanical devices (or systems, i.e. MEMS) are miniaturized structures that are mechanically stimulated by an input electromechanical transducer. The mechanical response under the form of static or dynamic motion is then translated back into an output electrical signal through another application-specific electromechanical transducer.

Very diverse actuation and detection schemes of the mechanical motion exist. Interestingly, the mechanical element, depending on its shape and mode of operation, can be applied to versatile sensing purposes. Pressure, temperature, angular rate and all types of chemical sensors as well as accelerometers, gas chromatographs and radio-frequency (RF) MEMS have been developed. In nature, MEMS science and technology are multi-disciplinary and require know-how in electronics and mechanical engineering as well as in material science, eventually in chemistry and theoretical physics.

The materials constituting MEMS, the mechanical part and its electrical connections, are generally the ones utilized in the microelectronics industry: silicon (single or- polycrystal), silicon compounds like silicon oxide ( $\text{SiO}_2$ ), silicon nitride ( $\text{Si}_3\text{N}_4$ ) and eventually silicon carbide ( $\text{SiC}$ ), III-V materials like GaAs, and metals like copper or aluminum.

The interest of scaling down mechanical devices can be understood considering the transformation of very general magnitudes affected by a scaling factor  $K$ , defined as  $K = \text{transformed dimension (miniaturized)} / \text{reference dimension (macro)}$  (i.e.  $K < 1$ ). Table I - 1 illustrates the improvements resulting from a miniaturization through an emphasis on the mechanical resonance frequency and the mass sensitivity (proportional to  $m/f_0$ ).

magnitude	scaling factor
length ( $L$ )	$K$
area ( $A$ )	$K^2$
volume ( $V$ ), i.e. mass ( $m$ )	$K^3$
stiffness ( $k$ )	$K$
resonance frequency ( $f_0$ )	$K^{-1}$
mass sensitivity ( $\mathcal{S}$ )	$K^4$
thermal time constant ( $\tau$ )	$K$

Table I - 1. Scaling factor for several magnitudes

Decreasing the size of the device (i.e.  $K$ ), higher resonance frequencies (scaled as  $K^{-1}$ ) can be obtained what is interesting for high frequency applications (telecommunication devices, etc...) and in parallel, a drastic enhancement of the mass sensitivity (equivalent to the ratio  $m/f_0$ , the precise calculation is detailed later) is yielded ( $K^4$  scale factor). The thermal time constant is also reduced what physically means that the dissipation of power may become an issue in small structures. This also has to see with the fact that the surface to volume ratio equal to  $K^{-1}$  is increased: surface-related effects like thermal losses will become increasingly important.

These specific examples give anyway general trends of the influence of the size reduction of mechanical devices. At smaller scales down to the micron range, the physics is still the same but the dominant effects are modified with respect to macroscopic scales.

Among all the existing types of MEMS, the main types are:

- pressure sensors. They generally rely on a bulk micromachined membrane of which one side is vacuum sealed. The deformation caused by the differential pressure between both sides is sensed using piezoresistors or capacitively.
- inertial sensors: accelerometers or gyroscopes. Such sensors are widely used for military and automotive applications. Generally, accelerometers are bulk micromachined and can be sensed either piezoresistively or capacitively. MEMS gyroscopes vibratory are so far exclusively vibratory [2]. They rely on the Coriolis force and are generally sensed capacitively.
- chemical sensors. For the monitoring of chemical reactions, very different approaches of chemical MEMS are reported: chemomechanics-based, thermal effects-based, integrated optics-based, or electrochemistry-based.
- RF MEMS. There exist four main types [3]: (i) switches, varactors and inductors operable from DC to 120 GHz in relatively mature technologies; (ii) micromachined transmission lines; (iii) thin film bulk acoustic resonators (FBAR) and filters that base on acoustic vibrations of thin films in the GHz range and with high quality factor (Q-factor, further defined) (>2000); (iv) RF micromechanical resonators and filters until 100 MHz. In general, they achieve high Q only in vacuum: this technology is not ready yet for commercial applications but represents a very promising way to form reference clock circuits.
- power related applications. In the last few years, these devices have faced an increasing interest. Fuel cells and microgenerators [4] are now two hot topics.
- scanning probes. The successful development in the mid-80s of scanning tunneling [5] and atomic force microscopy [6], constituting a breakthrough towards the further emergence of nanotechnology, partially relies on the development of the microfabrication techniques to make cantilever (singly clamped beams)-based scanning probes with sharp tip apex.

Since the early development of MEMS technology, researchers have been trying to co-integrate microelectromechanical devices with bipolar or CMOS on-chip circuitry to fabricate monolithic microsystems. Another opposite alternative is the heterogeneous integration of different types of components. Simple heterogeneous systems link the die wherein the sensing microdevices are located to a PCB containing IC chips by means of a wire bonding. Compacter solutions require an increasing complexity of the packaging process.

To make monolithic devices, a CMOS technology and micromachining (either bulk or surface) techniques have to be combined in order to fabricate smart microsystems that can be of all the previously cited types. These CMOS integrated sensors benefit from a reduction of parasitic loading due to the very short distance between the sensing and the circuit parts, thus allowing improving the signal over noise ratio (SNR) and drastically upscaling the number of parallel controllable sensors in a single chip. The CMOS circuitry offers convenient mixed-signal possibilities to collect, amplify and condition the raw electrical signal originated by the mechanical part of the MEMS: as an example of application the signal can be calibrated, compensated and linearized on-chip. In RF MEMS, monolithic implementations integrate a variety of high Q and low insertion loss components with RF transistors.

In terms of technology, three approaches exist: pre-, intra- and post-CMOS micromachining. In order not to interfere with reproducible and stable CMOS processes, the post-CMOS is mostly used owing to its flexibility. However, commonly to those three methods, the complexity of the combination between CMOS and micromachining processes, together with packaging issues have been a constant limitation to the achievement of fully integrated MEMS.

In this context, following a trend pulled by the development of modern deep submicron CMOS technologies, MEMS have further evolved towards the submicron scale, that is nanoscale, to constitute the new category of nanoelectromechanical systems (NEMS). In analogy with the new phenomena encountered in sub-50 nm MOS transistors related to quantum physics (like short channel effect), NEMS cannot be simply viewed as a smaller MEMS. Just like previously illustrated in the difference between macro and microdevices, there is effectively an effect of scaling factor that changes the dominant roles between classical physical effects but the novelty here is that additionally other effects rise like molecular or quantum effects.

### I.2. NEMS: interest and features

NEMS cannot be considered only as smaller MEMS, i.e. as a natural extension of MEMS. The difference here is that they combine classical phenomena together with quantum and molecular effects. Actually, existing NEMS are generally more of mesoscopic type than purely nanoscaled. This means that they generally involve two dimensions (typically width and thickness) in the deep submicron range (hundreds of nm) and the third in the 1-10  $\mu\text{m}$  range. However, although these devices are not strictly 'nano' regarding their dimensions, they feature specific phenomena that are effectively related to nanoscience: molecular recognition, adsorption/desorption processes, etc...

Existing NEMS could be classified between quasi-static and resonant NEMS [7]: the most versatile and widely used NEMS are vibrating singly- (cantilever) or doubly-clamped beams (bridge). In section III, resonating N/MEMS will be emphasized.

Compared to MEMS, NEMS have smaller area and volume but the resulting ratio area/volume is increased (see Table I - 1). In this sense, surface effects (roughness, adsorption, native oxides, and impurities) become more significant and influence the dynamic response through the Q-factor. In some cases, proximity forces like van der Waals or Casimir can start being more pronounced.

In terms of integration, the density can be increased by two or three orders of magnitude with respect to MEMS. Furthermore, 'true' nanodevices, whose all dimensions are submicronic, could ever be integrated in the IC itself in convergence with nano/microelectronics circuits. Otherwise, more classical post-CMOS integrations provide the same advantages as for MEMS in the sense that parasitic loading is much reduced.

One important question to answer is to what extent continuum mechanics can be applied to describe the mechanical behavior of NEMS. It appears from molecular dynamics (MD) simulations that for structures with a cross-sectional area larger than few  $\text{nm}^2$  continuum approximations are still mostly valid [7, 8]. If a further refinement of the mechanical modeling of mesoscopic structures was pursued, the first improvement would consist in not using bulk material properties but MD corrected ones.

NEMS operated as high-frequency resonators feature unprecedented attributes from both technical and scientific points of view: with dimensions in the deep sub-micron, they exhibit extremely high fundamental resonance frequencies in the microwaves, very low active masses in the femtograms and relatively high quality factors (Q-factor) around  $10^3$ - $10^4$ .

These properties make NEMS suitable for a wide range of technological applications such as ultra sensitive [9] and fast sensors, actuators and signal processing components. Mechanically based data storage using NEMS has been pursued for some years: IBM Zürich [10] was a pioneer some years ago with the 'Millipede' device, an array of AFM cantilevers that provides gigabit storage at high data rate. Since then, other nanomechanical memory elements relying on mechanical bistability have been reported: one approach consisting in using the hysteretic non-linear behavior of nanobridges [11, 12], the other in implementing a SiO<sub>2</sub> floating beam to form a high speed (1 GHz) nonvolatile memory cell [13].

For scientific purposes, NEMS open up the exploration of new topics like the quantum behavior of mesoscopic mechanical systems. A manifestation of quantum mechanics on such systems is claimed to have been observed [14-16].

The development of NEMS devices and technology is carried out worldwide following very different orientations. However, it faces nowadays two major challenges: the establishment of cheap and reproducible nanofabrication techniques and the development of more accurate transducing methods adapted to nanoscale devices

## II. Nanopatterning techniques overview

Since its early development, the semiconductor microelectronics industry has been using photolithography as a way to pattern the diverse structural layers of integrated circuits. A photolithography process flow implies coating the substrate with a photosensitive resist by spinning or spraying, exposing it to UV light through a mask containing chromium opaque patterns, either in contact or by projection, and finally developing the resist (in positive resists, exposed areas are dissolved by the development, in negative ones non-exposed areas are dissolved). In this way, 1-2  $\mu\text{m}$  line-widths are routinely achieved [17]. Along the years, the resolution of photolithography has continuously been improved [17] through the use of (i) shorter wavelength in projection exposure tools, and (ii) optimized resists and masks. The patterning of sub-100 nm features constitutes a threshold where diffraction issues appear to be the main limitation. However, further decreasing the wavelength to circumvent this issue does not represent the ideal solution: smaller wavelengths are actually strongly absorbed in many materials what requires the use of new resists, masks and processing techniques in general.

The most modern implementation of photolithography already in industry is deep UV (DUV) lithography that achieves 65 nm resolution with 193 nm wavelength thanks to a reduction lens system. Other improvements of optical lithography are immersion lithography, occurring in a liquid environment, and extreme UV (EUV). All these techniques have in common extremely high investment costs both for the exposure system and the related tools, resists and masks.

High-resolution (100 nm) alternative techniques are X-ray and Laser-Interference (LIL) lithography. In the first one, the problem comes from the complicated mask fabrication process as no image reduction is possible so that the mask must be a 1:1 replica. The second one is limited to periodic patterns only.

Charged particle beams lithography, namely electron beam (eBL) and ion beam (iBL) lithography, are other well-known techniques. They are maskless direct writing systems that use a narrow beam to expose the patterns in a charge sensitive resist writing sequentially, point by point. This means that no mask is involved and the pattern is originally computer-stored and directly written through the fine spatial control of the beam. A main advantage here is that the beam particle, in particular electrons, are not limited by diffraction effects, however the sequential patterning limits considerably the throughput. To circumvent this limitation, efforts are underway to design projection lithography systems that generate in parallel thousands of charged particle beams (see [www.charpan.com](http://www.charpan.com)). In chapter 4, eBL is presented in more detail.

Both the microelectronics industry, looking forward defining sub-100 nm transistors, and nanotechnology, pursuing the definition of NEMS or materials-related applications, require new alternative nanopatterning techniques.

One reason is the cost. The development of a new method for the low cost parallel definition of sub-100 nm patterns is actively pursued. In topics not specifically related to IC, a second direction consists in proposing other approaches than resist based lithography. In applications involving chemically functionalized surfaces, a cyclic process based on the use of resist is not optimum as the surface is continuously chemically treated. Also related to the use of resist, non-planar substrates with more or less pronounced topographies are difficult to coat uniformly what makes the exposure more delicate. Another reason that guides the development of

new nanopatterning methods is the need to structure ‘unconventional’ materials (for example organic materials for organic light emitting diode) on ‘unconventional’ surfaces (polymers, self-assembled monolayers).

These new techniques can be classified into three main types: nanoimprint lithography (NIL) [18-20], soft-lithography [21] (also named micro-contact printing) and MEMS-based nanopatterning. MEMS-based means actually that they use nano/micromachined Si frames as tools to perform local depositions of a patterning material; in this category we can distinguish the items for liquid nano/microdispensing [22, 23] and for vacuum nanostencil lithography (nSL) [24-26] consisting in depositing various solid materials. In Figure 1, the principle of NIL, soft-lithography and nSL is sketched taking as a reference the already well established eBL+lift-off process:

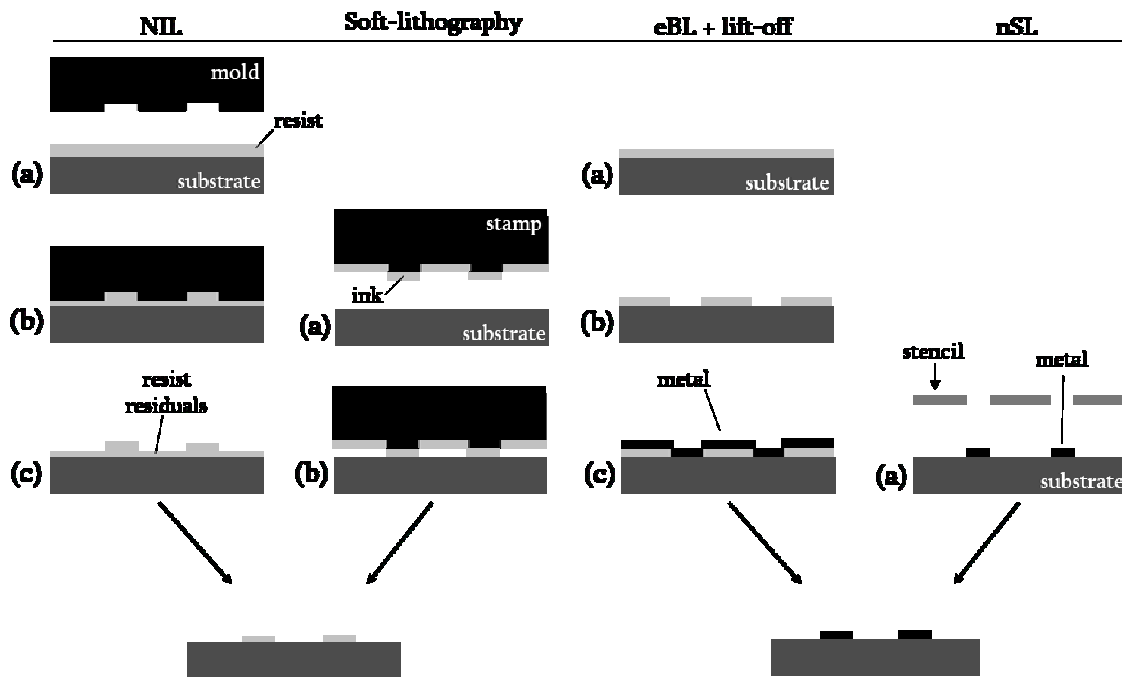


Figure 1. Schematic representations of the main alternative nanolithography techniques

The [eBL+lift-off] process consists in usually coating the substrate with PMMA (a), then this resist is exposed to the electron narrow beam and developed (b). After that, the top side of the substrate is metallized (c) with a metal thin layer (less than 50 nm thick). Finally, the sample in a resist dissolvent and the metal initially located on unexposed PMMA pillars is lifted-off what results in a structured surface with local nano/micropatterns.

In contrast to this process, the other three novel techniques are parallel. In NIL, a mold (a), generally defined previously by eBL and reactive ion etching (RIE), is pressed by hard contact onto a polymer resist [27] (b), what produces indentations (c). At this step, the resist is hardened by thermal or UV annealing and the unavoidable residuals remaining in-between the patterns are removed in general by an oxygen plasma etching. NIL can be applied according to a step-and-repeat approach with small molds and at full-wafer scale with wafer-sized molds. The problem here is the density of patterns in the mold and the ability of the system to apply a constant pressure all over the mold.

Micro-contact printing consists in fitting a stamp **(a)**, in general made of PDMS, with ink and then in pressing it by soft-contact onto the surface **(b)**. Compared to NIL, whose resolution has been demonstrated down to 10 nm, the resolution of soft-lithography lies more in the 100 nm range. The resulting pattern is very thin what makes difficult to implement it as an etch mask, however this technique can circumvent the issue of non-planar substrates.

Nano/micro dispensing techniques (not depicted here) of liquid sessile (i.e. attached) droplets (see chapter 6) face a major development for about ten years. The application of these non-lithographic techniques (for example dip-pen lithography [28]) lies mainly in biological assays and refilling of micro/nanofluidics networks.

Finally, the third alternative nanopatterning method is nanostencil lithography (nSL) and is one of the main topics of this thesis. As Figure 1 illustrates it, the principle of this technique is relatively simple. Its implementation is straightforward and requires less process steps compared to other approaches. It is a shadow-mask based parallel technique capable of patterning a full wafer with mesoscopic structures in one single deposition step. In the last few years, its resolution has been continuously pushed down and sub-50 nm patterns have been demonstrated [29].

A major advantage of nSL comes from the fact that it is a resistless non-contact method. In this sense, chemically functionalized and mechanically fragile surfaces can be structured with a wide, potentially unlimited, range of materials. Until a certain limit, surfaces with topography can also be patterned.

Nanostencil lithography is precisely described in chapter 4 and in the framework of this thesis it has been applied to the full-wafer patterning of nano/micromechanical devices on pre-fabricated CMOS substrates.

### III. Nano/micromechanical resonators. Interest and physical features

Nano/micromechanical structures operated in static or dynamic (resonant) mode are potentially extremely versatile sensors depending on the way they are implemented and detected. Very diverse signal domains like magnetic, thermal, electrical, chemical, mechanical, etc... can be transduced with the same structure. In the late 90s, different authors [30, 31] pioneered the development of micromechanical-based multi-sensors taking advantage of scanning probes with nanoscale tip apex. Since then, diverse sensors based on nano/microstructures have been reported.

Nano/micromechanical structures can also be implemented as low-power low phase noise high-Q radio- (RF) and intermediate-frequency (IF) components [32, 33], in particular as filters and reference oscillators.

In all these resonating devices, electrical energy is converted into mechanical energy by exciting one resonant mode. The resulting displacement is then converted back directly (using for instance capacitive or piezoresistive detection schemes) or indirectly (for example optical transducing schemes) into an electrical signal.

Hereafter, a short survey of the different existing types of nano/micromechanical resonators is proposed. The key mechanisms playing upon the resonance quality factor and noise levels of such resonators are discussed. Finally, the main readout methods for the characterization of the frequency response are exposed.

#### III.1. Types of nano/micromechanical resonators

The most classical resonators are singly clamped beams, namely cantilevers. One reason for that is that because of their simple shape, they can be easily modeled. Actually, cantilevers have been extensively studied for a long time both in static (stress-related effects) and dynamic (effects of the viscosity of the surrounding medium) mode. They have been used for a long time for Scanning Probe Microscopy (SPM), consequently their further implementation as versatile sensors has been a natural evolution. In all resonators-based sensing applications, the detection scheme relies on monitoring the mechanical response that is modified by specific physical changes in the environment which can be further quantified.

Cantilevers operated in the quasi-static mechanical regime have been widely used to assess the adsorption of specific (through polymer or gold coating) and non-specific species onto the cantilever through the measurement of deflection changes related to adsorption-induced surface stress [34-43]: DNA hybridization (when the complementary strand links), glucose, alcohol and other odorant analytes have been successfully detected. The advantage of the static approach is that it can be performed in liquids as the viscosity of the environment is not an issue. However, one drawback associated to this approach is that the analyte must be located on one side only (what can be achieved functionalizing one side only).

In dynamic mode, cantilevers can potentially access more information. All the features of its frequency response give indications on external physical effects: resonance frequency shifts with respect to the eigenfrequency (natural resonance frequency, i.e. without any external force) and the value of the Q-factor [44, 45] can be related to the density and viscosity of the surrounding

fluid. Additionally, when some mass is deposited or adsorbed on it, the resulting frequency shift can be dissociated between a decreasing contribution related to the mass and another increasing one related to stiffness [46] or surface stress changes [34]. Some authors have actually measured simultaneously bending and resonance frequency changes [47, 48] to decorrelate these effects.

The other most reported nano/microresonators are flexural doubly clamped beams (bridges) [7, 49, 50], and paddles with doubly clamped beams [51, 52] that are operated in flexion and torsion. Nanowires and nanotubes seem to be promising ultra-high frequency mechanical resonators. A resonator operated in the bulk acoustic (longitudinal extension) mode [53] with high  $Q$  in air has also been demonstrated.

There exist other resonator shapes which are mostly implemented as RF components. In this category, Nguyen and coworkers [33] have promoted for fifteen years the use of MEMS as filters and reference clock oscillators with the target of achieving the highest possible product  $Q$ -factor per resonance frequency. These devices involve a broad range of shapes [33]: in particular comb capacitors transducers [54], free-free beams, wine-glass disks ( $Q=161000$  at 62 MHz in vacuum), contour-mode disks ( $Q=10000$  at 1.5 GHz) and radial-mode disks ( $Q=1500$  at 1.14 GHz). Arrays of coupled resonators that form programmable band-pass filters have also been demonstrated. All these devices are very interesting for two reasons: first they illustrate very well the assumption that structures supported at resonance nodes rather than at their extremities minimize drastically anchor losses and achieve high  $Q$ . Second, they show that a miniaturization towards nanometer scale is not always directly the best solution to achieve high frequencies, in particular for power handling issues (the interface with micro and macro-components is difficult in terms of impedance matching).

This overview will end with the thin-film bulk acoustic resonator (FBAR). This is actually the type of MEMS that is equivalent to bulk acoustic wave macro-resonators (typically quartz-crystal resonators). Structurally, this is a parallel plate capacitor sandwiching a piezoelectric dielectric thin film. An alternate signal applied at the electrodes provokes bulk vibrational modes in the piezo-film. Very high  $Q$ -factors are obtained for frequencies in the GHz range minimizing anchors losses by releasing the membrane. Commercially available devices [55] are already in the market.

### III.2. Mechanisms determining the quality factor and the noise

A given resonance mode is characterized by (i) its resonance frequency, (ii) its amplitude and shape and (iii) its quality factor  $Q$ . Regarding the design and the operation of nano/micromechanical structures, it is important to assess, at least qualitatively, what are the dominant physical phenomena behind the  $Q$ -factor. For sensing and actuating purposes, maximizing the  $Q$ -factor is systematically an objective to pursue to improve the resolution and lower the noise.

Physically, the  $Q$ -factor can be understood as the ratio between the total elastic energy stored in one vibration cycle and the dissipated energy during this cycle, what is approximately equivalent to the ratio between  $f_0$  the resonance frequency and  $\Delta f$  the bandwidth at -3 dB (at the maximum amplitude divided by  $\sqrt{2}$ ):

$$Q = 2\pi \frac{E}{\Delta E} \approx \frac{f_0}{\Delta f} \quad (I.1)$$

In practice, the  $Q$  can be extracted from the resonance spectrum, for example fitting it with a Lorentz function, or can be obtained through the implementation of the “ring-down” technique [56, 57] that consists in brusquely stopping the driving and in monitoring the amplitude decay. Fitting the obtained curve to an exponential one, the  $Q$  can be obtained from the time constant  $\tau_0$  in this way:  $Q = \pi \tau_0 f_0$ .

It is always difficult to determine if energy dissipations affecting the resonance spectrum of the resonator are related to intrinsic or extrinsic processes caused by the detection set-up. The effective  $Q$  factor is the result of the combination of several losses mechanisms [57], in general the damping of the surrounding medium plays a key role but there are also clamping (anchor), thermoelastic, surface and volume-related effects:

$$\frac{1}{Q} = \sum_i \frac{1}{Q_i} = \frac{1}{Q_{CLAMPING}} + \frac{1}{Q_{THERMOELASTIC}} + \frac{1}{Q_{SURFACE}} + \frac{1}{Q_{VOLUME}} + \frac{1}{Q_{VISCOUS}} + \frac{1}{Q_{OTHERS}} \quad (I.2)$$

Some energy losses are localized in resonators clamping anchors [57, 58]. For vertically vibrating cantilevers, Hosaka et al. [59] report that the related  $Q$  factor is approximately given by  $Q_{CLAMPING} = 2.17l^3/t^3$  (where  $l$  and  $t$  are the cantilever length and thickness). To get free of this type of loss, the resonators should be operated in torsional mode or as previously said, they should be supported at vibration nodes (i.e. null motion) and not at their ends.

When the resonator bends, thermoelastic dissipation (TED) [57, 58] is generated owing to the irreversible thermal flux that is created through the device between the compressed and strained sides. In thin resonators (equal or less than few microns), TED is expected to be negligible.

One point on which all experimental data are in agreement concerns surface related losses. Several authors [56-58, 60] have shown experimental measurements demonstrating a clear correlation between increasing surface/volume ratio (when down scaling the devices) and lower  $Q$  factors (in [60], the authors even report a linear trend between both).

Internal losses, related to volume effects, are very difficult to model, however some authors [58] attribute these losses to phonon interactions between structural internal defects (charged impurities). Nano/micromechanical resonators are frequently coated with metal layers to ensure electrical conduction: in this sense the effect of the amount of deposited metal on the  $Q$  factor is investigated [52]. Metals are known to have important internal frictions and it has been experimentally confirmed that the  $Q$ -factor decreases with increasing deposited thickness.

The last main contribution is the damping of the surrounding medium, namely viscous losses. This effect is the one that is maybe the most analytically assessed [45]. For resonators exhibiting  $Q < 100\,000$ , a saturation in the enhancement of the  $Q$  factor is generally observed below pressure levels comprised between 0.1 and 1 mBar [58, 61].

Improving the quality factor of a mechanical structure is not straightforward. However, some guidelines could be the use of (i) crystalline materials as structural materials to reduce internal losses, (ii) surface treatments to passivate the surface in order to suppress free chemical bonds and (iii) a refined mechanical analysis to place adequately the supporting points of the vibrating structure (to reduce clamping-related losses). Surface thermal treatments have yet demonstrated to be effective only in a limited timeframe [57]. Another way recently illustrated in [62, 63] is to use highly strained structures (the exact explication for this is not yet agreed).

With regard to these matters, the fluctuation-dissipation theorem (known as Nyquist-Johnson theorem in electrical circuits) indicates that systems which dissipate energy are necessarily sources of noise [64]. For all kinds of sensing applications implementing resonators in dynamic mode, the frequency stability is an important feature governed both by extrinsic (from the transducer and the readout circuitry) and by intrinsic (related to the nanomechanical part itself) processes [65]. In macro and micro-elements, it is generally considered that the noise is determined by extrinsic processes. In contrast, in nanodevices the fluctuations related to higher sensing sensitivity and ultra-sensitive integrated transducing schemes are likely to become predominant over extrinsic processes.

Focusing on intrinsic processes, three main sources of noise affect the nanoresonator: thermomechanical, temperature and adsorption/desorption fluctuations [64].

Thermomechanical noise is generated because of the thermally driven random motion of the mechanical device:

$$\frac{1}{2} m_{EFF} \omega_0^2 \langle x_{TH}^2 \rangle = \frac{1}{2} k_B T \quad (1.3)$$

where  $m_{EFF}$ ,  $\omega_0$ ,  $x_{TH}$ ,  $k_B$  and  $T$  are respectively the resonator effective mass, the angular resonance frequency, the thermally driven mean-square displacement of the resonator, the Boltzmann constant and the temperature. In fact, the displacement noise also causes frequency fluctuations. The exact calculation depends from the type of readout scheme, either closed or open loop. In any case, this source is generally considered as the dominant one among intrinsic processes.

Because of their small heat capacity [65], NEMS face rather large temperature fluctuations. Since the resonator dimensions and material properties are both temperature dependent, this type of fluctuation will also convert into frequency fluctuations. This trend should amplify in ultra-small devices whose temperature should be lowered to diminish these effects.

Finally, the third main intrinsic noise process is related to permanent adsorption/desorption phenomena taking place on the resonator surface. Indeed, gas molecules located in the vicinity of the resonator constantly adsorb and desorb from its surface, i.e. mass load or unload it, and therefore create permanent resonance frequency fluctuations. This phenomenon is a surface effect; surface passivation should help in reducing the binding energy between gas molecules and the surface.

### III.3. Characterization techniques of frequency response

To characterize either the static or the dynamic mechanical response of nano/micromechanical resonators, several techniques have been reported. We propose to classify them into two categories: (i) techniques requiring an external set-up that cannot be easily miniaturized and integrated on-chip and (ii) techniques that can potentially be integrated on-chip.

In the first category, three main approaches emerge. The first, maybe the most expanded one, relies on optical methods. There exists (i) interference techniques [51, 52, 66-68] based on the Fabry-Pérot interferometer formed by the stack resonator/air gap/substrate and (ii) AFM-based set-up [35, 39, 69] which monitor the reflection of a laser beam off the resonator with a position sensitive photodiode. Resonator deflection is detected through the modification of the impact

point of the beam on the photodiode. The obtained resolution in motion is in the tenth of nanometer, however the micron range size of the laser spot limits the minimum size of the resonator. More generally, the relatively heavy set-up together with the required alignment step between the beam and the resonator constitute serious drawbacks if a portable implementation of the sensor is pursued. The samples measured with an optical technique can be actuated in many different ways: electrostatic (direct [51, 66] or parametric [70]), thermal [71, 72], or piezoelectric [69].

A second important detection methods relies on driving the resonator through the Lorentz force applying a magnetic field and passing a current across the resonator (magnetomotive approach). The resulting motion develops an electromotive voltage whose associated impedance depends upon the oscillation amplitude. Directly measuring this voltage [7, 49, 50, 64, 73] allows accessing the frequency response of the resonator. This method can be applied to almost any structure, its drawback arises from the heavy set-up requiring high magnetic fields. In the same order, resonator with a magnetic structural layer have directly been oscillated applying a time-varying magnetic field. This approach is too restrictive since only resonators fabricated with a magnetic material can be driven.

A third non portable method consists in using atomic force microscopy (AFM) to characterize the dynamic mechanical frequency response. In [74], the AFM is operated in dynamic non-contact mode to study the resonance of a cantilever. In this low force regime, the oscillation amplitudes are registered maintaining the tip at a fix position sweeping laterally. Constantly (but slowly) varying the driving frequency, a resonance ‘image’ is formed. In [75, 76], GHz oscillations of thin-film bulk acoustic resonators (FBAR) are studied according to a different procedure: the AFM tip is placed in contact. A modulated driving signal allows detecting low frequency oscillation amplitudes by means of a lock-in detection technique while driving (electrostatically) the FBAR at GHz frequencies. This method allows determining mode shapes and resonance frequencies in the GHz range. In the framework of this thesis, some preliminary work detailed in annex A.9 has been undertaken at INL (INSA Lyon) to use AFM as a versatile characterization technique of NEMS.

In the second category, we consider electrical readout techniques: piezoelectric [77], capacitive [33, 53, 54, 78-80] and piezoresistive [31, 61, 81, 82]. In N-MEMS, these last two are widely used. Piezoresistive detection is a smart solution that takes advantages of the high gauge factor provided by doped silicon. Basically, the deflection motion generates a change in the piezoresistor resistance. Placing such piezoresistors on a target resonator and on a reference non-driven one, a Wheatstone bridge can be formed to monitor the bending dependent differential output voltage. The principle of the capacitive method is relatively simple and easy to implement as well: the resonator is placed in front of a fixed driving electrode. The parallel plate capacitance thus formed is continuously measured (through its voltage or its current) while driven with an alternate voltage. Around resonance, a mechanical motion appears and modifies the gap between the two plates: a new component of the capacitive current (named motional current) is generated. It is specifically originated by the mechanical motion and maximized at the resonance frequency. This approach is the topic of this thesis and is going to be detailed in chapters 2 and 3.

Following one of these three approaches, smart and portable devices can be fabricated for sensing or actuating applications.

## IV. NEMS-based mass sensors

Nano/micromechanical resonators offer outstanding perspectives to measure ultra-small amounts of mass deposited on them. In the last decade, mass measurements based on resonating nano/microdevices have been a subject of growing interest. The principle of operation is based on the detection of the shift of resonance frequency when a small quantity of mass is deposited on top of the mechanical structure. In general, the smaller the resonator, the more sensitive it is because the relative change of mass is greater.

The reference device used for the purpose of measuring small masses, for example to monitor the deposition of thin layers in the semiconductor industry, is the commercially available quartz crystal microbalance (QCM). With respect to it, micro and nanomechanical resonators may offer drastic advantages in terms of mass sensitivity and system integration. In addition, their small size ensures intrinsically a high spatial resolution.

Hereafter, the basic features of a QCM are described and a survey of implementations of nano/micromechanical resonators as ultra-sensitive mass sensors is proposed. In direct connection with these studies, chapter 6 will present a series of mass sensing experiments based upon NEMS which all use this sensitivity attribute for other purposes than just measuring a small mass. Additionally, a comparison of the performance of QCM and nano/microdevices we have been fabricating will be carried out based on experimental results.

### IV.1. Quartz-crystal microbalances: applications and performance

Owing to their mechanical, electrical and chemical properties, quartz crystals are widely used piezoelectric devices that are very adequate for applications requiring well-controlled frequencies. They are mostly applied as controlling element in reference clock oscillating circuits and as precision microbalances. Due to their piezoelectricity, the application of an alternate voltage on two opposite sides creates bulk acoustic waves resulting in high-Q and high resonance frequency modes.

Quartz-crystal microbalances consist of a thin quartz disc sandwiched between a pair of electrodes. They have been used for a long time to monitor thin film deposition [83, 84] under vacuum or gaseous environments. The development of QCM systems (see for example [www.q-sense.com](http://www.q-sense.com)) for use in fluids or with visco-elastic deposits has dramatically increased the number of applications. In this sense, QCM also serve now to explore the electrochemistry of interfacial processes at electrode surfaces.

The main features of a QCM are an areal mass sensitivity of  $1.2 \cdot 10^{-8} \text{ g.cm}^{-2}.\text{Hz}^{-1}$  and a classical and optimum frequency resolution of 0.1 and 0.005 Hz respectively ([www.inficon.com](http://www.inficon.com)). In chapter 6, the theory of operation of a quartz-crystal with the aim of measuring ultra-thin (subatomic) gold layer thicknesses will be described.

### IV.2. State-of-the-art of mass sensors based on micro/nanomechanical resonators

In this section, a brief survey of existing NEMS-based mass sensors is exposed. According to criteria of mass sensitivity and minimum mass resolution (mass noise floor), we report in Table I -

2 some of the most relevant (according to our opinion) NEMS-based mass sensing experiments we are aware of and discuss them. Then the main applications, the experimental procedure and different ways to improve the mass sensor are discussed.

Research group & year	$f_{RES}$ (MHz)	$S$ (g.Hz <sup>-1</sup> )	$\delta m$ (g) (deposited)	resolution (10 <sup>-18</sup> g)	deposited material	conditions
Caltech [9] 2006	190	0.62 10 <sup>-21</sup> (zepto)	100 10 <sup>-21</sup>	0.02	N <sub>2</sub> (areal)	SiC bridge in ultra-high vacuum at 37 K
Caltech [49] 2004	32.8	0.39 10 <sup>-18</sup> (atto)	40 10 <sup>-18</sup>	2.5	Au (areal)	SiC bridge in ultra-high vacuum at 17 K
Cornell [85] 2004	13.3	≈ 0.1 10 <sup>-18</sup> (atto)	≈ 10 10 <sup>-18</sup>	0.4	Thiolate SAM (punctual)	Polysilicon paddles measured at 3 10 <sup>-6</sup> Torr
Caltech [81] 2007	127	1.4 10 <sup>-21</sup> (zepto)	1 10 <sup>-18</sup>	≈ 0.1 (in air)	chemisorption of di-fluoroethane (areal)	SiC nanocantilevers with metallic piezoresistive layer measured in air
UAB [86] 2007	1.3	0.9 10 <sup>-18</sup> (atto)	1.4 10 <sup>-15</sup>	12	Au (areal)	CMOS metal cantilever in vacuum (6 10 <sup>-7</sup> mBar)

Table I - 2. Main features of five state-of-the art NEMS-based mass sensing experiments in terms of resonance frequency ( $f_{RES}$ ), mass sensitivity ( $S$ ), reported deposited mass ( $\delta m$ ), mass noise floor, deposited material and specific conditions (device, environment, etc...)

The Caltech group (USA) [7, 9, 49, 65] is a leader in this topic and used to apply magnetomotive actuation and electromotive voltage detection schemes in cryogenic chambers (low temperatures and ultra-high vacuum). In [9], the authors suggest that NEMS can potentially provide a one Dalton (mass of a carbon atom) resolution. In [81], they use SiC cantilevers coated with a metallic piezoresistive layer for ultra-sensitive low noise measurements in air. In all the experiments, SiC bridges are embedded in a phase-locked loop (PLL) to directly track the resonance frequency and thereby the shifts related to mass loading.

At Cornell university (USA) [85, 87], they use paddle nanoresonators with optical detection and at UAB (Spain) [86] smart CMOS cantilevers in a capacitive scheme. In those papers, both groups have calibrated the mass sensing performance of their sensor respectively (i) removing a gold accretion of well-known mass (Cornell) and (ii) depositing a MgF<sub>2</sub> layer of well-known thickness (UAB).

The applications provided by this high-resolution mass sensing concept are multiple. Ultimately, the fact of continuously pushing down the mass sensitivity and resolution will allow studying theoretical physical and chemical surface phenomena through the monitoring of the adsorption and desorption of molecules on a surface. Bio-chemical, -medical and-technological applications are very promising, in particular to study molecular interactions. A group of the university of Basel (Switzerland) together with IBM Zürich [37-39, 47, 69] are very active in this field. In [69], they get to measure time-resolved adsorption of small masses based on protein-ligand interactions. For more industrial objectives, such sensors can likely replace in a future QCM to monitor the deposition of thin layers in vacuum in evaporation systems, or in FIB-aided depositions [88].

Depositing a mass on top of a nano/micromechanical resonator results in a resonance frequency shift that is a combination of three contributions: (i) a mass loading leading to a frequency decrease (this is the most general approach in first approximation), but also (ii) a

stiffening effect of the resonating structure caused by the adsorbate [46] and (iii) and an adsorption-induced surface stress [34] which both tend to increase the frequency. In some specific applications, the mass loading effect dominates over the others two: (i) depositing sub-monolayer areal accretions, or (ii) placing a punctual mass accretion at the maximum deflection point [46, 89], or (iii) using low-stress deposition materials.

Concerning the detection technique, capacitive readout seems to generate less temperature fluctuations than optical detection since the laser beam provokes a local heating effect [90], [91]. Electrical mass sensors, either CMOS integrated [78, 86] or discrete [92] capacitive devices and piezoresistive cantilevers [81], relax alignment requirements and may be potentially packaged as portable sensors.

To improve the NEMS-based mass sensing concept in terms of mass sensitivity and mass resolution, several approaches have been proposed. To enhance the sensitivity, Spletzer et al. [93] use mechanically coupled microcantilevers and basing on Anderson mode localization theory, they show that using such devices the relative change in amplitude is much bigger (two-three orders of magnitude) than the relative resonance frequency shifts (what is usually measured), furthermore the amplitude change is relatively independent of Q-factor changes and is quite insensitive to environmental drifts common to both cantilevers. In [94], [95] and [96], the authors insist that both the Q-factor and the mass sensitivity are enhanced using higher resonance modes, either flexural or torsional, provided the deposit is not located at nodal points (i.e. of minimum motion). In [97], the author demonstrates theoretically the intuitive assumption that operating the mass sensor at the onset of the mechanical nonlinear regime ensures a very high sensitivity since the slope is almost infinite at this point. In [98], the authors compare different resonator structural materials (among the ones classically available in a MEMS foundry: Al, Si, Ti, Au, etc.): at constant spring constant, thickness and width, they demonstrate that Al offers the best mass sensitivity. Finally, the authors in [99] study the influence of the resonator shape and suggest that increasing the  $I / A$  ratio (moment of inertia and the cross-section respectively) can help in decreasing the mass noise floor. With regard to this matter, they propose a simplified technological process flow that creates a double-triangle cross section, e.g. with a better  $I / A$  ratio.

## Bibliographical references

1. Petersen, K.E.  
**Silicon as a mechanical material**  
Proceedings of the IEEE, 1982. **70**(5): p. 420-457.
2. Bao, M.-H.  
**Micro Mechanical Transducers**  
Elsevier ed, Vol. 8, 2000, Amsterdam.
3. Rebeiz, G.  
**RF MEMS Theory, design and technology**  
Wiley ed, 2003.
4. Ma, W., R.Q. Zhu, L. Rufer, Y. Zohar, and M. Wong  
**An integrated floating-electrode electric microgenerator**  
Journal of Microelectromechanical Systems, 2007. **16**(1): p. 29-37.
5. Binnig, G. and H. Rohrer  
**Scanning Tunneling Microscopy**  
Surface Science, 1983. **126**(1-3): p. 236-244.
6. Binnig, G., C. Gerber, E. Stoll, T.R. Albrecht, and C.F. Quate  
**Atomic Resolution with Atomic Force Microscope**  
Europhysics Letters, 1987. **3**(12): p. 1281-1286.
7. Ekinci, K.L. and M.L. Roukes  
**Nanoelectromechanical systems**  
Review of Scientific Instruments, 2005. **76**(6).
8. Tang, Z., Y. Xu, G. Li, and N.R. Aluru  
**Physical models for coupled electromechanical analysis of silicon nanoelectromechanical systems**  
Journal of Applied Physics, 2005. **97**(11).
9. Yang, Y.T., C. Callegari, X.L. Feng, K.L. Ekinci, and M.L. Roukes  
**Zeptogram-scale nanomechanical mass sensing**  
Nano Letters, 2006. **6**(4): p. 583-586.
10. Vettiger, P., J. Brugger, M. Despont, U. Drechsler, U. Durig, W. Haberle, M. Lutwyche, H. Rothuizen, R. Stutz, R. Widmer, and G. Binnig  
**Ultrahigh density, high-data-rate NEMS-based AFM data storage system**  
Microelectronic Engineering, 1999. **46**(1-4): p. 11-17.
11. Badzey, R.L. and P. Mohanty  
**Coherent signal amplification in bistable nanomechanical oscillators by stochastic resonance**  
Nature, 2005. **437**(7061): p. 995-998.
12. Badzey, R.L., G. Zolfagharkhani, A. Gaidarzhy, and P. Mohanty  
**A controllable nanomechanical memory element**  
Applied Physics Letters, 2004. **85**(16): p. 3587-3589.
13. Tsuchiya, Y., K. Takai, N. Momo, T. Nagami, H. Mizuta, S. Oda, S. Yamaguchi, and T. Shimada  
**Nanoelectromechanical nonvolatile memory device incorporating nanocrystalline Si dots**  
Journal of Applied Physics, 2006. **100**(9).

14. Schwab, K.C., M.P. Blencowe, M.L. Roukes, A.N. Cleland, S.M. Girvin, G.J. Milburn, and K.L. Ekinci  
**Comment on "Evidence for quantized displacement in macroscopic nanomechanical oscillators"**  
Physical Review Letters, 2005. **95**(24).
15. Gaidarzhy, A., G. Zolfagharkhani, R.L. Badzey, and P. Mohanty  
**Comment on "Evidence for quantized displacement in macroscopic nanomechanical oscillators" - Reply**  
Physical Review Letters, 2005. **95**(24).
16. Gaidarzhy, A., G. Zolfagharkhani, R.L. Badzey, and P. Mohanty  
**Evidence for quantized displacement in macroscopic nanomechanical oscillators**  
Physical Review Letters, 2005. **94**(3).
17. Madou, M.J.  
**Fundamentals of Microfabrication, the Science of Miniaturization (2nd ed.)**  
CRC Press ed, 2002.
18. Chou, S.Y., P.R. Krauss, and P.J. Renstrom  
**Nanoimprint lithography**  
Journal of Vacuum Science & Technology B, 1996. **14**(6): p. 4129-4133.
19. Chou, S.Y., P.R. Krauss, and P.J. Renstrom  
**Imprint lithography with 25-nanometer resolution**  
Science, 1996. **272**(5258): p. 85-87.
20. Chou, S.Y., P.R. Krauss, and P.J. Renstrom  
**Imprint of Sub-25 Nm Vias and Trenches in Polymers**  
Applied Physics Letters, 1995. **67**(21): p. 3114-3116.
21. Xia, Y.N. and G.M. Whitesides  
**Soft lithography**  
Annual Review of Materials Science, 1998. **28**: p. 153-184.
22. Fang, A.P., E. Dujardin, and T. Ondarcuhu  
**Control of droplet size in liquid nanodispensing**  
Nano Letters, 2006. **6**(10): p. 2368-2374.
23. Meister, A., M. Liley, J. Brugger, R. Pugin, and H. Heinzelmann  
**Nanodispenser for attoliter volume deposition using atomic force microscopy probes modified by focused-ion-beam milling**  
Applied Physics Letters, 2004. **85**(25): p. 6260-6262.
24. Brugger, J., J.W. Berenschot, S. Kuiper, W. Nijdam, B. Otter, and M. Elwenspoek  
**Resistless patterning of sub-micron structures by evaporation through nanostencils**  
Microelectronic Engineering, 2000. **53**(1-4): p. 403-405.
25. van den Boogaart, M.A.F.  
**Stencil lithography: an ancient technique for advanced micro- and nanopatterning**  
Hartung-Gorre Verlag ed, Series in Microsystems, Vol. 20, 2006, Konstanz.
26. van den Boogaart, M.A.F., G.M. Kim, R. Pellens, J.P. van den Heuvel, and J. Brugger  
**Deep-ultraviolet-microelectromechanical systems stencils for high-throughput resistless. patterning of mesoscopic structures**  
Journal of Vacuum Science & Technology B, 2004. **22**(6): p. 3174-3177.
27. Schiff, H., L.J. Heyderman, M.A.D. Maur, and J. Gobrecht  
**Pattern formation in hot embossing of thin polymer films**  
Nanotechnology, 2001. **12**(2): p. 173-177.

28. Piner, R.D., J. Zhu, F. Xu, S.H. Hong, and C.A. Mirkin  
**"Dip-pen" nanolithography**  
Science, 1999. **283**(5402): p. 661-663.
29. Vazquez Mena, O., C.W. Park, M.A.F. van den Boogaart, and J. Brugger  
**Nanostencil lithography for nanowire patterning**  
in the proceedings of the *Nanoelectronics Days*. 2006. Aachen, Germany.
30. Berger, R., C. Gerber, H.P. Lang, and J.K. Gimzewski  
**Micromechanics: A toolbox for femtoscale science: "Towards a laboratory on a tip"**  
Microelectronic Engineering, 1997. **35**(1-4): p. 373-379.
31. Boisen, A., J. Thaysen, H. Jensenius, and O. Hansen  
**Environmental sensors based on micromachined cantilevers with integrated read-out**  
Ultramicroscopy, 2000. **82**(1-4): p. 11-16.
32. Motiee, M., R.R. Mansour, and A. Khajepour  
**Micromechanical resonators and filters for microelectromechanical system applications**  
Journal of Vacuum Science & Technology B, 2006. **24**(6): p. 2499-2508.
33. Nguyen, C.T.C.  
**MEMS technology for timing and frequency control**  
IEEE Transactions on Ultrasonics Ferroelectrics and Frequency Control, 2007. **54**(2): p. 251-270.
34. Chen, G.Y., T. Thundat, E.A. Wachter, and R.J. Warmack  
**Adsorption-Induced Surface Stress and Its Effects on Resonance Frequency of Microcantilevers**  
Journal of Applied Physics, 1995. **77**(8): p. 3618-3622.
35. Fritz, J., M.K. Baller, H.P. Lang, H. Rothuizen, P. Vettiger, E. Meyer, H.J. Guntherodt, C. Gerber, and J.K. Gimzewski  
**Translating biomolecular recognition into nanomechanics**  
Science, 2000. **288**(5464): p. 316-318.
36. Fritz, J., M.K. Baller, H.P. Lang, T. Strunz, E. Meyer, H.J. Guntherodt, E. Delamarche, C. Gerber, and J.K. Gimzewski  
**Stress at the solid-liquid interface of self-assembled monolayers on gold investigated with a nanomechanical sensor**  
Langmuir, 2000. **16**(25): p. 9694-9696.
37. Lang, H.P., M.K. Baller, R. Berger, C. Gerber, J.K. Gimzewski, F.M. Battiston, P. Fornaro, J.P. Ramseyer, E. Meyer, and H.J. Guntherodt  
**An artificial nose based on a micromechanical cantilever array**  
Analytica Chimica Acta, 1999. **393**(1-3): p. 59-65.
38. Lang, H.P., M. Hegner, and C. Gerber  
**Nanomechanics - The link to biology and chemistry**  
Chimia, 2002. **56**(10): p. 515-519.
39. Lang, H.P., M. Hegner, E. Meyer, and C. Gerber  
**Nanomechanics from atomic resolution to molecular recognition based on atomic force microscopy technology**  
Nanotechnology, 2002. **13**(5): p. R29-R36.
40. Pei, J.H., F. Tian, and T. Thundat  
**Glucose biosensor based on the microcantilever**  
Analytical Chemistry, 2004. **76**(2): p. 292-297.

41. Hu, Z.Y., T. Thundat, and R.J. Warmack  
**Investigation of adsorption and absorption-induced stresses using microcantilever sensors**  
Journal of Applied Physics, 2001. **90**(1): p. 427-431.
42. Baller, M.K., H.P. Lang, J. Fritz, C. Gerber, J.K. Gimzewski, U. Drechsler, H. Rothuizen, M. Despont, P. Vettiger, F.M. Battiston, J.P. Ramseyer, P. Fornaro, E. Meyer, and H.J. Guntherodt  
**A cantilever array-based artificial nose**  
Ultramicroscopy, 2000. **82**(1-4): p. 1-9.
43. Dareing, D.W. and T. Thundat  
**Simulation of adsorption-induced stress of a microcantilever sensor**  
Journal of Applied Physics, 2005. **97**(4).
44. Chon, J.W.M., P. Mulvaney, and J.E. Sader  
**Experimental validation of theoretical models for the frequency response of atomic force microscope cantilever beams immersed in fluids**  
Journal of Applied Physics, 2000. **87**(8): p. 3978-3988.
45. Sader, J.E.  
**Frequency response of cantilever beams immersed in viscous fluids with applications to the atomic force microscope**  
Journal of Applied Physics, 1998. **84**(1): p. 64-76.
46. Tamayo, J., D. Ramos, J. Mertens, and M. Calleja  
**Effect of the adsorbate stiffness on the resonance response of microcantilever sensors**  
Applied Physics Letters, 2006. **89**(22).
47. Battiston, F.M., J.P. Ramseyer, H.P. Lang, M.K. Baller, C. Gerber, J.K. Gimzewski, E. Meyer, and H.J. Guntherodt  
**A chemical sensor based on a microfabricated cantilever array with simultaneous resonance-frequency and bending readout**  
Sensors and Actuators B-Chemical, 2001. **77**(1-2): p. 122-131.
48. Cherian, S. and T. Thundat  
**Determination of adsorption-induced variation in the spring constant of a microcantilever**  
Applied Physics Letters, 2002. **80**(12): p. 2219-2221.
49. Ekinci, K.L., X.M.H. Huang, and M.L. Roukes  
**Ultrasensitive nanoelectromechanical mass detection**  
Applied Physics Letters, 2004. **84**(22): p. 4469-4471.
50. Blick, R.H., A. Erbe, L. Pescini, A. Kraus, D.V. Scheible, F.W. Beil, E. Hoehberger, A. Hoerner, J. Kirschbaum, and H. Lorenz  
**Nanostructured silicon for studying fundamental aspects of nanomechanics**  
Journal of Physics-Condensed Matter, 2002. **14**(34): p. R905-R945.
51. Evoy, S., D.W. Carr, L. Sekaric, A. Olkhovets, J.M. Parpia, and H.G. Craighead  
**Nanofabrication and electrostatic operation of single-crystal silicon paddle oscillators**  
Journal of Applied Physics, 1999. **86**(11): p. 6072-6077.
52. Olkhovets, A., S. Evoy, D.W. Carr, J.M. Parpia, and H.G. Craighead  
**Actuation and internal friction of torsional nanomechanical silicon resonators**  
Journal of Vacuum Science & Technology B, 2000. **18**(6): p. 3549-3551.
53. Mattila, T., J. Kiihamaki, T. Lamminmaki, O. Jaakkola, P. Rantakari, A. Oja, H. Seppa, H. Kattelus, and I. Tittonen  
**A 12 MHz micromechanical bulk acoustic mode oscillator**  
Sensors and Actuators a-Physical, 2002. **101**(1-2): p. 1-9.

54. Nguyen, C.T.C. and R.T. Howe  
**An integrated CMOS micromechanical resonator high-Q oscillator**  
IEEE Journal of Solid-State Circuits, 1999. **34**(4): p. 440-455.
55. Ruby, R., P. Bradley, J. Larson, III, Y. Oshmyansky, and D. Figueredo  
**Ultra-miniature high-Q filters and duplexers using FBAR technology**  
in the proceedings of the *IEEE International Solid-State Circuits Conference*. 2001.
56. Ono, T. and M. Esashi  
**Effect of ion attachment on mechanical dissipation of a resonator**  
Applied Physics Letters, 2005. **87**(4).
57. Yasumura, K.Y., T.D. Stowe, E.M. Chow, T. Pfafman, T.W. Kenny, B.C. Stipe, and D. Rugar  
**Quality factors in micron- and submicron-thick cantilevers**  
IEEE Journal of Microelectromechanical Systems, 2000. **9**(1): p. 117-125.
58. Mohanty, P., D.A. Harrington, K.L. Ekinici, Y.T. Yang, M.J. Murphy, and M.L. Roukes  
**Intrinsic dissipation in high-frequency micromechanical resonators**  
Physical Review B, 2002. **66**(8).
59. Hosaka, H., K. Itao, and S. Kuroda  
**Damping Characteristics of Beam-Shaped Micro-Oscillators**  
Sensors and Actuators a-Physical, 1995. **49**(1-2): p. 87-95.
60. Carr, D.W., S. Evoy, L. Sekaric, H.G. Craighead, and J.M. Parpia  
**Measurement of mechanical resonance and losses in nanometer scale silicon wires**  
Applied Physics Letters, 1999. **75**(7): p. 920-922.
61. Xu, Y., J.T. Lin, B.W. Alphenaar, and R.S. Keynton  
**Viscous damping of microresonators for gas composition analysis**  
Applied Physics Letters, 2006. **88**(14).
62. Cimalla, V., C. Foerster, F. Will, K. Tonisch, K. Brueckner, R. Stephan, M.E. Hein, O. Ambacher, and E. Aperathitis  
**Pulsed mode operation of strained microelectromechanical resonators in air**  
Applied Physics Letters, 2006. **88**(25).
63. Verbridge, S.S., J.M. Parpia, R.B. Reichenbach, L.M. Bellan, and H.G. Craighead  
**High quality factor resonance at room temperature with nanostrings under high tensile stress**  
Journal of Applied Physics, 2006. **99**(12).
64. Cleland, A.N. and M.L. Roukes  
**Noise processes in nanomechanical resonators**  
Journal of Applied Physics, 2002. **92**(5): p. 2758-2769.
65. Ekinici, K.L., Y.T. Yang, and M.L. Roukes  
**Ultimate limits to inertial mass sensing based upon nanoelectromechanical systems**  
Journal of Applied Physics, 2004. **95**(5): p. 2682-2689.
66. Carr, D.W. and H.G. Craighead  
**Fabrication of nanoelectromechanical systems in single crystal silicon using silicon on insulator substrates and electron beam lithography**  
Journal of Vacuum Science & Technology B, 1997. **15**(6): p. 2760-2763.
67. Carr, D.W., L. Sekaric, and H.G. Craighead  
**Measurement of nanomechanical resonant structures in single-crystal silicon**  
Journal of Vacuum Science & Technology B, 1998. **16**(6): p. 3821-3824.

68. Karabacak, D., T. Kouh, and K.L. Ekinci  
**Analysis of optical interferometric displacement detection in nanoelectromechanical systems**  
Journal of Applied Physics, 2005. **98**(12).
69. Braun, T., V. Barwich, M.K. Ghatkesar, A.H. Bredekamp, C. Gerber, M. Hegner, and H.P. Lang  
**Micromechanical mass sensors for biomolecular detection in a physiological environment**  
Physical Review E, 2005. **72**(3).
70. Carr, D.W., S. Evoy, L. Sekaric, H.G. Craighead, and J.M. Parpia  
**Parametric amplification in a torsional microresonator**  
Applied Physics Letters, 2000. **77**(10): p. 1545-1547.
71. Sekaric, L., M. Zalalutdinov, S.W. Turner, A.T. Zehnder, J.M. Parpia, and H.G. Craighead  
**Nanomechanical resonant structures as tunable passive modulators of light**  
Applied Physics Letters, 2002. **80**(19): p. 3617-3619.
72. Ilic, B., S. Krylov, K. Aubin, R. Reichenbach, and H.G. Craighead  
**Optical excitation of nanoelectromechanical oscillators**  
Applied Physics Letters, 2005. **86**(19).
73. Beil, F.W., L. Pescini, E. Hohberger, A. Kraus, A. Erbe, and R.H. Blick  
**Comparing schemes of displacement detection and subharmonic generation in nanomachined mechanical resonators**  
Nanotechnology, 2003. **14**(7): p. 799-802.
74. Abadal, G., Z.J. Davis, X. Borriase, O. Hansen, A. Boisen, N. Barniol, F. Perez-Murano, and F. Serra  
**Atomic force microscope characterization of a resonating nanocantilever**  
Ultramicroscopy, 2003. **97**(1-4): p. 127-133.
75. Liu, X., A. San Paulo, M. Park, and J. Bokor  
**Characterization of acoustic vibration modes at GHz frequencies in bulk acoustic wave resonators by combination of scanning laser interferometry and scanning acoustic force microscopy**  
in the proceedings of the *IEEE MEMS*. 2005.
76. San Paulo, A. and J. Bokor  
**Scanning acoustic force microscopy characterization of thermal expansion effects on the electromechanical properties of film bulk acoustic resonators**  
Applied Physics Letters, 2005. **86**(8).
77. Kobayashi, T., J. Tsaur, M. Ichiki, and R. Maeda  
**Fabrication and performance of a flat piezoelectric cantilever obtained using a sol-gel derived PZT thick film deposited on a SOI wafer**  
Smart Materials & Structures, 2006. **15**(1): p. S137-S140.
78. Li, Y.C., M.H. Ho, S.J. Hung, M.H. Chen, and M.S.C. Lu  
**CMOS micromachined capacitive cantilevers for mass sensing**  
Journal of Micromechanics and Microengineering, 2006. **16**(12): p. 2659-2665.
79. Abadal, G., Z.J. Davis, B. Helbo, X. Borriase, R. Ruiz, A. Boisen, F. Campabadal, J. Esteve, E. Figueras, F. Perez-Murano, and N. Barniol  
**Electromechanical model of a resonating nano-cantilever-based sensor for high-resolution and high-sensitivity mass detection**  
Nanotechnology, 2001. **12**(2): p. 100-104.
80. Davis, Z.J., G. Abadal, O. Kuhn, O. Hansen, F. Grey, and A. Boisen  
**Fabrication and characterization of nanoresonating devices for mass detection**  
Journal of Vacuum Science & Technology B, 2000. **18**(2): p. 612-616.

81. Li, M., H.X. Tang, and M.L. Roukes  
**Ultra-sensitive NEMS-based cantilevers for sensing, scanned probe and very high-frequency applications**  
Nature Nanotechnology, 2007. **2**(2): p. 114-120.
82. Villanueva, G., J. Montserrat, F. Perez-Murano, G. Rius, and J. Bausells  
**Submicron piezoresistive cantilevers in a CMOS-compatible technology for intermolecular force detection**  
Microelectronic Engineering, 2004. **73-74**: p. 480-486.
83. Narine, S.S., R. Hughes, and A.J. Slavin  
**The use of inductively coupled plasma mass spectrometry to provide an absolute measurement of surface coverage, and comparison with the quartz crystal microbalance**  
Applied Surface Science, 1999. **137**(1-4): p. 204-206.
84. Narine, S.S. and A.J. Slavin  
**Use of the quartz crystal microbalance to measure the mass of submonolayer deposits: Measuring the stoichiometry of surface oxides**  
Journal of Vacuum Science & Technology a-Vacuum Surfaces and Films, 1998. **16**(3): p. 1857-1862.
85. Ilic, B., H.G. Craighead, S. Krylov, W. Senaratne, C. Ober, and P. Neuzil  
**Attogram detection using nanoelectromechanical oscillators**  
Journal of Applied Physics, 2004. **95**(7): p. 3694-3703.
86. Verd, J., A. Uranga, J. Teva, G. Abadal, F. Torres, J. Arcamone, J.L. López, F. Pérez-Murano, J. Fraxedas, J. Esteve, and N. Barniol  
**Monolithic 0.35um CMOS cantilever for mass sensing in the attogram range with self-excitation**  
in the proceedings of the *IEEE Transducers*. 2007. Lyon, France.
87. Ilic, B., Y. Yang, and H.G. Craighead  
**Virus detection using nanoelectromechanical devices**  
Applied Physics Letters, 2004. **85**(13): p. 2604-2606.
88. Friedli, V., C. Santschi, J. Michler, P. Hoffmann, and I. Utke  
**Mass sensor for in situ monitoring of focused ion and electron beam induced processes**  
Applied Physics Letters, 2007. **90**(5).
89. Ramos, D., J. Tamayo, J. Mertens, M. Calleja, and A. Zaballos  
**Origin of the response of nanomechanical resonators to bacteria adsorption**  
Journal of Applied Physics, 2006. **100**(10).
90. Kim, S.J., T. Ono, and M. Esashi  
**Capacitive resonant mass sensor with frequency demodulation detection based on resonant circuit**  
Applied Physics Letters, 2006. **88**(5).
91. Vig, J.R. and Y. Kim  
**Noise in microelectromechanical system resonators**  
IEEE Transactions on Ultrasonics Ferroelectrics and Frequency Control, 1999. **46**(6): p. 1558-1565.
92. Dohn, S., O. Hansen, and A. Boisen  
**Cantilever based mass sensor with hard contact readout**  
Applied Physics Letters, 2006. **88**(26).
93. Spletzer, M., A. Raman, A.Q. Wu, X.F. Xu, and R. Reifengerger  
**Ultrasensitive mass sensing using mode localization in coupled microcantilevers**  
Applied Physics Letters, 2006. **88**(25).
94. Dohn, S., R. Sandberg, W. Svendsen, and A. Boisen  
**Enhanced functionality of cantilever based mass sensors using higher modes**  
Applied Physics Letters, 2005. **86**(23).

95. Sharos, L.B., A. Raman, S. Crittenden, and R. Reifenberger  
**Enhanced mass sensing using torsional and lateral resonances in microcantilevers**  
Applied Physics Letters, 2004. **84**(23): p. 4638-4640.
96. Tseytlin, Y.M.  
**High resonant mass sensor evaluation: An effective method**  
Review of Scientific Instruments, 2005. **76**(11).
97. Buks, E. and B. Yurke  
**Mass detection with a nonlinear nanomechanical resonator**  
Physical Review E, 2006. **74**(4).
98. Davis, Z.J. and A. Boisen  
**Aluminum nanocantilevers for high sensitivity mass sensors**  
Applied Physics Letters, 2005. **87**(1).
99. De Vlaminck, I., K. De Greve, L. Lagae, and G. Borghs  
**Silicon nanomechanical resonators with a double-triangle cross section leading to an enhanced mass sensitivity**  
Applied Physics Letters, 2006. **88**(6).



# CHAPTER 2

## CONCEPTS OF NANO/MICROMECHANICAL RESONATORS FOR MASS SENSING APPLICATIONS WITH ALL ELECTRIC ACTUATION AND DETECTION

I.	Response of micro/nanomechanical resonators-based systems.....	34
I.1.	Equations of oscillating systems.....	34
I.1.a.	Harmonic (undamped non-driven) oscillators.....	34
I.1.b.	Damped non-driven oscillators.....	35
I.1.c.	Driven damped oscillators.....	35
I.2.	Resonance frequency of nano/micromechanical resonators: Analytical modeling.....	37
I.2.a.	General equations.....	37
I.2.b.	Cantilever and bridge.....	40
I.2.b.i)	Cantilever.....	40
I.2.b.ii)	Bridge.....	42
I.2.c.	Quad-beams resonators.....	42
I.3.	Mass sensitivity of nano/micromechanical resonators.....	48
I.3.a.	Calculation of mass sensitivity.....	48
I.3.a.i)	Punctual mass sensitivity.....	48
I.3.a.ii)	Areal mass sensitivity.....	49
I.3.b.	Dynamic linear range.....	50
II.	Electrical response of electrostatically driven resonators.....	51
II.1.	Transduction principle: capacitive detection with electrostatic actuation.....	51
II.2.	Equivalent electrical modeling of a mechanical resonator.....	52
II.2.a.	Global equivalent electrical scheme.....	52
II.2.b.	RLC equivalent model of the motional impedance.....	54
II.2.b.i)	Phenomenological approach of a RLC oscillator.....	54
II.2.b.ii)	Parameters calculation.....	57
II.2.c.	Global response.....	59
II.3.	Response to electrostatic actuation.....	60
II.3.a.	Deflection and pull-in voltage related to electrostatic force.....	60
II.3.b.	Spring-softening effect.....	62

## Chapter 2. Concepts of nano/micromechanical resonators for mass sensing applications with all electric actuation and detection

---

II.3.c.	Generalization .....	63
III.	Two approaches of flexural mode resonators: Out-of-plane and in-plane vibrating resonators .....	65
III.1.	Out-of-plane flexion mode resonators .....	65
III.1.a.	Comparison in terms of electrical response of three discrete devices with simplified RLC model .....	65
III.1.b.	Comparison in terms of mass sensitivity (punctual and distributed).....	67
III.1.b.i)	Punctual mass sensitivity .....	67
III.1.b.ii)	Distributed mass sensitivity.....	67
III.1.c.	Analysis of the quad-beams device.....	68
III.1.c.i)	Electromechanical modeling.....	68
III.1.c.ii)	Fabrication of discrete devices: e-beam lithography on SOI .....	70
III.1.c.iii)	Measurement of discrete devices .....	72
III.2.	In-plane flexion mode resonators. Cantilevers .....	74
	Conclusion of chapter 2.....	76
	Bibliographical references .....	77

The concept of measuring ultra-small masses using resonating micro and nanomechanical devices has been a subject of growing interest in the last few years [1-3]. The principle of operation is based on the detection of the shift of resonance frequency when a small quantity of mass is deposited on top of the mechanical structure. In general, the smaller the resonator, the more sensitive it is because the relative change of mass is greater. Compared to quartz crystal microbalances (QCM), micro and nanomechanical resonators may offer advantages in terms of sensitivity and system integration. In addition, if they are small enough, they can provide mass sensing with spatial resolution (concept of spatially localized detection).

For the readout of resonator oscillations, magnetomotive [3-5] and optical characterization techniques are the most cited in the literature. The first requires a heavy set-up while the second offers very high resolution under various configurations (through interferometric technique [6, 7] or with atomic force microscopy (AFM) based set-ups). However, with the aim of conceiving a portable and non-invasive system, our research has been focused on a purely electric actuation and detection method. The reasons of this choice and the features of this technique will be exposed later in this chapter.

In relation with this aspect, this thesis has been focused on the study of silicon based micro and nanomechanical devices since they can be fabricated in batch using standard silicon technology process and they can be combined with CMOS technology to fabricate monolithic integrated microsystems. It allows the assembly of arrays and matrices of resonators [8, 9], and the development of portable systems with integrated read-out circuitry for signal processing and conditioning. With regard to this matter, the monolithic integration of nano/micromechanical resonators [10, 11] is precisely the topic of chapters 3, 4 and 5.

In this chapter, the basic physical concepts related to the application of silicon nano/micromechanical resonators as ultra-sensitive mass sensors will be tackled. First, the prediction of their mechanical frequency response will be studied.

## **Chapter 2. Concepts of nano/micromechanical resonators for mass sensing applications with all electric actuation and detection**

---

Second, their electrical response to electrostatic actuation will be analyzed: in particular the issue of converting a mechanical motion into an electrical signal with a capacitive readout scheme will be addressed. Then it will be explained how to model such a mechanical component like an electrical element. This will help in predicting the resonance signal level and open up possibilities of performing SPICE-type simulations for the study of the coupled system resonator/CMOS circuit. Then, the influence of the excitation signal upon the mechanical frequency response will be analyzed.

Third, two ways of operating micromechanical resonators will be studied: in their out-of-plane and in their in-plane flexural mode. Both modes of operation have well distinct features and these will be compared in terms of electrical and sensing performances.

## I. Response of micro/nanomechanical resonators-based systems

This section describes the general behavior of a mechanical oscillator. We will consider in detail the calculation of the mechanical resonance frequency for three specific shapes:

- cantilevers, i.e. singly clamped beams (only anchored at one end)
- bridges, i.e. doubly clamped beams
- quad-beams (QB), that consist of a central plate with four beams

Finally, the basic modeling for obtaining the mechanical mass sensitivity will be developed.

### I.1. Equations of oscillating systems

The description of a mechanical resonator as a harmonic oscillator is useful to catch the main features of a resonant structure. In this sense, the simplest way to model a mechanical resonator is the mass-spring system (Figure 1):

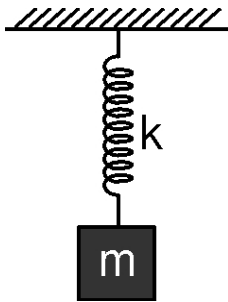


Figure 1. Mass spring system

$m$  is the dynamic (or effective) mass of the system,  $k$  is the spring constant (or stiffness). Both depend on the vibration mode and on the characteristics of the applied force (uniformly or punctually applied, and at which point). By solving the equation of motion, the resonance frequency can be addressed.

In the following section, three general configurations of force balances are tackled.

#### I.1.a. Harmonic (undamped non-driven) oscillators.

In a first and simplified approach, the oscillator is considered purely harmonic, what means that (i) the damping of the medium in which dynamic motion occurs is not considered and that (ii) no external force drives it. Then, only the spring force acting in the opposite direction of the spring stretching intervenes. It is proportional to the displacement  $x$  and the stiffness  $k$ . The balance is:

$$F = -kx = m \frac{d^2x}{dt^2} \quad (\text{II.1})$$

a general solution is  $x = A \sin(\omega t + \varphi)$ . From eq.(II.1), we deduce:

$$\omega_0 = 2\pi f_0 = \sqrt{\frac{k}{m}} \quad (\text{II.2})$$

where  $\omega_0$  is the natural angular resonance frequency, and  $f_0$  the natural resonance frequency also named eigenfrequency.

### I.1.b. Damped non-driven oscillators.

Let us consider now a damping force acting on the resonator and arising from the surrounding medium (air, liquid, etc...). The damping is modeled as a force proportional to the displacement velocity that acts in the opposite direction of the bending. Compared to eq.(II.1), one additional term must be included in the force balance:

$$-kx - D \frac{dx}{dt} = m \frac{d^2x}{dt^2} \quad (\text{II.3})$$

$D$  is called coefficient of damping force. Rewriting eq.(II.3) and given  $\omega_0^2 = \frac{k}{m}$ , then:

$$\ddot{x} + 2n \dot{x} + \frac{k}{m} x = 0 \quad \text{with } n = \frac{D}{2m} \quad (\text{II.4})$$

The solutions of this homogeneous differential equation are given by  $\lambda^2 + 2n\lambda + \omega_0^2 = 0$ . This results in:

$$\lambda_{1,2} = -n \pm \sqrt{n^2 - \omega_0^2} \quad (\text{II.5})$$

The response of the system can be discussed according to the ratio  $\xi = \frac{n}{\omega_0}$ :

- case of slight damping,  $n < \omega_0$ , then  $\lambda_{1,2} = -n \pm i\sqrt{\omega_0^2 - n^2}$ . One solution is:

$$x = Ae^{-nt} \sin\left(\sqrt{\omega_0^2 - n^2}t + \alpha\right) = Ae^{-nt} \sin(\omega_D t + \alpha) \quad (\text{II.6})$$

with

$$\omega_D = \sqrt{\omega_0^2 - n^2} = \omega_0 \sqrt{1 - \xi^2} \quad (\text{II.7})$$

This means that the system oscillates at a certain angular frequency with a time decreasing amplitude (first term of the solution).

$\omega_D$  is the angular resonance frequency of the oscillator in presence of slight damping, it differs from pure resonance towards lower values depending on the magnitude of the damping coefficient  $n$ . In practice, in air,  $\omega_0$  and  $\omega_D$  differ very few.

- for critical damping and heavy damping ( $n \geq \omega_0$ ), no oscillations occur, only a limited displacement returning to stationary position.

### I.1.c. Driven damped oscillators

In practice, mechanical systems are always confronted to damping arising from both the surrounding medium and internal energy losses (c.f. chapter 1).

This requires a permanent external solicitation to provide energy in order to maintain the oscillations; this is the so-called forced regime in which a periodic external force is applied. Let us formulate again the balance with a sinusoidal external excitation:

$$m \frac{d^2 x}{dt^2} + c \frac{dx}{dt} + kx = F_{exc}(t) = F_0 \sin(\omega t) \quad (II.8)$$

A solution is  $x = x_1 + x_2$ , where  $x_1$  is the solution of the homogeneous differential equation like eq.(II.6). For  $x_2$  we assume:  $x_2 = W_2 \sin(\omega t - \varphi)$ . Setting  $A = \frac{F_0}{m}$ , so:

$$W_2 = \frac{A}{\sqrt{(\omega_0^2 - \omega^2)^2 + 4n^2 \omega^2}} \text{ and } \varphi = \arctan \frac{2n\omega}{\omega_0^2 - \omega^2} \quad (II.9)$$

Transient oscillations arising from  $x_1$  are disregarded; only the steady solution  $x_2$  is considered. The frequency of the steady vibration is the same as the one of the driving force, but there is a phase lag  $\varphi$  (function of free vibration frequency  $f_0$ , driving force  $F_0$  and damping coefficient  $n$ ). According to eq.(II.9), there is a  $180^\circ$  phase change around  $f_0$ . From the expression of  $W_2$ , the Q-factor can be theoretically estimated as:

$$Q \approx \frac{1}{2\xi} = \frac{\omega_0}{2n} \quad (II.10)$$

The resonance frequency  $f_r$  corresponds to a maximum in amplitude, in other words when  $W_2$  is maximized. It is actually shifted downward with respect to  $f_0$  according to:

$$f_r = f_0 \sqrt{1 - 2\xi^2} \quad (II.11)$$

From eq.(II.11), we learn that, theoretically, if  $\xi \geq 0.7$ , the peak would disappear.

As an example, the amplitude-frequency response given by eq.(II.9) is plotted for  $A=1$ ,  $\omega_0=1$ , and  $n=0.05, 0.125, 0.25, 0.375$  and  $0.5$ . It is clear from this graph that the higher is  $n$ , the lower are the peak magnitude and the quality factor (see eq.(II.10)). Furthermore, the resonance frequency is clearly shifted down to lower values when  $n$  increases:

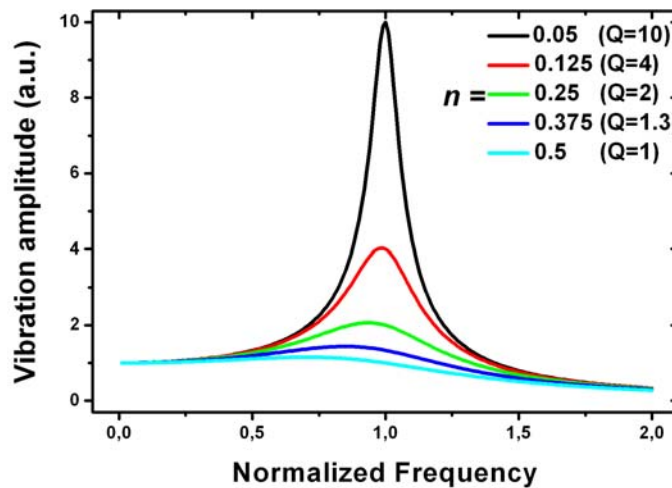


Figure 2. Amplitude-frequency response normalized to a frequency of 1 for several  $n$  factors

As a conclusion, and after validation of this observation based on experimental results, in practice our resonators (operated either in air or vacuum) are always in the case of slight damping, and thereby  $f_0$ ,  $f_D$  and  $f_r$  are very close to each other. Indeed, Q-factors of at least 10 have always been observed: according to eq.(II.10), this corresponds to  $\xi = 0.05$ . Consequently, the resonance frequency of the driven damped resonator is  $f_r = 0.997 f_0$  following eq.(II.11).

A practical consequence of this is that if we wish to theoretically predict the resonance frequency of nano/micromechanical devices, in first approximation the effects of driving and damping do not need to be taken in account.

## **I.2. Resonance frequency of nano/micromechanical resonators: Analytical modeling**

This section deals with mechanics of nano/micromechanical elements and, in particular, with methods allowing the determination of the resonance frequency. An analytical approach is followed trying to find out direct methods for three different resonator shapes: cantilever, bridge and quad-beams. The analytical study of most practical problems give good enough results for design optimization, as in most cases the performances of mechanical sensors are more significantly affected by process variations than by analytical approximations.

Our samples have dimensions in the micron and submicron scale (typically between 200 nm and 20  $\mu\text{m}$ ), but still equations of macroscopic elastic continuum mechanics are employed. The experimental results will further justify this approach since these laws still seem to predict relatively accurately the resonance frequency at these scales, in other words no mechanical effect specifically related to the nanoscale has been significantly observed.

### **I.2.a. General equations**

#### **EULER-BERNOULLI EQUATION**

This approach [12] is also called method of differential equations. This is a fundamental method for finding the vibration frequencies and the shape functions of all the vibration modes. In principle, it can be applicable to any structure but very often numerical methods are needed due to the complexity of the calculation. Here, the study is restricted to the relatively simple case of beam structures.

The free vibration of a beam at small amplitude can be described by a partial differential equation. According to section I.1, the calculation can be simplified neglecting the damping and driving forces. Then, making a balance of forces on an element section of a beam (provided the ratio length/thickness is much larger than 1) and neglecting its own loading (gravitational force), the Newton's law can be written under the form [12]:

$$\rho_m A \frac{\partial^2 w}{\partial t^2} + E I \frac{\partial^4 w}{\partial x^4} = 0 \quad (\text{II.12})$$

where  $A$  is the cross-section area,  $w$  is the displacement in the direction of vibration,  $x$  is the cantilever length axis,  $t$  is the time,  $\rho_m$  is the cantilever material density,  $E$  is the Young modulus

(according to elastic Hooke's law).  $I$  is the moment of inertia of the beam for out-of-plane motions and is given by:

$$I = \int_{-h/2}^{h/2} z^2 b(z) dz = \frac{bh^3}{12} \quad (\text{II.13})$$

where  $b$  and  $h$  are respectively the beam width and thickness

A general solution is a linear combination of each mode of vibration:

$$w(x,t) = \sum_{i=0}^n C_i \sin(\omega_i t + \varphi_i) \phi_i(x) \quad (\text{II.14})$$

where  $\omega_i$  is the resonance frequency and  $\phi_i$  the shape of the  $i^{\text{th}}$  mode.

Thus, eq.(II.12) can be reduced to  $\frac{\partial^4 \phi_i}{\partial x^4} = -\frac{\rho_m A \omega_i^2}{EI} \phi_i$  of which a solution is:

$$\phi_i(x) = a_i \cos\left(\frac{x}{\kappa_i}\right) + b_i \cosh\left(\frac{x}{\kappa_i}\right) + c_i \sin\left(\frac{x}{\kappa_i}\right) + d_i \sinh\left(\frac{x}{\kappa_i}\right) \quad (\text{II.15})$$

where  $\kappa_i = \sqrt[4]{\frac{EI}{\rho_m A \omega_i^2}}$

Then, depending on the considered structure (singly, doubly clamped, etc...), specific boundary conditions must be applied to  $\phi_i$  so that the detailed expression of  $\omega_i$  can be extracted.

#### RAYLEIGH-RITZ METHOD [12]

In this method also, the mechanical properties of silicon nano and microstructures are assumed to be ideally elastic and homogeneous. In these conditions, the vibration frequency of a specific mode can be determined if the shape function of this mode is known. The problem is that in general it is not straightforward to foresee the shape functions of complex structures. However, the vibration frequency of the fundamental mode (i.e. with the lowest resonance frequency) whose shape function is generally known, can be found with high accuracy (however the result provided by this method will always be only an approximation of the real eigenfrequency).

The strategy to follow is to find first the shape function  $w(x)$ . For this purpose, the total bending moment  $M(x)$  acting on the beam is expressed. This is a classical approach in mechanics that consists in calculating the integral of the moment of forces across the cross section of the beam. This expression can be put under the form [12]:

$$M(x) = \int z dF = -EI w''(x) \quad (\text{II.16})$$

where  $x$  is the cantilever length axis,  $E$  is the Young modulus,  $I$  the moment of inertia of the beam and  $w''(x)$  is the second derivative of the shape function with respect to  $x$ .

Eq. (II.16) can be applied to any specific beam-like structure adapting the left part  $[M(x)]$  of the equation by making the adequate balance of the moments and applying the specific boundary conditions. Hence,  $w''(x)$  must be twice integrated so that  $w(x)$  (the so-called shape function) is finally determined.

The total potential energy (related to the bending) and kinetic energy of the whole beam are respectively [12]:

$$E_p = \frac{1}{2} \int_0^l E I(x) w''^2(x,t) dx \quad (II.17)$$

$$E_k = \frac{1}{2} \int_0^l \rho b(x) h(x) \left( \frac{dw}{dt} \right)^2 dx \quad (II.18)$$

where  $b(x)$ ,  $h(x)$  and  $l$  are the beam width, thickness and length respectively ( $x$  is still axis in the direction of the length). In general, the vibration of a beam structure can be described by:

$$w(x,t) = \sum_{n=0}^{\infty} c_n w_n(x,t) = \sum_{n=0}^{\infty} c_n [w_n(x) \sin(\omega_n t + \varphi_n)] \quad (II.19)$$

where  $w_n(x,t)$  indicates a specific vibration mode (with specific coefficient  $c_n$ ) corresponding to a sinusoidal vibration of frequency  $\omega_n$  and whose shape function is  $w_n(x)$ . Mathematically,  $w_n(x,t)$  are the eigenfunctions of the vibration system.

Computing eq. (II.17) and (II.18) with eq.(II.19), the potential and kinetic energy can be expressed for each mode thus containing a time-varying sinusoidal component:

$$E_p = \frac{1}{2} c_n^2 \int_0^l E I(x) w_n''^2(x) \sin^2(\omega_n t + \varphi_n) dx \quad \text{and} \quad E_k = \int_0^l \rho b(x) h(x) w_n^2(x) \omega_n^2 \cos^2(\omega_n t + \varphi_n) dx \quad (II.20)$$

According to the principle of energy conservation ( $E_{Pmax} = E_{Kmax} = E$ ), both maximum are equal:

$$E_{Pmax} = \frac{1}{2} c_n^2 \int_0^l E I(x) w_n''^2(x) dx = E_{Kmax} = \frac{1}{2} c_n^2 \int_0^l \rho b(x) h(x) w_n^2(x) \omega_n^2 dx \quad (II.21)$$

From that, the angular resonance frequency contained in the term of kinetic energy can be extracted to define the so-called Rayleigh-Ritz quotient [12] that provides the radial resonance  $\omega_n$  frequency for any vibration mode:

$$\omega_n^2 = \frac{\int_0^l E I(x) w_n''^2(x) dx}{\int_0^l \rho b(x) h(x) w_n^2(x) dx} \quad (II.22)$$

I.2.b. Cantilever and bridge

I.2.b.i) Cantilever

Beams clamped in one side only are named cantilevers. This is the simplest resonator design.

In this section, the cantilever dimension in the direction of vibration will be named  $h$ .

Following the Euler-Bernoulli approach, the following boundary conditions are applied to eq.(II.15):

$$\phi_1(0) = 0, \phi_1'(0) = 0 \text{ and } \phi_1''(l) = 0$$

what results in:

$$\omega_1 = 1.015 \sqrt{\frac{E}{\rho_m}} \frac{h}{l^2} \text{ and } \omega_2 = 6.361 \sqrt{\frac{E}{\rho_m}} \frac{h}{l^2} \quad (\text{II.23})$$

and more generally

$$\omega_n = \sqrt{\frac{(2n-1)^4 \pi^4}{192}} \sqrt{\frac{E}{\rho_m}} \frac{h}{l^2} = \psi_n \sqrt{\frac{E}{\rho_m}} \frac{h}{l^2} \quad [\text{13}] \quad (\text{II.24})$$

where  $\psi_n$  is a constant depending on the vibration mode.

A second approach, more convenient to subsequently estimate the mass sensitivity of the device, is to rely on the equation of a mass-spring system (eq.(II.2)):  $\omega_n = \sqrt{\frac{k_n}{m_{EFF\_n}}}$ , what implies the separate determination for a given mode  $n$  of (i) the cantilever stiffness  $k_n$ , and (ii) its effective mass  $m_{EFF\_n}$ . Nevertheless, in the case of a cantilever, this formula must be manipulated with caution since the mass is not located in one single point at the extremity, like in the mass-spring model originating this formula, but uniformly distributed. Consequently a corrective term  $\alpha_{1\_n}$  must be applied to  $m$  in order to obtain the efficient mass  $m_{EFF\_n}$ :

$$m_{EFF\_n} = \alpha_{1\_n} m = \alpha_{1\_n} l b h \quad (\text{II.25})$$

Regarding the stiffness  $k_n$ , it depends on the point of application of the force and on its distribution upon the cantilever. Another corrective term  $\alpha_{2\_n}$  needs to be applied:

$$k_n = \alpha_{2\_n} \frac{E h^3 b}{l^3} \quad (\text{II.26})$$

Books of Mechanics (for example [12]) generally provide the value of  $\alpha_{2\_n}$  in general cases. Considering eq.(II.24), it comes that  $\alpha_{1\_n}$  can be deduced from  $\alpha_{2\_n}$  through the relation:

$$\alpha_{1\_n} = \frac{\alpha_{2\_n}}{\psi_n^2} \quad (\text{II.27})$$

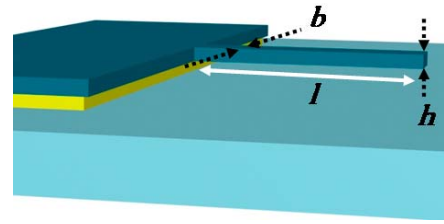


Figure 3. Cantilever resonator.  $l$ ,  $h$  and  $b$  are its length, thickness and width respectively

Table II - 1 reports  $\alpha$  coefficients for the fundamental flexural mode (here, out-of-plane) in two common cases:

	$\alpha_1$	$\alpha_2$
Punctual force applied at the free end	0.243	0.25
Distributed force uniformly applied on the cantilever	0.647	$\frac{2}{3}$

Table II - 1.  $\alpha$  coefficients of a cantilever for two different force loadings

A third approach consists in employing the Rayleigh-Ritz method. Relying on the balance of bending moments, it becomes relatively easy to evaluate the resonance frequency of a cantilever with and without a mass at the free end. Following the strategy previously exposed, the shape function of a cantilever under an uniform load  $F_U$  of any nature is given by [12]:

$$w(x) = \frac{F_U}{2Ebh^3} x^2 (x^2 - 4lx + 6l^2) \quad (\text{II.28})$$

what results in the following expression after making the Rayleigh-Ritz quotient (eq.(II.22)):

$$\omega_1 = 1.019 \sqrt{\frac{E}{\rho_m}} \frac{h}{l^2} \quad (\text{II.29})$$

Comparing with eq.(II.23), one can notice that the value provided by this method is slightly higher but extremely close to it ( $\psi_1=1.019$  with this method instead of 1.015).

Following again the strategy previously exposed, we try to calculate the resonance frequency of a cantilever loaded at its free end with a punctual force  $F_P$  (for example with a mass much larger than its own mass). First, the shape function is estimated through a balance of moments without taking into account the mass of the beam, so that the shape expression is much simplified [12]:

$$w(x) = \frac{2F_P}{Ebh^3} x^2 (3l - x) \quad (\text{II.30})$$

Then, the Rayleigh-Ritz quotient (eq.(II.22)) is calculated including also the beam mass (by integrating it along its length) in the term of kinetic energy what gives:

$$\omega_1 = \sqrt{\frac{Ebh^3}{4\left(M + \frac{33}{140}M_b\right)L^3}} \equiv \sqrt{\frac{k_{BEAM}}{m_{TOTAL}}} \quad (\text{II.31})$$

where  $M_b$  is the beam mass,  $M$  the mass located at the free end,  $k_{BEAM} = \frac{Ebh^3}{4L^3}$  and  $m_{TOTAL} = M + \frac{33}{140}M_b$ .  $k_{BEAM}$  corresponds to the stiffness for a punctual force applied at the free

end ( $\alpha_2=0.25$ ); while  $m_{TOTAL}$  expresses the equivalent mass of the beam in a mass-spring model. If  $M=0$ , then it comes that:

$$\omega_1 = 1.03 \sqrt{\frac{E}{\rho_m} \frac{h}{l^2}}, \text{ not differing much from eq. (II.23)}$$

This demonstrates that the Rayleigh Ritz quotient is sufficiently accurate even with approximated shape functions.

### I.2.b.ii) Bridge

The doubly clamped beam, also named bridge, is rigidly anchored at its two extremities.

In this section, the bridge dimension in the direction of vibration will be named  $h$ .

Following the Euler-Bernoulli approach, the following boundary conditions are applied to eq.(II.15):

$$\phi_1(0) = \phi_1(l) = 0, \quad \phi_1'(0) = \phi_1'(l) = \phi_1'\left(\frac{l}{2}\right) = 0$$

Following the second approach of previous section whereby the angular resonance frequency is estimated basing on the mass-spring model,  $\alpha$  coefficients and angular resonance frequency are reported in Table II - 2 for the fundamental out-of-plane flexural mode in two common cases:

	$\alpha_1$	$\alpha_2$	$\omega_1$
Punctual force applied at the mid-point	0.379	16	$6.5 \sqrt{\frac{E}{\rho_m} \frac{h}{l^2}}$
Distributed force uniformly applied on the cantilever	0.757	32	

Table II - 2.  $\alpha$  coefficients of a bridge for two different force loadings

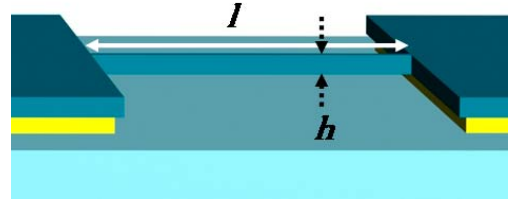


Figure 4. Bridge resonator.  $l$  and  $h$  are its length and thickness respectively.  $b$ , not depicted here, is the bridge width.

### I.2.c. Quad-beams resonators

A quad-beam (QB) resonator is formed by a central plate and four (doubly clamped) beams (Figure 5).

This configuration is a nice example of structure intrinsically equivalent to a spring-mass system in the sense that both elements are well dissociated: on one part four beams acting like a spring of negligible mass, and on another a plate, that does not deform, acting as a mass.

By shrinking the dimensions of the beams down to the micron/submicron range, resonance frequencies in the MHz can be attained for the out-of-plane flexural fundamental mode while maintaining the central plate area relatively large.

This large area is an advantage regarding the capacitive coupling with the substrate (as it will be detailed in section II, the technique of resonance detection we employ is capacitive).

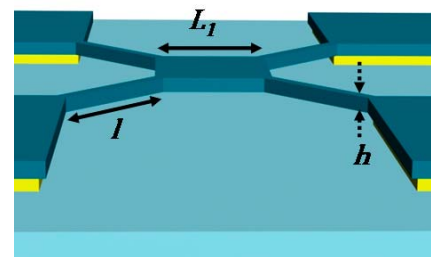


Figure 5. Quad beam resonator with a central square plate of width  $L_1$ , and four beams of length and thickness of  $l$  and  $h$  respectively.  $b$ , not depicted here, is the width of the beams.

Concerning the further objective of implementing the device as a mass sensor (depositing mass on the central plate), the QB is adequate for the following reasons:

- mechanically speaking, it remains relatively insensitive both to the adsorbate stiffness (which ensures the mass loading effect is mechanically dominant [14-16]) and to the adsorbate position within the central plate. On the opposite, a cantilever is very sensitive to the location of the adsorbate [17].
- the large area of the central plate makes more convenient the deposition of particles or the dispensing of liquid for their mass measurement.

In order to find out the most accurate way to predict the resonance frequency, a comparison between several approaches is undertaken, all based on more or less refined Rayleigh-Ritz methods. Methods 1, 2 and 3 are the most simple (the effect caused by the underetching of the anchors is neglected), although methods 4 and 5 are more complex as they do take into account the effect of the underetching of the anchors and the own mass of the beams.

According to Figure 5, the following dimensions are defined:  $L_1$  as plate width (square shaped plate),  $l$  as beam length,  $b$  as beam width,  $h$  as structural layer thickness.  $E$  is the Young modulus,  $\rho$  the polysilicon density (structural material),  $\omega$  the angular frequency,  $m$  the plate mass ( $= \rho L_1^2 h$ ) and  $m_b$  the mass of one single beam ( $= \rho l w h$ ). Quad-beams with diagonal beams (like in Figure 5) and with parallel beams have been analyzed. In methods 1, 2 and 3, these two configurations do not require separate calculations. On the contrary, when considering the effect of the underetching of the anchors, like in methods 4 and 5, both cases must be dissociated.

**Method 1** The Rayleigh-Ritz method is applied to an anchored beam with final mass  $m/4$  (one quarter of the central plate mass). The own mass of the beams is neglected and the effect caused by the underetching of the anchors as well. Making a balance of the bending moments, a punctual force  $F_p$  is considered at the end of each beam (on the side of the central plate):

$$M(x) = -EIw''(x) = F_p x - M_0 \quad (\text{II.32})$$

where  $M_0$  is a restrictive moment to be determined. Here  $w(0)=w'(0)=0$ ,  $w(l)=0$  and  $w'(l/2)=0$ , so  $M_0 = \frac{1}{2} F_p l$  and  $EIw''(x) = F_p \left( \frac{l}{2} - x \right)$ , so  $w''(x) = \frac{12 F_p}{E b h^3} (l/2 - x)$ . After a double integration, the shape function is obtained:

$$w(x) = \frac{F_p}{E b h^3} \left( \frac{l x^2}{4} - \frac{x^3}{3} \right) \quad (\text{II.33})$$

The Rayleigh-Ritz quotient is applied to this shape function. In the term of kinetic energy, we only consider the punctual mass  $m/4$  located at the beam end ( $x=l$ ):

$$\omega_1^2 = \frac{\int_0^l EI(x)w''^2(x)dx}{\frac{1}{4}mw^2(l)} \quad (\text{II.34})$$

what results in:

$$\omega_1 = \sqrt{\frac{4Eb h^3}{ml^3}}, \text{ equivalent to } \omega_1 = 2\sqrt{\frac{E}{\rho_m} \frac{h b^{0.5}}{L_1 l^{1.5}}} \quad (\text{II.35})$$

**Method 2** Eq.(II.31) is taken as a basis. This corresponds to the case of a cantilever beam: (i) loaded with a punctual mass located at its moving end and (ii) whose own mass is also taken into account. However here, the total spring constant is assumed to be equal to four times the one of a single beam:

$$\omega_1 = \sqrt{4 \left( \frac{Eb h^3}{4l^3} \right) \frac{1}{\left( m + \frac{33}{140} m_b \right)}} = \sqrt{\frac{Eb h^3}{\left( m + \frac{33}{140} m_b \right) l^3}} \quad (\text{II.36})$$

**Method 3** A similar approach to method 2 is followed, but considering a spring constant of one single beam that is loaded at its moving end with a punctual mass  $m/4$ .

$$\omega_1 = \sqrt{\frac{Eb h^3}{4l^3} \frac{1}{\left( \left[ \frac{m}{4} \right] + \frac{33}{140} m_b \right)}} = \sqrt{\frac{Eb h^3}{\left( m + \frac{132}{140} m_b \right) l^3}} \quad (\text{II.37})$$

In practice, the results provided by methods 2 and 3 are very close since the beam mass is rather small compared to the plate mass.

Now, more exhaustive methods are going to be detailed. The related calculations have required the use of the *Mathematica* software ([www.wolfram.com](http://www.wolfram.com)) and the resulting analytical expressions are so long and complex that they are not provided in this manuscript. Hereafter, we describe and insist on the guidelines of these calculations.

**Method 4** In this method, the aim is to calculate the resonance frequency of diagonal or parallel quad-beams taking into account the effect caused by the underetching of the anchors but neglecting the mass of the four beams.

The anchor underetching arises from the wet etching performed to release the central plate. In Figure 6, a quad-beam (fabricated at CNM in the framework of this thesis) is depicted. It has been successfully released but the counter consequence is that the anchors of the four beams are also underetched over a distance  $S$  since the etching is isotropic. In first approximation, this extension  $S$  is equivalent to the half-width of the plate:

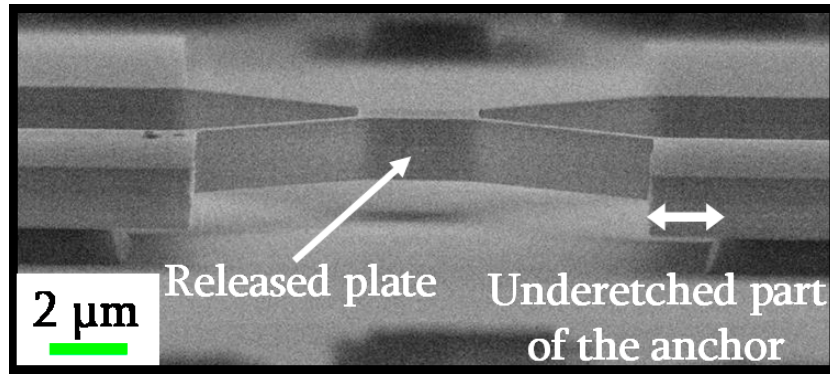


Figure 6. SEM image of a Si quad-beam with underetched anchors

### DIAGONAL QUAD-BEAMS

The first step is to make the balance of bending moments:

$$M(x) = -EI w''(x) = F_p x - M_0 \quad (\text{II.38})$$

The boundary conditions are:  $w(0)=w'(0)=0$ ,  $w'(l)=0$ . However here,  $w''(l/2)=0$  is not true since the exact location of the inflexion point is not known (the symmetry is modified by the underetching extension). Consequently,  $M_0$  cannot be directly determined.

In the Rayleigh-Ritz method, it is necessary to predict the shape function  $w(x)$  of the movable part. Figure 7 depicts the part that is bent:

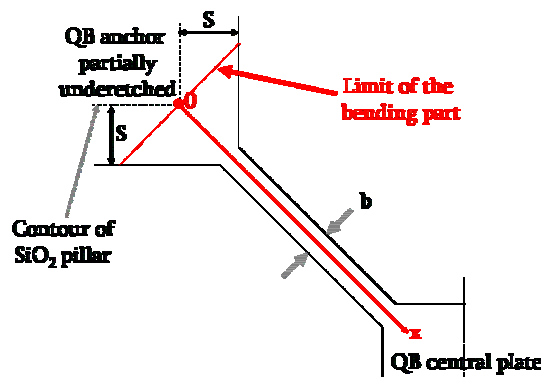


Figure 7. Schematic partial top-view of a QB whose anchor is affected by underetching

This modifies the calculation of the moment of inertia. For out-of-plane vibrations,  $I = \int_{-h/2}^{h/2} z^2 b(x, z) dz = \frac{b(x)h^3}{12}$  but here specifically,  $b$  is not constant and depends on  $x$ . Introducing this expression into eq.(II.38), the second derivative of the shape function can be expressed as:

$$w''(x) = \frac{12 M_0 - 12 F_p x}{E b(x) h^3}$$

with the following conditions:

$$\text{for } x \in \left[0; \sqrt{2S} - \frac{b}{2}\right], \mathbf{b}(x) = 2\sqrt{2S} - 2x \text{ resulting in } w_1''(x) = \frac{12M_0 - 12F_P x}{E(2\sqrt{2S} - 2x)h^3} \quad (\text{II.39})$$

$$\text{for } x \in \left[\sqrt{2S} - \frac{b}{2}; l + \sqrt{2S} - \frac{b}{2}\right], \mathbf{b}(x) = b \text{ resulting in } w_2''(x) = \frac{12M_0 - 12F_P x}{Eb h^3} \quad (\text{II.40})$$

### PARALLEL QUAD-BEAMS

For parallel QB, the balance of bending moments is identical but here the movable part is totally different. What potentially moves is the whole anchor width. Intuitively, the effect of the underetching is lessened compared to the case of diagonal beams because the movable part of the anchor is much wider and therefore much stiffer.

The shape function to consider here is:  $w''(x) = \frac{12M_0 - 12F_P x}{Eb(x)h^3}$  with the following conditions:

$$\text{for } x \in [0; S], \mathbf{b}(x) = P \text{ resulting in } w_1''(x) = \frac{12M_0 - 12F_P x}{EP h^3} \quad (\text{II.41})$$

$$\text{for } x \in [S; l + S], \mathbf{b}(x) = b \text{ resulting in } w_2''(x) = \frac{12M_0 - 12F_P x}{Eb h^3} \quad (\text{II.42})$$

where  $P$  is the width of the anchor.

### DETERMINATION OF THE RESONANCE FREQUENCY FOR PARALLEL AND DIAGONAL QB:

Starting from the second derivative of the shape functions (eq.(II.39) and (II.40), or (II.41) and (II.42)), we integrate them a first time according to  $w_1'(0) = 0$  and  $w_2'(l) = 0$ . At this stage, the first derivatives ( $w_1'$  and  $w_2'$ ) are equaled at their junction point ( $x = \sqrt{2S} - \frac{b}{2}$  for the diagonal ones, and  $x = S$  for the parallel ones) what also allows determining  $M_0$ . Then,  $w_1'$  and  $w_2'$  are integrated according to  $w_1(0) = 0$  and equaling  $w_1$  and  $w_2$  at their junction point. When making the Rayleigh-Ritz quotient, the term of kinetic energy is calculated considering a punctual mass ( $m/4$ ) only located at the moving extremity of the beam (i.e. where it is anchored to the central plate).

**Method 5** In this method, the aim is to calculate the resonance frequency of diagonal or parallel quad-beams taking into account both the effect caused by the underetching of the anchors and the mass of the beams.

Knowing that the Rayleigh-Ritz method is not very sensitive to the shape function and in order to simplify the balance of bending moments, that becomes very complex when considering the mass of the beam, the shape function is approximated with the one of methods 4. Then, the kinetic term of the Rayleigh-Ritz quotient is calculated integrating the mass all over the length of the moving part plus the punctual mass ( $m/4$ ) located at the end of the beam.

The results of all the methods are reported in Table II - 3 and Table II - 4, in which experimental data of real devices (fabricated and measured according to techniques explained in forthcoming sections) are listed. Among these seven devices, six are diagonal and one is parallel while four have a monocrystalline silicon structural layer and three a polycrystalline one:

Device	$E$ (GPa)	$L_1$ ( $\mu\text{m}$ )	$l$ ( $\mu\text{m}$ )	$b$ (nm)	$h$ ( $\mu\text{m}$ )	$S$ ( $\mu\text{m}$ )	$f_0$ (exp) (MHz)
Diag1 (single-crystal Si)	160	14	17.5	660	1.48	8	<b>1.72</b>
Diag2 (single-crystal Si)	160	14.6	22	700	1.47	9.5	<b>1.38</b>
Diag3 (single-crystal Si)	160	11.4	19.2	1050	1.47	9.5	<b>2.20</b>
Diag4 (single-crystal Si)	160	9.4	19.6	670	1.45	5.9	<b>2.58</b>
Diag5 (polySi)	130	6.25	13.45	765	450	3.5	<b>1.45</b>
Diag6 (polySi)	130	6.25	13.45	765	450	3.5	<b>1.49</b>
Par7 (polySi)	130	6.2	19.4	685	450	4	<b>1.23</b>

Table II - 3. Experimental characteristics of real devices and measured resonance frequency

Device	$f_0$ (M1) (MHz)	$f_0$ (M2) (MHz)	$f_0$ (M3) (MHz)	$f_0$ (exp) (MHz)	$f_0$ (M4) (MHz)	$f_0$ (M5) (MHz)	$4 \cdot m_{\text{BEAM}} / m_{\text{PLATE}}$ (%)
Diag1 (single-crystal Si)	3.09	1.54	1.51	<b>1.72</b>	2.67	2.54	24
Diag2 (single-crystal Si)	2.15	1.07	1.04	<b>1.38</b>	1.9	1.79	29
Diag3 (single-crystal Si)	4.14	2.03	1.93	<b>2.20</b>	3.4	3.01	50
Diag4 (single-crystal Si)	3.84	1.89	1.80	<b>2.58</b>	3.46	3.1	59
Diag5 (polySi)	3.03	1.47	1.36	<b>1.45</b>	2.66	2.22	105
Diag6 (polySi)	1.67	0.8	0.72	<b>1.49</b>	1.65	1.34	138
Par7 (polySi)	1.67	0.8	0.72	<b>1.23</b>	1.65	1.34	138

Table II - 4. Comparison between theoretical (for the five methods) and experimental resonance frequency of real devices. The last column indicates the proportion of the mass of the beams respect to the plate mass

## DISCUSSION OF THE RESULTS

The first remark to do is the major uncertainty in the determination of the devices parameters. Regarding the Young modulus, the one of monocrystalline Si depends upon the crystallographic orientation and can vary from 170 to 130 GPa whereas here a fixed value of 160 GPa has been considered. Concerning the polycrystalline structures, their Young modulus is not precisely known neither as it depends upon the deposition parameters.

Regarding the dimensions, it has been assumed in the models that all the four beams have identical dimensions and a rectangular shape. In practice it is not completely the case what complicates much the study. It has not been easy neither to measure the underetching affecting each device and additionally some dispersion in the thicknesses has been noticed although it has not been possible to check it for each device.

Second, another important uncertainty comes from the experimental value of the natural resonance frequency. It is estimated from a fit (of the curve that plots the resonance frequency as a function of the excitation voltage, c.f. section II.3.b). Experimentally, the curve is not always as linear as it should theoretically be.

Methods 2 and 3 seem to be the most accurate. In monocrystalline structures, theoretical values are smaller than experimental ones: one the reason for this may be that the Young modulus is underestimated. In polycrystalline structures, theoretical values are also smaller than experimental ones but probably because of the internal stress (some curvature has been observed).

### I.3. Mass sensitivity of nano/micromechanical resonators

Regarding our aim of performing mass sensing experiments with nano/micromechanical resonators, methods to evaluate their mass sensitivity  $S$  are required. An usual and convenient way to determine the mass sensitivity of a given vibration mode is to start from the expression of the resonance frequency (of this mode) put under the form of the mass-spring system approach:

$$f = \frac{1}{2\pi} \sqrt{\frac{k_{EFF}}{m_{EFF}}} = \frac{1}{2\pi} \sqrt{\frac{k_{EFF}}{\alpha_1 m_{RES}}} \quad (\text{II.43})$$

where  $k_{EFF}$ ,  $m_{EFF}$  and  $m_{RES}$  are respectively the effective spring constant, effective mass and the resonator mass ( $\alpha_1 = m_{EFF}/m_{RES}$  has been previously defined) of a given mode.

#### I.3.a. Calculation of mass sensitivity

For the determination of the mass sensitivity, our approach is based on the previous equation. In chapter 1, a survey of existing NEMS-based mass sensors has been proposed and it has been stated that depositing some mass on top of the resonator results in a resonance frequency shift that is a combination of three phenomena: (i) a mass loading leading to a frequency decrease (c.f. eq.(II.43) as the denominator increases), but also (ii) a stiffening effect caused by the additional contribution of the adsorbate and (iii) an adsorption-induced surface stress. Effects (ii) and (iii) both tend to increase the frequency (as the numerator of eq.(II.43) is increased). Here, the study is restricted to the case of very small mass accretions and to the deposition of low-stiffness low-stress materials (like liquids). Therefore, we will assume that the spring constant is not affected by the mass deposition and therefore that the mass loading effect exclusively dominates.

At this stage, two cases must be distinguished according to the type of mass deposition: either punctual or areal (also named distributed).

##### I.3.a.i) Punctual mass sensitivity

The punctual mass sensitivity corresponds to the measurement of punctual, spatially localized species like particles, droplets, bacteria, molecular aggregates, etc...

With the aim of determining the sensing attribute of a device, let us reformulate first eq.(II.43) to express the effective mass  $m_{EFF\_P}$  :

$$m_{EFF\_P} = \alpha_{1\_P} m_{RES} = \frac{1}{4\pi^2} \frac{k_{EFF\_P}}{f^2} \quad (\text{II.44})$$

In this expression, the effective mass  $m_{EFF\_P}$  corresponds to the equivalent mass of the whole resonator as if it were located in one single point. Depending on the position of this point, a specific corrective coefficient  $\alpha_{1\_P}$  must be applied. In the case of a cantilever, the  $\alpha_{1\_P}$  coefficient is equal to 0.25 for the free end point what means that the whole cantilever mass is equivalent to a four times smaller punctual mass exerted at its free end.

Considering an addition of mass upon the resonator restricted to a punctual location, the first derivative of the mass with respect to the frequency is calculated. It is necessary to derive the

effective mass  $m_{EFF}$ , and not the resonator mass  $m_{RES}$ , since the effective mass considered in eq.(II.44) can be directly seen as a true mass exerted at the point of mass deposition, in other words:

$$m_{EFF\_FINAL} = \alpha_1 m_{RES} + \Delta m \quad (II.45)$$

where  $\Delta m$  is the punctual mass accretion. Hence,  $S$ , the punctual mass sensitivity, can be estimated in this way:

$$S = \left| \frac{\partial m_{EFF\_P}}{\partial f} \right| = \left| \frac{\partial}{\partial f} \left( \frac{1}{4\pi^2} \frac{k_{EFF\_P}}{f^2} \right) \right| \approx \frac{1}{2\pi^2} \frac{k_{EFF\_P}}{f^3} = 2 \frac{m_{EFF\_P}}{f} \quad (g \cdot Hz^{-1}) \quad (II.46)$$

This value of sensitivity is valid only around the initial resonance frequency and for small deviations. However, there is a more accurate way to estimate the corresponding amount of mass as a function of the frequency deviation. Considering that the effective mass before depositing is:

$$m_{EFF\_P\_i} = \alpha_1 m_{RES} = \frac{1}{4\pi^2} \frac{k_{EFF\_P}}{f_i^2}, \text{ and after depositing is: } m_{EFF\_P\_f} = \alpha_1 m_{RES} + \Delta m = \frac{1}{4\pi^2} \frac{k_{EFF\_P}}{f_f^2}$$

so:

$$\Delta m = \frac{k_{EFF\_P}}{4\pi^2} \left( \frac{1}{f_f^2} - \frac{1}{f_i^2} \right) \quad (II.47)$$

This method is more reliable as one directly bases on the initial and final value of the resonance frequency what is more confident than relying on an estimated mass sensitivity that is only valid around the unloaded resonance frequency value.

### I.3.a.ii) Areal mass sensitivity

The determination of the areal mass sensitivity is required to quantify in terms of mass some resonance frequency shifts related to uniformly deposited masses, like when depositing layers of a material in an evaporation chamber. Let us reformulate eq.(II.43) to express the effective mass  $m_{EFF\_A}$ :

$$m_{EFF\_A} = \alpha_{1\_A} m_{RES} = \frac{1}{4\pi^2} \frac{k_{EFF\_A}}{f^2} \quad (II.48)$$

In this case, on the contrary to punctual deposition, the new value of the effective mass after uniform deposition is

$$m_{EFF\_A} = \alpha_{1\_A} (m_{RES} + \Delta m) \quad (II.49)$$

where  $\Delta m = \rho_M A \Delta e = S_A A \Delta f$  ( $\rho_M$  is the deposited material density,  $A$  the resonator area on the side where the mass is deposited,  $\Delta e$  the deposited thickness,  $S_A$  the areal mass sensitivity and  $\Delta f$  the resulting frequency shift). Actually, the accreted mass must be corrected by  $\alpha_{1\_A}$  (areal effective mass coefficient) as it is spread all over the resonator area.

Considering a uniform addition of mass upon the resonator, the first derivative of the mass with respect to the frequency is calculated. From eq.(II.49), it is clear that the proper resonator

mass, and not the effective mass, must be derived.  $S_A$ , the areal mass sensitivity, can therefore be estimated in this way:

$$S_A = \frac{1}{A} \left| \frac{\partial m_{RES}}{\partial f} \right| = \frac{1}{A} \left| \frac{\partial}{\partial f} \left( \frac{1}{4\pi^2 \alpha_{1_A}} \frac{k_{EFF\_A}}{f^2} \right) \right| \approx \frac{1}{A} \frac{1}{2\pi^2 \alpha_{1_A}} \frac{k_{EFF\_A}}{f^3} = 2 \frac{1}{A} \frac{m_{RES}}{f} \quad (\text{g.Hz}^{-1}.\text{cm}^{-2}) \quad (\text{II.50})$$

This value of sensitivity is valid only around the initial resonance frequency and for small deviations. However, as previously said, there is another approach, more accurate. Considering that the effective mass before depositing is:

$$m_{EFF\_A\_i} = \alpha_{1_A} m_{RES} = \frac{1}{4\pi^2} \frac{k_{EFF\_A}}{f_i^2}, \text{ and after depositing is: } m_{EFF\_A\_f} = \alpha_{1_A} (m_{RES} + \Delta m) = \frac{1}{4\pi^2} \frac{k_{EFF\_A}}{f_f^2}$$

this results in [14]:

$$\Delta m = \rho A \Delta e = \frac{k_{EFF\_A}}{4\pi^2 \alpha_{1_A}} \left( \frac{1}{f_f^2} - \frac{1}{f_i^2} \right) \quad (\text{II.51})$$

### I.3.b. Dynamic linear range

The linear range of the mass sensor is given at its lower limit by the frequency noise floor while its upper limit is reached when the effective spring constant  $k_{EFF}$  is modified (either by an additional stiffening caused by the accretion or by an adsorption induced surface-stress).

When depositing mass on top of the resonator, one can make the assumption that until a certain limit the resonator will still remain in its linear elastic mechanical regime, i.e. that  $k_{EFF}$  still remains constant. Hence, a change in  $S$  does not mean automatically that the resonator enters a mechanical nonlinear regime but rather simply that  $m_{EFF}$  and  $f_0$  vary in eq.(II.46) or (II.50). Thus, a quasi-linear approach can be followed to predict the sensor response. Let us write the resonance frequency as a function of the deposited mass for a punctual (left) or distributed (right) mass loading:

$$f_{RES} = \frac{1}{2\pi} \sqrt{\frac{k_{EFF\_P}}{m_{EFF\_P} + m_{DEPOSITED\_PUNCTUAL}}} \quad \text{and} \quad f_{RES} = \frac{1}{2\pi} \sqrt{\frac{k_{EFF\_A}}{\alpha_{1_A} (m_{RES} + m_{DEPOSITED\_AREAL})}} \quad (\text{II.52})$$

what can be re-written as:

$$f_{RES} = f_0 \sqrt{\frac{m_{EFF\_P}}{m_{EFF\_P} + m_{DEPOSITED\_PUNCTUAL}}} \quad \text{and} \quad f_{RES} = f_0 \sqrt{\frac{\alpha_{1_A} m_{RES}}{\alpha_{1_A} (m_{RES} + m_{DEPOSITED\_AREAL})}} \quad (\text{II.53})$$

what can be further simplified as:

$$f_{RES} = f_0 \sqrt{\frac{1}{1 + \frac{m_{DEPOSITED\_PUNCTUAL}}{m_{EFF\_P}}}} \quad \text{and} \quad f_{RES} = f_0 \sqrt{\frac{1}{1 + \frac{m_{DEPOSITED\_AREAL}}{m_{RES}}}} \quad (\text{II.54})$$

These two equations can help in predicting the resonance frequency decrease along the mass deposition. They remain valid only while the stiffness remains constant, what is true until the mass deposit is large enough so that it generates an additional stiffening of the structure or a surface stress.

## II. Electrical response of electrostatically driven resonators

In chapter 1, different techniques have been mentioned to actuate and detect the mechanical resonance spectrum of nano/micromechanical devices. We have chosen an all electric actuation and detection scheme, concretely electrostatic actuation and capacitive detection. The advantages of this approach compared to other methods are detailed hereafter.

Optical characterization is an expanded and classical way to measure resonance frequencies as it offers a very high resolution in terms of spatial displacements (i.e. oscillation amplitudes). Yet, its implementation is not suitable here for several reasons.

In particular, issues related to the laser spot are problematic. The spot size, in general in the micron range, may be a limitation compared to nanometer scale resonator dimensions, and its alignment with the device may be another issue. Furthermore, AFM-based and interferometric optical techniques are limited to out-of-plane vibrations only. For measuring several devices at the same time, for example an array of resonators for multiple samples detection, several laser beams would be required and the resulting practical implementation is rather complex.

Magnetomotive detection is another approach to detect mechanical oscillations but it requires a heavy set-up under high magnetic fields (1-10 Tesla).

Piezoelectric and piezoresistive detection schemes are also possible but the capacitive technique provides a favorable trade-off between simplicity of implementation, displacement sensitivity and system portability. It does not require any material (unlike the piezoelectric approach) incompatible with a CMOS process. It also opens up possibilities of simultaneously operating multiple devices (arrays) without requiring heavy set-ups neither alignment.

The smartest realization of NEMS embedded in a capacitive detection scheme is a monolithic integration with CMOS circuitry. It makes possible “on-chip” signal processing (amplification and conditioning), additionally arrays of sensors can be operated while the overall system remains ultra-compact and light. The integration of NEMS on CMOS will be described in chapters 3, 4 and 5.

### II.1. Transduction principle: capacitive detection with electrostatic actuation

In our approach, mechanical resonators are electrostatically actuated and a capacitive detection scheme converts mechanical oscillations into an electrical signal.

The global system is illustrated, taking the example of a cantilever, in Figure 8: it consists of a driver, mechanically fixed, and a cantilever placed in parallel very close to the driver. It can freely bend around the static position at a given oscillation frequency.

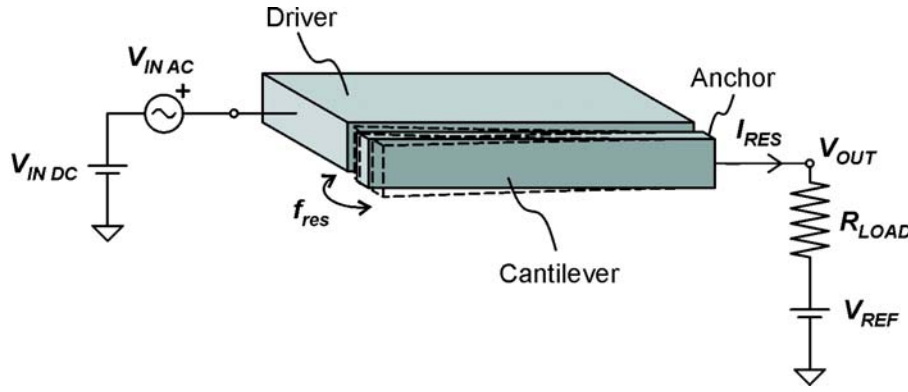


Figure 8. All electric actuation and detection scheme for a cantilever

The fixed driver is devoted to bias the required DC voltage ( $V_{IN DC} - V_{REF}$ ) (typically 1 V to 30 V) and to act as the input terminal for the alternate voltage stimulation  $V_{IN AC}$  (typically -30 dBm to 0 dBm). On the other hand, the cantilever plays the role of the output terminal, allowing the readout of the resonator oscillation current  $I_{RES}$  (typically in the range of nA), subsequently converted into a voltage  $V_{OUT}$  by the load resistor  $R_{LOAD}$ . The resonance frequency depends on the resonator material, shape and dimensions as previously detailed.

The mechanical motion is translated into an electrical signal (subsequently collected and conditioned by a read-out device) through a capacitive transduction. In fact, the capacitive current generated by the two-electrodes system can be described as:

$$\begin{aligned} i_{RES}(t) &= \frac{dQ_{RES}}{dt} = C_{NEMS} \frac{d(V_{IN DC} - V_{REF} + V_{IN AC})}{dt} + (V_{IN DC} - V_{REF} + V_{IN AC}) \frac{dC_{NEMS}}{dt} \\ &\approx C_0 \frac{dV_{IN AC}}{dt} + (V_{IN DC} - V_{REF}) \frac{dc}{dt} \end{aligned} \quad (II.55)$$

where  $C_{NEMS}(t) = C_0 + c(t)$ ,  $C_0$  is the static component and  $c$  the time dependant one of the (here, in-plane) capacitor cantilever/air/electrode. It is assumed that  $V_{IN DC} - V_{REF} \gg V_{IN AC}$ .

Thus, the NEMS current can be understood as a sum of two contributions of current: (i) one arising from the static structure:  $i_s = C_0 \frac{dV_{IN AC}}{dt}$  and (ii) the other coming from the resonator mechanical motion  $i_M = (V_{IN DC} - V_{REF}) \frac{dc}{dt}$ . This latter component allows measuring the frequency response of the resonator.

## II.2. Equivalent electrical modeling of a mechanical resonator

### II.2.a. Global equivalent electrical scheme

Equation (II.55) describes an ideal case in which no parasitic capacitances affect the measurement. As a matter of fact, the total generated capacitive current is not only a sum of

motion and static components but also of a parasitic component, usually the most significant fraction of the total. In fact, this high parasitic component may even “hide” the motional current. For a more accurate prediction of the resonance signal level, the mechanical resonator is modeled in the following way:

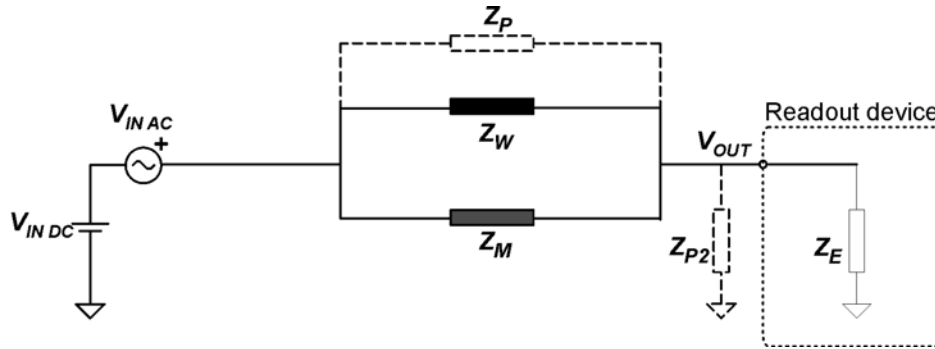


**Figure 9. Actuation and detection electrical scheme including parasitic components**

where  $Z_P$  is a parasitic impedance existing between input and output terminals,  $Z_W$  the impedance associated to the static capacitor,  $Z_M$  the impedance associated to the mechanical motion occurring around resonance,  $Z_{P2}$  the equivalent parasitic impedance at the output port and  $Z_E$  the input impedance of the readout device (a network analyzer in the case of discrete devices, a CMOS circuit in monolithic systems).

#### GENERAL BEHAVIOR

As a first remark, it should be stated that all over the work presented in this thesis, the resonators structural layer (either mono- or polycrystalline silicon) is always sufficiently doped with phosphorous (n-type) so that we consider it as a good conductor of negligible resistivity.

$Z_P$  deeply depends upon the type of resonator and on its electrodes configuration. It can be approximated as:

$$Z_P \approx \frac{1}{C_P \omega} \quad (\text{II.56})$$

where  $C_P$  is the parasitic stray capacitance and  $\omega$  the angular frequency of operation.

In the case of in-plane vibrating cantilevers, this impedance corresponds to the capacitance related to the fringing electrostatic field and the resulting impedance is usually very high. For other types of resonators, in particular out-of-plane vibrating devices, it may be dramatically low because of a strong capacitive coupling between the underlying layer acting as input terminal and the resonator anchors (belonging to the structural layer, i.e. the output terminal). This will be detailed in section III.1.c.i). As a design rule,  $Z_P$  should be maximized (i.e.  $C_P$  reduced).

$Z_W$  depends on the resonator geometry: it is associated to the static capacitance  $C_W$  of the resonator/air/input terminal capacitor:

$$Z_W \approx \frac{1}{C_W \omega} \approx \frac{d}{\epsilon_0 A \omega} \quad (\text{II.57})$$

where  $\epsilon_0$  is the vacuum dielectric constant,  $A$  the capacitor area,  $d$  the gap between resonator and input port, and  $\omega$  the angular frequency of operation.

$Z_M$  is the motional impedance of the resonator. The lower it is, the higher is the signal generated by the mechanical resonance. An important challenge to address is the implementation of a reliable model in order to be able to translate mechanical parameters such as  $k$ ,  $m$  and  $D$  (refer to eq. (II.3)) into electrical equivalent parameters. Thus, the levels of electrical signal generated during mechanical resonance could be assessed.

$Z_{P2}$  is related to parasitic capacitances located at the output terminal. In an experimental set-up for discrete devices, the total parasitic capacitance arises from the measurement instrumentation and is in the order of tens of pF (what corresponds to parasitic capacitances respectively of the wire bonding between chip and printed circuit board (PCB), of the PCB itself and of the coaxial cables).

In case of a monolithic integration, this capacitance is in the order of tens of fF (three orders of magnitude less) and corresponds to a parasitic physical capacitor related to the routing between the resonator output terminal and the CMOS circuit input. As a design rule,  $Z_{P2}$  should be maximized (i.e.  $C_{P2}$  reduced).

$Z_E$  is the input impedance of the readout device. The network analyzer we use for device frequency characterization is configurable at either 50  $\Omega$  or 1 M $\Omega$ .

The resulting load resistance  $R_{LOAD}$  (see Figure 8) that converts the resonance current into  $V_{OUT}$  is given by:

$$\frac{1}{R_{LOAD}} = \frac{1}{Z_{P2}} + \frac{1}{Z_E} \Rightarrow R_{LOAD} = \frac{Z_{P2} Z_E}{Z_{P2} + Z_E} \quad (II.58)$$

Usually,  $C_{P2}$  is quite high what is equivalent to a low  $Z_{P2}$ . Yet,  $Z_{P2}$  is usually larger than 50  $\Omega$  and in this case, it is more favorable to set  $Z_E$  to 1 M $\Omega$ , what makes that  $Z_{P2}$  dominates and acts as load resistance (instead of 50  $\Omega$ ).

## II.2.b. RLC equivalent model of the motional impedance

This section presents a model that allows estimating the electrical behavior of a mechanical resonator. From a phenomenological point of view, a  $D$ ,  $m$ ,  $k$  [c.f. eq.(II.3)] mechanical oscillator is equivalent to a small signal electrical RLC oscillator [18-21]. A conversion scale factor is needed to transfer mechanical signals domain to an electrical signals domain. These issues are detailed hereafter.

### II.2.b.i) Phenomenological approach of a RLC oscillator

The objective here is to determine the frequency response, and its key features, of two oscillators, pure RLC and RLC in parallel with C, by calculating their transfer function. Through the study of such classical electrical components, the electrical behavior of a mechanical resonator can be qualitatively predicted.

#### RESPONSE OF A SINGLE RLC BRANCH

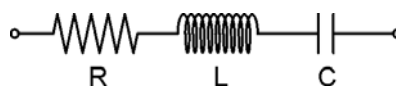


**Figure 10. RLC branch**

A single RLC branch provides a similar response than a pure mechanical resonator. The intrinsic mechanical response is accessible for instance via optical techniques, what is not the case of capacitive detection as it will subsequently explained. The impedance of the branch is:

$$Z_{RLC} = \frac{1}{jC\omega} + jL\omega + R \quad (\text{II.59})$$

setting  $s = j\omega = j2\pi f$ , then:  $Z_{RLC} = \frac{1}{jC\omega} + jL\omega + R = \frac{LCs^2 + RCs + 1}{Cs}$

The resonator current is given by:  $i_{RLC} = \frac{V}{Z_{RLC}}$ . Setting  $V=1$ , the frequency response is:

$$i_{RLC} = \frac{1}{Z_{RLC}} = \frac{Cs}{LCs^2 + RCs + 1} \quad (\text{II.60})$$

while the resonance frequency is  $f_{RES} = \frac{1}{2\pi} \frac{1}{\sqrt{LC}}$

In Figure 11 and Figure 12, typical magnitude and phase responses are plotted in different conditions:  $L$  and  $C$  are set to about 1 H and 10 fF (what results in  $f_{RES} \approx 1.5$  MHz) while  $R$  is set to 5, 25 and 50 k $\Omega$ .

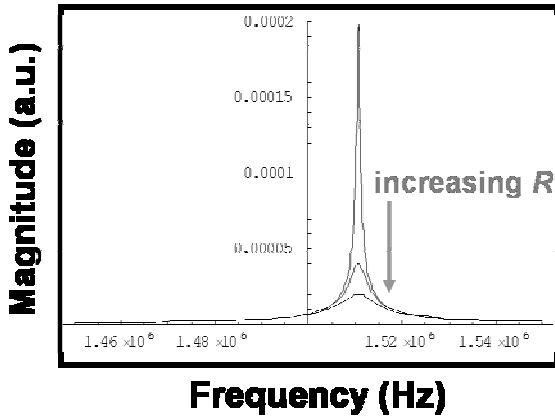


Figure 11. Typical magnitude response of a RLC branch

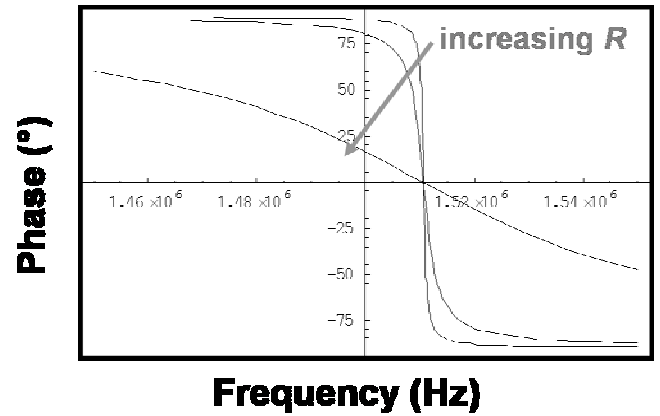


Figure 12. Typical phase response of a RLC branch

The key features here are the single peak in the magnitude spectrum and the 180° phase shift downwards around the resonance frequency.

At a given resonance frequency, the general trends are (i) increasing the inductance (i.e. decreasing the capacitance) tends to lower the peak magnitude and (ii) increasing  $R$  (maintaining  $L$  and  $C$  constant) tends to decrease the peak magnitude as well, worsens the peak quality factor and produces a less steep phase shift.

RESPONSE OF A DOUBLE BRANCH: RLC PARALLEL WITH C

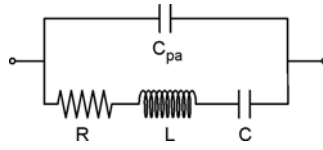


Figure 13. Double branch RLC in parallel with (parasitic)  $C_{PA}$

This system is the most similar to the configurations of Figure 8 and Figure 9 whereby the mechanical resonator, equivalent to a RLC branch, is embedded in an electrical readout system based on a capacitive scheme. Let us see to what extent the unavoidable parallel capacitance (sum of parasitic and static contributions) modifies the NEMS frequency response.

The impedance of each branch is:  $Z_{RLC} = \frac{1}{jC\omega} + jL\omega + R$  and  $Z_{PA} = \frac{1}{jC_{PA}\omega}$

$$\text{Setting } s = j\omega = j2\pi f, \text{ then } Z_{eq} = \frac{1}{\frac{1}{Z_{PA}} + \frac{1}{Z_{RLC}}} = \frac{1}{C_{PA}s + \frac{1}{\frac{1}{jC\omega} + jL\omega + R}}$$

$$\Rightarrow Z_{eq} = \frac{LCs^2 + RCs + 1}{LCC_{PA}s^3 + RCC_{PA}s^2 + (C + C_{PA})s} = \frac{1}{C_{PA}s} \left( \frac{LCs^2 + RCs + 1}{LCs^2 + RCs + \left(1 + \frac{C}{C_{PA}}\right)} \right)$$

Normalizing again V to 1, the frequency response of the resonator current is given by:

$$i_{RES} = \frac{1}{Z_{eq}} = C_{PA}s \left( \frac{LCs^2 + RCs + \left(1 + \frac{C}{C_{PA}}\right)}{LCs^2 + RCs + 1} \right) \quad (\text{II.61})$$

In Figure 14 and Figure 15, typical magnitude and phase responses are plotted in different conditions:  $L$  and  $C$  are set to about 1 H and 10 fF (what results in  $f_{RES} \approx 1.5$  MHz),  $C_{PA}$  is set to 1.5 pF while  $R$  is set to 2, 0.7 and 0.2 M $\Omega$ .

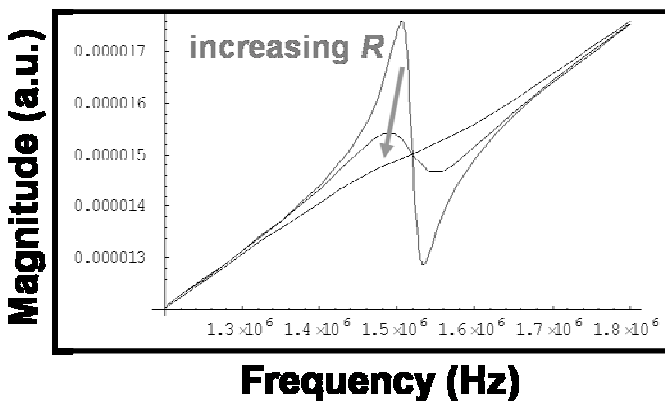


Figure 14. Typical magnitude response of a double branch RLC//C

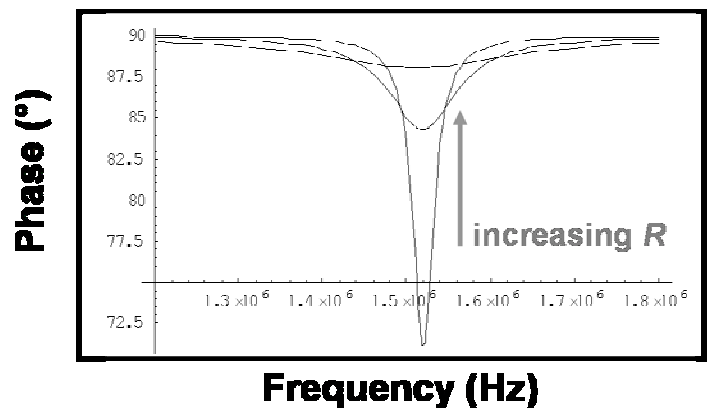


Figure 15. Typical phase response of a double branch RLC//C

Magnitude and phase spectra change radically compared to the behavior of a single RLC branch. Here, the magnitude response exhibits the proper resonance immediately followed by an anti-resonance peak. The background level is determined by  $C_{PA}$ . The phase response is no more stairs-like; the resonance provokes a phase shift down to lower values but comes back rapidly to the background value.

$C_{PA}$  plays a key role: the higher it is the more pronounced is the magnitude anti-peak and the less pronounced is the phase peak.

### II.2.b.ii) Parameters calculation

Now, the qualitative response of the system depicted in Figure 9 is known. Let us quantify  $Z_M$  the impedance illustrating the mechanical motion. Ideally,  $Z_M$  should be as low as possible in order to predominate against either  $Z_P$  or  $Z_W$ .

The mechanical resonator, characterized by its mechanical parameters  $k$  (resonator stiffness),  $m$  (resonator mass) and  $D$  (viscous damping coefficient related to the resonance quality factor  $Q$ , according to  $D = \frac{\sqrt{km}}{Q} = \frac{m\omega}{Q}$ ), can be electrically modeled as a RLC branch. This electromechanical model assigns to each mechanical parameter an equivalent electrical value. We follow the approach from Mattila et al. [19]. Let us express the electrostatic force:

$$F_E = \frac{1}{2} \frac{\partial C}{\partial x} (V_{IN AC} + V_{IN DC})^2 = \frac{1}{2} \frac{\partial C}{\partial x} (v_{AC}^2 \sin^2 \omega t + 2v_{AC} V_{IN DC} \sin \omega t + V_{IN DC}^2) \text{ with } V_{IN AC} = v_{AC} \sin \omega t$$

actually,  $\sin^2 \omega t = \frac{1 - \cos 2\omega t}{2}$ , so

$$F_E = \frac{1}{2} \frac{\partial C}{\partial x} \left[ \left( \frac{v_{AC}^2}{2} + V_{IN DC}^2 \right) + 2v_{AC} V_{IN DC} \sin \omega t - \frac{v_{AC}^2}{2} \cos 2\omega t \right] \quad (II.62)$$

The time-varying part of the capacitive driving force actuating the driven damped mass-spring system (eq.(II.8)) to the first order is:

$$F_E(t) = \frac{1}{2} \frac{\partial C}{\partial x} [2v_{AC} V_{IN DC} \sin \omega t] = \frac{\partial C}{\partial x} V_{IN AC} V_{IN DC}$$

The global equation is: 
$$m \frac{d^2 x}{dt^2} + D \frac{dx}{dt} + kx = F_E(t) = \frac{\partial C}{\partial x} V_{IN AC} V_{IN DC}$$

that is to say: 
$$m \omega^2 x + D \omega x + kx = F_E(t) = \frac{\partial C}{\partial x} V_{IN AC} V_{IN DC} \quad (II.63)$$

As previously said (eq.(II.55)), the motional current  $i_M$  can be expressed as:

$$i_M \approx V_{IN DC} \frac{\partial C}{\partial t} = V_{IN DC} \frac{\partial C}{\partial x} \frac{\partial x}{\partial t} \Rightarrow V_{IN DC} \frac{\partial C}{\partial x} = \frac{i_M}{\dot{x}} = \frac{i_M}{\omega x} \quad (II.64)$$

Inserting (eq.(II.64)) into (eq.(II.63)), we obtain  $m\omega^2 x + D\omega x + kx = \frac{i_M}{\omega x} V_{IN AC}$  and rewrite it as:

$$V_{IN AC} = \frac{m\omega^3 x^2}{i_M} + \frac{D\omega^2 x^2}{i_M} + \frac{k\omega x^2}{i_M} \quad (II.65)$$

On another part, basing on eq.(II.59),

$$V_{IN AC} = jL_M \omega i_M + R_M i_M + \frac{i_M}{jC_M \omega} \quad (II.66)$$

Identifying the complex modulus of the left terms of eq.(II.65) and (II.66),

$$L_M \omega i_M = \frac{m\omega^3 x^2}{i_M} \Rightarrow L_M = m \left[ \frac{\omega^2 x^2}{i_M^2} \right] = \frac{m}{\eta^2} \quad (II.67)$$

we define  $\eta$  the electromechanical coupling coefficient that puts in relation electrical current and mechanical transducer velocity:

$$\eta = \frac{i_M}{\omega x} = \frac{i_M}{v(t)} = V_{IN DC} \frac{\partial C}{\partial x} \quad (II.68)$$

where  $v(t)$  is the mechanical velocity

For small displacements,  $\eta \approx \frac{\epsilon_0 A}{d^2} V_{IN DC}$  where  $\epsilon_0$  is the vacuum dielectric constant,  $d$  the gap between resonator and input port, and  $A$  the capacitor area.

Identifying the two other terms of eq (II.65) and (II.66), it results in:

$$R_M = \frac{D}{\eta^2} = \frac{\sqrt{k m}}{Q \eta^2} = \frac{1}{Q} \sqrt{\frac{L_M}{C_M}} \quad C_M = \frac{\eta^2}{k} \quad L_M = \frac{m}{\eta^2} \quad (II.69)$$

Note that the resonance frequency of the electrical RLC branch is equal to the mechanical resonance:

$$f_{RES} = \frac{1}{2\pi \sqrt{L_M C_M}} = \frac{1}{2\pi} \sqrt{\frac{k \eta^2}{\eta^2 m}} = \frac{1}{2\pi} \sqrt{\frac{k}{m}} \quad (II.70)$$

Around resonance,  $C_M$  and  $L_M$  cancel each other and the branch becomes equivalent to a simple resistance whose value is  $R_M$ .

### II.2.c. Global response

A general expression of the total capacitive current  $I_{MEMS}$  generated around resonance frequency is:

$$I_{MEMS}(t) = \frac{V_{INAC}}{Z_{TOT}} = \sum i = i_P + i_W + i_M \approx V_{INAC} \left( C_P \omega + C_W \omega + \frac{1}{R_M} \right) \quad (II.71)$$

where  $i_P$ ,  $i_W$  and  $i_M$  are the currents respectively associated to  $Z_P$  (i.e.  $C_P$ ),  $Z_W$  (i.e.  $C_W$ ) and  $R_M$ .  $V_{INAC}$  is the AC excitation voltage.

We define a figure of merit ( $FM$ ), calculated at the resonance frequency, that points up the trend to generate a high resonance current compared to the currents arising from parasitic and static capacitances:

$$FM = 100 \frac{i_M}{i_P + i_W} \quad \text{in \%} \quad (II.72)$$

Efforts on resonator design and readout configuration should focus on increasing  $FM$ .

So, computing eq.(II.71) with eq.(II.72),

$$FM = 100 \frac{i_M}{i_P + i_W} = 100 \frac{V_{AC}}{R_M} \frac{1}{V_{AC} \omega_0 (C_P + C_W)} = 100 \frac{Q \eta^2}{\sqrt{km}} \frac{1}{\sqrt{k} (C_P + C_W)} = 100 \frac{Q \eta^2}{k (C_P + C_W)}$$

Inserting eq.(II.68) into the previous expression, we obtain the general formula:

$$FM = 100 \frac{Q \varepsilon_0^2 A^2 V_{INDC}^2}{d^4 (C_P + C_W)} \frac{1}{k} \quad \text{in \%} \quad (II.73)$$

where  $Q$  is the resonance quality factor,  $\varepsilon_0$  is the vacuum dielectric constant,  $A$  is the resonator / gate electrode capacitor area and  $d$  the capacitor gap (assuming  $d$  is much larger than the resonator displacement).  $V_{INDC}$  is the applied DC voltage (assuming  $V_{INDC} \gg V_{INAC}$ ), and  $k$  the spring constant of the considered resonator.

## II.3. Response to electrostatic actuation

This section is focused on the impact of electrostatic actuation on either the static or dynamic mechanical response of the resonator.

### II.3.a. Deflection and pull-in voltage related to electrostatic force

Electrostatic actuation results in an attractive force that tends to bend the resonator towards the excitation electrode. It is of interest to quantify this deflection as it gives indications on the sensitivity of the displacement transducing scheme and allows predicting the pull-in voltage in order to prevent collapse and irreversible stiction of the resonator on its driving electrode.

In order to estimate the deflection, we equal the restoring spring force and the electrostatic force, neglecting air damping:

$$|F_e| = |F_k| \Rightarrow kx = \frac{1}{2} \frac{\partial C}{\partial x} V^2 \quad \text{with } V = V_{IN DC} + v_{AC} \sin \omega t$$

The electrostatic force involves time-constant and time-varying parts [see eq.(II.62)]:

$$F_E(\omega t) = \frac{1}{2} \frac{\partial C}{\partial x} \left[ \left( \frac{v_{AC}^2}{2} + V_{IN DC}^2 \right) + 2v_{AC} V_{IN DC} \sin \omega t - \frac{v_{AC}^2}{2} \cos 2\omega t \right] \quad (\text{II.74})$$

Let us separate the two cases of static and dynamic deflection.

For the determination of the static deflection, the equation to solve is (assuming  $V_{IN DC} \gg v_{IN AC}$ ):

$$kx = \frac{1}{2} \left( \frac{v_{ac}^2}{2} + V_{dc}^2 \right) \epsilon_0 A \frac{\partial}{\partial x} \left( \frac{1}{d-x} \right) \Rightarrow x(d-x)^2 = \frac{\epsilon_0 A}{2k} V_{IN DC}^2 \quad (\text{II.75})$$

It comes that stable equilibrium positions only exist in the domain  $0 < x < \frac{d}{3}$ .

Let us introduce now the useful notion of pull-in voltage. Above this voltage, the electrostatic force is always greater than the spring force and the resonator is pulled towards the fixed electrode. The pull-in voltage is calculated at the limit  $d/3$  of the stable domain:

$$V_{PI} = \sqrt{\frac{8kd^3}{27\epsilon_0 A}} \quad (\text{II.76})$$

In Table II - 5, the expression of the pull-in voltage is reported for two devices:

Device	$k$ (N/m)	$A$ (m <sup>2</sup> )	$V_{PI}$ (V)
Cantilever In-plane flexion	$\frac{2 E b^3 h}{3 l^3}$	$hl$	$\sqrt{\frac{16 E b^{3/2} d^{3/2}}{81 \varepsilon_0 l^2}}$
Quad-beam Out-of-plane flexion	$\lambda_{QB} \frac{E h^3 b}{l^3}$	$L_1^2$	$\sqrt{\frac{8 \lambda_{QB} E h^{3/2} b^{1/2} d^{3/2}}{27 \varepsilon_0 l^{3/2} L_1}}$

**Table II - 5. Pull-in voltage formula for specific resonator designs**

where  $\lambda_{QB}$  is a fitting factor in order to take into account deviations from the experimental resonance frequency. The effective factor of the cantilever spring constant (see  $\alpha_2$ , section I.2.b.i) is set to 2/3 since the electrostatic force is uniformly applied.

Around the static bending given by eq.(II.75), an additional periodic deflection is driven by the time-varying part of the electrostatic force. Neglecting the air damping, the oscillation amplitude  $x$  can be calculated as:

$$kx = \left| \frac{1}{2} 2v_{AC} V_{INDC} \varepsilon_0 A \frac{\partial}{\partial x} \left( \frac{1}{d-x} \right) \right| \Rightarrow x(d-x)^2 = \frac{\varepsilon_0 A}{k} v_{AC} V_{INDC} \quad (II.77)$$

At large amplitudes, the resonator enters a mechanical nonlinear regime with hysteresis. In this regime, the dependence of the amplitude of vibration upon the axial force has to be taken into account, resulting in a non-linear term in eq.(II.3). The threshold amplitude, named critical amplitude [5, 22, 23] is given by:

$$x_c = \frac{\sqrt{2} b}{\left[ \beta_n Q (1-\nu^2) \right]^{\frac{1}{2}}} \quad (II.78)$$

where  $b$  is the resonator dimension in the direction of vibration,  $\beta_n$  is a coefficient depending on the mode and on the resonator shape, and  $\nu$  is the Poisson's ratio of the structural material (for silicon:  $\nu=0.28$ ).

$\beta_n$  depends on the structure and on the operated mode  $n$ . It is given by [23]:

$$\beta_n = \frac{3}{w_{n,MAX}^2(x)} \frac{\int_0^l \left( \frac{dw_n(x)}{dx} \right)^4 dx}{\int_0^l \left( \frac{d^2 w_n(x)}{dx^2} \right)^2 dx} \quad (II.79)$$

where  $w_n(x)$  is the approximate shape function of the  $n^{\text{th}}$  mode and  $w_{n,MAX}$  its maximum (see part I for the corresponding expressions of  $w_n(x)$ ). For a cantilever beam vibrating in its fundamental mode,  $\beta_n=1.58$ ; for a bridge  $\beta_n=0.528$  for the fundamental (flexural) mode.

In chapter 5, vibration amplitudes will be calculated when analyzing experimental results obtained on resonators that have been fabricated.

### II.3.b. Spring-softening effect

To what extent electrostatic actuation influences the mechanical resonance frequency is an important issue. It has been experimentally observed, for example on cantilevers that an increasing applied voltage decreases the resonance frequency: this phenomenon arises from the so-called “spring-softening” effect [24, 25]. Hereafter, we propose an analytical explanation providing formulas of two specific mechanical structures. Let us consider the equation of the mass-spring system:

$$m \frac{d^2 x}{dt^2} = F_{SP} = \frac{\partial F_{SP}}{\partial x} x = -kx \text{ leading to } f_o = \frac{1}{2\pi} \sqrt{\frac{k}{m}} \text{ (natural resonance frequency)}$$

If an electrostatic force is applied, then

$$m \frac{d^2 x}{dt^2} = F_{SP} + F_E = \left( \frac{\partial F_{SP}}{\partial x} + \frac{\partial F_E}{\partial x} \right) x \equiv (-k + k_E) x$$

$$\text{leading to } f' = \frac{1}{2\pi} \sqrt{\frac{k - k_E}{m}} \text{ (modified resonance frequency) with } k_E = \frac{\partial F_E}{\partial x}$$

$$\text{then, } f' = f_o \sqrt{1 - \frac{k_E}{k}}$$

At this stage, we use a Taylor development (since  $k_E \ll k$ ) to obtain the relation between  $f'$  and  $f_o$ :

$$f' = f_o \left( 1 - \frac{k_E}{2k} \right) \quad (\text{II.80})$$

The spring-softening effect depending on what point of view it is considered may represent either a drawback or an advantage. It tends to decrease the mass sensitivity according to eq.(II.46) ( $2 m/f$ ) but it makes the device more controllable as its resonance frequency is tunable, what may be interesting in particular to circumvent process-induced variations of dimensions.

#### RESONANCE FREQUENCY REDUCTION FOR AN IN-PLANE VIBRATING CANTILEVER

In this configuration,  $F_E = -\frac{\epsilon_0 l h}{2(d-x)^2} V_{IN DC}^2$  assuming  $V_{IN DC} \gg V_{IN AC}$ . Deriving  $F_E$ , we detail eq.(II.80) assuming  $d \gg x$  ( $x$  is the vibration amplitude):

$$f' = f_o \left( 1 - \frac{\epsilon_0 l h}{d^3} V_{IN DC}^2 \frac{1}{2k} \right) \text{ and } k_{LATERAL} = \alpha_2 \frac{E h b^3}{l^3}$$

where  $l$ ,  $b$  and  $h$  are respectively the cantilever length, width and thickness. The electrostatic force is uniformly applied on the cantilever, consequently  $\alpha_2 = \frac{2}{3}$ . ( $\alpha_2 = \frac{1}{4}$  is widely spread but is actually restricted to punctual force applied at the free end).

The detailed expression becomes:

$$f' = f_o \left( 1 - \frac{3 \varepsilon_0 l^4}{4 E b^3 d^3} V_{IN DC}^2 \right) = f_o (1 - K V_{IN DC}^2) \quad \text{with} \quad K = \frac{3 \varepsilon_0 l^4}{4 E b^3 d^3} \quad (\text{II.81})$$

where  $K$  stands as the electromechanical coupling factor.

#### RESONANCE FREQUENCY REDUCTION FOR AN OUT-OF-PLANE VIBRATING QUAD-BEAM

In this configuration,  $F_e = -\frac{\varepsilon_0 L_1^2}{2(d-z)^2} V_{DC}^2$  assuming  $V_{IN DC} \gg V_{IN AC}$ . Deriving  $F_e$ , we detail eq.(II.80) assuming  $d \gg z$  ( $z$  is the vibration amplitude):

$$f' = f_o \left( 1 - \frac{\varepsilon_0 L_1^2}{d^3} V_{IN DC}^2 \frac{1}{2k} \right) \quad \text{and} \quad k = \lambda_{QB} \frac{E b h^3}{l^3}$$

where  $L_1$ ,  $l$ ,  $b$  and  $h$  are respectively the central plate width, the beams length, width and the common thickness. To maintain a simple expression for the spring constant, we introduce  $\lambda_{QB}$ , an empirical factor extracted to fit with experimental values. We need to proceed with such an approximation since the effect of the underetching of the anchors, previously cited, drastically complicates the analytical formula. Typically,  $\lambda_{QB}$  is the range 1 – 4.

$$f' = f_o \left( 1 - \frac{\varepsilon_0 L_1^2 l^3}{2 \lambda_{QB} E b h^3 d^3} V_{IN DC}^2 \right) \quad (\text{II.82})$$

#### GENERAL COMMENT ON HOW TO LESSEN SPRING-SOFTENING EFFECT

Looking at the expanded expression of the electrostatic force (eq.(II.74)), one can observe that both time-varying terms do not oscillate at the same frequency: the first term oscillates at the frequency  $\omega$  of the driving signal and the second one at  $2\omega$  twice the driving frequency.

On the contrary to the term oscillating at  $\omega$ , the second term depends exclusively on  $V_{IN AC}$  and not on  $V_{IN DC}$ . Therefore, we might expect a less pronounced spring-softening effect as the alternate voltage magnitude is generally much weaker than the DC one. However, it must be stated that without DC voltage, the AC voltage must be much increased to excite enough the system. This tends to operate the resonator in its non-linear regime, what may be unwanted.

### II.3.c. Generalization

In the literature, resonance frequency tuning with electrostatic actuation has been demonstrated [26, 27] both upward and downward. Very few authors have clearly explained the origins of both opposite trends in electrostatic nano/microresonators. Let us call the influence of the driving electrostatic signal on the resonance frequency as amplitude-frequency ( $A-f$ ) effect.

Some authors have recently developed relatively general theoretical and qualitative models but focusing only on doubly clamped resonators (bridges). Basing on their statements, we propose a general qualitative explanation of both phenomena applicable to every resonator.

The opportunity to tune the resonance frequency is particularly interesting for applications oriented to telecommunications systems and more primarily to compensate unavoidable variations of devices dimensions related to technological process fluctuations. Various reversible frequency tuning mechanisms have been explored in the past: in particular stiffness variation with thermal stress [28] and electrostatic tuning [29, 30].

In quartz [31] devices and Si NEMS, the nonlinear  $A-f$  effect limits the maximum sustainable drive amplitude and hence the maximum SNR that can be achieved [32, 33]. Beyond the sustainable drive current, the resonant amplitude and phase response exhibit Duffing bifurcation instabilities [33, 34], as well as excess phase noise induced by amplitude noise [35]. It is of interest to determine the optimal bias condition in order to maximize the response.

These tuning behaviors are characteristic of nonlinearities. Actually, they come from the nonlinearities of two counterbalancing forces: spring force and electrostatic force resulting respectively in mechanical stiffening and electrical softening.

The most general rule than we can establish is:

- when the frequency is tuned upwards with increasing voltage (either AC or DC or a sum of both), it means that elastic frequency tuning dominates. In other words, the effect of the capacitive forces is weaker than the mechanical stiffening  $A-f$  effect: the electrostatic attraction stretches the resonator and causes an additional tensile axial force that tends to increase the resonance frequency (like in a guitar string, this effect is also named 'hard-spring' effect [23]).
- when the frequency is tuned downwards with increasing voltage, capacitive frequency tuning dominates: the softening  $A-f$  effect related to the capacitive forces [see eq.(II.80)] is stronger than the mechanical stiffening  $A-f$  effect.

Based on these two statements, each resonator will exhibit a specific behavior depending on its configuration (direction of the driving electrostatic field with respect to the direction of vibration [27]), and initial state (for example, stress in resonators may impose a bending towards or opposite the electrode and favor one type of behavior or another). This behavior can be either monotonous or with several states [26]. What can be added is that for optimal driving polarization, the interaction of the opposing mechanical stiffening and electrical softening leads to an increase in the amplitude while the frequency remains stationary. Agarwal [26] reports that the  $A-f$  coefficient in Si NEMS/MEMS is several orders of magnitude larger than quartz crystals what may be interesting for tuning.

### III. Two approaches of flexural mode resonators: Out-of-plane and in-plane vibrating resonators

The performance and, more generally, the response of a nano/micromechanical resonator embedded in a capacitive readout system depends much on how the configuration of Figure 9 is realized in practice. Considering only resonators operated in their fundamental flexural mode, we identify two cases of study with very distinct electrical responses: out-of-plane and in-plane vibration devices.

It must be clearly stated that in terms of mechanical behavior, there is absolutely no difference in the theoretical treatment between both categories. The single but very significant difference concerns the electrical response because those two types of devices are affected in a very different way by parasitic capacitances.

#### III.1. Out-of-plane flexion mode resonators

With the aim of selecting a type of resonating device to undertake its fabrication and its electrical test to subsequently implement it as mass sensor, three types of silicon resonators operated in the fundamental out-of-plane flexural mode are compared in terms of electrical response and mass sensitivity [36].

Cantilevers (Figure 3), bridges (Figure 4) (common structures used for mass sensing [37, 38]) and quad-beam resonators (Figure 5) are studied hereafter.

##### III.1.a. Comparison in terms of electrical response of three discrete devices with simplified RLC model

The goal is to compare the electrical response of those three devices in a capacitive readout scheme. For this purpose, the electrical figure of merit  $FM$  defined in section II.2.c (page 59) is used.  $FM$  must be adapted to the specific case of out-of-plane flexion resonators:

$$FM = 100 \frac{i_M}{i_p + i_w} = 100 \frac{Q \varepsilon_0^2 A^2 V_{INDC}^2}{d^4 (C_P + C_W)} \frac{1}{k}$$

- actuation is performed by applying a voltage (AC+DC) between resonator and substrate, that acts as driving electrode
- $C_P$  is the capacitance related to the physical capacitor Si/SiO<sub>2</sub>/Si formed between resonators anchors, lines and pads, and substrate. Its gap is  $d$  (i.e. SiO<sub>2</sub> thickness)
- $C_W$  is the static capacitance related to the physical capacitor formed between the resonator area, the air and the substrate (modeled as parallel finite plates with a constant gap  $d$  equal to the sacrificial SiO<sub>2</sub> layer thickness).

For device specific  $FM$  calculation ( $k$  depends upon the type of structure), useful expressions are reported in Table II - 6:

	Cantilever	Bridge	Quad beam (*)
$f_0$ resonance frequency of the first out-of-plane flexion mode	$\frac{1.015}{2\pi} \sqrt{\frac{E}{\rho}} \frac{h}{l^2}$	$\frac{6.5}{2\pi} \sqrt{\frac{E}{\rho}} \frac{h}{l^2}$	$\frac{\sqrt{\lambda_{QB}}}{2\pi} \sqrt{\frac{E}{\rho}} \frac{h b^{0.5}}{l^{1.5} L_1}$
$FM$ with $\left\{ \gamma = \frac{Q \varepsilon_0^2 V_{INDC}^2}{(C_p + C_w) d^4 E h^3} \right\}$	$\frac{3}{2} \gamma l^5 b$	$\frac{1}{32} \gamma l^5 b$	$\frac{1}{\lambda_{QB}} \gamma \frac{L_1^4 l^3}{b}$
<b>Punctual:</b> $\alpha_{1_P} = m_{EFF} / m_{RESONATOR}$	0.24	0.379	1
$k_{EFF_P}$ spring constant for punctual mass loading at the free end	$\frac{1}{4} \frac{E h^3 b}{l^3}$	$16 \frac{E h^3 b}{l^3}$	$\lambda_{QB} \frac{E h^3 b}{l^3}$
$S$ (g.Hz <sup>-1</sup> )	$\left( \frac{4\pi \alpha_{1_P} \rho^{3/2}}{1.015 E^{1/2}} \right) l^3 b$	$\left( \frac{4\pi \alpha_{1_P} \rho^{3/2}}{6.5 E^{1/2}} \right) l^3 b$	$\left( \frac{4\pi \alpha_{1_P} \rho^{3/2}}{\sqrt{\lambda_{QB}} E^{1/2}} \right) \frac{L_1^3 l^{1.5}}{b^{0.5}}$
<b>Distributed:</b> $\alpha_{1_A} = m_{EFF} / m_{RESONATOR}$	0.65	0.757	1
$k_{EFF_A}$ spring constant for uniform force distribution	$\frac{2}{3} \frac{E h^3 b}{l^3}$	$32 \frac{E h^3 b}{l^3}$	$\alpha_{QB} \frac{E h^3 b}{l^3}$
$S_D$ (g.cm <sup>-2</sup> .Hz <sup>-1</sup> )	$\left( \frac{4\pi \rho^{3/2}}{1.015 E^{1/2}} \right) l^2$	$\left( \frac{4\pi \rho^{3/2}}{6.5 E^{1/2}} \right) l^2$	$\left( \frac{4\pi \rho^{3/2}}{\sqrt{\alpha_{QB}} E^{1/2}} \right) \frac{L_1 l^{1.5}}{b^{0.5}}$

Table II - 6. Basic equations used to compare quantitatively three kinds of electrostatically actuated and detected resonators implemented as mass sensors, where  $b$  is the beam width,  $h$  the beam thickness,  $l$  the beam length,  $L_1$  the QB plate width,  $E$  the Young modulus and  $\rho$  the density of the structural material.

In Figure 16,  $FM$  has been plotted as a function of the characteristic length of the device (defined as the most varying parameter, see Table II - 6): for bridges and cantilevers this is their length  $l$ ; for QB this the plate width  $L_1$ . The rest of parameters is: constant thickness ( $h = 600$  nm), beam width ( $b = 0.5 \mu\text{m}$ ) and gap ( $d = 0.8 \mu\text{m}$ ). A Q-factor equal to 20 for all devices is considered (corresponding to ambient conditions in air). QB are DC biased with 50 V, bridges and cantilevers with 20 V: these voltages are below the pull-in voltage threshold. The spring-softening effect lowering the resonance frequency is neglected. To calculate the spring constant inside the  $FM$  formula, we have considered a uniform electrostatic force (see Table II - 6).

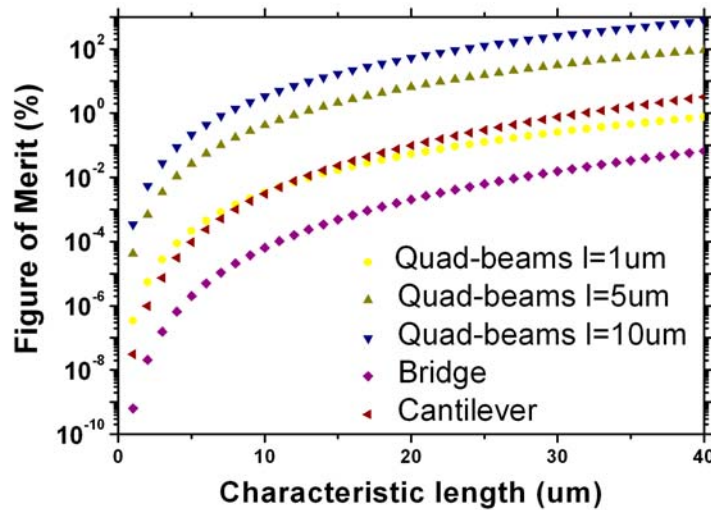


Figure 16. Electrical figure of merit (FM) in air for three kinds of resonators for  $b=0.5 \mu\text{m}$ ,  $h=600$  nm as a function of the characteristic dimension.

It is seen that the QB resonator exhibits increasing  $FM$  according as its arms increase in length. Among those three out-of-plane vibrating devices, this is probably the most appropriate one in terms of electrical response for an operation in air (i.e. low  $Q$  and high  $R_M$ ).

### III.1.b. Comparison in terms of mass sensitivity (punctual and distributed)

In this section, we compare the mass sensing attributes of the three devices for punctual and distributed mass accretions.

#### III.1.b.i) Punctual mass sensitivity

We study the case of masses deposited at the point of highest deflection (mid-point for bridges, free end for cantilevers and central plate for QB). The punctual mass sensitivity  $S$  is calculated from eq.(II.46) and plotted in Figure 17 as a function of  $l$  and  $L_1$  (characteristic length of each device) for the same conditions of Figure 16.  $k_{EFF\_P}$  and  $m_{EFF\_P}$  get specific coefficients reported in Table II - 6, in the grey zone.

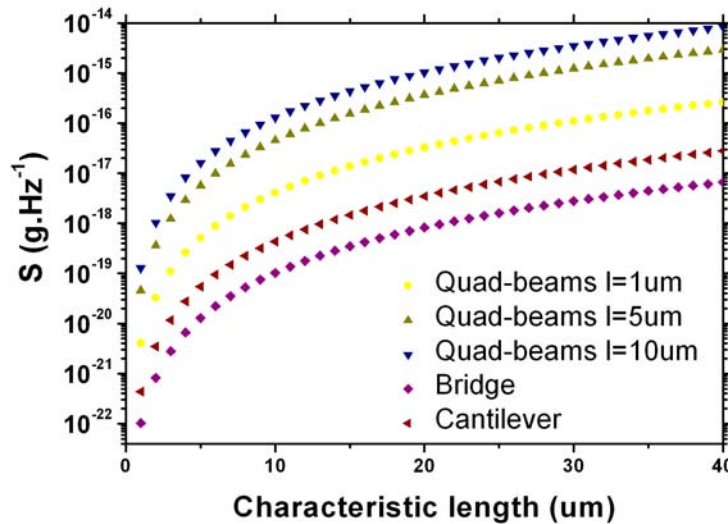


Figure 17. Punctual mass sensitivity for three kinds of resonators for  $b=0.5 \mu\text{m}$ ,  $h=600 \text{ nm}$  as a function of the characteristic dimension.

This graph shows that the bridge is the most sensitive, about one order of magnitude better than the cantilever. Concerning QB, they are about three orders of magnitude less sensitive than cantilevers, however they have a bigger active area what can be convenient for the deposition of the target adsorbate.

#### III.1.b.ii) Distributed mass sensitivity

Distributed (or areal) mass sensing is another application of a mass sensor. This is the field of quartz-crystal microbalances, generally implemented as mass rate sensors to monitor the thickness of thin layers deposited inside commercial evaporation chambers: they represent a reliable tool for this purpose but have a very poor punctual mass sensitivity.

Applying equation (II.50) to those three structures, we calculate the distributed mass sensitivity  $S_A$ . Additionally, we find that for any kind of flexural out-of-plane vibrating structure, the following quantity is constant:

$$\frac{f S_A}{h} = 2\rho \quad (\text{II.83})$$

where  $\rho$  is the resonator structural layer density and  $h$  its thickness. Therefore, for a given thickness, the higher the resonance frequency, the better is the sensitivity.

Based on formulas of Table II - 6, we have plotted  $S_A$  (distributed mass sensitivity) in Figure 18 as a function of  $l$  and  $L_l$  (characteristic length of each device) for the same conditions of Figure 16:

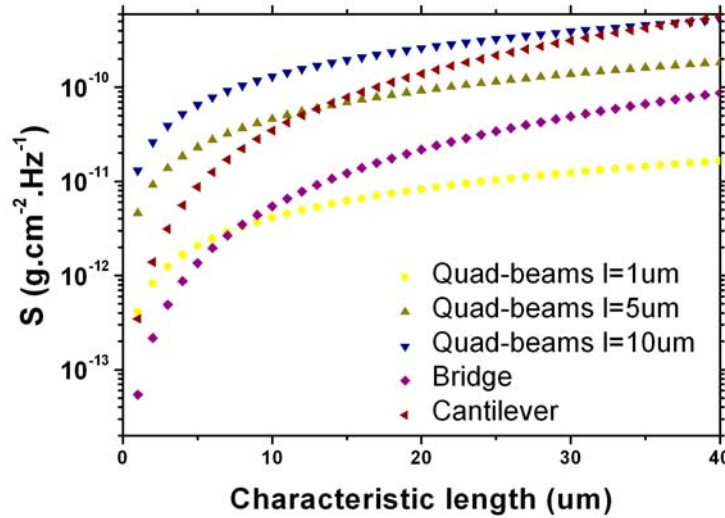


Figure 18. Distributed mass sensitivity for three kinds of resonators for  $b=0.5 \mu\text{m}$ ,  $h=600 \text{ nm}$  as a function of the characteristic dimension.

Globally, only the bridge differentiates notably from the other devices: it is between one and two orders of magnitude better in terms of distributed mass sensitivity.

However, the bridge has the poorest electrical response. A trade-off between reasonably high electrical response and sensitivity must be found in function of the targeted sensitivity of the mass measurement.

### III.1.c. Analysis of the quad-beams device

Among the three devices that have just been presented, the QB resonator exhibits the highest electrical response and is therefore the most convenient device regarding the detection aspect. This is why our study of out-of-plane flexion devices will now be exclusively focused on it. For mass sensing purposes, this is also an interesting device as its large active area (i.e. the central plate) makes more convenient the punctual deposition of a target specie.

Hereafter, a simplified electromechanical model is developed for qualitative estimation of the resonance signal as a function of geometrical dimensions, materials and device polarization.

#### III.1.c.i) Electromechanical modeling

Neglecting air damping and any other type of loss, the resonance frequency of the first out-of-plane flexural mode is approximately given (see Table II - 6) by:

$$f_1 = \frac{\sqrt{\lambda_{QB}}}{2\pi} \sqrt{\frac{E}{\rho}} \frac{hb^{0.5}}{l^{1.5} L_1} \quad (\text{II.84})$$

where  $E$  and  $\rho$  are the Young modulus and the density of the material.  $b$  and  $h$  are the beam width and the thickness of the device (see next figure).  $\lambda_{QB}$  stands as a corrective empiric factor to maintain the resonance frequency under such a form that makes its manipulation easier for simple electromechanical calculations.

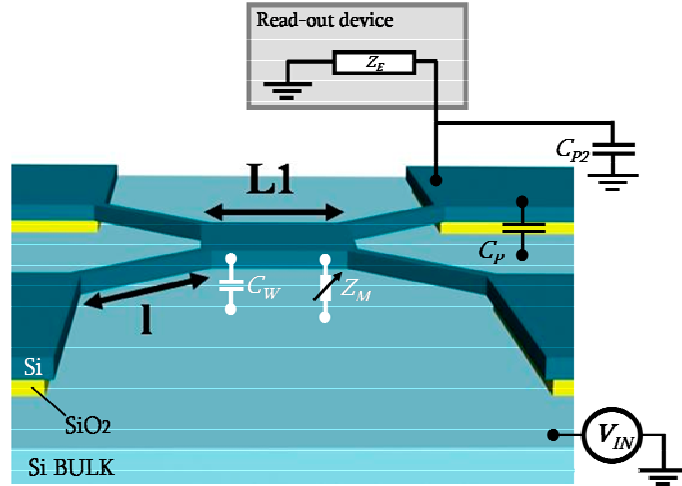


Figure 19. QB geometrical dimensions and characteristic impedances in a capacitive readout scheme

Figure 19 is a specific implementation of out-of-plane vibrating QB in a capacitive detection system. Let us discuss the meaning and the typical value of each parameter:

- $C_P$  (parallel parasitic capacitance) and  $C_W$  (parallel static capacitance) have been defined already (section III.1.a)
- At resonance, the motional impedance  $Z_M$  can be assimilated to  $R_m$ , a simple resistance whose general value is given by eq.(II.69). In this specific case, the detail of  $R_m$  is:

$$R_m = \frac{\sqrt{\lambda_{QB}} d^4 \rho^{0.5} E^{0.5}}{\epsilon_0^2 Q V_{IN DC}^2} \frac{b^{0.5} h^2}{L_1^3 l^{1.5}} \quad (\text{II.85})$$

- $C_{P2}$  is associated to the measurement instrumentation (coaxial cables, etc...), therefore it does not depend on the resonator shape and dimensions. It contributes to attenuate the available output level of resonance signal.
- $Z_E$  is the input impedance of the readout device. For the measurement of discrete devices, a network analyzer (see next section III.1.c.iii)) is implemented (input impedance adjustable to 50 or 1M $\Omega$ ).

Considering eq.(II.85) of motional impedance, it appears that the most decisive parameters for increasing the level of resonance motional current are  $L_1$  (that should be increased) and  $h$  (that should be decreased). In parallel, considering the electrical  $FM$  (eq.(II.73)), basically  $C_P$  should be lowered. Regarding this objective, one should notice that it does not depend on the resonator

shape but is only related to the anchor and contact pads area. Consequently, special efforts in terms of device design should focus on reducing this area.

The most significant features of this system are:

- for dimensions in the micron and submicron range ( $b$  in the submicron range, 10  $\mu\text{m}$  range for  $L_1$  and  $l$ ),  $R_M$  is high [1-100M $\Omega$  range] and always between one and two orders of magnitude larger than the impedance associated to  $C_P$ .

Consequently, the resonance motional current ( $i_M = V_{IN\ AC} / R_M$ ) never dominates over the two other parallel branches ( $R_M // C_W // C_P$ ).

- based on these statements and on results of section II.2.b.i), we can therefore expect from QB a poor phase peak around resonance and a resonance current magnitude systematically 'sunk' in a high background signal (mostly related to  $C_P$ , while  $C_W$  plays a minor role).
- however, QB may achieve lower  $R_M$  than other devices like cantilevers or bridges, between other reasons because they can endure much higher polarization voltages since the pull-in voltage threshold is higher.
- CMOS integration would not improve the  $FM$  (defined between the three branches contributions), however more signal would be collected because of the decrease of  $C_{P2}$  and an improvement of SNR (signal to noise ratio) would be achieved.

As a conclusion, out-of-plane vibrating flexural quad-beams embedded in a capacitive detection scheme offer contrasted features: (i) high levels of resonance current are obtained owing to potentially low  $R_M$  but (ii) this resonance signal is poorly differentiated with respect to a high intrinsic background signal (low  $FM$ ), that is related to stray parasitic capacitances originated by QB anchors.

### III.1.c.ii) Fabrication of discrete devices: e-beam lithography on SOI

As a preparatory step before the CMOS integration, discrete (i.e. on bare wafers without CMOS circuitry) quad-beams devices have been fabricated using a technological process based on standard silicon surface micromachining using silicon-on-insulator (SOI) wafers. The thickness of the SOI layer is 1.5  $\mu\text{m}$ , the thickness of the  $\text{SiO}_2$  is 1  $\mu\text{m}$ . Pads and anchors areas have been minimized in order to decrease physical parasitic capacitances (see previous section): device routing and contact pads are solely realized with silicon.

Therefore, for the whole process, a single lithography step is required. We have used electron beam lithography: first to be able to define submicron patterns, second because of its flexibility for prototyping new devices. The lithography is followed by a lift-off process of aluminum optimized for nanometer scale features. Al is used as mask for the subsequent reactive ion etching (RIE) of Si because of its excellent selectivity with respect to Si even for very thin layers (24 nm) what makes the lift-off process easier. Then, QB plates and beams are released by selective wet under-etching of  $\text{SiO}_2$  in HF.

Hereafter, all process steps are detailed. Figure 20 shows scanning electron micrographs of mechanical resonators at the end of the process. The right image reveals that the mechanical structure is successfully released from the substrate:

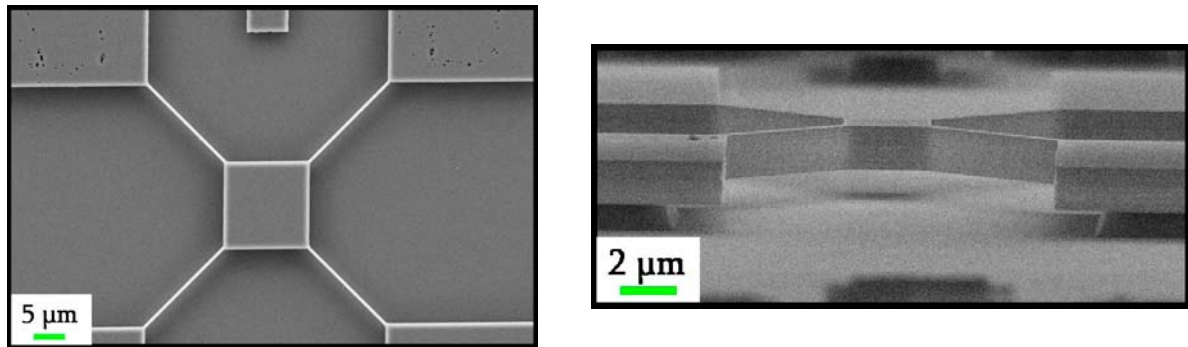


Figure 20. Scanning electron micrographs (left: top view; right: tilted view) of a mono crystalline Si quad-beam resonator fabricated by surface micromachining of a SOI wafer

#### WAFER DOPING

First, the monocrystalline Si upper layer n doped ( $N_d \approx 10^{18} \text{ at}\cdot\text{cm}^{-3}$ ) at wafer level.

- **Step 1.** n-type doping per diffusion of  $\text{POCl}_3$   
Recipe: OPOC4800 (T3), 18 min at  $950^\circ\text{C}$  in order to dope superficially 480 nm of Si
- **Step 2.** Wet etching of PSG (Phospho-Silicate-Glass) (this particular type of Si oxide forms at the Si surface because of doping impurities during diffusion).  
Recipe: QDPSGC25 (AC 5/2)
- **Step 3.** Activation of P doping atoms.  
First, Si surface oxidation at  $1100^\circ\text{C}$  to impede posterior exodiffusion of impurities  
Second, annealing at  $1000^\circ\text{C}$  under  $\text{N}_2$ .  
Recipe: O&R-ESP (T1 or T8)
- **Step 4.** Removal of thermal Si oxide formed during previous step.  
Wet etching to remove a 70 nm thick Si oxide. Overetching to make the process surer  
Recipe: QDOXTXXX (AC 2/1)

At this step, the wafer is diced and we start working at chip level.

#### PMMA DEPOSITION

- **Step 1.** Cleaning in acetone, water, IPA and water. Drying with nitrogen spray
- **Step 2.** Dehydration. 30 min at  $200^\circ\text{C}$
- **Step 3.** Spinner.  $v=1500 \text{ rpm}$ ;  $a=4500 \text{ rpm/s}$ ; 30 s with PMMA 950 KmW. (resulting in  $\sim 115 \text{ nm}$  thick layer)
- **Step 4.** Post-bake. 30 min at  $180^\circ\text{C}$  in oven or 1 min at  $180^\circ\text{C}$  with a hot plate

#### E-BEAM LITHOGRAPHY STEP

System: Raith controller interfaced to a LEO SEM column

- **Step 1.** Exposure with an extraction voltage of 10 kV, aperture:  $20 \mu\text{m}$ .
- **Step 2.** Development: MIBK (metilisobutylketona) : IPA [1:3], 30 s.
- **Step 3.** Rinsing in IPA, 30 s. Drying with nitrogen spray

#### METALLIZATION

System: Leybold-Heraeus Z-550 sputtering (Magnetron circular cathode type)

Recipe MZ550ING

Type of Al: Al/Cu 0.5% (Cu decreases Al electromigration in CMOS processes)

LIFT-OFF

- **Step 1.** 5 min immersion in heated acetone (40°C): heating makes PMMA lift off more easily
- **Step 2.** 5 min immersion in room temperature (RT) acetone with ultrasounds
- **Step 3.** 5 min immersion in IPA (RT) for cleaning
- **Step 4.** 5 min immersion in water with ultrasounds
- **Step 5.** Rinsing and drying

RIE (REACTIVE ION ETCHING) OF THE UPPER SI LAYER

- **Step 1.** Chamber conditioning.  
The chip is placed onto a bare Si carrier wafer. First, the system must be adequately conditioned: a bare Si wafer is etched with the etching recipe until it overpasses 10 minutes without having any reflected power pulse above 6 W.  
Once this step is completed, the sample is etched by proceeding with discrete steps of 14 s (equivalent to 4 cycles, one cycle representing the injection of the passivating gas  $C_4F_8$  followed by the injection of the etching gas  $SF_6$ ). The lateral overetching is around 50 nm for an etched depth of 1.3  $\mu m$ .
- **Step 2.** Etching.  
System: Alcatel A601-E (recipe *NanoI*)  
t: 4 discontinued steps of 14 s (14 s are equivalent to 4 cycles of 3.5 s)  
 $C_4F_8$ : 100 sccm (1 s)  
 $SF_6$ : 150 sccm (2.5 s)  
Pressure:  $1.4 - 2.8 \cdot 10^{-2}$  mbar  
ICP Power: 1500 W  
Plate power: 15 W  
Nominal etching speed: 1300 nm/min at 20°C

RELEASE ETCHING

Objective: wet etch in a controllable way the sacrificial buried  $SiO_2$  layer in order to release the mechanical structures

Etchant: HF 49%

Etching velocity:  $\sim 1.6 \mu m/min$ . This value tends to decrease with old bottles.

Rinsing in water, drying with a critical point drying (CPD) system

**III.1.c.iii) Measurement of discrete devices**

Prototypes of discrete quad-beams resonators were measured in air. First, to enhance substrate polarization and to facilitate the electrical contact with a probe, we used a paintbrush to manually coat the surface around the resonators with a conductive Au-based resist. Through a manually controllable contact probe, an AC voltage ( $<10$  V, provided by a network analyzer, AGILENT E5100A) summed to a DC voltage (50-100 V) by means of a bias tee (MINI-CIRCUITS ZFBT-4R2GW) are applied to the substrate.

The resonator layer is accessed via a contact pad using another probe connected to the network analyzer wherein the capacitive current produced by the resonator is converted into a voltage according to the adjustable input impedance (50 or 1  $M\Omega$ ). Due to the  $M\Omega$  range values of the resonator impedance around the resonance frequency, the allowed parasitic capacitance  $C_{P2}$  (Figure 9) at the output port is limited far below the pF range. In practice,  $C_{P2}$  is around 50 pF, equivalent to about 2  $k\Omega$  in the MHz range. Consequently an input impedance of 1  $M\Omega$  is

preferably employed so that  $2\text{ k}\Omega$  dominate at output (otherwise,  $50\ \Omega$  would dominate resulting in a still worse transimpedance amplification of the current).

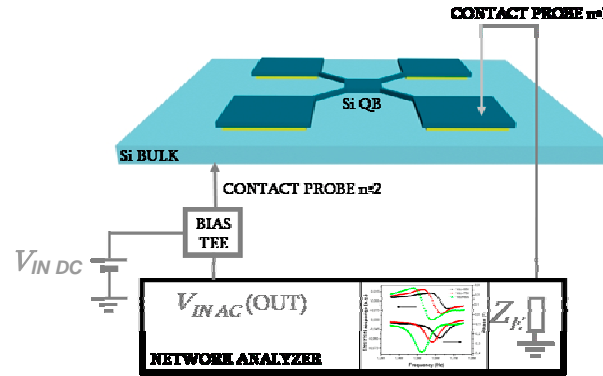


Figure 21. Measurement set-up of discrete QB resonators

The response in air of a QB (whose dimensions are:  $L_1=14\ \mu\text{m}$ ,  $l=18\ \mu\text{m}$ ,  $b=0.55\ \mu\text{m}$ ,  $h=1.5\ \mu\text{m}$ ) is depicted in Figure 22 for several values of  $V_{IN\ DC}$ :

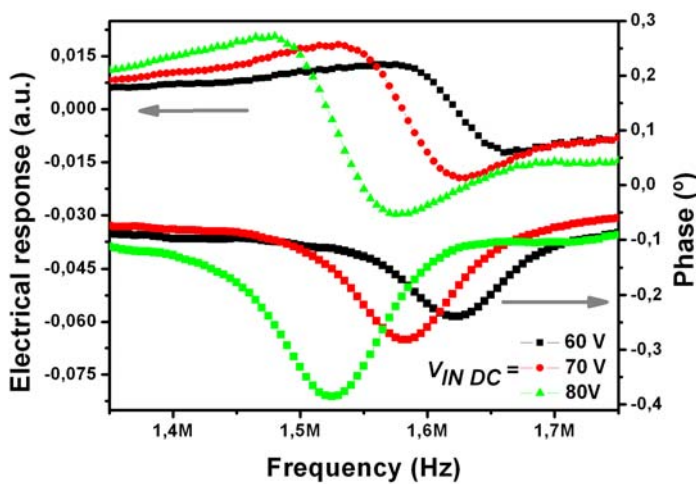


Figure 22. Resonance curves of a measurement in air for several applied dc voltages. They are obtained after calibration of the background signal with the network analyzer

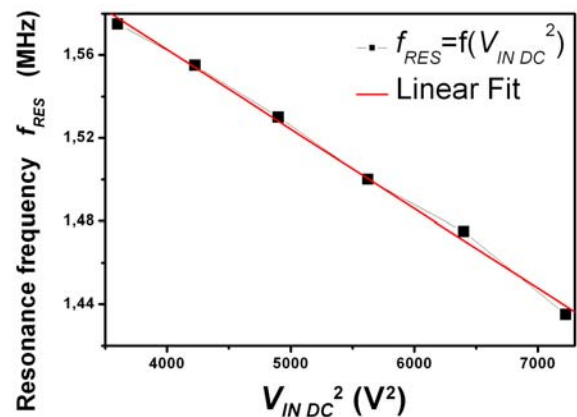


Figure 23. Experimental curve and linear fit of the voltage dependant resonance frequency as a function of the squared applied voltage ( $V_{IN\ DC}^2$ )

The amplitude spectrum exhibits one maximum and one minimum corresponding to resonance and anti-resonance respectively (see II.2.b.i)). The anti-resonance is related to parallel parasitic capacitances. In Figure 23, the evolving resonance frequency (i.e. amplitude maxima) is plotted as a function of  $V_{IN\ DC}^2$  [eq.(II.82)], the natural resonance frequency  $f_0$  is obtained by linear extrapolation (very conformal linear fit as expected from eq.(II.82)): its natural value (at  $V_{IN\ DC}=0$ ) is found to be around 1.72 MHz. This is in good agreement with analytical mechanical calculations, based on Rayleigh-Ritz quotient (see Table II - 4, first row).

Yet, the resulting level of signal is very low because of the output low-pass filter created by the high parasitic output capacitance  $C_{P2}$  (around 50 pF). CMOS integration is expected to overcome this effect by decreasing the output parasitic capacitance down to around 10 – 50 fF.

### III.2. In-plane flexion mode resonators. Cantilevers

With respect to out-of-plane vibrating resonators, in-plane vibrating flexural devices present a completely distinct electrical response, as it is going to be illustrated hereafter. We focus here exclusively on the cantilever design for two reasons: according to the previous comparative study (i) bridge resonators generate much less capacitive signal than cantilevers because of their superior stiffness and (ii) QB resonators cannot be easily integrated in-plane as 3D (or tricky 2D) lithography would be required to form non-planar beams.

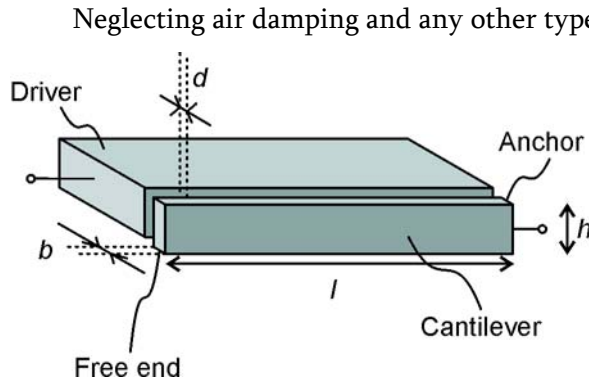


Figure 24. Cantilever geometrical dimensions

Neglecting air damping and any other type of loss, the resonance frequency of the first in-plane flexural mode is given (see section I.2.b.i)) by:

$$f_0 = \frac{1.015}{2\pi} \sqrt{\frac{E}{\rho}} \frac{b}{l^2} \quad (\text{II.86})$$

where  $E$  and  $\rho$  stand for the Young modulus and the density of the structural material.  $b$  and  $l$  are the width and the length (see Figure 24).

Figure 25 is a specific implementation of in-plane vibrating cantilevers in a capacitive detection system. Let us discuss the meaning and the typical value of each parameter:

- $C_P$  is called fringing field capacitance. It is associated to the three dimensional electric field between cantilever and front electrode. Its value is in the same order as  $C_W$  (it is calculated in chapter 5)
- $C_W$  is the static capacitance related to the cantilever/air/electrode capacitor. A bias dependent corrective factor  $K$  [21], also named electromechanical coupling factor, is applied to take into account the bending of the cantilever (i.e. to correct the non-parallelism of the capacitor) when a DC voltage is applied:

$$C_w = (1 + K V_{IN DC}^2) C_0 \quad (\text{II.87})$$

where  $K = \frac{3\varepsilon_0 l^4}{4Eb^3 d^3}$  [see eq.(II.81)] assuming  $V_{IN DC} \gg V_{IN AC}$  and  $C_0$  represents the

static parallel capacitor:  $C_0 = \frac{\varepsilon_0 h l}{d}$ .

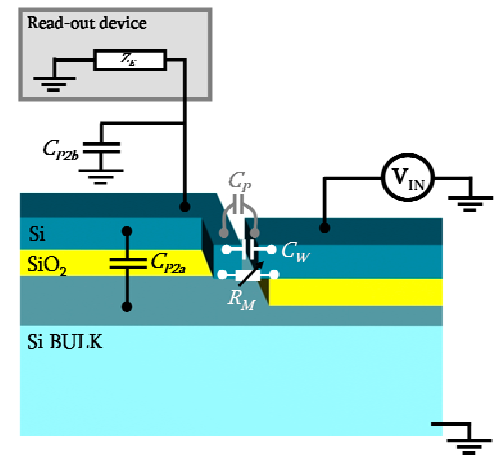


Figure 25. 3D view of an in-plane vibrating cantilever system. All main impedances are represented.

- At resonance, the motional impedance can be assimilated to a simple resistance  $R_M$  whose general value is given by eq.(II.69). In this specific case, a more accurate approach that takes into account the DC voltage-related static bending is followed [21]. This method starts by evaluating  $C_M$  (the motional capacitance), then  $L_M$  is deduced from the resonance frequency and  $C_M$ , and finally  $R_M$  is estimated from  $C_M$  and  $L_M$  (see eq.(II.69):

$$C_M = 1.798 K V_{IN DC}^2 C_0, \quad L_M = \frac{1}{4\pi^2 f_{RES}^2 C_M}, \quad \text{and} \quad R_M = \frac{1}{Q} \sqrt{\frac{L_M}{C_M}} \quad (\text{II.88})$$

- $C_{P2}$  is a sum of two contributions (see Figure 25)  $C_{P2a}$  and  $C_{P2b}$ .  $C_{P2a}$  corresponds to the physical capacitor between anchor and substrate. However,  $C_{P2b}$  associated to wiring (coaxial cables, etc...) dominates here.  $C_{P2}$  tends to attenuate the available output level of resonance signal.
- $Z_E$  is the input impedance of the readout device.

The most significant features of this system are:

- for dimensions in the micron and submicron range (down to 100 nm),  $R_M$  is very high [10M-100M $\Omega$  range] but is of the same order of magnitude (and even smaller) than the impedance associated to  $C_W$  and/or  $C_P$ . Consequently, the motional current ( $i_M = V_{IN AC} / R_M$ ) is the highest contribution of the three parallel branches ( $R_M // C_W // C_P$ ) and is not sunk in a high background signal unlike QB.
- based on these statements and on results of section II.2.b.i), we can therefore expect from the cantilever much higher phase changes than the QB. This feature is very interesting regarding the possibility of a future insertion of the cantilever in a closed loop as self-oscillator.
- however, in-plane vibrating cantilever beams produce very low resonance signals, owing to their high  $R_M$ , which consequently are closer to the noise floor. The additional strong attenuation at resonator output (related to  $C_{P2}$ ) makes even more difficult resonance measurements of discrete devices.
- in this sense, in-plane vibrating cantilever configuration would benefit much from a monolithic integration as  $C_{P2}$  would drastically be reduced.

As a conclusion, in-plane vibrating cantilevers embedded in a capacitive detection scheme also offer contrasted features: (i) low resonance signal levels are obtained, (ii) however, these resonance signals are not sunk in the background signal caused by parallel parasitic capacitances. Therefore, relatively high phase changes can be expected.

## Conclusion of chapter 2

In this chapter, the mechanical and electrical behaviors of electrostatically actuated nano/microresonators (cantilevers, bridges and quad-beams) embedded in a capacitive detection scheme have been analytically analyzed. In parallel, methods to calculate the mass sensitivity of a nano/micromechanical resonator have been described.

A comparative study of in-plane and out-of-plane vibrating flexural resonators has been carried out. Although they have identical mechanical features except the direction of vibration, their electrical response differ much. This arises from the fact that in a capacitive detection scheme, parasitic parallel capacitances can drastically degrade the performance of the transduction.

In this sense, in-plane vibrating devices are much less affected than the out-of-plane ones since the driving and the readout electrodes are sufficiently decoupled: much higher amplitude and phase relative changes can be obtained with respect to the background signal. However, in practice in-plane vibrating resonators present reduced capacitive coupling areas what results in low absolute signal levels. Additionally, output parasitic capacitances related to the measurement instrumentation (wirings, etc...) can further reduce the available signal levels.

For this reason, the opportunity to integrate monolithically nano/micromechanical resonators on CMOS in order to detect the signal through a specific CMOS circuitry is studied in next chapter (n°3). Such integration should provide two relevant advantages: (i) reducing all the parasitic loads at the resonator output, and (ii) amplifying and conditioning 'on-chip' the resonance signal.

## Bibliographical references

1. Berger, R., C. Gerber, H.P. Lang, and J.K. Gimzewski  
**Micromechanics: A toolbox for femtoscale science: "Towards a laboratory on a tip"**  
Microelectronic Engineering, 1997. **35**(1-4): p. 373-379.
2. Boisen, A., J. Thaysen, H. Jensenius, and O. Hansen  
**Environmental sensors based on micromachined cantilevers with integrated read-out**  
Ultramicroscopy, 2000. **82**(1-4): p. 11-16.
3. Ekinici, K.L. and M.L. Roukes  
**Nanoelectromechanical systems**  
Review of Scientific Instruments, 2005. **76**(6).
4. Cleland, A.N. and M.L. Roukes  
**External control of dissipation in a nanometer-scale radiofrequency mechanical resonator**  
Sensors and Actuators a-Physical, 1999. **72**(3): p. 256-261.
5. Blick, R.H., A. Erbe, L. Pescini, A. Kraus, D.V. Scheible, F.W. Beil, E. Hoehberger, A. Hoerner, J. Kirschbaum, and H. Lorenz  
**Nanostructured silicon for studying fundamental aspects of nanomechanics**  
Journal of Physics-Condensed Matter, 2002. **14**(34): p. R905-R945.
6. Carr, D.W. and H.G. Craighead  
**Fabrication of nanoelectromechanical systems in single crystal silicon using silicon on insulator substrates and electron beam lithography**  
Journal of Vacuum Science & Technology B, 1997. **15**(6): p. 2760-2763.
7. Carr, D.W., L. Sekaric, and H.G. Craighead  
**Measurement of nanomechanical resonant structures in single-crystal silicon**  
Journal of Vacuum Science & Technology B, 1998. **16**(6): p. 3821-3824.
8. Gupta, A., D. Akin, and R. Bashir  
**Single virus particle mass detection using microresonators with nanoscale thickness**  
Applied Physics Letters, 2004. **84**(11): p. 1976-1978.
9. Villarrojo, M., J. Teva, E. Forsen, J. Verd, G. Abadal, J. Montserrat, J. Esteve, F. Pérez-Murano, A. Boisen, and N. Barniol  
**MEMS mass sensor with attogram/Hz sensitivity based on a polysilicon cantilever array integrated monolithically with CMOS circuit**  
in the proceedings of the *XIX Eurosensors*. 2005. Barcelona.
10. Arcamone, J., M.A.F.v.d. Boogaart, F. Serra-Graells, S. Hansen, J. Brugger, F. Torres, G. Abadal, N. Barniol, and F. Pérez-Murano  
**Full-wafer integration of NEMS on CMOS by nanostencil lithography**  
in the proceedings of the *IEEE IEDM*. 2006. San Francisco (USA).
11. Brand, O. and G.K. Fedder  
**CMOS-MEMS**  
Wiley-VCH ed, Vol. 2, 2005, Weinheim.
12. Bao, M.-H.  
**Micro Mechanical Transducers**  
Elsevier ed, Vol. 8, 2000, Amsterdam.

## Chapter 2. Concepts of nano/micromechanical resonators for mass sensing applications with all electric actuation and detection

---

13. Villanueva, G.  
**Development of cantilevers for biomolecular measurements**  
PhD thesis, UAB (CNM-CSIC) (2006)
14. Chen, G.Y., T. Thundat, E.A. Wachter, and R.J. Warmack  
**Adsorption-Induced Surface Stress and Its Effects on Resonance Frequency of Microcantilevers**  
Journal of Applied Physics, 1995. **77**(8): p. 3618-3622.
15. Ramos, D., J. Tamayo, J. Mertens, M. Calleja, and A. Zaballos  
**Origin of the response of nanomechanical resonators to bacteria adsorption**  
Journal of Applied Physics, 2006. **100**(10).
16. Tamayo, J., D. Ramos, J. Mertens, and M. Calleja  
**Effect of the adsorbate stiffness on the resonance response of microcantilever sensors**  
Applied Physics Letters, 2006. **89**(22).
17. Dohn, S., R. Sandberg, W. Svendsen, and A. Boisen  
**Enhanced functionality of cantilever based mass sensors using higher modes**  
Applied Physics Letters, 2005. **86**(23).
18. Mattila, T., O. Jaakkola, J. Kiihamaki, J. Karttunen, T. Lamminmaki, P. Rantakari, A. Oja, H. Seppa, H. Kattelus, and I. Tittonen  
**14 MHz micromechanical oscillator**  
Sensors and Actuators a-Physical, 2002. **97-8**: p. 497-502.
19. Mattila, T., J. Kiihamaki, T. Lamminmaki, O. Jaakkola, P. Rantakari, A. Oja, H. Seppa, H. Kattelus, and I. Tittonen  
**A 12 MHz micromechanical bulk acoustic mode oscillator**  
Sensors and Actuators a-Physical, 2002. **101**(1-2): p. 1-9.
20. Nguyen, C.T.C. and R.T. Howe  
**An integrated CMOS micromechanical resonator high-Q oscillator**  
IEEE Journal of Solid-State Circuits, 1999. **34**(4): p. 440-455.
21. Abadal, G., Z.J. Davis, B. Helbo, X. Borrise, R. Ruiz, A. Boisen, F. Campabadal, J. Esteve, E. Figueras, F. Perez-Murano, and N. Barniol  
**Electromechanical model of a resonating nano-cantilever-based sensor for high-resolution and high-sensitivity mass detection**  
Nanotechnology, 2001. **12**(2): p. 100-104.
22. Carr, D.W., S. Evoy, L. Sekaric, H.G. Craighead, and J.M. Parpia  
**Measurement of mechanical resonance and losses in nanometer scale silicon wires**  
Applied Physics Letters, 1999. **75**(7): p. 920-922.
23. Tilmans, H.A.C., M. Elwenspoek, and J.H.J. Fluitman  
**Micro Resonant Force Gauges**  
Sensors and Actuators a-Physical, 1992. **30**(1-2): p. 35-53.
24. Davis, Z.J., G. Abadal, O. Kuhn, O. Hansen, F. Grey, and A. Boisen  
**Fabrication and characterization of nanoresonating devices for mass detection**  
Journal of Vacuum Science & Technology B, 2000. **18**(2): p. 612-616.
25. Zhao, J.H., G.E. Bridges, and D.J. Thomson  
**Direct evidence of "spring softening" nonlinearity in micromachined mechanical resonator using optical beam deflection technique**  
Journal of Vacuum Science & Technology A, 2006. **24**(3): p. 732-736.

## Chapter 2. Concepts of nano/micromechanical resonators for mass sensing applications with all electric actuation and detection

---

26. Agarwal, M., S.A. Chandorkar, R.N. Candler, B. Kim, M.A. Hopcroft, R. Melamud, C.M. Jha, T.W. Kenny, and B. Murmann  
**Optimal drive condition for nonlinearity reduction in electrostatic microresonators**  
Applied Physics Letters, 2006. **89**(21).
27. Kozinsky, I., H.W.C. Postma, I. Bargatin, and M.L. Roukes  
**Tuning nonlinearity, dynamic range, and frequency of nanomechanical resonators**  
Applied Physics Letters, 2006. **88**(25).
28. Syms, R.R.A.  
**Electrothermal frequency tuning of folded and coupled vibrating micromechanical resonators**  
IEEE Journal of Microelectromechanical Systems, 1998. **7**(2): p. 164-171.
29. Sazonova, V., Y. Yaish, H. Ustunel, D. Roundy, T.A. Arias, and P.L. McEuen  
**A tunable carbon nanotube electromechanical oscillator**  
Nature, 2004. **431**(7006): p. 284-287.
30. Schwab, K.  
**Spring constant and damping constant tuning of nanomechanical resonators using a single-electron transistor**  
Applied Physics Letters, 2002. **80**(7): p. 1276-1278.
31. Gagnepain, J.J.  
**Nonlinear Properties of Quartz Crystal and Quartz Resonators: A Review**  
in the proceedings of the *35th IEEE annual Frequency Control Symposium*. 1981. New York (USA).
32. Kaajakari, V., T. Mattila, A. Oja, and H. Seppa  
**Nonlinear limits for single-crystal silicon microresonators**  
IEEE Journal of Microelectromechanical Systems, 2004. **13**(5): p. 715-724.
33. Agarwal, M., K. Park, R. Candler, M. Hopcroft, C. Jha, R. Melamud, B. Kim, B. Murmann, and T.W. Kenny  
**Non-linearity cancellation in MEMS resonators for improved power-handling**  
in the proceedings of the *IEEE IEDM*. 2005. Washington (USA).
34. Landau, L.D. and E.M. Lifshitz  
**Mechanics**  
Butterworth-Heinemann ed, Course of theoretical physics, Vol. 1, 1982, Reading, MA. 87-92.
35. Agarwal, M., K.K. Park, B. Kim, M.A. Hopcroft, S.A. Chandorkar, R.N. Candler, C.M. Jha, R. Melamud, T.W. Kenny, and B. Murmann  
**Amplitude noise induced phase noise in electrostatic MEMS resonators**  
in the proceedings of the *Solid state sensor, actuator and microsyst. Workshop*. 2006. Hilton Head'06.
36. Arcamone, J., G. Rius, G. Abadal, J. Teva, N. Barniol, and F. Perez-Murano  
**Micro/nanomechanical resonators for distributed mass sensing with capacitive detection**  
Microelectronic Engineering, 2006. **83**(4-9): p. 1216-1220.
37. Ekinci, K.L., X.M.H. Huang, and M.L. Roukes  
**Ultrasensitive nanoelectromechanical mass detection**  
Applied Physics Letters, 2004. **84**(22): p. 4469-4471.
38. Sharos, L.B., A. Raman, S. Crittenden, and R. Reifenberger  
**Enhanced mass sensing using torsional and lateral resonances in microcantilevers**  
Applied Physics Letters, 2004. **84**(23): p. 4638-4640.



# CHAPTER 3

## DEVICE MODELING AND IC DESIGN OF NANO/MICROMECHANICAL RESONATORS ON CMOS CIRCUITRY

I.	Interest of monolithic integration with CMOS .....	83
I.1.	Comparison integrated/discrete structures.....	83
I.2.	State-of-the-art of circuit topologies .....	84
II.	Integration of NEMS on CMOS.....	86
II.1.	Design of CMOS integrated NEMS resonators.....	86
II.1.a.	In-plane vibrating cantilevers.....	86
II.1.b.	Out-of-plane vibrating QB.....	86
II.2.	CCII CMOS circuit characteristics.....	87
II.2.a.	CCII Circuit topology .....	87
II.2.b.	CCII circuit performance .....	90
II.2.b.i)	Determination of operation points (DC) .....	91
II.2.b.ii)	AC response .....	92
II.2.b.iii)	Transient simulations .....	95
II.2.b.iv)	Conditions of saturation .....	97
II.2.b.v)	Linearity of the circuit response .....	97
II.2.b.vi)	Noise analysis .....	98
II.2.c.	CCII circuit performance with NEMS model at input .....	99
II.2.c.i)	Electrical simulations of cantilevers-CCII mixed circuit.....	99
II.2.c.ii)	Electrical simulations of QB-CCII mixed circuit .....	105
II.3.	NEMS/CMOS circuit layout.....	108
II.3.a.	CCII Circuit layout, integration areas layout.....	108
II.3.b.	Chip layout .....	111
	Conclusion of chapter 3.....	113
	Bibliographical references .....	114

As a continuation of chapter 2, chapter 3 is focused on the monolithic integration of nano/micromechanical resonators on CMOS circuitry. The motivation and advantages are detailed in terms of device operation. Later, chapter 4 will be related to the fabrication process of M-NEMS/CMOS integrated systems.

As demonstrated in chapters 1 and 2, nano/micromechanical resonators have a strong interest mainly in two areas: as high sensitivity sensors [1, 2] and as building blocks for high frequency telecommunication systems [3-5]. Many practical applications of mechanical resonators require all electric actuation and detection methods whose smartest and most efficient implementation is monolithic integration with a CMOS circuit: this solution is optimum for 'on-chip' signal processing since parasitic capacitances are drastically reduced. The integrated circuit (IC), interfaced with the M/NEMS, efficiently collects the resonance signal and can subsequently amplify and condition it

Concerning sensing applications, several recent publications confirm that nanotechnology is becoming a promising approach to integrate both sensors [6-10] and actuators [11] in CMOS technologies.

On another hand, the semiconductor market exhibits an increasing demand on products for mobile applications, requiring in general very low-power and compact IC. In this sense, nanotechnologies also seem a suitable partner for CMOS circuits, since mechanical implementations of RF components may achieve larger power consumption savings and size reductions than their electronic counterparts. In particular, the possibility of using NEMS to replace the quartz crystal devices (as reference clock oscillator) is of high interest for the implementation of integrated oscillators [12, 13]. With respect to quartz devices, NEMS consume much less energy, offers outstanding perspectives of integration and are compatible with batch fabrication processes.

In this context, this chapter will start by the comparison in terms of electrical performance between discrete and integrated devices, and then a state-of-the-art of reported CMOS circuits for N-MEMS interfacing will be presented.

Specific CMOS circuits either for testing NEMS or for their interfacing within the final mixed electromechanical system-on-chip (SoC) need to be developed. Here, an approach is followed whereby electrostatic actuation and capacitive readout by an IC are used to detect the oscillations of the nanomechanical resonators. The RLC model presented in chapter 2 is implemented to predict the electrical response of nano/micromechanical resonators: the expected low signal levels in the range of nA and the required bandwidth in the MHz range imposed a series of challenging circuit specifications.

Thereby, a specific built-in low-power CMOS readout circuit [14] has been developed in the framework of this thesis and is presented hereafter. Its function is to interface NEMS resonators by collecting the motional current and to provide the frequency response in order to be able to detect the mechanical resonance frequency; more specifically the behavior of cantilevers and QB operated in in-plane and out-of-plane flexion respectively is studied. The IC architecture is inspired from second generation current conveyors (CCII). Circuit topology, layout and simulated response are detailed in this chapter.

## I. Interest of monolithic integration with CMOS

Major enhancements in terms of device performance can be achieved by integrating nanomechanical structures with CMOS circuitry to form NEMS/CMOS systems. Following an all electric actuation and detection scheme (capacitive transduction), a monolithic integration provides a better readout of the output signal through a decrease of parasitic capacitances at NEMS output. This signal can subsequently be amplified and conditioned 'on chip'. This opens perspectives of closed loop operation as stand alone electromechanical oscillator. NEMS/CMOS devices also offer unique advantages in terms of compactness and packaging for portable applications like sensors or electronic devices (mobile phones, etc...).

### I.1. Comparison integrated/discrete structures

Following the electrical modeling presented in chapter 2, the behavior of discrete and integrated cantilevers and QB is compared. Figure 1 sketches the equivalent electrical modeling of a nanomechanical resonator (cf. chapter 2, fig. 9), whereby the key elements are:

- $Z_P$ , the parasitic impedance (related to parasitic capacitances  $C_P$ ) and  $Z_W$  the 'static' impedance (related to the resonator static capacitance  $C_W$ )
- $Z_M$ , the motional impedance, equivalent around the resonance frequency to a simple resistance  $R_M$
- $Z_{P2}$ , the NEMS output impedance (related to parasitic output capacitances  $C_{P2}$ ).

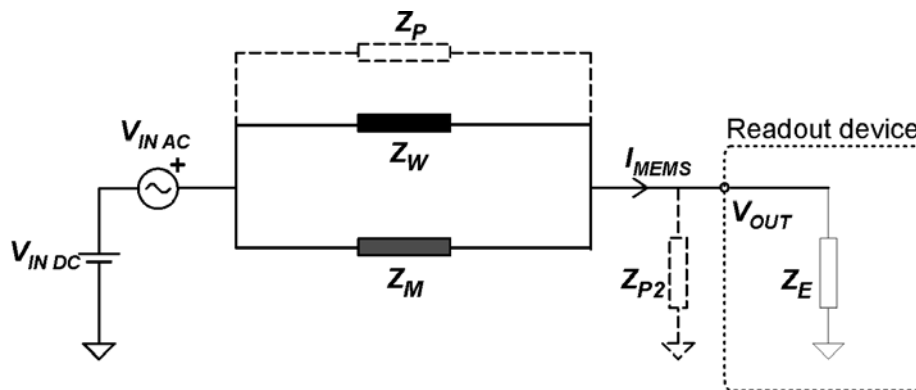


Figure 1. Equivalent electrical modeling of a nanomechanical resonator

Three criteria determine both the magnitude of the collected NEMS current ( $I_{MEMS}$ ) and the relative contribution of the resonance current  $I_{RES}$  within  $I_{MEMS}$  :

- CRITERIA 1 the lower is  $R_M$ , the higher is the generated resonance signal ( $I_{RES}$ )
- CRITERIA 2 the smaller is the ratio  $\frac{R_M}{Z_P + Z_W}$  ( $= 1/FM$ ), the larger is the ratio  $\frac{I_{RES}}{I_{MEMS}}$  and better is the 'quality' of the resonance signal. Concretely, it means that higher amplitude peaks are obtained with respect to the background signal created by  $Z_P$  and  $Z_W$ . The same happens concerning the phase: more significant phase peaks (phase changes) are generated (c.f. chapter 2).

- CRITERIA 3 the higher is  $Z_{P2}$  (e.g. the smaller are the output capacitances), the higher is the available resonance signal for the readout device, in other words the lower are the losses.

Criteria 1 and 2 are intrinsic to a NEMS structure and do not depend on whether it is discrete or integrated.

From previous studies, it states that in-plane vibrating cantilevers are limited by criteria 1 (high  $R_M$ ) and produce very low signals. However, the motional signal (the interesting one) is equal or bigger than the parallel parasitic ones, what makes that criteria 2 is fully satisfied.

Concerning quad-beams, the situation is reversed: criteria 1 is correctly satisfied while their response to criteria 2 is very poor, possibly complicating irreversibly an implementation of QB in closed loop operation, on the contrary to cantilevers.

Monolithic integration provides a drastic enhancement facing criteria 3, independently of the NEMS structure. The insertion of a built-in interface IC at the output electrode reduces  $C_{P2}$  ( $= \frac{1}{Z_{P2} \omega}$ ) to a low capacitance physical capacitor formed by the routing between NEMS output electrode and IC input.

For discrete devices,  $C_{P2}$  is related to the measurement set-up (wire bonding, probe station, coaxial cables, etc...) and is in the order of tens of pF. For integrated,  $C_{P2}$  is in the order of tens of fF, what represents an improvement by three or four orders of magnitude. Therefore signal losses at NEMS output are almost nulled and the entire resonator current ( $I_{MEMS} = I_{RES} + I_W + I_P$ ) is collected for the readout through the IC.

As a conclusion, CMOS integrated NEMS ensures better transduction efficiency as more resonance signal is collected for subsequent readout due to the reduction of losses at NEMS output, and provided CMOS circuitry does not generate any additional noise, better SNR (signal to noise ratio) are consequently obtained.

## I.2. State-of-the-art of circuit topologies

Monolithic integration of nano/micromechanical resonators with CMOS readout circuitry is more efficient in terms of transduction; however the global performance of the mixed NEMS-CMOS system depends on the type of readout IC. Different approaches have been reported in the literature to get to the result of electrically measuring the resonance frequency of nano/micromechanical resonators.

Circuit topologies depend on the type of transduction, mainly either capacitive or piezoresistive. The frequency of operation is also a relevant factor: very high frequency N-MEMS require more complex circuits, and signal transmission issues also perturb the readout process. Hereafter, a short survey of existing CMOS circuits for the readout of mechanical oscillations is presented.

Concerning piezoresistively sensed mechanical resonators, the integrated detection electronics is generally based on specific implementations of Wheatstone bridge. A solution relying on an off-chip high impedance buffer amplifier wire bonded to the sensor die has been proposed to measure the variation of resistance of an implanted piezoresistor in a half bridge scheme [15]. Regarding monolithic solutions, a chopper amplifier placed after a half bridge configuration has been used for low frequency devices [16-19] to circumvent the effect of  $1/f$  noise as the signal is moved from low to the chopping frequency and amplified there.

An original approach consists in employing stressed transistors as deflection sensors [20]. Four diode-connected PMOS-transistors (acting as active loads) are used to sense the mechanical stress created by cantilever vibrations: orientating adequately four well-matched transistors, an 'on-resonator' Wheatstone bridge is formed where strained MOS channels play the role of resistors.

However, most examples of CMOS integrated resonators use capacitive transduction.

In [21], an integrated floating-electrode electric microgenerator is proposed. The mechanical motion of a metallic resonator creates charges in an in-front (permanently charged) insulated electrically floating fixed electrode working like a conventional non-volatile memory. This floating electrode is connected to the gate of a transistor acting as sensor for charge monitoring.

In [12, 22, 23] and [10], the current/voltage conversion is realized at resonator output, not inside the CMOS circuit. Indeed, the capacitive motional current is integrated through the parasitic capacitance formed by the parallel routing and intrinsic CMOS input capacitances. The resulting voltage passes through an unity gain differential pair, the output stage is a source follower. The DC input node voltage is controlled with a bias resistance in [12], with a PMOS transistor operated in the subthreshold region (high impedance is ensured so that no current flows in) in [10].

In [4, 13, 24-28], the motional current is converted to a voltage in the first stage of the circuit. In [4, 13, 24, 25], this operation is realized through the use of a low input impedance shunt-shunt feedback amplifier: the transimpedance gain is achieved by a nearly linear cross-coupled configuration [24] or using a MOS resistor [4, 13, 25].

In [24], an interesting solution is proposed to diminish the cross-talk of feed-through capacitances: differential signaling is put in practice through the simple analog subtraction of the currents arising both from the readout electrode and from an auxiliary electrode, non-movable and with the same feed-through capacitance.

In many cases, these CMOS circuits that amplify the motional current in a way or another actually make part of a closed loop MEMS/CMOS oscillator [4, 13, 26-28].

In this thesis, an original and new CMOS topology [14] is proposed based on a low input impedance second generation current conveyor (CCII)-based circuit that collects and amplifies the motional current. The current/voltage conversion is realized externally at circuit output by means of a load resistor.

## II. Integration of NEMS on CMOS

In this section, a detailed description of our approach for the monolithic integration of NEMS resonators on CMOS is given. The guidelines for the choice of adequate geometrical dimensions for integrated cantilevers and QB are explained. Then, a new topology of interfacing CMOS readout circuit is presented: its schematic and layout are exposed. Its intrinsic behavior and its behavior when coupling it to the NEMS are discussed based on electrical simulations.

### II.1. Design of CMOS integrated NEMS resonators

The maximum cut-off frequency permitted by CNM CMOS technology is limited to 5-10 MHz. As we will explain it in more details in chapter 4, this CMOS technology was selected for its flexibility in terms of fabrication (all process steps are well-known and may be slightly modified). The process strategy of integration is based on using existing layers of the CMOS as structural (polysilicon) and sacrificial (field SiO<sub>2</sub>) layers.

Focusing this work on cantilevers and QB integration, their geometrical dimensions must be optimally chosen so that (i) their resonance frequency (that depends only on resonator dimensions and material) does not exceed a limit of 5 MHz (limitation caused by the technology), (ii) the electrical figure of merit ( $FM$ ) is maximized and (iii) an areal mass sensitivity around  $10^{-10}$  g.cm<sup>-2</sup>.Hz<sup>-1</sup> is provided for further mass sensing experiments. To get free of unavoidable deviations due to process fluctuations, the resonance frequency was limited to 1-2 MHz.

#### II.1.a. In-plane vibrating cantilevers

The vibration mode to be transduced is the first in-plane flexural mode. Considering a limitation in the resonance frequency of 2 MHz, cantilever length and width ( $l$  and  $b$  respectively) are the two parameters to be adjusted since polysilicon thickness has a fixed value determined by the technology ( $h \approx 600$  nm) (see chapter 2, fig. 24).

Improving the electrical figure of merit ( $FM$ ) can be achieved reducing  $b$  or increasing  $l$ . At the same time,  $l$  should be as short as possible (i) in order to increase the value of the pull-in voltage, (ii) shorter cantilevers are stiffer what makes them less sensitive to 'sticking' effect which may collapse them against their in-front electrode or against the underneath substrate during their release.

Concerning fabrication aspects, a demonstration of high nanopatterning resolution has been pursued (NaPa project, see chapter 4) therefore  $b$  has been chosen around 200 nm. In this context, length around 13 -14  $\mu$ m enter the specifications in terms of resonance frequency.

#### II.1.b. Out-of-plane vibrating QB

The vibration mode to be transduced is the first out-of-plane flexural mode. According to table II.6,  $L_1$ , the plate width, is the key parameter governing the electrical  $FM$  while  $l$ , the beam length, is the key parameter governing the resonance frequency and the distributed mass sensitivity  $S_D$ .

$l$  and  $L_1$  have contrary effects, increasing  $L_1$  will result in a better  $FM$ , however it will deteriorate  $S_D$ , and vice versa for  $l$ . Considering a limitation in the resonance frequency of 2 MHz,

the choice of  $l$  and  $L_1$  is a trade-off between  $FM$  and  $S_D$ : the final values must be selected in function of the desired target, either a better electrical response or better sensing attributes. Regarding the beam width  $b$ , it does not influence much nor  $FM$  neither  $S_D$ , however it is kept in the submicron range due to the technology (test parameter of patterning resolution).

In this context,  $l$  and  $L_1$  being both in the 10  $\mu\text{m}$  range and  $b$  around 500 nm, the three aforementioned requirements are satisfied.

## II.2. CCII CMOS circuit characteristics

A specific integrated capacitive readout system [14] is proposed for the electrical detection of the mechanical resonance. The proposed monolithic CMOS new implementation is based on a second generation current conveyor (CCII) circuit coupled to a NEMS resonator:

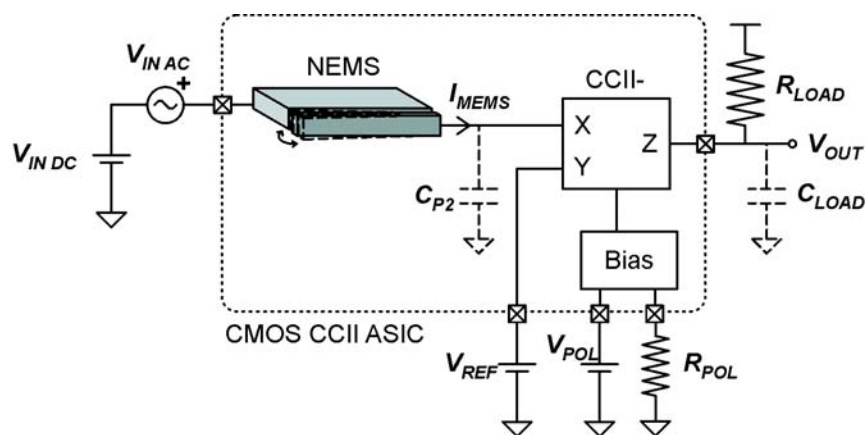


Figure 2. Proposed monolithic CMOS-NEMS system. Example of an in-plane vibrating cantilever

The nano/micromechanical resonator is electrostatically actuated by a DC+AC voltage. The readout electrode (i.e. the resonator anchor), electrically connected to the IC input, collects a capacitive current whose one part is specifically generated (see chapter 2) by the variation of electrode-resonator capacitance due to mechanical motion.

With the aim of reading out the output current of the resonator, a CMOS CCII is inserted at the output electrode. The circuit keeps a constant voltage at the NEMS output electrode (node X) according to the control electrode (node Y) and the monolithic integration ensures values of  $C_{P2}$  (parasitic capacitance determined by the routing) in the far sub-pF range. Furthermore, the CCII supplies flat spectral amplification of  $I_{MEMS}$  at the circuit output (node Z) for either external measurement at  $V_{OUT}$  or internal feedback for future implementations as stand-alone oscillator.

### II.2.a. CCII Circuit topology

The CMOS interfacing circuit of Figure 2 must ensure a constant bias at the output of the NEMS so that the circuit input (node X) behaves like a low impedance node in order to readout its current like an ammeter. Its complementary function is to amplify it and convert it externally into a voltage according to a load resistor.

For this purpose, the compact CMOS circuit shown in Figure 3 is proposed (the complete schematic is given in annex A.6). Basically, it is a transimpedance amplifier (input in current, output in voltage) whose architecture is divided into two main blocks that consist of an input low-impedance stage (M1-M4) and an output current scaler (M5-12).

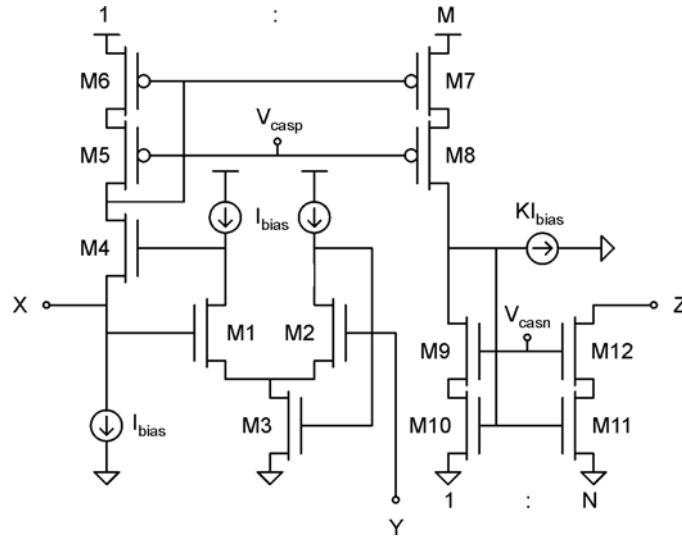


Figure 3. Simplified schematic of the CMOS CCII circuit

On one hand, the low-input impedance is achieved by the cascode transistor M4. Its gate is continuously regulated by the telescopic differential amplifier M1-M3, whose negative feedback tends to compensate any difference between  $V_X$  and  $V_Y$ . As a result, this input stage behaves like a voltage source  $V_X$  controlled by  $V_Y$ , sinking or sourcing the  $I_{MEMS}$  current demanded by the NEMS resonator. In this sense, the  $I_{MEMS}$  full scale that can drive the CCII-circuit from X is defined by its Class-A bias level  $I_{BIAS}$ . Class-A is optimum to maintain a good linearity and by reducing the complexity of the circuit, a smaller circuit area is obtained. The associated higher static consumption is not an issue here. According to the advanced EKV MOSFET model [29], the small-signal input resistance of this controlled voltage source is found to be:

$$r_{in} = \left( \frac{1}{n + \frac{gm_{g1}}{gm_{d1}}} \right) \frac{1}{gm_{g4}} \quad (\text{III.1})$$

where  $n$  stands for the subthreshold slope factor,  $gm_{g1}$  for the gate transconductance of transistor M1,  $gm_{d1}$  for the drain transconductance of transistor M1, and  $gm_{g4}$  for the gate transconductance of transistor M4. Hence the error amplifier scales down  $r_{IN}$  by its gain factor  $\frac{gm_{g1}}{gm_{d1}}$  compared to the impedance of the single M4 transistor  $\frac{1}{gm_{g4}}$ .

On the other hand, the NEMS current sensed by M4 is amplified by the geometrical scaling factors  $M$  and  $N$  of the two-stage cascode current mirrors M5-M8 and M9-12 biased at  $V_{CASp}$  and  $V_{CASn}$ , respectively. In order to reduce the overall power consumption, a  $K/M$  fraction of the biasing is subtracted before the second amplification stage.

In conclusion, the proposed circuit qualitatively behaves like a classic CCII- [30], but with an extra gain from the  $I_X$  to  $I_Z$  signals:

$$\begin{bmatrix} I_Y \\ V_X \\ I_Z \end{bmatrix} = \begin{bmatrix} 0 & 0 & 0 \\ 1 & 0 & 0 \\ 0 & -MN & 0 \end{bmatrix} \begin{bmatrix} V_Y \\ I_X \\ V_Z \end{bmatrix} \quad (\text{III.2})$$

In fact, the new CCII-topology introduced in Figure 3 is an improvement of the input stage of [31] in order to allow a wider voltage range for both  $V_X$  and  $V_Y$  thanks to the symmetry of the M1 and M2 drain connections. Also, compared to other CCII- evolutions like [32], the proposed circuit saves power consumption by minimizing the transistor count of the input stage.

Applying the circuit model (matrix (III.2)) to the general readout scheme of Figure 1, the following characteristics are obtained:

$$V_{OUT AC} = R_{LOAD} M N I_{MEMS} \quad (III.3)$$

$$V_X = V_{NEMS OUT} = V_{REF} \quad (III.4)$$

where  $I_{MEMS} = I_{RES} + I_W + I_{PA}$  is the total MEMS current with the three contributions previously mentioned while  $V_{NEMS OUT}$  stands for the DC voltage at resonator output.

Additionally, the DC output voltage is given by:

$$V_{OUT DC} = V_{DD} - R_{LOAD} [(M - K) N I_{BIAS}] \quad (III.5)$$

where  $I_{BIAS}$  is given in first approximation by:

$$I_{BIAS} \approx V_{POL} / R_{POL} \quad (III.6)$$

$V_{POL}$  and  $R_{POL}$  are externally controllable through contact pads and are a DC voltage and a variable resistance respectively. In the next section, the calculation of  $I_{BIAS}$  is detailed.

The external output stage consisting of  $R_{LOAD}$  and  $C_{LOAD}$  represents a low-pass filter whose cut-off frequency is given by:

$$f_{MAX -3dB} = \frac{1}{2\pi R_{LOAD} C_{LOAD}} \quad (III.7)$$

From initial tests, an approximate value of 50 pF for the output parasitic capacitance  $C_{LOAD}$  (related to the probe station, PCB and coaxial cables) had been estimated and implemented in initial circuit simulations. Final experimental tests with fully fabricated samples yielded 30 pF. The corresponding maximum value for  $R_{LOAD}$  is 2.65 k $\Omega$  for a cut-off frequency of 2 MHz. This corresponds to a global transimpedance amplification of 2.65  $10^5$  (108.5 dB). For instance, an  $I_{MEMS}$  (NEMS AC current) of 10 nA would result in an AC output voltage of about 2.65 mV.

MOS transistors dimensions of this circuit implementation are listed in Table III - 1:

Transistor	$\alpha * W/L$ ( $\mu\text{m}/\mu\text{m}$ )
M1-2	4 * 30/5
M3	2 * 15/10
M4	30/3
M5-6	10/5
M7-8	M * 10/5
M9-10	50/5
M11-12	N * 50/5

Table III - 1. Transistor dimensions for the CCII circuit of Figure 3, where  $\alpha$ ,  $W$  and  $L$  stand for the device multiplicity, channel width and length, respectively

The resulting specifications for a CCII circuit fabricated with CNM CMOS technology are summarized in Table III - 2 for a typical set of values:  $I_{BIAS} = 10 \mu A$ ,  $M = N = 10$ ,  $K = 5$ ,  $R_{LOAD} = 2.65 \text{ k}\Omega$  and  $C_{LOAD} = 30 \text{ pF}$ .

	Specifications	Simulation results from layout extraction (including parasitic capacitors)
Technology	CNM25, 1 metal	-
Supply	0 - 5V	-
CMIR (Common Mode Input Range) for $V_{REF}$	[1.5 V – 2.5 V]	[1.3 V – 3 V]
Transimpedance	100 dB	108.5 dB
Bandwidth	$\geq 1 \text{ MHz}$	2 MHz for $R_{LOAD} = 2.65 \text{ k}\Omega$
In-band input impedance	as low as possible	$< 3 \text{ k}\Omega$
In-band input current noise	$\leq 1 \text{ pA rms} / \sqrt{\text{Hz}}$	$0.5 \text{ pA rms} / \sqrt{\text{Hz}}$
Current consumption	-	230 $\mu A$

Table III - 2. Initial circuit specifications and results of layout SPICE simulations

Concerning the range of AC input current, the inferior limit is set by the noise floor depending on the measurement bandwidth. The upper limit is reached when the output AC voltage saturates and loses symmetry. This can be avoided by decreasing adequately  $R_{LOAD}$ , actually an extreme case would be if  $R_{LOAD} = 10 \Omega$ , then the upper limit for  $I_{MEMS}$  would be in the order of a few mV (what represents between four and six orders of magnitude more than the expected signal levels).

**ADDITIONAL FEATURE**

A start-up p-type transistor has been placed within the transistor network that generates  $I_{BIAS}$ .

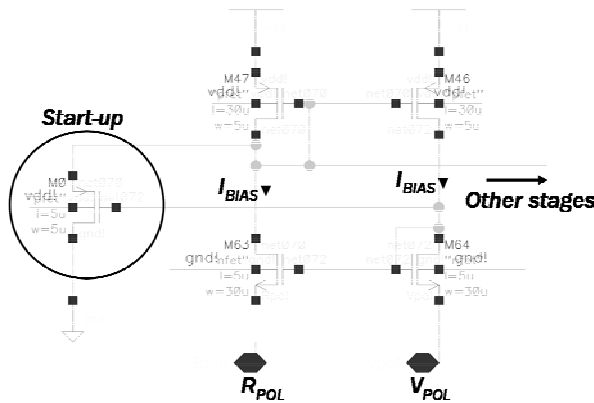


Figure 4. Transistors network generating  $I_{BIAS}$ . A start-up transistor is inserted to ensure a correct initialization

In normal steady state operation, this transistor is operated in its deep sub-threshold regime and no current flows into it.

This network consists of two crossed current mirrors that force the  $R_{POL}$  voltage node to the voltage of (externally controllable)  $V_{POL}$  node.

In this way,  $I_{BIAS}$  is generated according to eq.(III.6), flows in both branches and can thereby be replicated in any other parallel stages with a mirror.

Yet, a very hypothetic scenario (and alternative steady solution) is that no current flows in both branches. In this case, the source of the start-up transistor would be at  $V_{DD} = 5 \text{ V}$  and its gate at  $0 \text{ V}$ . In these conditions of polarization, the transistor would generate a current pulse that would switch on the circuit anyway.

**II.2.b. CCII circuit performance**

Simulations of the intrinsic frequency response of this new built-in CCII IC were performed with HSPICE under ICFB of CADENCE 4.46. The simulation cell is represented in Figure 5: at CCII input, an ideal current source is placed to substitute the NEMS output signal. A series of

parameters ( $R_{LOAD}$ ,  $C_{LOAD}$ ,  $R_{POL}$ ,  $V_{POL}$  and  $V_{REF}$ ) is adjustable so that the circuit can be fully characterized.

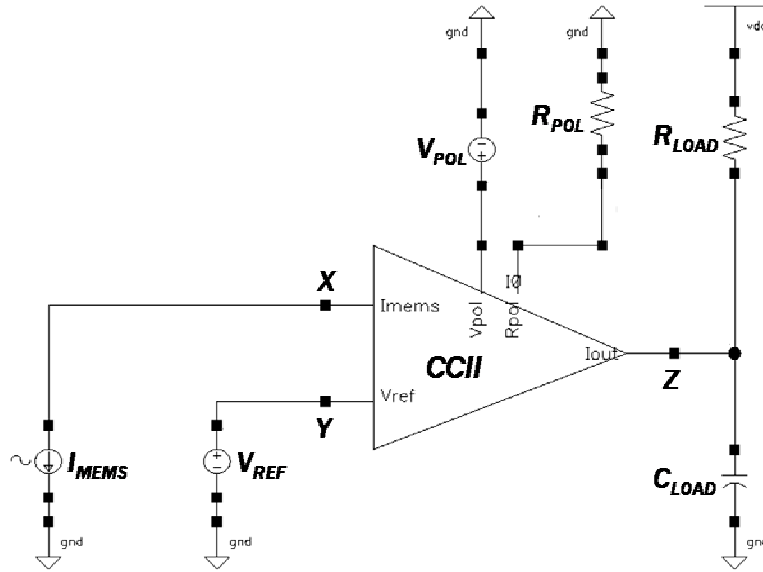


Figure 5. SPICE simulation cell for the characterization of the CCII response

Hereafter, an exhaustive analysis of the behavior of the CCII circuit is undertaken. DC simulations are made to determine the operating point and  $I_{BIAS}$  is calculated. AC simulations of the extracted layout (including physical parasitic capacitances) are made in order to study the influence on the frequency response of every externally adjustable parameter. Transient simulations are performed to check the functionality of the starter switch, and then the conditions of saturation and of linearity are determined. Finally, a brief noise analysis is proposed.

### II.2.b.i) Determination of operation points (DC)

The DC behavior is investigated when  $V_{POL}$  and  $V_{REF}$  are set to the same value (what is realized in practice in experimental measurements), in particular the calculation of  $I_{BIAS}$  is addressed. According to Figure 4, the feedback loop (optimized for  $V_{POL} = 1$  V) forces the  $R_{POL}$  node to  $V_{POL}$  resulting in  $I_{BIAS} = V_{POL}/R_{POL} = 1/R_{POL}$ . However, if  $V_{POL}$  takes another value than 1 V,  $R_{POL}$  node is not completely forced to 1 V. The rigorous  $V_{POL}$  expression for  $I_{BIAS}$  is:

$$I_{BIAS} = \frac{V_{R_{POL} \text{ node}}}{R_{POL}} \quad (III.8)$$

In the next table, the results of DC simulation for two values of  $R_{POL}$  are listed as a function of  $V_{POL} = V_{REF}$ . The resulting CCII input voltage (node X), the voltage at  $R_{POL}$  node and the resulting  $I_{BIAS}$  are given while the resulting DC output voltage is calculated according to eq.(III.5):

$R_{POL} = 200 \text{ k}\Omega$					$R_{POL} = 1 \text{ M}\Omega$				
$V_{REF}/$ $V_{POL}$ (V)	node X (V)	node $R_{POL}$ (V)	$I_{BIAS}$ ( $\mu\text{A}$ )	$V_{OUT DC}$ (V)	$V_{REF}/$ $V_{POL}$ (V)	node X (V)	node $R_{POL}$ (V)	$I_{BIAS}$ ( $\mu\text{A}$ )	$V_{OUT DC}$ (V)
1	1.29	1	5	4.75	1	1	1	1	4.95
2	2	1.59	8	4.60	2	2	2	2	4.90
3	2.93	1.6	8	4.60	3	2.95	2.6	2.6	4.87

Table III - 3. Results of DC simulations for several  $V_{REF} = V_{POL}$  for a typical set of values for  $R_{LOAD} = 1000 \Omega$

II.2.b.ii) AC response

In this section, the factors affecting the transimpedance gain  $\left( G_{dB} = 20 \log \frac{V_{OUT AC}}{I_{MEMS}} \right)$ , the bandwidth and the circuit input impedance are studied. Simulations are performed with the following standard conditions:

Parameter	Value
$R_{LOAD}$	1 k $\Omega$
$C_{LOAD}$	30 pF
$R_{POL}$	200 k $\Omega$
$V_{POL}$	1 V
$V_{REF}$	2 V

Table III - 4. Standard simulations parameters

▪ Study of  $R_{LOAD}$  influence

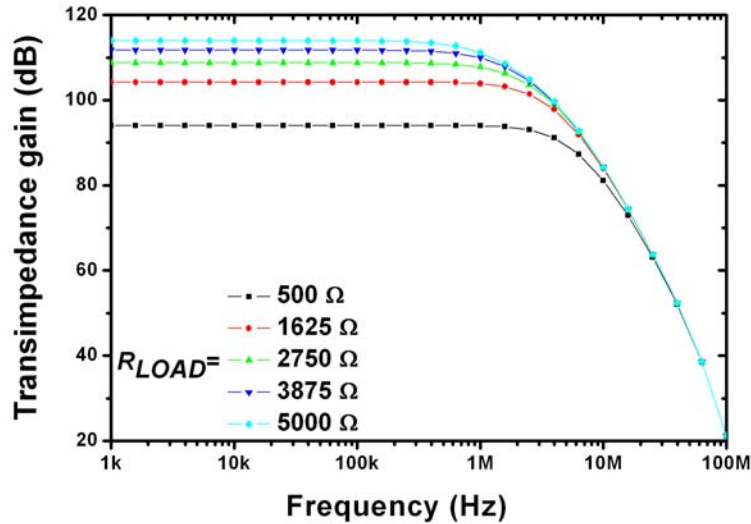


Figure 6. Bode diagram as a function of  $R_{LOAD}$

The Bode diagram for several values of  $R_{LOAD}$  is depicted in Figure 6. As expected according to eq. (III.3) and (III.7), when  $R_{LOAD}$  increases the gain increases while the bandwidth decreases. In next table, the simulated cut-off frequencies and the calculated cut-off frequencies corresponding to the output low-pass  $R_{LOAD} // C_{LOAD}$  filter are listed for a typical set of values:

$R_{LOAD}$ ( $\Omega$ )	$f_{MAX-3dB}$ (simul.) CCII (MHz)	$f_{MAX-3dB}$ of the filter $R_{LOAD} // C_{LOAD}$ (MHz)
500	4.99	10.6
1625	2.88	3.26
2033	2.42	2.61
2750	1.88	1.93
3875	1.40	1.37
5000	1.07	1.06

Table III - 5. Simulation and calculated results of frequency response

Table III - 5 demonstrates that for  $C_{LOAD} = 30$  pF, the low-pass filter is the limiting factor of the CCII bandwidth while  $R_{LOAD} > 2$  k $\Omega$ , but at lower  $R_{LOAD}$  values, the limitation arises from an internal high impedance pole of the circuit itself, that is the drain of M1 (see Figure 3).

▪ **Study of  $C_{LOAD}$  influence**

The previous section revealed that the bandwidth is limited by an internal pole and above a critical value of  $R_{LOAD}$ , the bandwidth becomes limited by the  $R_{LOAD} // C_{LOAD}$  output low-pass filter. Studying now the influence of  $C_{LOAD}$ , the analysis is consequently carried out for a low and a high value of  $R_{LOAD}$ : the incidence of  $C_{LOAD}$  is overviewed for realistic orders of magnitude from 1 to 100 pF. In Figure 7, the Bode diagram of the CCII circuit is depicted for  $R_{LOAD} = 700 \Omega$ :

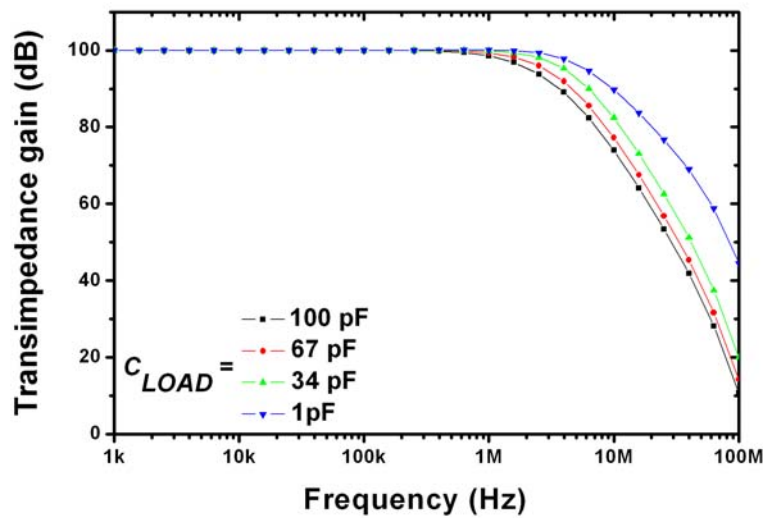


Figure 7. Bode diagram as a function of  $C_{LOAD}$

From Figure 7, it is clear that  $C_{LOAD}$  has no influence on the transimpedance gain. This statement remains true independently of  $R_{LOAD}$ . Nevertheless, it logically acts as a parameter limiting the bandwidth (according to eq.(III.7)).

$R_{LOAD} = 700 \Omega$			$R_{LOAD} = 4000 \Omega$		
$C_{LOAD}$ (F)	$f_{MAX-3dB}$ (simul.) CCII (MHz)	$f_{MAX-3dB}$ of filter $R_{LOAD} // C_{LOAD}$ (MHz)	$C_{LOAD}$ (F)	$f_{MAX-3dB}$ (simul.) CCII (MHz)	$f_{MAX-3dB}$ of filter $R_{LOAD} // C_{LOAD}$ (MHz)
1p	5.896	227	1p	5.508	40
34p	4.281	6.69	34p	1.196	1.17
67p	2.959	3.39	67p	0.609	0.594
100p	2.176	2.27	100p	0.409	0.398

Table III - 6. Simulation and calculated results of CCII response

In Table III - 6, the simulated cut-off frequencies and the calculated cut-off frequencies corresponding to the output low-pass  $R_{LOAD} / C_{LOAD}$  filter are listed for two values of  $R_{LOAD}$ : 700 and 4000  $\Omega$ .

The results at low  $C_{LOAD}$  confirm the existence of an internal pole, which makes that the limiting factor of the cut-off frequency is not systematically the output RC filter.

▪ Study of  $R_{POL}$  (i.e.  $I_{BIAS}$ ) influence

In next curve, the Bode diagram for several values of  $R_{POL}$  is plotted. Since  $R_{POL}$  governs  $I_{BIAS}$  through eq.(III.8), it is interesting to study its incidence on the speed of the circuit. More biasing current should likely decrease the commutation time of the transistors and enlarge the bandwidth.

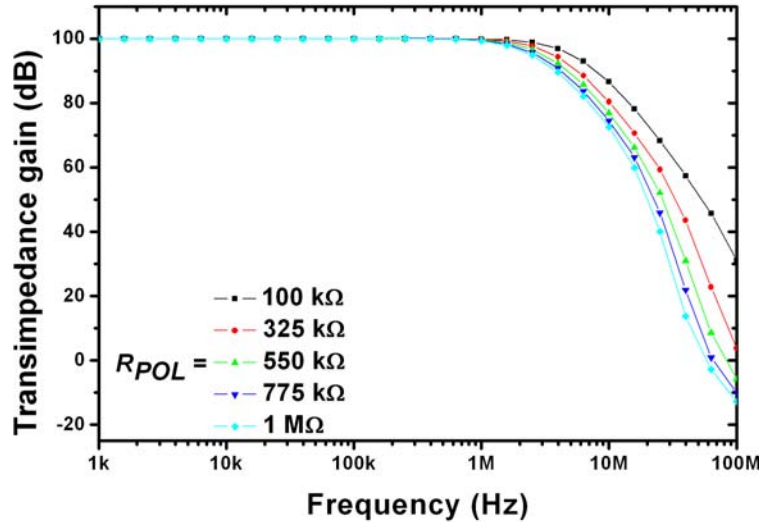


Figure 8. Bode diagram as a function of  $R_{POL}$

Figure 8 confirms this assumption: by decreasing  $R_{POL}$  (i.e. increasing  $I_{BIAS}$ ) the bandwidth can be increased. Physically, this corresponds to a faster charging of capacitance (analogy with the slew rate  $SR=I/C$ ) when more current flows. As a conclusion,  $I_{BIAS}$  magnitude and circuit bandwidth follow the same trend.

▪ Input Impedance analysis

One of the required features of the CCII circuit is a low input impedance for an accurate

current sensing (like an ammeter) as well as to decrease the influence of NEMS output capacitances.

To estimate the input impedance, a parallel capacitance ' $C_{PA}$ ' is added at CCII input to simulate the presence of parasitic capacitances at NEMS output. Its influence on the circuit input impedance ( $Z_E$ ) is analyzed.

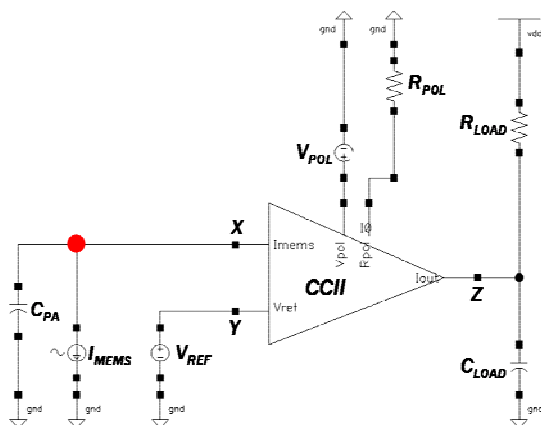


Figure 9. Input impedance test module

For this purpose, simulations are performed with the test module of Figure 9 where  $C_{PA}$  is swept from 1 fF to 1 pF.  $I_{MEMS}$  AC amplitude is set to 1, hence  $Z_E = V_X/I_{MEMS} = V_X$ . Measuring  $V_X$  directly provides the value of  $Z_E$ .

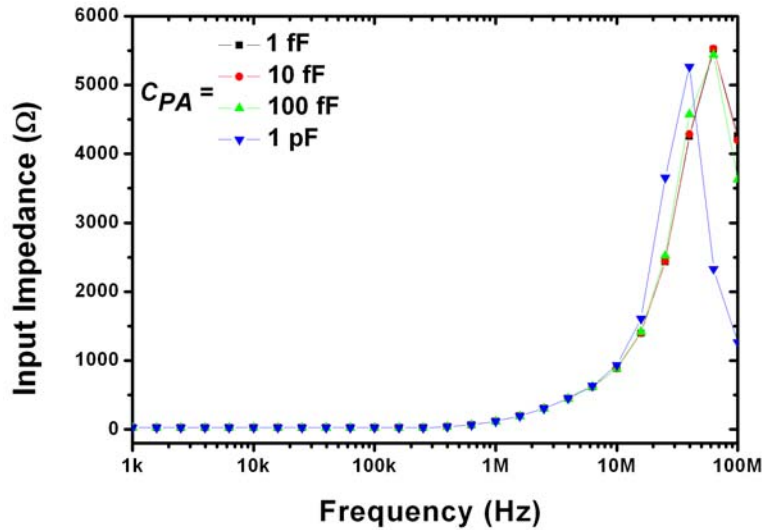


Figure 10. Input impedance ( $Z_E$ ) (measured through  $V_X$ ) versus frequency in function of  $C_{PA}$

From this simulation, it is clear that in the 1-2 MHz range, the parallel parasitic capacitance has no influence on  $Z_E$ . In this frequency range,  $Z_E$  is in the order of 100-500  $\Omega$ . This range of value is satisfactory as it is sufficiently low:

- compared to the equivalent impedance of  $C_{PA2}$  which is in the range of the  $M\Omega$
- not to perturb the stability of the  $X$  node forced to  $V_{REF}$ . If  $I_{MEMS}$  was as high as 10  $\mu A$  (extreme case), this would generate a fluctuation of about  $[10 \cdot 10^{-6} * 500] = 5$  mV what is still negligible compared to 2 V (typical value of  $V_{REF}$ ).

### II.2.b.iii) Transient simulations

In this section, the circuit initialization and its conditions of stability are investigated realizing transient simulations.

#### ▪ Transient analysis of circuit initialization

It is necessary to check if the functionality of start-up mechanism, i.e. if the circuit will adequately switch on when polarizing  $V_{DD}$  and  $V_{SS}$ .

For this purpose,  $I_{MEMS}$  is set to 0. At  $t=0$ ,  $V_{DD} = 0$ . Then  $V_{DD}$  is progressively polarized with a ramp from 0 to 5V in 100 ns, and then a constant 5 V voltage is applied.

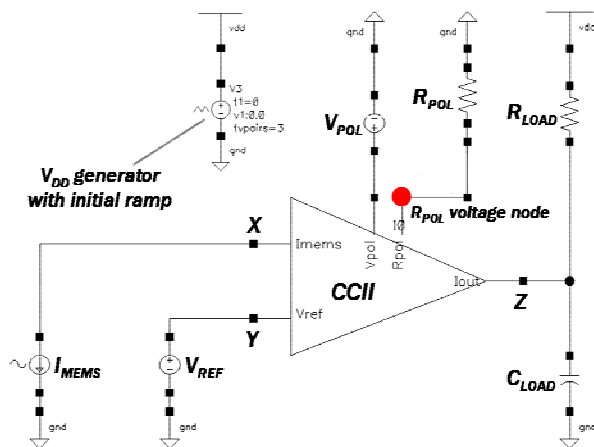


Figure 11. Initialization test module

The initialization is measured through  $R_{POL}$  node voltage (red node), e.g. where  $I_{BIAS}$  is produced: as previously explained, two crossed current mirrors, depicted in Figure 4, are supposed to force this node to  $V_{POL}$  value (1 V here). If everything works correctly, this node must reach 1 V within some microseconds.

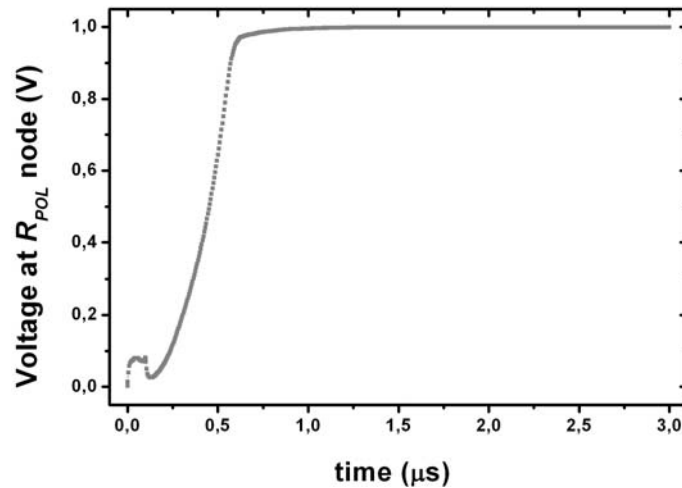


Figure 12. Transient analysis of circuit initialization. Voltage measurement at  $R_{POL}$  node versus time

According to this graph, the circuit initiates properly since  $R_{POL}$  node voltage reaches 1 V (=  $V_{POL}$ ) after 0.8  $\mu$ s. From this instant on,  $I_{BIAS}$  is constantly produced and the circuit is properly switched on.

#### ▪ Analysis of circuit stability

The influence of the NEMS output parasitic capacitance (modeled here as an input capacitance  $C_{PA}$ ) on the CCII stability is investigated for several  $C_{PA}$  values. Actually, the negative feedback loop constituted of M1 and M4 transistors (Figure 3) contains a high impedance pole at the drain of M1 ( $\equiv$  gate of M4 and drain of another transistor generating  $I_{BIAS}$ ). It represents in fact the second main pole of the CCII after the one consisting of the output low-pass RC filter. If  $C_{PA}$  increases, the frequency of the internal pole shifts down to lower frequencies and gets closer the main pole. The potentially insufficient phase margin can generate some instability materialized by unwanted oscillations. Actually this parasitic input capacitance is equivalent to  $C_{P2}$  in Figure 2: it is estimated around 50-100 fF, as a maximum, taking into account the anchor area and the routing area between resonator and CCII input.

To test this, a simulation module sketched in Figure 13 is built up. A parallel capacitance ' $C_{PA}$ ' is added at CCII input to simulate the NEMS output parasitic capacitances. A single step current is applied at  $I_{MEMS}$  source and the response at the output  $Z$  node is measured.

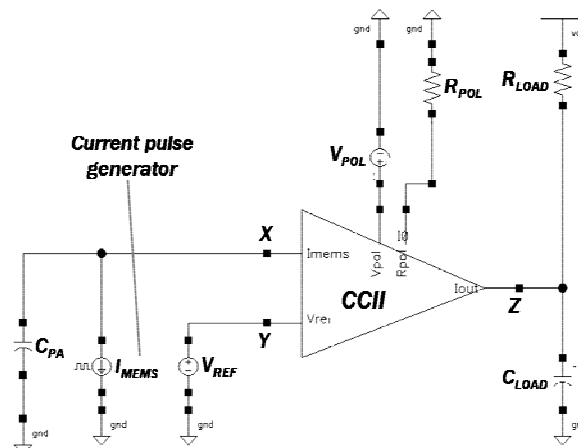


Figure 13. Stability test module

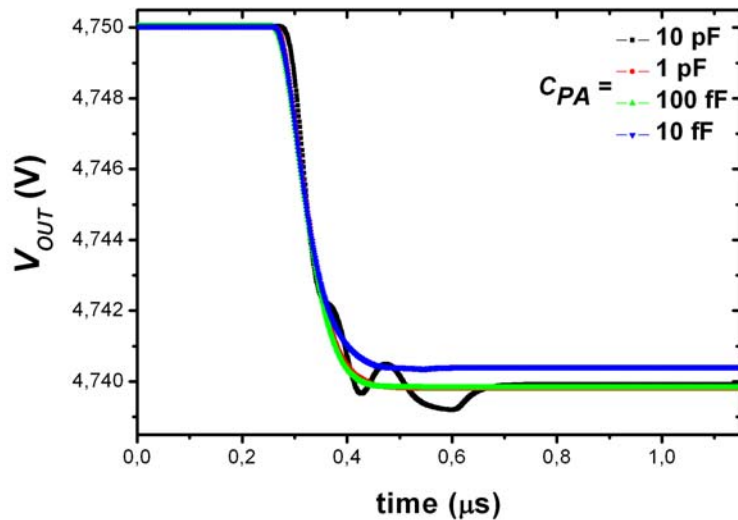


Figure 14. Transient analysis in function of  $C_{PA}$ . Output voltage versus time.

This graph indicates that for values of 10 fF and 100 fF, the system should be perfectly stable. However, for 1 pF, slight oscillations start to appear and from 10 pF on, the system is no more stable. If both poles get nearer, an overshoot peak should appear in the Bode diagram.

#### II.2.b.iv) Conditions of saturation

The conditions for circuit saturation can be derived mathematically. The results of this analytical approach have actually been confirmed by simulations.

The maximum value of the output AC peak-peak voltage  $(V_{OUT AC pp})_{MAX}$  is limited by the DC output voltage offset  $\Delta V_{OUT DC}$  generated by the amplification  $I_{BIAS}$  ( $\Delta V_{OUT DC} = V_{DD} - V_{OUT DC}$ ) (see eq.(III.5)). This can be described numerically as:

$$(V_{OUT AC pp})_{MAX} / 2 = \Delta V_{OUT DC} \quad (III.9)$$

Expressing the left and the right term according to eq.(III.3) and (III.5), one can write:

$$\frac{(V_{OUT AC pp})_{MAX}}{2} = 100 R_{LOAD} \left[ \frac{(I_{MEMS pp})_{MAX}}{2} \right] \quad \text{and} \quad \Delta V_{OUT DC} = 50 R_{LOAD} I_{BIAS} = 50 R_{LOAD} \frac{V_{R_{POL}}}{R_{POL}} \quad (III.10)$$

what results in:

$$(I_{MEMS pp})_{MAX} = I_{BIAS} = \frac{V_{R_{POL}}}{R_{POL}} \quad (III.11)$$

This means that the peak-peak magnitude of  $I_{MEMS}$  must be inferior or equal to  $I_{BIAS}$  to avoid any saturation of the output voltage.

#### II.2.b.v) Linearity of the circuit response

In order to further analyze the linearity of the response of the nano/micromechanical resonator, it is necessary to be able to decorrelate it from the linearity of the electrical response of

the circuit. In practice, if the circuit response is linear, any deviation in the electrical response of the resonator from a linear behavior can be attributed to its own mechanical behavior only and not to any electrical artifact. In this section, the linearity of the circuit is checked in the range of  $I_{MEMS} = 1 \mu\text{V AC}$ . Actually, a DC analysis is performed and the resulting output voltage is plotted in next figure for several values of  $R_{POL}$ . The output voltage is normalized to remove the DC offset that depends on the  $R_{POL}$  value (see eq.(III.5) and (III.8)).

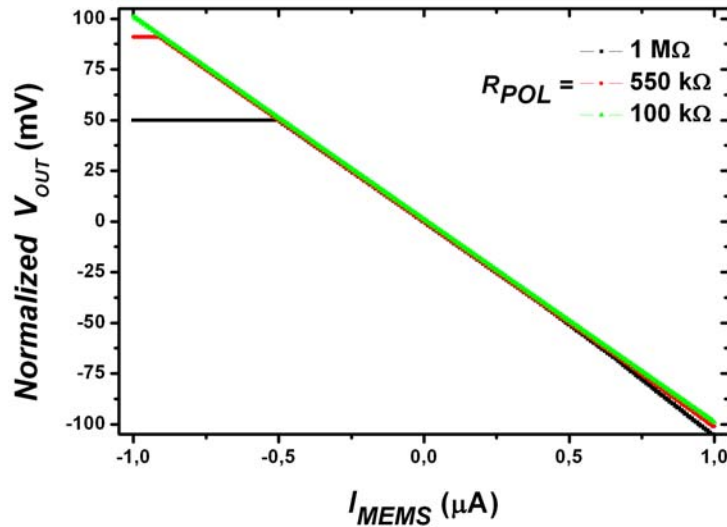


Figure 15. Output AC voltage versus  $I_{MEMS}$  for several  $R_{POL}$  values

This graph indicates that the response is very linear, particularly for values of  $R_{POL}$  inferior to  $1 \text{ M}\Omega$ . The curves for  $R_{POL} = 550 \text{ k}\Omega$  and  $1 \text{ M}\Omega$  exhibit plateaus in the output voltage for negative values of  $I_{MEMS}$ . This phenomenon is not related to any loss of linearity but to saturation effects according to eq.(III.11) (the observed saturation threshold is in perfect agreement with that equation). In fact, these two curves are normalized but if the DC offset had not been removed, a saturation at  $5 \text{ V}$  ( $V_{DD}$ ) could be observed.

### II.2.b.vi) Noise analysis

Based on simulations, a noise analysis is undertaken to evaluate the noise of the output voltage which is a combination of the global noise generated internally by the circuit itself and by the external load resistor (thermoelectrical noise called ‘Nyquist and Johnson’ noise). It comes that the spectral density of the output voltage noise is constant until  $5 \text{ MHz}$ , e.g. in all the bandwidth of the CCII circuit.

In Table III - 7 and Table III - 8, the spectral density is provided for different conditions of operation. Then, the resulting output voltage noise is given as function of the bandwidth of a  $2 \text{ MHz}$  mechanical resonator for two values of  $Q$ :  $10$  (like for a measurement in air) and  $10000$  (like for a measurement in vacuum). The resonator bandwidth is approximated as:

$$BW = \frac{f_0}{Q} \quad (III.12)$$

Let us define the voltage gain  $G_V$  as:

$$G_V = 20 \log \left( \frac{V_{OUT AC}}{V_{IN AC}} \right) \quad (III.13)$$

these two tables also provide the resulting voltage gain  $G_V$  of the output voltage noise floor:

$R_{POL}$ ( $\Omega$ )	Density of output voltage noise $D_{OVN}$ (nV / Hz <sup>1/2</sup> )	$BW$ (Hz) for $f_0=2$ MHz	Output noise $V_{OUTAC}$ ( $\mu$ V)	$G_V$ (dB) for $V_{INAC}=1V$
100 k	100	200 k (for Q=10)	45	-79
		200 (for Q=10000)	1.41	-109
1 M	55	200 k (for Q=10)	25	-84
		200 (for Q=10000)	0.8	-114

Table III - 7. Noise study for  $R_{LOAD}=1$  k $\Omega$

$R_{LOAD}$ ( $\Omega$ )	Density of output voltage noise $D_{OVN}$ (nV / Hz <sup>1/2</sup> )	$BW$ (Hz) for $f_0=2$ MHz	Output noise $V_{OUTAC}$ ( $\mu$ V)	$G_V$ (dB) for $V_{INAC}=1V$
500	36	200 k (for Q=10)	16	-88
		200 (for Q=10000)	0.5	-118
1000	69	200 k (for Q=10)	31	-82
		200 (for Q=10000)	1.0	-112

Table III - 8. Noise study for  $R_{POL} = 200$  k $\Omega$

To reduce the noise,  $R_{POL}$  should be as high as possible: low values of  $R_{POL}$  result in more bias current what naturally generates more noise current. Depending on the measurement bandwidth, the total output noise varies from hundreds of nV to tens of  $\mu$ V.

On the opposite, the results of Table III - 8 reveal that the CCII circuit dominates over  $R_{LOAD}$ . In fact, the signal to noise ratio (SNR) is fixed within the circuit and the output noise current is converted by  $R_{LOAD}$  into an output voltage noise but it is not increased by the load resistor. Indeed, according to Table III - 8 the density of output voltage noise is proportional to  $R_{LOAD}$ . If  $R_{LOAD}$  was the dominant factor, it would create a 'Nyquist-Johnson' voltage noise which is in principle proportional to the square root of  $R_{LOAD}$ : this is not the case here. This means that the equivalent input noise is independent of  $R_{LOAD}$ .

### II.2.c. CCII circuit performance with NEMS model at input

In chapter 2, it has been demonstrated that a mechanical resonator can be electrically modeled as an equivalent RLC component. The calculation of these electrical parameters opens up the possibility of performing electrical simulations of the cluster RESONATOR-CCII CIRCUIT. Simulations cells are built up where the NEMS device modeled by three parallel branches (c.f. chapter 2) replaces the ideal current source utilized in previous simulations.

Provided the RLC model is accurate, the experimental frequency response should be well predicted. In addition, it is necessary to check that the CCII circuit carries on working with a more realistic input device than an ideal current source.

#### II.2.c.i)Electrical simulations of cantilevers-CCII mixed circuit

Figure 16 is a scheme of the simulation cell of the mixed electromechanical system CANTILEVER-CCII CIRCUIT. Cantilevers are placed at CCII input and modeled by three branches (c.f. chapter 2). The first one contains the RLC components (called  $R_M$ ,  $L_M$  and  $C_M$  in this schematic), the second the static capacitance  $C_{DC}$  (called  $C_W$  in chapter 2) and the third one the parallel parasitic capacitance  $C_{PA}$  (called  $C_P$  in chapter 2). The NEMS output parasitic capacitance is named  $C_{PA2}$  (called  $C_{P2}$  in chapter 2).

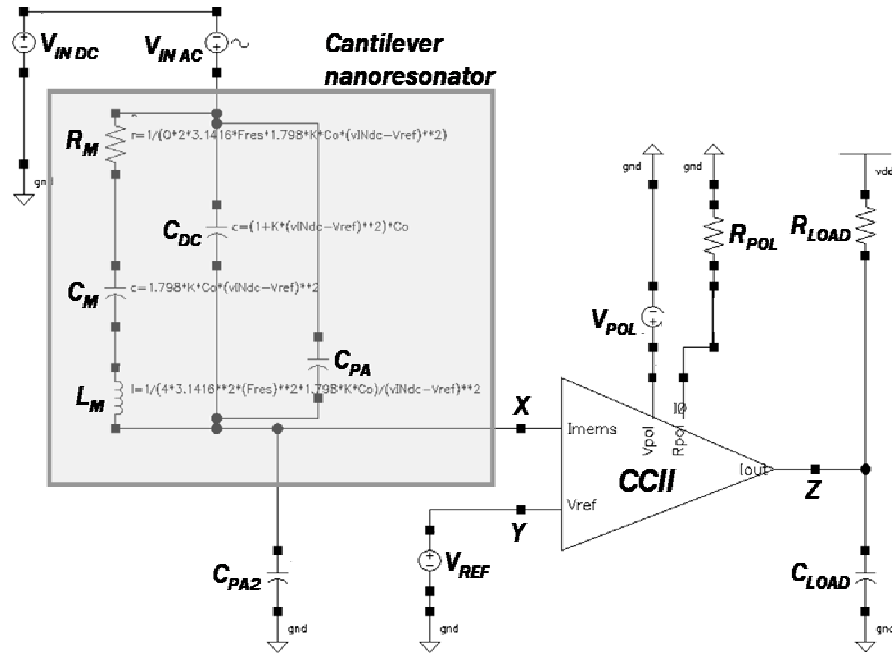


Figure 16. Simulation module based on a RLC model that represents the cantilever at CCII input

In this model, the spring-softening effect that shifts the resonance frequency down to lower values when the excitation voltage is increased is neglected. The resonator parameters are calculated in the following way (c.f. section III.2 chapter 2):

$$C_{DC} = (1 + KV_{DCIN}^2)C_0 \quad \text{where } C_0 = \frac{\varepsilon_0 hl}{d} \quad \text{and } K = \frac{3\varepsilon_0 l^4}{4Eb^3 d^3} \quad (\text{III.14})$$

$$C_M = 1.798KV_{DCIN}^2 C_0 \quad L_M = \frac{1}{4\pi^2 f_{RES}^2 C_M} \quad R_M = \frac{1}{Q} \sqrt{\frac{L_M}{C_M}} \quad (\text{III.15})$$

$C_{PA}$  is related to the fringing field and is in the order of magnitude of  $C_{DC}$  or slightly higher.  $C_{PA2}$  is estimated between 10 and 100 fF from direct measurements of dimensions in the layout:

$$C_{PA2} = C_{ANCHOR} + C_{CONTACTS} + C_{ROUTING} \quad (\text{III.16})$$

Regarding the NEMS part, adjustable variables in the simulation cell are:  $f_{RES}$ ,  $K$ ,  $C_0$ ,  $C_{PA}$ , and  $C_{PA2}$ , accurately calculated as a function of geometrical dimensions of the cantilever.  $V_{IN AC}$  and  $V_{IN DC}$ , the AC and DC excitation voltages, are also tunable. The Q-factor is the last variable: initially it was estimated based on previous experimental measurements of discrete devices. HSPICE subsequently calculates  $C_M$ ,  $L_M$ ,  $R_M$  and  $C_{DC}$  following equations (III.14) and (III.15).

Regarding the CCII part, adjustable variables in the simulation cell are the same as in the previous simulations:  $R_{POL}$ ,  $R_{LOAD}$ ,  $C_{LOAD}$ ,  $V_{POL}$  and  $V_{REF}$  (set to the same value).

Complementarily with the study of the intrinsic behavior of the CCII circuit, the influence of characteristic parameters, like  $R_{LOAD}$  or  $R_{POL}$ , on the frequency response of the mixed NEMS/CMOS system is investigated.

Realistic values for all parameters, evaluated from experimental data, are implemented into the model and reported into Table III - 9, Table III - 10 and Table III - 11. These data are

calculated as a function of the geometrical dimensions of the cantilever:  $l$  (length),  $b$  (width),  $h$  (thickness) and  $d$  (gap with driver), and for  $E=130$  GPa. Subsequent simulations are performed based on these conditions.

Parameter	Value
$l; b; h; d$	14.5 ; 0.29; 0.56 ; 0.75 ( $\mu\text{m}$ )
$f_{RES}$	1.66 MHz
$Q$	13
$K$	$2.2 \cdot 10^{-4}$
$C_0$	96 aF
$C_{PA}$	1 fF ( $\approx 10 \cdot C_0$ )
$C_{PA2}$	50 fF
$V_{IN AC}$	0.9 V pp (0 dBm)
$^1 V_{IN DC}$	20 V (22 applied)

Table III - 9. NEMS parameters

Parameter	Value
$R_M$	490 M $\Omega$
$L_M$	605 H
$C_M$	15 aF

Table III - 10. Equivalent motional parameters

Parameter	Value
$R_{LOAD}$	1 k $\Omega$
$C_{LOAD}$	30 pF
$R_{POL}$	200 k $\Omega$
$V_{POL} / V_{REF}$	2 V

Table III - 11. CCII parameters

The resulting  $C_{DC}$  is 104 aF according to eq.(III.14). The influence of  $C_{PA2}$  is analyzed in the 1fF - 1pF range, and seems to be negligible; therefore it is not depicted later. In all the following simulations, the frequency response is given in terms of voltage gain (see eq.(III.13))

▪ Comparison with discrete cantilevers

The electrical frequency responses of two identical cantilevers, one integrated with the CCII, the other discrete, are plotted in Figure 17 in order to measure the incidence of the CMOS integration. For the discrete one,  $C_{PA2}$  is actually equal to  $C_{LOAD}=30$  pF, while for the integrated one  $C_{PA2}=50$  fF, e.g. three orders of magnitude less.

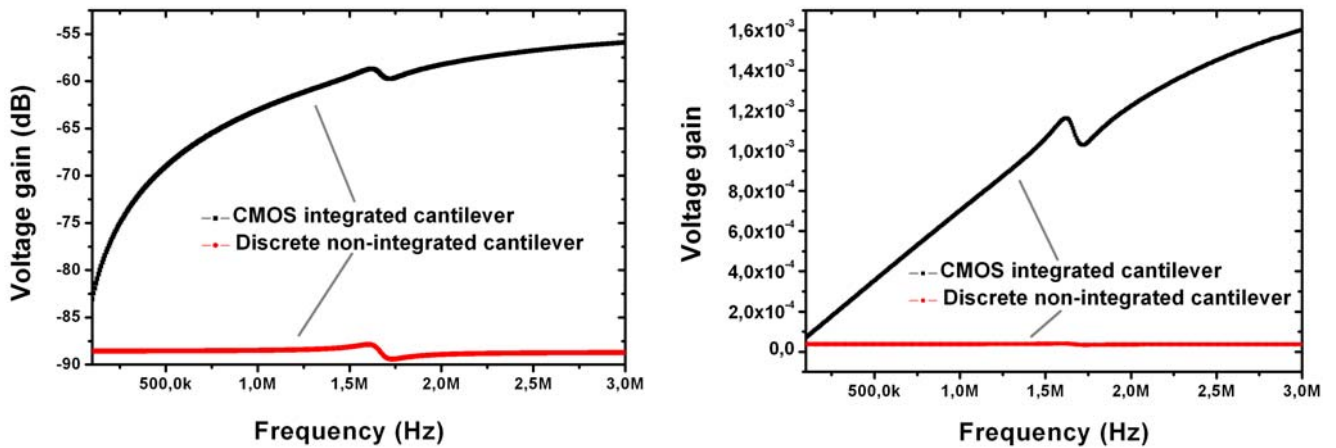


Figure 17. Comparison integrated/discrete cantilever. Left: gain in dB; right: normal gain.

In this specific context, where  $R_{LOAD}$  is relatively low, the circuit already provides a 30 dB (equivalent to a factor 30) enhancement in terms of signal level. Elevating  $R_{LOAD}$  is a straightforward way to increase even more this difference. As future prospect, the same CCII topology with one or more additional internal amplification stages (through cascode mirrors) would provide even higher output signals.

<sup>1</sup> since the resonator is biased at  $V_{REF}$ , in order to apply  $XV$  to the resonator,  $V_{IN DC}$  value must be  $X + V_{REF}$ . For simplification purposes,  $V_{IN DC}$  will be cited as  $X$  only.

### ▪ Study of $R_{LOAD}$ influence

In Figure 18, the output frequency spectrum is plotted for several values of  $R_{LOAD}$  from 0.5 to 5 k $\Omega$ .

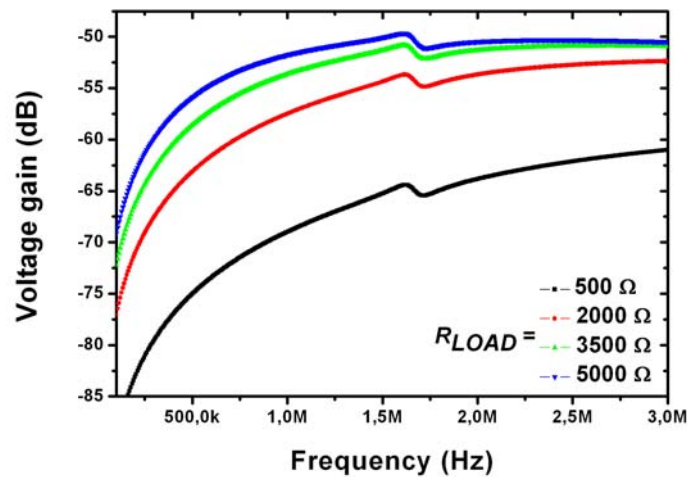


Figure 18. CMOS cantilever frequency response as a function of  $R_{LOAD}$

$R_{LOAD}$  increases the level of both the resonance peak and the background signal (arising mainly from  $C_{PA}$ ) even if the relative amplitude of one with respect to the other remains constant (same offset in dB). It can be observed that above 3500  $\Omega$ , the response curve is attenuated (flatter) before  $f_{RES}$  since for these values of  $R_{LOAD}$  the cutting frequency becomes inferior to  $f_{RES}$ . This graph reveals that for  $C_{LOAD}$  around 30 pF, there is no sense adjusting  $R_{LOAD}$  to more than 3 k $\Omega$  (in all subsequent simulations,  $R_{LOAD}$  is set to 1 k $\Omega$ ).

### ▪ Study of $C_{LOAD}$ influence

In Figure 19, the output frequency spectrum is plotted for three values of  $C_{LOAD}$ : 1, 10 and 100 pF.

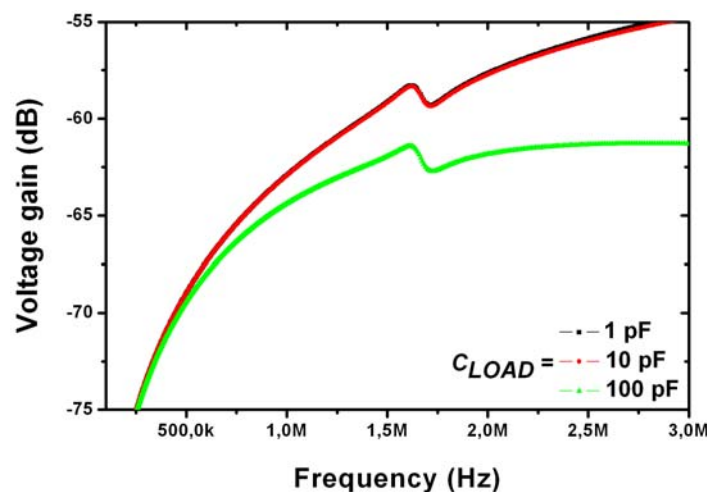


Figure 19. CMOS cantilever frequency response as a function of  $C_{LOAD}$

For values of  $C_{LOAD}$  resulting in cut-off frequencies larger than the resonance frequency of the resonator, the spectrum pattern remains unaffected by  $C_{LOAD}$ . However, for  $C_{LOAD} = 100$  pF, cut-off frequency and resonance frequency take the same value and the signal level starts decreasing. Since  $C_{LOAD}$  is intrinsic to the measurement set-up,  $R_{LOAD}$  must be adequately chosen to avoid signal attenuation.

- Study of  $R_{POL}$  influence

In Figure 20, the output frequency spectrum is plotted for  $R_{POL} = 0.01, 0.1$  and  $1\text{M}\Omega$ .

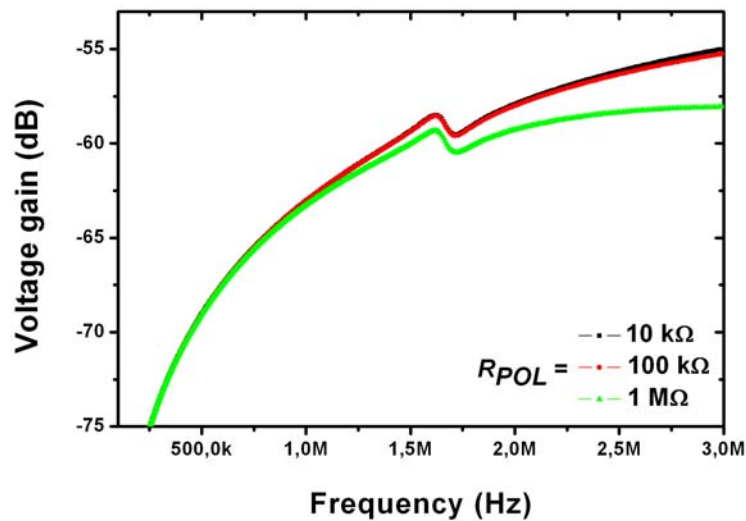


Figure 20. CMOS cantilever frequency response as a function of  $R_{POL}$

In agreement with Figure 8, this graph shows that  $R_{POL}$  does not influence the resonance peak level but the lower it is the higher is the bandwidth what avoids signal attenuations.

- Study of  $C_{PA}$  influence

In Figure 21, the output frequency spectrum is plotted for several values of  $C_{PA}$  from 1 aF to 10 fF.

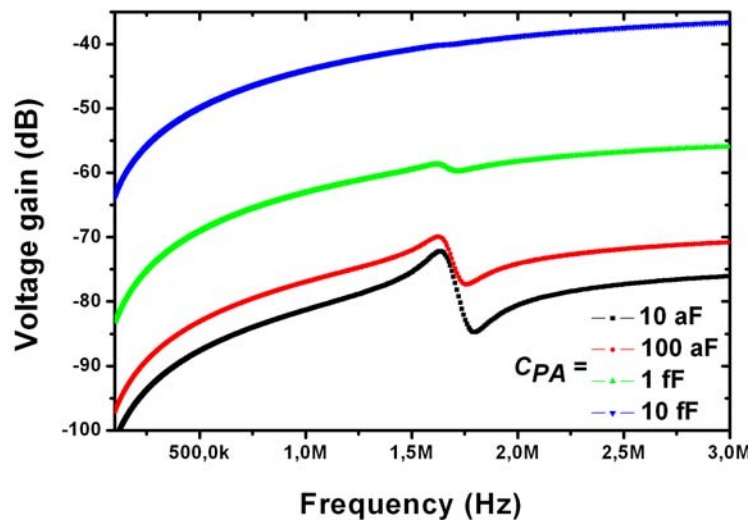


Figure 21. CMOS cantilever frequency response as a function of  $C_{PA}$

This graph reveals that  $C_{PA}$  is one of the most critical parameters in the resonance spectrum pattern. As the background signal level is mainly related to  $C_{PA}$ , when  $C_{PA}$  is low the background level is low and the resonance peak emerges much: see for  $C_{PA} = 10$  and  $100$  aF. Then, there is a critical domain for  $100 \text{ aF} < C_{PA} < 1 \text{ fF}$  where the background signal becomes really dominant over the resonance peak. The cantilever resonators of this work are situated in this domain.

- Study of  $V_{IN\ DC}$  influence

In Figure 22, the output frequency spectrum is plotted for several values of  $V_{IN\ DC}$  from 15 to 25 V.

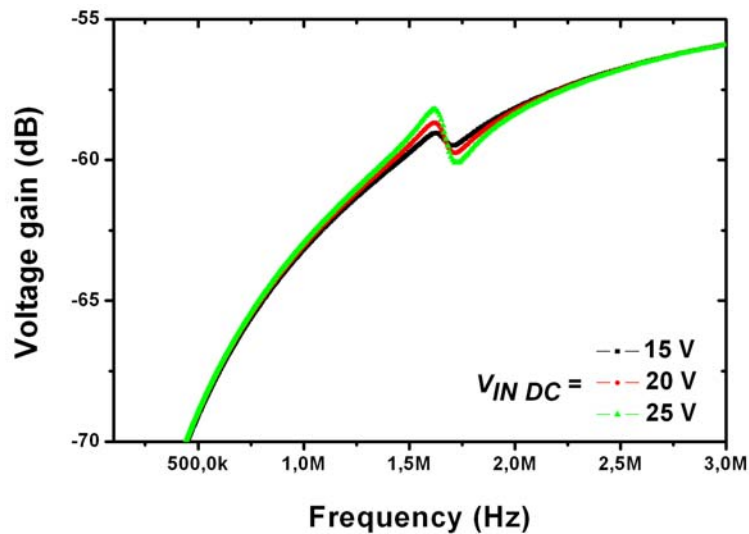


Figure 22. CMOS cantilever frequency response as a function of  $V_{IN\ DC}$

This graph shows the major role played by  $V_{IN\ DC}$  on the peak amplitude (neglecting the frequency translation owing to spring-softening effect).

#### CONCLUSION

According to these simulations, the parameters that most affect the resonance peak amplitude are  $C_{PA}$  and  $V_{IN\ DC}$ , as well as the  $Q$ -factor, not analyzed here.  $Q$  and  $C_{PA}$  are intrinsic parameters that cannot be varied (unless measurements are performed in vacuum what would drastically improve the  $Q$ -factor). Regarding  $V_{IN\ DC}$ , its upper limit is the value of the pull-in voltage which provokes irreversible lateral sticking of the cantilever on its in-front electrode.

The parameters that most affect the background level of the resonance peak are  $C_{PA}$  and the adjustable  $R_{LOAD}$ .  $C_{LOAD}$  and  $R_{POL}$  are less determining than other parameters but they must be adequately chosen to avoid signal attenuations. Reducing  $C_{LOAD}$  would allow increasing  $R_{LOAD}$  but in the present conditions  $C_{LOAD}$  is not modifiable as it is determined by the measurement set-up.

## II.2.c.ii) Electrical simulations of QB-CCII mixed circuit

Figure 23 is a scheme of the simulation cell of the mixed electromechanical system QB-CCII CIRCUIT. QB are placed at CCII input and modeled by three branches (c.f. chapter 2). With respect to Figure 16, their meaning is identical except for  $C_{PA}$ . The  $C_{PA}$  branch is related to anchors capacitors.

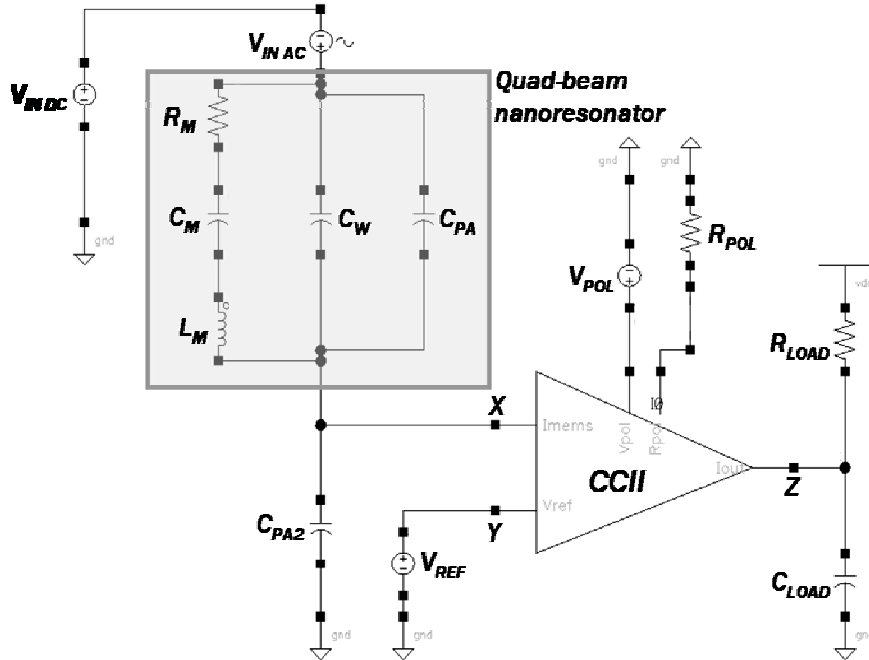


Figure 23. HSPICE simulation cell of a QB coupled to the CCII

In this model, the spring-softening effect (that shifts the resonance frequency down to lower values with increasing driving voltage) is also neglected. The resonator parameters are calculated according to a RLC model (c.f. chapter 2):

$$C_W = \frac{\varepsilon_0 L_1^2}{d} \quad (III.17)$$

$$R_M = \frac{D}{\eta^2} = \frac{\sqrt{km}}{Q\eta^2} \quad C_M = \frac{\eta^2}{k} \quad L_M = \frac{m}{\eta^2} \quad (III.18)$$

where

$$\eta \approx \frac{\varepsilon_0 L_1^2}{d^2} V_{INDC} \quad k = \alpha_{QB} \frac{E h^3 b}{l^3} \quad m = \rho L_1^2 h \quad (III.19)$$

$C_{PA}$  is related to the physical capacitor constituted of polysilicon anchor // SiO<sub>2</sub> pillar // Si bulk. It is approximated as:

$$C_{PA} = 4 \frac{\varepsilon_{SiO_2} A_{ANCHOR}}{h_{SiO_2}} \quad (III.20)$$

$C_{PA2}$  is estimated between 10 and 100 fF from direct measurements of dimensions in the layout:

$$C_{PA2} = C_{CONTACTS} + C_{ROUTING} \quad (III.21)$$

Regarding the NEMS part, adjustable variables in the simulation cell are:  $k$ ,  $m$ ,  $\eta$ ,  $C_W$ ,  $C_{PA}$ ,  $C_{PA2}$ , accurately calculated as a function of geometrical dimensions of the QB.  $V_{IN\ AC}$  and  $V_{IN\ DC}$ , AC and DC excitation voltages, and  $Q$ -factor are also tunable. HSPICE subsequently calculates  $C_M$ ,  $L_M$ ,  $R_M$  following equations (III.18).

Regarding the CCM part. adjustable variables in the simulation cell are:  $R_{POL}$ ,  $R_{LOAD}$ ,  $C_{LOAD}$ ,  $V_{POL}$  and  $V_{REF}$ .

Taking into account previous results, the study of the influence of characteristic parameters on the frequency response of the mixed QB/CMOS system is restricted to  $C_{PA}$ , the parallel parasitic capacitance, since the phenomenological incidence of the other parameters is already known. In the case of QB,  $C_{PA}$  is so high that it constitutes de facto the most critical parameter determining the level of background signal and the resonance peak amplitude (to what extent it emerges from this background signal).

Realistic values for all parameters, evaluated from experimental data, are implemented into the model and reported into Table III - 12, Table III - 13 and Table III - 14. These data are calculated as a function of the geometrical dimensions of the QB:  $L_1$  (square paddle width),  $l$  (beam length),  $b$  (beam width),  $h$  (thickness) and  $d$  (gap with substrate), and for  $E=130$  GPa.

Parameter	Value
$L_1 ; l$	5.9 ; 13.2 ( $\mu\text{m}$ )
$b ; h ; d$	0.42; 0.45; 1.1 ( $\mu\text{m}$ )
$k$	3.7 N/m
$m$	36 pg
$\eta$	$5 \cdot 10^{-9}$
$Q$	35
$C_W$	280 aF
$C_{PA}$	80 fF
$C_{PA2}$	25 fF
$V_{IN\ AC}$	0.9 V pp (0dBm)
$V_{IN\ DC}$	20 V (22 applied)

Table III - 12. QB NEMS parameters

Parameter	Value
$R_M$	380 M $\Omega$
$L_M$	1400 H
$C_M$	8 aF

Table III - 13. Equivalent motional parameters

Parameter	Value
$R_{LOAD}$	0.92 k $\Omega$
$C_{LOAD}$	30 pF
$R_{POL}$	200 k $\Omega$
$V_{POL} - V_{REF}$	2 V

Table III - 14. CCM parameters

▪ Study of  $C_{PA}$  influence

In Figure 24, the output frequency spectrum is plotted for three values of  $C_{PA}$  from 10 fF to 1 pF.

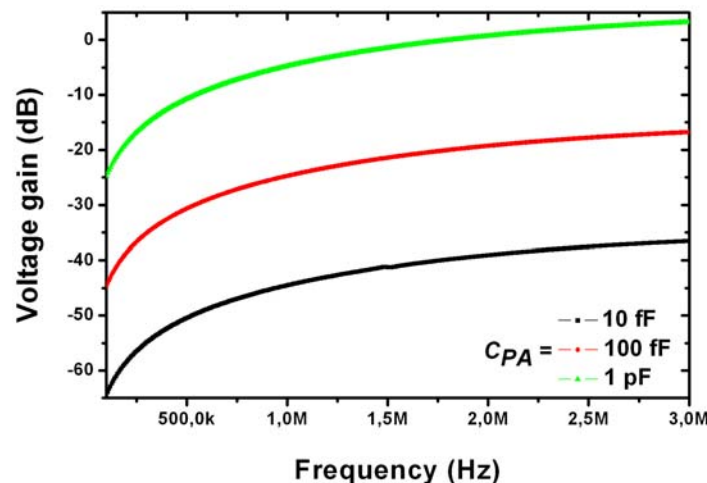


Figure 24. CMOS QB frequency response as a function of  $C_{PA}$

From Figure 24, it is clear that for  $C_{PA}$  values in the 10 fF-1 pF range, the induced background signal is so high that the resonance peak is totally masked. This is consistent with the predictions of chapter 2. To circumvent this issue, a ‘calibration’ of the background signal is made: it can be performed with a network analyzer during experimental measurements (for detailed explanations, refer to chapter 5).

A simulation cell is built up according to this calibration approach. Like in Figure 24, the output frequency spectrum is plotted in Figure 25 for three values of  $C_{PA}$  from 10 fF to 1 pF, but with a calibrated signal.

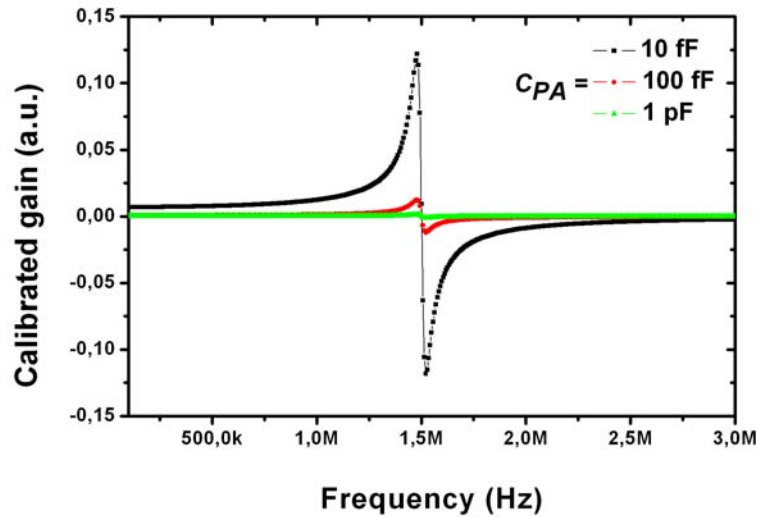


Figure 25. CMOS QB frequency response (calibrated) as a function of  $C_{PA}$

This graph confirms the major role played by  $C_{PA}$  regarding the amplitude of the peak.

## CONCLUSION

Apart from the Q-factor, the parameter that most affect both the resonance peak amplitude and the level of background signal is  $C_{PA}$ . Unfortunately,  $Q$  and  $C_{PA}$  are intrinsic parameters that cannot be varied. At least, special efforts should be dedicated to the resonator design in order to decrease as much as possible the area of the four anchors.

With respect to discrete devices, CMOS integration does not provide any improvements regarding the role of  $C_{PA}$ , nevertheless signal attenuation due to  $C_{PA2}$  is drastically reduced.

## II.3. NEMS/CMOS circuit layout

The CCII layout was made using CADENCE ICFB with CNM process library. Hereafter, the guide lines followed during the design of the layout of the CCII and its integration areas are explained. An exhaustive description of the entire chip layout is provided

### II.3.a. CCII Circuit layout, integration areas layout

The layout of the CMOS CCII circuit has been done according to several requirements. Concerning the circuit itself, transistor matching and routing optimization have been the two critical points. Indeed, CNM CMOS technology contains one single metal layer and the routing has to associate two materials: so-called *poly1* (polysilicon) and *metal* (Al).

The resulting size of the CCII circuit without pads is about  $500 * 400 \mu\text{m}^2$  ( $0.2 \text{ mm}^2$ ). Since CNM CMOS technology is a  $2.5 \mu\text{m}$  lithography process, a considerably smaller implementation can be obtained using modern submicron CMOS technologies.

Regarding the objective of integrating NEMS on CMOS, a fabrication strategy (detailed in chapter 4) is chosen whereby nanomechanical resonators are defined by post-processing pre-fabricated CMOS substrates. In other words, the nanopatterning step for NEMS definition and the subsequent process steps are carried out after complete fabrication of the CMOS circuit. This approach requires the use of specific areas, subsequently called '**integration areas**' (*IA*), in which NEMS devices will be defined.

As explained later in chapter 4, the layout of the entire chip ( $7.5 * 7.5 \text{ mm}^2$ ) is not trivial: all the clusters CCII circuits + integration areas had to be placed adequately in order to be able to align a full-wafer nanostencil membrane a posteriori. Since the design of the stencil responds to specific rules owing to the mechanical behavior of the membrane, the position of the integration areas had to respect the position of the membranes apertures.

Each resonating nano/micromechanical device is connected to its own readout circuit. Indeed, the CCII circuit has not been designed for operating arrays of resonators. This means that every ensemble CIRCUIT+RESONATOR is electrically isolated and independent one from each other. Each ensemble has its own contact Al pads for electrical test.

At the end of the fabrication process, the whole surface of the chip is covered with a passivation bi-layer (800 nm thick) constituted of silicon nitride (SiN) and silicon oxide (SiO<sub>2</sub>). Local apertures into the passivation layers are only defined on top of:

- all Al contact Al pads
- all **integration areas**. These are the special areas where nano/micromechanical devices are fabricated in a post-processing module after CMOS fabrication. One resonator per area is fabricated. They are electrically connected on one side to Al contact pads and on the other to CCII input. Their layout is detailed hereafter.

#### INTEGRATION AREA (*IA*) LAYOUT

They are located on an n-well to isolate them from the surrounding p-bulk and for independent polarization. Their fabrication is realized along the CMOS process whose steps are



CCII CIRCUIT LAYOUT WITH INTEGRATION AREA

Three kinds of devices are integrated with CMOS: cantilevers, quad-beams and torsional paddles. We have focused specifically on in-plane vibrating cantilevers and out-of-plane vibrating quad-beams. Figure 28 represents the ensemble READOUT CIRCUIT + INTEGRATION AREA + NANODEVICE PATTERN + CONTACT PAD for cantilevers integration; Figure 29 represents integrated quad-beams. The green pattern corresponds to the Al pattern deposited by metal evaporation and structured either by nSL or by eBL and lift-off. This gives an idea of how nanodevices have to be aligned within an integration area. In the case of cantilevers, the left anchor is electrically connected to the  $V_{EXC}$  pad (for excitation voltage), the right one is connected to CCII input. This kind of layout contains 8 pads depicted in Figure 28:

- Pads  $V_{REF}$ ,  $V_{DD}$ ,  $V_{POL}$ ,  $R_{POL}$  and  $V_{SS}$  for circuit polarization
- Pad  $I_{OUT}$  collecting the amplified AC ( $I_{MEMS}$ ) + DC ( $I_{BIAS}$ ) current that subsequently flows externally into  $R_{LOAD}$ .
- Pads  $V_{EXC}$  for polarizing the resonator through its driving electrode ( $V_{INDC} + V_{INAC}$ )
- Pads  $V_{GND-NANOAREA}$  for polarizing the underlying n-well like  $V_{REF}$  in order to diminish parasitic capacitances and to be at the same voltage as the resonator (connected to CCII input, i.e.  $V_{REF}$ ) so that it is not attracted and does not collapse downwards

In the case of quad-beams, all pads have the same meaning except that the device (resonating ‘vertically’, i.e. out-of-plane) is polarized through the underlying n-well connected to the  $V_{EXC}$  pad (see Figure 29).

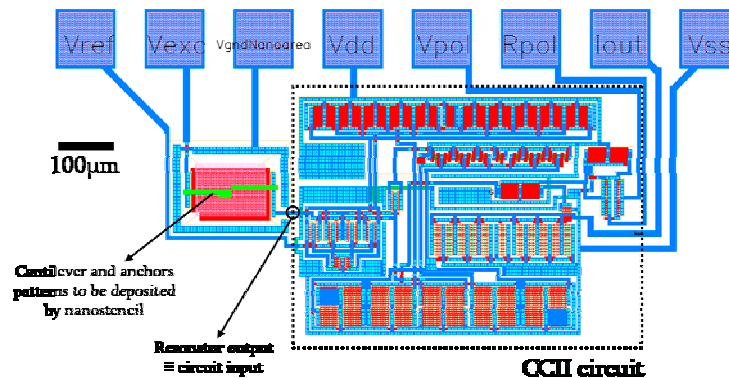


Figure 28. CCII layout with cantilevers-specific integration area

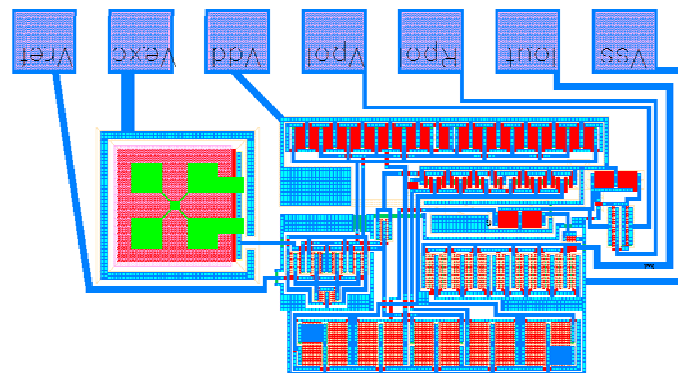


Figure 29. CCII layout with quad-beams-specific integration area

By a simple calculation of a p-n junction, the necessary distance between integration area and circuit can be estimated to prevent excessive extension of the depletion zone formed at the n-well/p-bulk interface. If this depletion zone reaches the p-substrate of the n-transistors of the CCII-, their operation can be perturbed. A 5  $\mu\text{m}$  distance between the n-well of the integration area and the CCII CMOS circuit has been foreseen what limits the polarization voltage of the n-well to 6 V. A posteriori, it is clear that it has not been sufficient for QB which require higher voltages.

### II.3.b. Chip layout

The layout of the whole chip contains 37 CCII CIRCUIT + RESONATOR ensembles together with 41 integration areas for discrete devices. The chip has a 7.32 \* 7.32 mm<sup>2</sup> area. Integration areas for discrete devices have an identical architecture but they have no associated circuitry, their output electrode is connected to a contact pad for external detection.

Figure 30 illustrates the devices distribution within the chip:

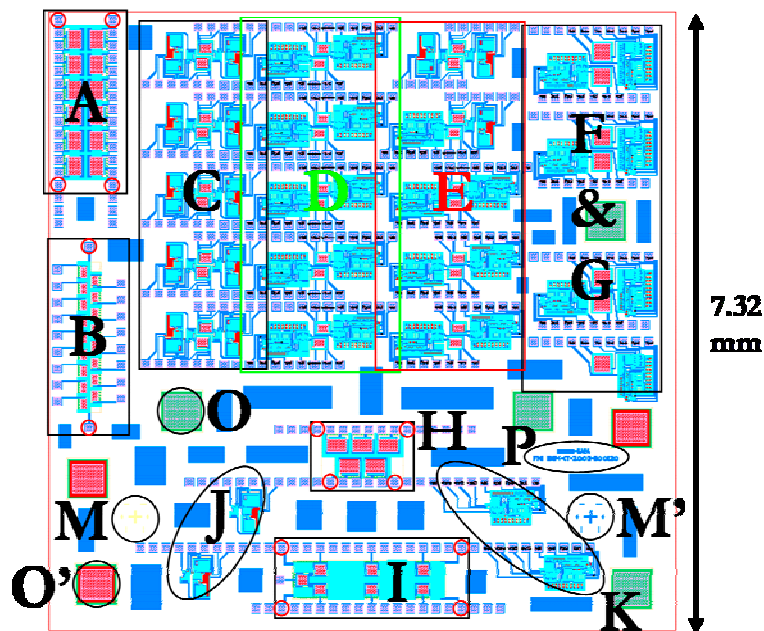


Figure 30. NaPa chip layout

Zones A, B, H and I contain *IA* for different types of discrete devices and are all located on a n-well. In-between each *IA*, electrical contacts metal (connected to the pads) / n<sup>+</sup> substrate have been inserted to polarize the well more efficiently (possible until 100 V).

Big metal rectangles (in blue) were included in order to homogenize the metal spatial distribution and therefore to improve the metal etching homogeneity.

- zone A** 12 *IA* for discrete devices (longitudinal mode dual beams, not described in this thesis) controllable with 2 pads. The n-well can be accessed by 4 pads visible on Figure 30 (red circles at extremities).
- zone B** 17 *IA* for discrete paddle resonators (not described in this thesis) controllable with 1 pad. The n-well can be accessed by 2 pads visible on Figure 30 (red circles at extremities).

<b>zone C</b>	10 BSNN circuits (not described in this thesis) for integration of in-plane vibrating cantilevers.
<b>zone D</b>	10 CCII circuits for integration of in-plane vibrating cantilevers.
<b>zone E</b>	from left to right and up to down: 3 BSNN circuits for integration of double cantilevers 2 CCII circuits for integration of double cantilevers 5 CCII circuits for integration of paddle resonators
<b>zone F &amp; G</b>	7 CCII circuits for integration of quad-beams
<b>zone H</b>	5 <i>IA</i> for discrete devices (longitudinal mode dual beams) controllable with 2 pads. The n-well can be accessed by 4 pads visible on Figure 30 (red circles at extremities).
<b>zone I</b>	7 <i>IA</i> for discrete QB resonators, controllable with 1 pad. The n-well can be accessed by 4 pads visible on Figure 30 (red circles at extremities).
<b>zone J</b>	2 BSNN test circuits (not described). J1 above, J2 below.
<b>zone K</b>	2 CCII test circuits. K1 above, K2 below.
<b>zone M</b>	<i>poly0</i> patterns serving as nanostencil-CMOS alignments marks (see chapter 4)
<b>zone M'</b>	<i>metal</i> patterns serving as nanostencil-CMOS alignments marks see chapter 4)
<b>zone O</b>	cell for testing [passivation+interlevel oxide] RIE (see chapter 4)
<b>zone O'</b>	cell for testing <i>poly1</i> RIE (see chapter 4)
<b>zone P</b>	CNM logo and NaPa project references

## Conclusion of chapter 3

In this chapter, a specific low-power CMOS readout circuit designed in the framework of this thesis has been described in detail: its function is to read out the capacitive current generated by resonating nano/micromechanical devices.

Complementarily, a whole CMOS chip has been designed, responding both to the requirements of the design rules of the CMOS technology and of the posterior integration of NEMS.

The topology and the corresponding layout of the second-generation current conveyor (CCII) circuit have been presented. The circuit behavior (intrinsic and coupled to resonating N-MEMS) has also been fully simulated. Electrical simulations show that CMOS integration greatly enhances the capacitive detection of the resonance of mechanical resonators by (i) drastically reducing parasitic loads at the resonator output and (ii) amplifying ‘on-chip’ the resonance signal.

These two statements remain true for any type of resonator. However, for out-of-plane vibrating resonators CMOS integration does not solve the issue of ‘vertical’ (out-of-plane) stray capacitances. In fact, this issue can mainly be solved through an optimization of the design of the resonator anchors.

In terms of processing, combining the technology for the fabrication of nanomechanical resonators with a standard CMOS technology is challenging. However, this issue has been addressed through a novel technology that is going to be detailed in chapter 4. In chapter 5, the experimental electrical characterization of successfully fabricated NEMS/CMOS together with an analysis of their frequency response will be carried out.

## Bibliographical references

1. Yang, Y.T., C. Callegari, X.L. Feng, K.L. Ekinici, and M.L. Roukes  
**Zeptogram-scale nanomechanical mass sensing**  
Nano Letters, 2006. **6**(4): p. 583-586.
2. Ekinici, K.L. and M.L. Roukes  
**Nanoelectromechanical systems**  
Review of Scientific Instruments, 2005. **76**(6).
3. Wong, A.C. and C.T.C. Nguyen  
**Micromechanical mixer-filters ("Mixlers")**  
IEEE Journal of Microelectromechanical Systems, 2004. **13**(1): p. 100-112.
4. Nguyen, C.T.C.  
**MEMS technology for timing and frequency control**  
IEEE Transactions on Ultrasonics Ferroelectrics and Frequency Control, 2007. **54**(2): p. 251-270.
5. Rebeiz, G.  
**RF MEMS Theory, design and technology**  
Wiley ed, 2003.
6. Le, H.P., K. Shah, J. Singh, and A. Zayegh  
**Design and implementation of an optimised wireless pressure sensor for biomedical application**  
Analog Integrated Circuits and Signal Processing, 2006. **48**(1): p. 21-31.
7. van Schaik, A. and S. Shamma  
**A neuromorphic sound localizer for a smart MEMS system**  
Analog Integrated Circuits and Signal Processing, 2004. **39**(3): p. 267-273.
8. Sadat, A., H.W. Qu, C.Z. Yu, J.S. Yuan, and H.K. Xie  
**Low-power CMOS wireless MEMS motion sensor for physiological activity monitoring**  
IEEE Transactions on Circuits and Systems I-Regular Papers, 2005. **52**(12): p. 2539-2551.
9. Wu, J.F. and L.R. Carley  
**Electromechanical Delta Sigma modulation with high-Q micromechanical accelerometers and pulse density modulated force feedback**  
IEEE Transactions on Circuits and Systems I-Regular Papers, 2006. **53**(2): p. 274-287.
10. Li, Y.C., M.H. Ho, S.J. Hung, M.H. Chen, and M.S.C. Lu  
**CMOS micromachined capacitive cantilevers for mass sensing**  
Journal of Micromechanics and Microengineering, 2006. **16**(12): p. 2659-2665.
11. Tang, M., A.Q. Liu, A. Agarwal, Q.X. Zhang, and P. Win  
**A new approach of lateral RF MEMS switch**  
Analog Integrated Circuits and Signal Processing, 2004. **40**(2): p. 165-173.
12. Verd, J., A. Uranga, J. Teva, J.L. Lopez, F. Torres, J. Esteve, G. Abadal, F. Perez-Murano, and N. Barniol  
**Integrated CMOS-MEMS with on-chip readout electronics for high-frequency applications**  
IEEE Electron Device Letters, 2006. **27**(6): p. 495-497.
13. Nguyen, C.T.C. and R.T. Howe  
**An integrated CMOS micromechanical resonator high-Q oscillator**  
IEEE Journal of Solid-State Circuits, 1999. **34**(4): p. 440-455.

14. Arcamone, J., B. Misischi, F. Serra-Graells, M.A.F. van den Boogaart, J. Brugger, F. Torres, G. Abadal, N. Barniol, and F. Perez-Murano  
**A Compact and Low-Power CMOS Circuit for Fully Integrated NEMS Resonators**  
IEEE Transactions on Circuits and Systems II, 2007. **54**(5): p. 377-381.
15. Reichenbach, R.B., M. Zalalutdinov, J.M. Parpia, and H.G. Craighead  
**RF MEMS oscillator with integrated resistive transduction**  
IEEE Electron Device Letters, 2006. **27**(10): p. 805-807.
16. Enz, C.C., E.A. Vittoz, and F. Krummenacher  
**A Cmos Chopper Amplifier**  
IEEE Journal of Solid-State Circuits, 1987. **22**(3): p. 335-342.
17. Menolfi, C. and Q.T. Huang  
**A fully integrated, untrimmed CMOS instrumentation amplifier with submicrovolt offset**  
IEEE Journal of Solid-State Circuits, 1999. **34**(3): p. 415-420.
18. Menolfi, C. and Q.T. Huang  
**A low-noise CMOS instrumentation amplifier for thermoelectric infrared detectors**  
IEEE Journal of Solid-State Circuits, 1997. **32**(7): p. 968-976.
19. Uranga, A., X. Navarro, and N. Barniol  
**Integrated C-MOS amplifier for ENG signal recording**  
IEEE Transactions on Biomedical Engineering, 2004. **51**(12): p. 2188-2194.
20. Lange, D., C. Hagleitner, C. Herzog, O. Brand, and H. Baltes  
**Electromagnetic actuation and MOS-transistor sensing for CMOS-integrated micromechanical resonators**  
Sensors and Actuators a-Physical, 2003. **103**(1-2): p. 150-155.
21. Ma, W., R.Q. Zhu, L. Rufer, Y. Zohar, and M. Wong  
**An integrated floating-electrode electric microgenerator**  
IEEE Journal of Microelectromechanical Systems, 2007. **16**(1): p. 29-37.
22. Uranga, A., J. Teva, J. Verd, J.L. Lopez, E. Torres, J. Esteve, G. Abadal, E. Perez-Murano, and N. Barniol  
**Fully CMOS integrated low voltage 100 MHz MEMS resonator**  
Electronics Letters, 2005. **41**(24): p. 1327-1328.
23. Verd, J., G. Abadal, J. Teva, M.V. Gaudo, A. Uranga, X. Borrise, F. Campabadal, J. Esteve, E.F. Costa, F. Perez-Murano, Z.J. Davis, E. Forsen, A. Boisen, and N. Barniol  
**Design, fabrication, and characterization of a submicroelectromechanical resonator with monolithically integrated CMOS readout circuit**  
IEEE Journal of Microelectromechanical Systems, 2005. **14**(3): p. 508-519.
24. Bertz, A., H. Symanzik, C. Steiniger, A. Hoffer, K. Griesbach, K. Stegemann, G. Ebest, and T. Gessner  
**A single-crystal Si-resonator with on-chip readout amplifier in standard CMOS**  
Sensors and Actuators a-Physical, 2001. **93**(2): p. 163-172.
25. Weigold, J.W., A.C. Wong, C.T.C. Nguyen, and S.W. Pang  
**A merged process for thick single-crystal Si resonators and BiCMOS circuitry**  
IEEE Journal of Microelectromechanical Systems, 1999. **8**(3): p. 221-228.
26. Bienstman, J., H.A.C. Tilmans, E. Peeters, M. Steyaert, and R.R. Puers  
**An oscillator circuit for electrostatically driven silicon-based one-port resonators**  
Sensors and Actuators a-Physical, 1996. **52**(1-3): p. 179-186.
27. Nguyen, C.T.C.  
**Frequency-selective MEMS for miniaturized low-power communication devices**  
IEEE Transactions on Microwave Theory and Techniques, 1999. **47**(8): p. 1486-1503.

28. Otis, B.P. and J.M. Rabaey  
**A 300- $\mu$ W 1.9-GHz CMOS oscillator utilizing micromachined resonators**  
IEEE Journal of Solid-State Circuits, 2003. **38**(7): p. 1271-1274.
29. Enz, C.C., F. Krummenacher, and E.A. Vittoz  
**An Analytical Mos-Transistor Model Valid in All Regions of Operation and Dedicated to Low-Voltage and Low-Current Applications**  
Analog Integrated Circuits and Signal Processing, 1995. **8**(1): p. 83-114.
30. Sedra, A. and K.C. Smith  
**A Second-Generation Current Conveyor and Its Applications**  
IEEE Transactions on Circuit Theory, 1970. **CT17**(1): p. 132-&.
31. Surakampontrorn, W., V. Riewruja, K. Kumwachara, and K. Dejhan  
**Accurate Cmos-Based Current Conveyors**  
IEEE Transactions on Instrumentation and Measurement, 1991. **40**(4): p. 699-702.
32. Hassanein, W.S., I.A. Awad, and A.M. Soliman  
**New wide band low power CMOS current conveyors**  
Analog Integrated Circuits and Signal Processing, 2004. **40**(1): p. 91-97.

# CHAPTER 4

## FABRICATION OF NANO/MICROMECHANICAL RESONATORS ON CMOS CIRCUITRY

I.	Lithography techniques for integration of NEMS on CMOS.....	120
I.1.	Nanostencil lithography, a full-wafer high-resolution technique .....	120
I.1.a.	State of the art, features and advantages of the technique .....	120
I.1.b.	Fundamental aspects of the fabrication of a full-wafer stencil by DUV .....	122
I.1.c.	Specific nanostencil layout for CNM CMOS wafer .....	125
I.2.	Electron beam lithography .....	127
II.	Fabrication of micro/nanomechanical resonators on CMOS by nanostencil lithography (nSL).....	128
II.1.	CNM CMOS technology .....	129
II.2.	Optimization of nSL process on CMOS: alignment and blurring corrections.....	131
II.2.a.	Alignment .....	131
II.2.b.	Blurring of Al patterns deposited by nSL.....	133
II.2.c.	Dummy wafers .....	139
II.3.	Post-processing of pre-fabricated CMOS wafers based on nSL.....	141
II.3.a.	<i>poly1</i> removal .....	141
II.3.b.	Alignment .....	142
II.3.c.	Al deposition.....	144
II.3.d.	Blurring correction.....	145
II.3.e.	Pattern transfer and release .....	145
II.3.f.	Test of CMOS compatibility of nSL.....	148
III.	Fabrication of nano/micromechanical resonators on CMOS by electron-beam lithography (eBL)	150
	Conclusion of chapter 4.....	151
	Bibliographical references .....	152

As a continuation to chapter 3, chapter 4 is focused on the technological aspect of the monolithic integration of nano/micromechanical resonators with CMOS circuitry.

Chapter 3 detailed to what extent such a monolithic integration implies a drastic enhancement in terms of device operation through the low-loss coupling with a CMOS circuit for on-chip signal conditioning and amplification. In chapter 4, we address the technological realization of this objective.

Regarding processing, the key issue of the fabrication of devices with submicron scale dimensions arises from lithography. In this connection, the technological process flow is mostly determined by the choice of nanopatterning technique.

We follow an approach [1, 2] based on post-processing pre-fabricated standard CMOS wafers. The fabrication strategy consists in using existing CMOS layers as structural layer (capacitor polysilicon) and sacrificial layer (field oxide) of the resonators. This method facilitates the interconnection between the nanomechanical device and the CMOS circuit, avoiding the need to use any additional layer and/or material.

The post-processing approach also allows using a different lithography technique for CMOS circuit fabrication and NEMS definition: in this way, potentially cheaper, not ultra-advanced CMOS technologies can be utilized for circuitry fabrication while a higher resolution nanolithography technique is implemented for subsequent (single step) NEMS patterning.

To define the nanodevices dimensions, we have chosen two different nanolithography techniques: nanostencil (nSL) and electron beam lithography (eBL). Actually, most of the work exposed in this thesis has been devoted to nSL, an emerging technique, still in development, in particular to demonstrate that it represents an outstanding tool to define nanometer scale devices on CMOS wafer at full wafer level. In parallel, we have developed another post-processing technology based on eBL for rapid, but serial, prototyping of new devices.

The development of nSL technique for this purpose has been realized in the framework of the NaPa<sup>1</sup> project, whose goals are the development of emerging nanopatterning techniques like nanoimprint, soft-lithography or self-assembly. The fabrication of nanomechanical devices monolithically integrated into CMOS circuit has represented an ideal platform to demonstrate the full-wafer patterning of nanodevices on CMOS wafers by nSL, what was one of the initial objectives of NaPa. This task has given occasion to a close collaboration with the Microsystems laboratory LMIS1 from EPFL, in particular with Dr Marc.A.F. van den Boogaart and Prof. Jürgen Brugger. Initially, this work partially relied on the previous experience of CNM in FP5 EU project NANOMASS<sup>2</sup> in which a similar approach was followed but using alternative nanolithography methods: in that project, the functionality of few prototypes was demonstrated but not the patterning of a whole CMOS wafer.

---

<sup>1</sup> “Emerging Nanopatterning methods” project funded by the European Commission within FP6 (6<sup>th</sup> Framework Program), 31 (academic and industrial) partners from 14 countries (contract NMP4-CT-2003-500120)

<sup>2</sup> Project funded by the European Commission within the FP5 (5<sup>th</sup> Framework Program), contract n° IST-1999-14053

Pursuing a monolithic integration of NEMS on CMOS, several nanolithography techniques may be adequate but only a few simultaneously ensure parallel patterning for rapid processing at wafer scale and nanometer-sized features definition. Moreover, CMOS circuits require compatibility of the patterning technique for proper circuitry operation, in other words, to avoid any damage during the post-processing related to NEMS definition.

Nanostencil lithography (nSL) is a suitable technique to fulfill those requirements. It is a flexible (easy to apply), parallel and resistless patterning method based on a high-resolution wafer-scaled shadow mask.

It allows a wide choice of materials and surfaces to be selectively deposited (i.e. only where needed). On the contrary to deep-ultraviolet (DUV), X-ray, electron beam, or ion beam exposure, mechanically fragile and chemically functionalized surfaces can be structured, due to the absence of cyclic (resist-based) process steps and to the absence of etching processes (unlike nanoimprint lithography). Additionally, nSL potentially has a sub-100 nm (maybe sub-50 nm) resolution what is better than DUV, for example.

Its parallelism and its associated potentially high throughput make it a serious candidate for industrialization. Nevertheless, as it will be explained in this chapter, some limitations still exist for its industrial implementation but some of them have been solved during the development of this thesis.

This chapter will review the main aspects of the fabrication and applications of nanostencils. Then the fabrication of a full-wafer stencil will be explained. The challenges and the related necessary optimization of nSL-based process on CMOS will be exposed. All process steps will be detailed before concluding on the obtained results. At the end, the CMOS compatibility of the nSL-based process in terms of circuit operation will be commented.

Much more briefly, the interest and limitations of e-beam lithography for integration of NEMS on CMOS as well as the details upon the corresponding process flow we have been defining will be exposed.

## I. Lithography techniques for integration of NEMS on CMOS

### I.1. Nanostencil lithography, a full-wafer high-resolution technique

Nanostencil lithography (nSL) is a shadow-mask based lithography technique (see Figure 1). Potentially, patterning techniques implementing shadow-masks are not limited in resolution and towards the confirmation of this assumption, some authors have applied single-walled carbon nanotubes as shadow masks for the fabrication of 1-2 nm wide gaps [3, 4].

In this work, the shadow-masks are under the form of stencils that are micromachined Si wafers containing hundreds of nanostencils in the form of thin (200 nm thick) free-standing silicon nitride (SiN<sub>x</sub>) membranes with micro- and nano-scale apertures (see Figure 2). As it will be demonstrated along this chapter, this type of stencil allows local nanopatterning of a whole CMOS wafer in one deposition step.

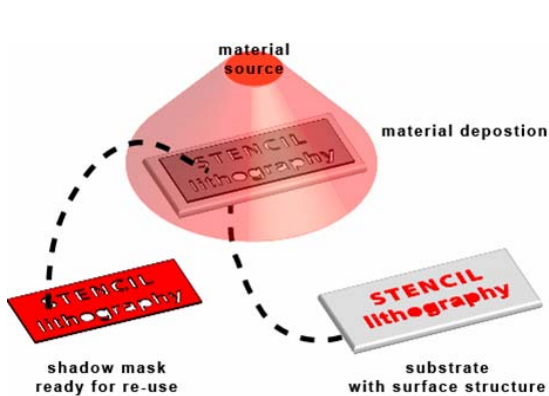


Figure 1 [5]. Principle of nanostencil lithography

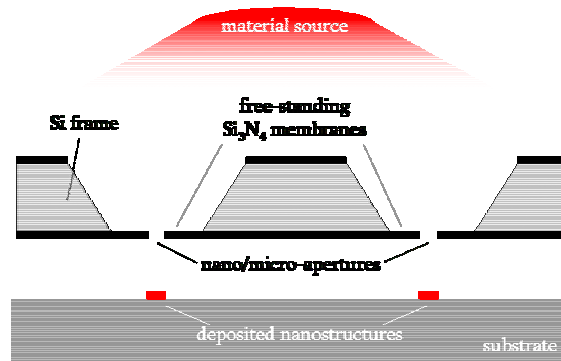


Figure 2. Specific implementation of nanostencil lithography in this thesis. Nanostencils free-standing membranes (framed by a Si wafer) with local nano/microapertures

First, the applications and various fabrication processes of nanostencil membranes reported in the literature will be discussed. After this introduction, the fabrication of a full-wafer (100 mm) nanostencil based on advanced bulk and surface nano-micromachining [6] will be described.

#### I.1.a. State of the art, features and advantages of the technique

##### ADVANTAGES OF THE TECHNIQUE

Stencil lithography (SL) is a versatile method that can be used in a variety of applications. There has been recently a strong interest regarding the use of shadow masks, mostly related to combinatorial materials science [7, 8], organic based device fabrication [9, 10], as well as rapid prototyping of nanoscale structures using dynamic [11-13] or quasi-dynamic [14] stencil deposition. These papers are mainly focused on process related topics [6, 15-18]; few ones are more focused on the application itself [1, 19, 20].

From the study of almost all reported variants of SL, a series of intrinsic generic advantages emerges. Its main features are its 'cleanliness', its flexibility, its parallelism and its high resolution.

Moreover, it is a non-contact and resistless (i.e. clean) technique. This exclusive characteristic makes that ultra-clean surfaces with high purity deposits can be obtained. From that, mechanically fragile [16] and chemically functionalized surfaces [21] can be structured, due to the absence of cyclic (resist-based) process steps.

More generally, SL allows a wide choice of materials (the limitation comes from the deposition technique and not from SL itself) and surfaces to be selectively deposited (i.e. only where needed). In particular, several examples of deposition of complex oxides by Pulsed Laser Deposition (PLD) through nanostencils have recently been reported [22, 23].

Its parallelism makes it much faster than presently existing charged particle techniques (FIB or eBL) and in this context one objective of NaPa project, relying on a collaboration between EPFL and CNM, has been the demonstration of its implementation at full-wafer scale while providing 150 nm resolution.

### TYPES OF SHADOW-MASK

There are basically two types of shadow masks: in-situ and membrane-based. In-situ shadow masks were used, for example, to fabricate the first single electron transistor [24]; this is also a well-known technique in MBE (Molecular Beam Epitaxy) experiments with II-VI and III-V semiconductor compounds [25, 26]. In practice, such a shadow mask consists of a two-layer stack onto the substrate to be patterned: the top layer is the proper shadow mask and the bottom one, generally a sacrificial layer, acts as spacer. A clear disadvantage of in-situ SL is the need to remove this mask after evaporation what involves a chemical treatment contaminating the substrate.

The other approach is based on the implementation of a locally perforated membrane. Its material may be a metal, Si, Si<sub>3</sub>N<sub>4</sub> or even polymers. To release the membrane from the backside, several distinct techniques were already reported. Membrane thickness and area are two key features.

It is important to obtain a final thin membrane mainly for two reasons: it makes its perforation easier (shorter etching) and it increases the uniformity of the structures whose replication patterns are located at the extremities of the stencil: otherwise the apertures sidewalls may shadow the incoming flux and deform the obtained pattern shape.

Nanoapertures are generally defined from the membrane front-side either by eBL (and subsequent pattern transfer by RIE) [27] or FIB [11, 18, 28] but these two techniques are serial and impede large area fabrication of apertures and consequently the available throughput.

Concerning the area of thin membranes, it generally does not exceed 1 mm<sup>2</sup> [5, 28, 29] because of its fragility. Mechanical in-situ reinforcements could permit to increase the membrane area but in general this tends to decrease the density of apertures [29].

### LIMITATIONS

The resolution of the deposited structures is both determined by the stencil aperture resolution and the geometrical configuration of the deposition chamber (source size, source-substrate distance and gap between stencil and substrate). In practice, a deposited structure is composed of a main structure, a penumbra, whose dimensions are calculable in a simple way through geometrical laws [28, 30], and surface interaction effects such as surface migration and re-deposition (scattering). The penumbra formation depends exclusively on the geometrical conditions and together with those surface-related effects, they cause a distortion of the pattern

resulting in blurred edges and pattern widening. This so-called ‘blurring effect’ has been observed by numerous authors [10, 16, 25, 28, 30, 31]. The gap between stencil and surface appears to be the key parameter of this issue. In contrast, the deposition of a material through the apertures of a stencil directly put in contact with the substrate yields a perfect 1:1 replication of the aperture pattern [16]. ‘Blurring effect’ is the topic of section II.2.b.

Another source of pattern distortion, associated to ‘blurring effect’, is the stress-related increasing deflection of membranes around specific apertures (for example U-shape) during material deposition. As the gap is constantly varying, the resulting pattern is not well defined and its edges are smooth and blurred. To circumvent that, reinforced membranes have been demonstrated by EPFL [32, 33]. Their full-wafer fabrication process is actually detailed in next section.

A third relevant effect causing pattern distortion is clogging. It always occurs but can be more or less significant: when evaporating a material, a certain amount is deposited on the membrane itself and inside its apertures (on the sidewalls). Kölbel et al. [15] proposes a solution to remedy to this problem by coating stencils with an anti-adhesive self-assembled monolayer (SAM): this reduces the adhesion of the evaporated material inside the apertures and thereby the clogging of nano/micro apertures.

### OBJECTIVE AND CONTEXT OF THIS WORK

It has been shown that the fabrication of apertures as small as 15-20 nm [27] is possible with the use of thin suspended SiN membranes. However in this paper the membranes have a limited area (max. 100 x100  $\mu\text{m}^2$ ).

In this context, EPFL has demonstrated the possibility of fabricating full-wafer scale (100 mm) stencils with local free-standing membranes, whose apertures result in arbitrary shaped patterns between 200 nm up to 300  $\mu\text{m}$  [6, 18] (this large range of pattern size, simultaneously obtainable, is clearly a key feature of the technique).

To compete or complement with other standard micro and nanofabrication technologies, nSL needs to fulfill the following requirements: high resolution, high pattern density, large area and further integration into existing processes, like for example CMOS. This was the purpose of the collaboration undertaken within NaPa project between EPFL and CNM.

### **I.1.b. Fundamental aspects of the fabrication of a full-wafer stencil by DUV**

#### FABRICATION PROCESS OF STABILIZED MEMBRANES [5, 6]

Limited stencil size is mainly due to the lack of a suitable high-resolution and high-throughput lithography and of MEMS fabrication methods for creating nanoscale structures on large areas combined with well-controlled wafer-through etching of thin solid-state membranes. Serial fabrication technologies like FIB or eBL have been used to obtain apertures at nanoscale, however with limited throughput. Laser interference lithography (LIL) can achieve 100 nm scale patterning on large areas, but is exclusively limited to periodic structures. In order to overcome these limitations for the fabrication of large-area nanostencils with arbitrary apertures, a 100 mm wafer scale combined DUV (Deep Ultra Violet)/MEMS fabrication process was developed at EPFL. Using this method, aperture patterns covering multiple length scales, from 200 nm up to 300  $\mu\text{m}$ ,

can be defined in a thin silicon nitride layer by a wafer stepper DUV exposure followed by dry etching. Additional local FIB milling can introduce sub-200 nm features in these stencils.

In order to overcome or limit the effects of membrane deformation, two distinct fabrication processes have been developed in which the membranes were mechanically stabilized. This is done in such a way that the local membrane stabilization does not interfere with the normal stencil deposition process, e.g. the line of sight is not affected by the stabilization. These fabrication processes have resulted in silicon supported SiN membranes and corrugated SiN membranes. The improved micro/nanostencils incorporate in-situ, local stabilization structures increasing their moment of inertia,  $I$ , which is the structural property directly related to stiffness or deformability [33]. Since the corrugated stabilized stencil membranes add only one process step to the standard stencil fabrication process, it has been tried to combine this stabilization fabrication process with a wafer stepper DUV exposure.

Figure 3 shows a schematic overview of the fabrication process of a full-wafer stencil with corrugated membrane stabilization. The process begins with the definition of stabilization structures or rims by UV lithography and anisotropic dry etching into a double-side polished, 380  $\mu\text{m}$  thick Si wafer (Figure 3a). Then the deposition of 100, 200, or 500 nm thick low-stressed silicon nitride (LS-SiN) by low pressure chemical vapor deposition (LPCVD) follows as illustrated in Figure 3b. Mesoscopic patterns which will form the membrane apertures were defined in a DUV resist via a 4 times reduced projection in a DUV wafer stepper. Transfer of the resist pattern into the low-stress SiN layer was done by means of anisotropic etching (RIE) (Figure 3c).

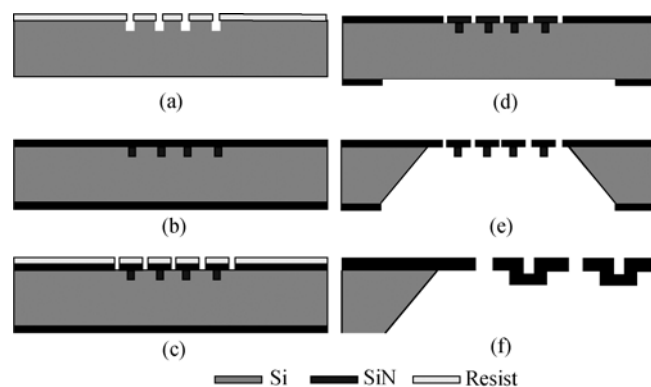


**Figure 3 [5]: Simplified schematic illustration of the fabrication process for a corrugated stencil fabrication. (a) definition of stabilization structures/rims; (b) LPCVD low-stress SiN deposition; (c) transfer by RIE of the DUV resist patterns into SiN; (d) membrane etch window definition by backside lithography and pattern transfer (e) KOH etching of bulk Si to release membranes; (f) schematic detail of the corrugated membrane.**

The key process parameters for the transfer of the patterned DUV resist into the low-stress SiN layer is the selectivity of the etching agent between the DUV resist mask layer and the SiN structural layer. In order to optimize the pattern transfer conditions, a  $\text{C}_2\text{F}_6$  gas flow of 20 sccm is used with additional 20 sccm of  $\text{CH}_4$ . The backside patterns are defined in photoresist by means of conventional photolithography. The SiN layer on the backside is opened using ICP (Inductive Coupled Plasma) anisotropic etching. This backside patterned SiN (Figure 3d) forms the etch mask for the subsequent membrane release (Figure 3e). A schematic detail of the corrugated membrane can be seen in Figure 3f.

DUV RETICLE

The 4 times reduced projection in a DUV wafer stepper of the mesoscopic patterns into a DUV resist required the design and fabrication of a suitable reticle (mask). The general layout of the reticle was designed at EPFL containing several specific designs provided by and for NaPa partners. In our case, the chip design for full-wafer replication of NEMS devices on CMOS was done by us respecting design rules defined by EPFL. Because of the 4 times reduced projection used in the DUV exposure, 200 nm features in a stencil design become 800 nm features in the reticle.

This reticle contains standard structures and markers related to the used exposure equipment (ASML, PAS 5500/700 system). In the middle of the reticle lies an exposure field in which all the designs are placed. The DUV stepper allows exposing one single structure of the reticle on a wafer in contrast to a 1:1 exposure, in which an entire wafer is directly exposed in a single exposure. The step and repeat exposure has been utilized to expose NaPa partner specific wafer stencils and chip-based stencils.

Figure 4 shows a schematic overview of the reticle containing the markers and the individual designs together with two examples of wafers, exposed according to NaPa partner specifications. At CNM, we have made our chip design (presented in the next section) and sent it to EPFL to incorporate it in the exposure field of the reticle: CNM patterns are the so-called “stencil 1” in Figure 4.

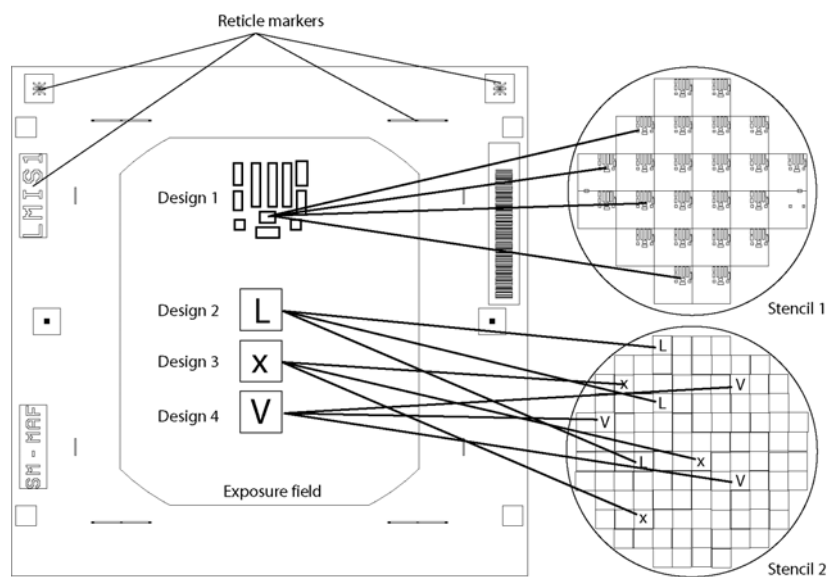


**Figure 4. Schematic representation of NaPa reticle and 2 examples of stencils. This reticle contains several designs which can be selectively exposed on custom wafers enabling large freedom in reticle designs.**

DUV EXPOSURE [5, 6]

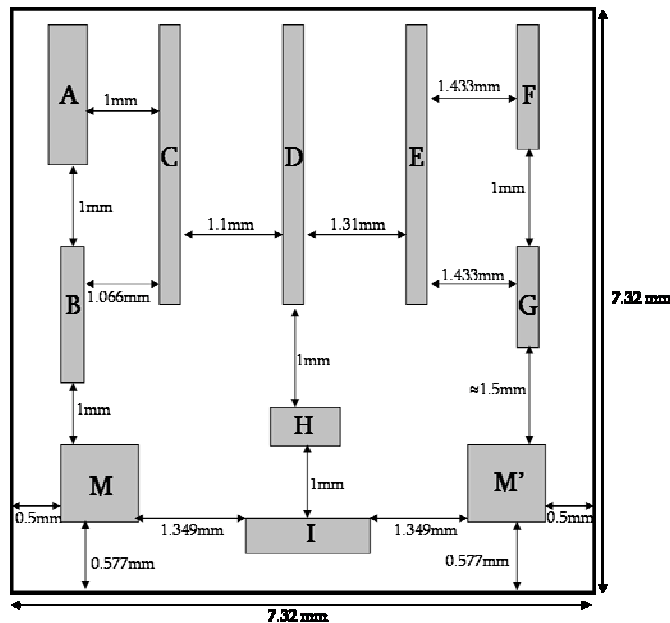
The DUV exposure was done in cooperation with ASML directly at their labs in Veldhoven, The Netherlands. It was realized on a modified PAS 5500/700 system. In order to obtain a higher process window bottom- and top anti-reflective coatings were applied. Four different wafers were exposed of which two wafer designs had a stabilized option integrated. The stabilized series of stencils were exposed with the same setting as the normal stencils.

**I.1.c. Specific nanostencil layout for CNM CMOS wafer**

The fabricated full-wafer nanostencil contains 24 identical chips (7.5 \* 7.5 mm<sup>2</sup>) per wafer. The corresponding layout of the chip to replicate had to combine two independent requirements:

- adaptation to nanostencil fabrication and robustness-related design rules:
  - SiN membranes are released from the back side of the Si wafer (380 μm thick). This wet etching is made by KOH through photolithographic apertures: consequently the etch profile is not vertical but inclined of 54°. For this reason, two membranes must be separated of at least 0.6 mm. For enhanced stability of non stabilized membranes, their area should not exceed 1 mm<sup>2</sup>.
- adaptation to CMOS chip design (and vice versa) for alignment of the resonators patterns (nanostencil apertures) with the integration areas of the CMOS substrate. Actually, both CMOS and nanostencil chip layouts were made interactively to respond to all respective spatial limits: membrane separation and area, CCII circuit size, etc...

Figure 5 depicts a schematic view of the nanostencil layout (chip level) with all the membranes (grey rectangles) and their in-between separation. Table IV - 1 reports the characteristics of each membrane depending on the type of patterned device and whether they contain integrated (connected to a CCII CMOS readout circuit) and discrete (without integrated readout circuitry) devices. We will focus on the study of integrated cantilevers and QB (membranes C, D, E, F and G).



Membrane	number and type of devices (apertures)	Area (mm <sup>2</sup> )
A	12; discrete paddles	0.9
B	17; discrete paddles	0.51
C	10; int. cantilevers	0.98
D	10; int. cantilevers	0.98
E	10; int. cantilevers	0.98
F	4; int. QB	0.44
G	3; int. QB	0.36
H	5; discrete paddles	0.45
I	7; discrete QB	0.72
M	set of alignment	1
M'	marks	1

Table IV - 1. Membrane characteristics

Figure 5. Nanostencil layout at chip level.

In total, there are 78 patterns of nano/micromechanical structures per nanostencil chip, distributed over 9 membranes, 37 of them are integrated with CMOS, the others are discrete. This

number of 37 is not a limitation; the entire chip could have exclusively contained integrated devices. The limiting factor here was the CMOS technology whose big transistors size (gate length 2.5  $\mu\text{m}$ ) resulted in big circuit areas.

COMMENT ON ALIGNMENT

Initially, the accuracy of the full-wafer alignment to perform between nanostencil and CMOS wafers was difficult to predict although we targeted it in the sub-10  $\mu\text{m}$ . Therefore, a minimum 15  $\mu\text{m}$  margin between stencil pattern and passivation window was foreseen to make nanostencil alignment easier within the integration area.

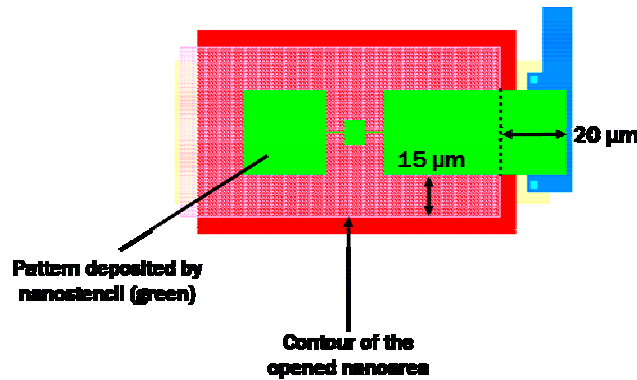
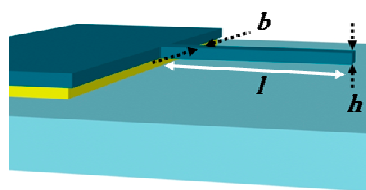


Figure 6: Integration area (in CMOS) + corresponding nanostencil pattern to be defined (in green). The aperture in the passivation layers is depicted in pink. Examples of margin foreseen for the correct insertion of the pattern within the integration area is depicted.

LIST OF DEVICES

Hereafter, we provide the list of nominal dimensions of the devices according to the nomenclature used in the GDS Cadence file. Note that the nominal thickness is 600 nm for all, determined by the CMOS technology.

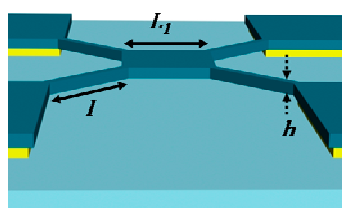
Cantilevers



Name	Characteristics	$l(\mu\text{m})$	$b(\text{nm})$	$g(\text{nm})$
C1	Simple	14	250	900
CN_2 CI_2	double	14	250	900

$l$  is the cantilever length ( $\mu\text{m}$ ),  $b$  its width ( $\mu\text{m}$ ) and  $g$  the gap separating from the electrode ( $\mu\text{m}$ )

Quad-beams



Name	$L_1(\mu\text{m})$	$l(\text{nm})$	$b(\text{nm})$
A1	14.1	18	600
A2	14.1	18	400
A3	14.1	18	800
A4	14.1	15	600
A5	14.1	21	600
A6	11.1	18	600
A7	17.1	18	600

$L_1$  is the plate width ( $\mu\text{m}$ ),  $l$  the beam length ( $\mu\text{m}$ ) and  $b$  the beam width ( $\mu\text{m}$ ).

### I.2. Electron beam lithography

Electron beam lithography (eBL) started its development in early 70s and since then, it has represented an alternative to conventional optical lithography (OL) for the definition of submicron patterns. Actually, eBL consists in irradiating by means of a focused electron beam a surface coated with an electron sensitive resist. eBL is a direct writing technique utilizing electrons as irradiation support, on the contrary to optical techniques that require an opaque mask and light respectively. Physically, enhanced resolution is obtained basically since electronic radiation is not limited by diffraction effects that affect the resolution of OL.

With such an eBL system, a layout is directly written through the spatial monitoring of a high energy electron beam applied upon a surface whose top material (a coated resist) properties are physically or chemically modified by the incident beam. The subsequent step is the development of the sample in order to remove the irradiated part of the resist (if it is positive).

The key parameters determining the efficiency of an eBL step [34] are the beam shape and its characteristics, its electronic energy, electron-matter interactions, resist thickness and molecular structure, the development solution and time, but also the design of the structure to be drawn. In recent years, every element of the system has known a big progress; more stable filaments are now available, beam diameter has been reduced down to few nm, and globally the whole eBL process (electron generation and focus, sample displacement, etc...) is fully automated.

At CNM, our eBL consists of a Scanning Electron Microscope (SEM) completed by a set of electronic devices that control beam deflection and blanking. The SEM system provides the electron source, focusing elements and a movable substrate holder for nano/micropositioning. PMMA (PolyMethylMethacrylate) is used as a resist.

In industry and research areas, eBL is mainly applied to the fabrication of masks, for device prototyping and fabrication in low amounts. More generally, it is useful in research for very specific applications (nano/microelectrodes patterning, etc...). For us at CNM, the use of eBL is of interest for its high resolution and versatility. Indeed, it allows rapid fabrication of new prototypes, since it is a direct writing method that does not require purchasing a mask each time that first prototypes of a new device have to be produced. In this sense, it is cost and time effective. eBL is also capable of realizing patterns in a large range of dimensions (50 nm - 100  $\mu$ m).

Nevertheless, intrinsically and comparatively with nSL, eBL suffers a series of limitations. First, the cost of the system is relatively high. Second, its slowness and low throughput must be pointed out. Compared to nSL, OL or NIL which are parallel, eBL is serial what considerably slows the patterning of a full wafer. In comparison with nSL, eBL requires more related process steps: resist coating, exposure, development, metallization and lift-off, in other words five steps, while nSL only requires one evaporation, i.e. one single step (two if counting alignment and clamping).

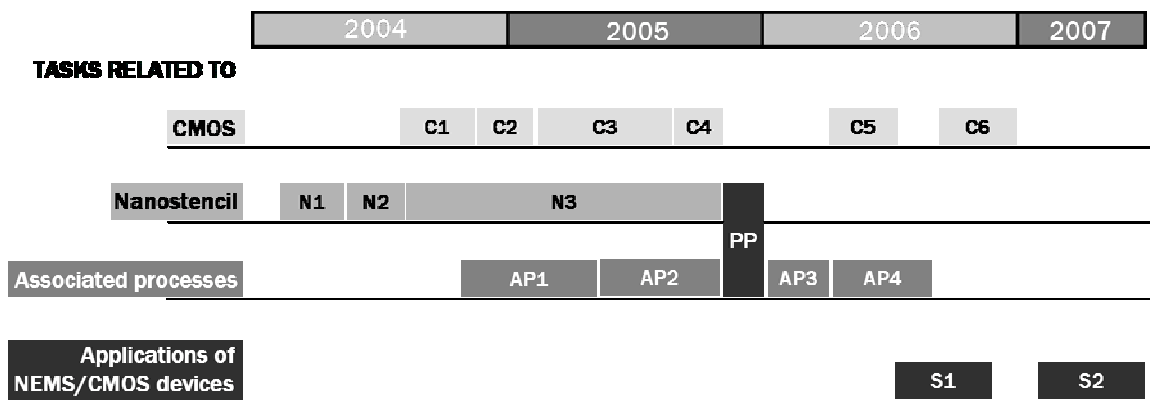
Third, the large quantity of parameters and the complexity of operation imply a low reproducibility of eBL systems. Constant technical support is required and only big foundries can afford having an entire team devoted to the optimization of the system.

Last but not least, some authors have pointed out the fact that eBL degrades the performance of the CMOS circuitry [35] when it is implemented as nanolithography technique for the fabrication of nanodevices on pre-fabricated CMOS substrates. In contrast, in section II.3.f, CMOS compatibility of nSL is discussed: in our samples, no relevant change between before and after post-processing has been observed.

## II. Fabrication of micro/nanomechanical resonators on CMOS by nanostencil lithography (nSL)

This work is the result of an intensive collaboration realized with LMIS1 (Microsystems Laboratory 1) from EPFL (Lausanne, Switzerland) in the frame of the NaPa European project, in particular with Dr. Marc .A.F. van den Boogaart, who was pursuing his PhD at this time on Stencil Lithography, and Professor Jürgen Brugger. To less extent, SÜSS MICROTEC also participated in the development of tools for stencil/CMOS alignment, in particular a specific chuck was designed for adapting to a standard SÜSS MICROTEC bond aligner.

Figure 7 shows the time evolution of different tasks related to NaPa project and my thesis. Between the beginning of the project (in 2004) and the first demonstration of device functionality, about 20-22 months passed. It has been a success and further advancements are still in course.



### TASKS CORRESPONDANCE

CMOS	Nanostencil (nSL)	Associated processes	Applications of NEMS/CMOS devices
<b>C1:</b> CCII circuit design and simulations	<b>N1:</b> design (CNM) and fabrication (EPFL) of 1 <sup>ST</sup>	<b>AP1:</b> characterization of 'blurring effect'	<b>S1:</b> implementation of NEMS/CMOS as highly sensitive mass sensors to monitor the deposition of ultra-thin gold layers
<b>C2:</b> circuit layout	generation of chip-sized stencils	<b>AP2:</b> fabrication of dummy wafers for process tests	<b>S2:</b> implementation of NEMS/CMOS as positioning sensors in quasi-dynamic stencil lithography system
<b>C3:</b> circuit fabrication	<b>N2:</b> first tests with non-custom CMOS chips	<b>PP:</b> post-processing of CMOS wafers by nSL	
<b>C4:</b> circuit pre-test	<b>N3:</b> design (CNM) and fabrication (EPFL) of full-wafer nanostencils	<b>AP3 and AP4:</b> development of release etchings of integrated cantilevers (AP3) and QB (AP4)	

Figure 7. Time evolution of my thesis work for NaPa project

Up to our knowledge, this work represents the first time that patterning of full CMOS wafers with nanostencil lithography is achieved and probably even the first time that a relatively low cost full wafer monolithic integration of nanodevices on CMOS has been demonstrated. Actually, advanced optical lithography can be used to define devices on CMOS at nanometer scale, but it requires the use of expensive equipment and materials, as well as complex processing only available for large microelectronics companies specialized in the fabrication of large series of semiconductor memories and microprocessors. Other emerging lithography techniques have

already been used to pattern devices on CMOS, like e-beam lithography [36], laser lithography [37] or nanoimprint lithography, but none of them had simultaneously demonstrated a reliable and CMOS compatible full wafer patterning.

By combining the technology for the fabrication of nanomechanical resonators with a standard CMOS technology, we present a novel wafer-scale (100 mm) technological process based on post-processing pre-fabricated CMOS circuits using nSL. This approach separates CMOS circuit fabrication and nanodevice fabrication, so that two different lithography techniques for each phase are used. Thus, a rather low-cost nanolithography technique may be implemented on CMOS substrates whose processing does not require an ultra-advanced patterning technique. In this context, nSL is adequate since it is clean (resistless), direct and parallel.

As it will be shown, we have succeeded in the parallel definition and fabrication of multiple (~2000) silicon nanomechanical resonators at the 200 nm scale that are monolithically integrated into CMOS circuits. Further decreasing the resolution should be soon possible.

### II.1. CNM CMOS technology

The CMOS circuit fabrication is based on CNM ‘in house’ process ([www.cnm.es](http://www.cnm.es)) (described in detail in annex A7.1). This technology includes two polysilicon layers and a single metal level. The minimum feature size of the channel length is limited to 2.5  $\mu\text{m}$ . Two different polysilicon layers are employed for specific functions:

- the so-called *poly0* layer is implemented as a capacitor electrode material
- the so-called *poly1* layer is implemented as transistor gate material

This is not a leading CMOS technology, but it allows a certain degree of flexibility on the process flow; in other words some parameters can be modified. In particular, it has been possible to change the initial deposition parameters of *poly0* in order to improve its crystalline quality so that it may be used as structural layer of the resonator. It has been possible as well to choose its thickness for optimizing the resonator dimensions.

Taking into account the know-how acquired during previous projects, different aspects of the technology regarding the combination with NEMS fabrication have been optimized for reaching a much higher final fabrication yield.

The main modification, that is schemed in Figure 8, has consisted not in changing the process but in modifying the layout of given photolithography masks in order to obtain with high yield viable **integration areas** for posterior integration of nano/micromechanical resonators inside them. Basically, in the new CMOS circuit layout no aperture in the *interlevel oxide* is made on top of the integration areas so that this dielectric layer protects the underlying polysilicon layers during the subsequent metal etching. Indeed, the dry etching of metal is not uniform and from one point of the wafer to another the removal of metal is not realized at the same speed: while in some integration areas some metal still has to be etched, in others the process has already started overetching and damaging the two underlying layers: *poly1* and thin  $\text{SiO}_2$ .

Now, the structuring by dry etching of *interlevel oxide* within all integration areas is made immediately after the etching of the *passivation* layer with the same masking resist (photolithography reticule nº8 named *passivation*): a single mask level allows opening both layers with a prolonged reactive ion etching (RIE). In this way, the *interlevel oxide* protects the integration area during the whole process.

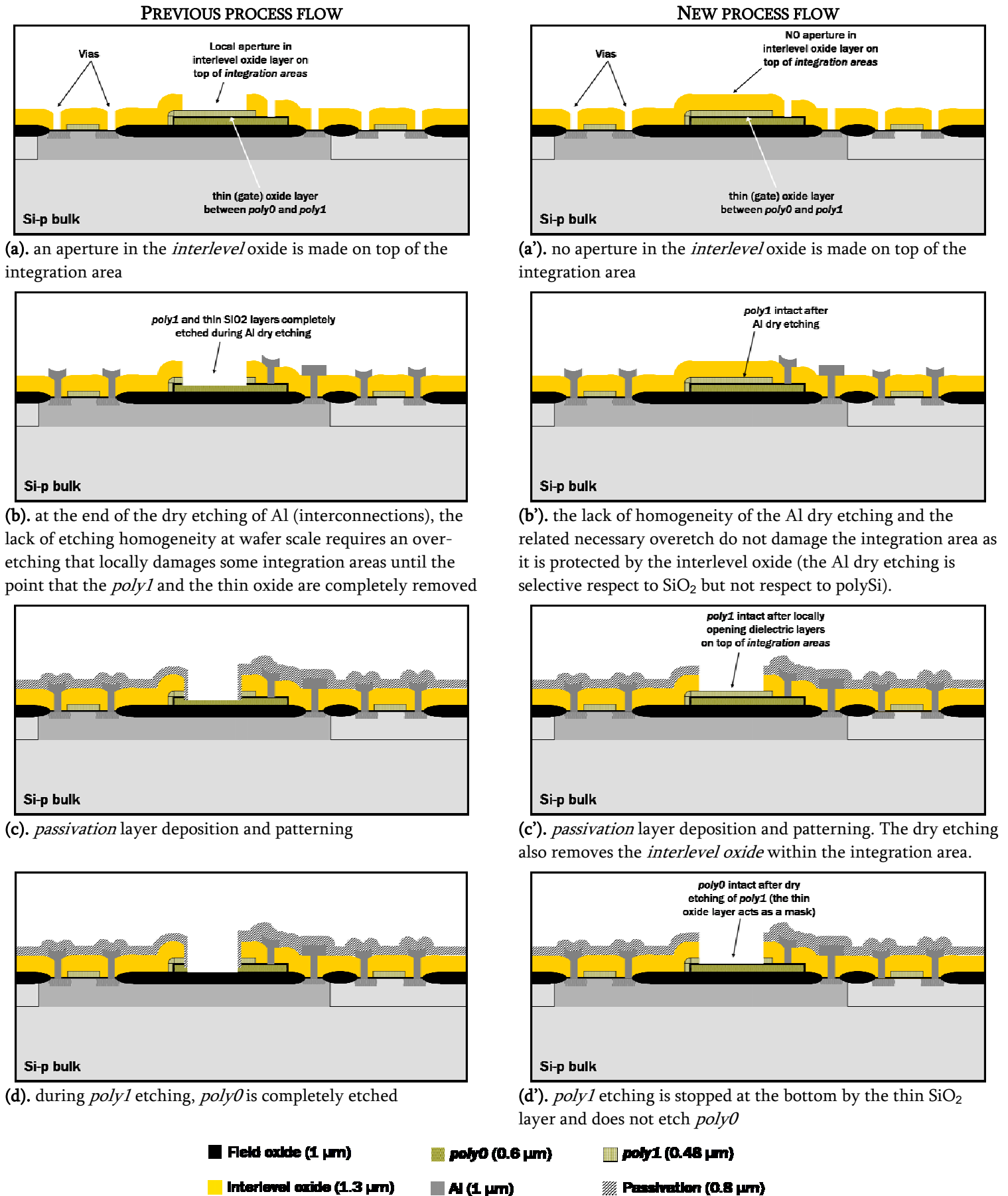


Figure 8. Previously and newly implemented CMOS process (partial) flows for posterior NEMS integration

## II.2. Optimization of nSL process on CMOS: alignment and blurring corrections

Our global fabrication strategy of nanodevices on CMOS is based on using existing CMOS layers as structural layer (600 nm thick polysilicon) and sacrificial layer (1  $\mu\text{m}$  thick field oxide) of the resonators. This strategy simplifies the processing and facilitates the further electrical contact between the nanomechanical devices and the circuits [1, 2]. After concluding CMOS circuits fabrication, integration areas are patterned by evaporation of 80 nm of aluminum using nSL. At this stage, several challenges concerning nSL and its related fabrication process steps were identified at the beginning of the project.

Concerning nSL itself, issues like the alignment between CMOS wafer and nanostencil wafer, clamping uniformity, blurring effect (pattern widening), membrane stability, clogging and cleaning (reusability) have been identified.

In the present work, we have focused on addressing two processing challenges: (i) alignment between CMOS wafer and nanostencil wafer and (ii) elimination of pattern blurring. Indeed, as previously mentioned, a major limitation in nSL is gap-induced pattern blurring naturally occurring if a planar stencil is used in combination with a substrate containing topography (e.g. CMOS). The characterization of this phenomenon has been undertaken and a corrective technique has been implemented. These two issues are detailed in next sections.

Membrane stability was solved by fabricating corrugated membranes (see section I.1.b). Clogging and cleaning issues are still being characterized at EPFL.

Regarding related process steps (prior or posterior to nSL), various dry etchings of either dielectric or polysilicon layers have been optimized in the framework of this thesis. For this purpose, special test wafers with similar topography to CMOS substrates were designed and fabricated. They will be described in section II.2.c.

### II.2.a. Alignment

In order to match the stencil nano/micropatterns with the integration areas contained in the CMOS substrate, full-wafer nanostencil (nS) and CMOS wafer (both 100 mm diameter) must be aligned one to each other before evaporation of metal through nanostencil apertures. An alignment procedure is established that leads at the end to the rigid clamping of both aligned elements into one portable piece that can be placed into the evaporation chamber.

This operation is performed within a bond aligner SÜSS MICROTEC MA/BA6, equipped with two microscopes, for which a special chuck was designed by SÜSS MICROTEC. This chuck responds to several requirements: it can be inserted in the mask aligner and after optical alignment it mechanically clamps rigidly stencil and substrate at three different sites; therefore they can be transported with safety, i.e. without relative motion, to the evaporation chamber and be fixed inside. Moreover, this chuck allows moving one element with respect to the other, which is fixed, while a thin controllable gap (down to 15  $\mu\text{m}$ ) is maintained between both objects, in order to ensure good optical visualization (optical focus can be achieved almost simultaneously).



Figure 9. Custom chuck developed by SÜSS MICROTEC for the purpose of optically aligning a 100 mm nS wafer to a 100 mm substrate and then clamping at 3 points for transportation to the evaporation chamber

Special patterns, called alignment marks (*AM*), were foreseen in both layouts of nS and CMOS substrates in order to allow optical alignment. They have been designed to reach a 1  $\mu\text{m}$  accurate alignment at 100 mm wafer scale. Alignment marks contained in CMOS substrates and used to align one reticule to another during CMOS process were not utilized (moreover, dicing lines area is too reduced). For the purpose of aligning nanostencils to CMOS wafers, specific alignment marks were designed and included inside the chip layout (see Figure 10 and Figure 5). There are two sets of alignment marks per chip: one made of *poly0* (grey circle in Figure 10), another made of *metal* (black circle in Figure 10 with zoom). Both have an identical design, depicted in the zoom of next figure. Taking into account that the vision area is restricted by the limited motion of the two microscopes, eight sets per whole wafer are potentially visible in each objective.

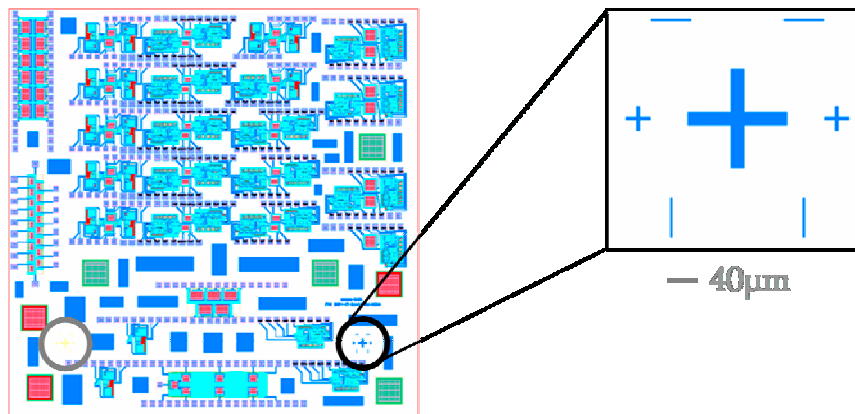


Figure 10. Alignment marks design and positions within the CMOS chip layout.  
Grey circle: *AM* made of *poly0*; Black circle and related zoom: *metal AM*.

The alignment marks included in the nanostencil layout have a complementary design for an enhanced alignment. Figure 11 contains two optical images taken during the alignment procedure within the mask aligner when both elements are being aligned and are still separated by a thin controllable gap that is small enough to ensure simultaneous visualization of membrane and substrates. The alignment marks of CMOS substrate can be observed through nanostencil apertures.

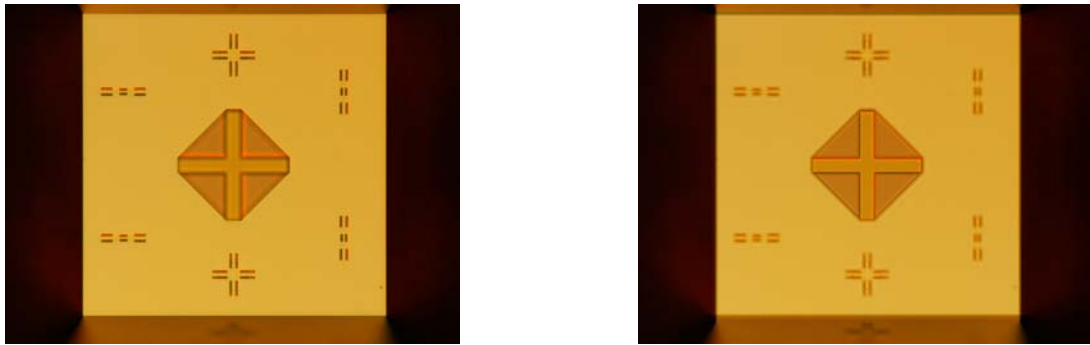


Figure 11. Optical image of a SiN membrane (in yellow) accessed by KOH wet etching through the Si frame (in black). Underneath *AM* of CMOS substrate are visible through the membrane apertures. Left image: focus on the membrane. Right image: focus on the CMOS substrate.

The experimental results of this procedure in terms of implementation and accuracy are detailed in section **Erreur ! Source du renvoi introuvable.**

Once stencil and substrate are aligned, the chuck clamps one element to the other without lateral displacement and with a sufficient pressure that impedes any misalignment during transportation of the piece and its fixing into the evaporation chamber.

### II.2.b. Blurring of Al patterns deposited by nSL

In our process, the patterns deposited by nSL serve as etch mask for pattern transfer to the polysilicon structural layer by reactive ion etching (RIE). In this context, aluminum (Al) has been chosen as pattern material for two reasons. First, its RIE selectivity with respect to silicon and silicon oxide is very high even for very thin Al layers; second, due to its specific properties in terms of blurring compared to other materials like Cu.

Hereafter, the characteristics of the blurring behavior of Al deposits is detailed.

#### CHARACTERISTICS OF BLURRING EFFECT [31]

When a nanostencil and a wafer are put in contact, the gap between nanostencil membranes and substrate areas to be patterned varies from 0 to several microns depending on substrate curvature and topography. Disregarding surface migration considerations, a non-zero gap generates a blurring of the resulting pattern by a geometrical dispersive effect schemed on Figure 12:

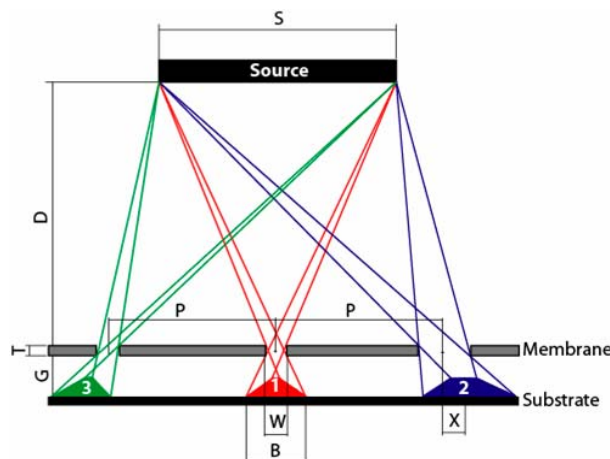


Figure 12 [5]. Metal flux scheme during evaporation of a metal patterned by nanostencil lithography

- $D = 100$  cm is the source-stencil distance
- $S = 2$  cm is the source diameter
- $T = 200$  nm is the stencil thickness
- $G$  is the gap stencil-substrate.  $G$  is nominally around  $3.1 \mu\text{m}$  high: the maximum height between the bottom of an ‘integration area’ (i.e. deposition area, *poly*/gate oxide stack) and the top of the substrate on which the nS membrane leans on, is equivalent to an interlevel oxide/metal/passivation stack ( $1.3 + 1 + 0.8 \mu\text{m}$  high in total). This can be measured with a profilometer. After clamping the nanostencil wafer to the CMOS substrate,  $G$  may be locally larger because of the eventual inclusion of particles and because of wafer tolerances (e.g. wafer curvature).
- $W$  is the stencil aperture size
- $B$  is the resulting pattern size on the substrate
- $P$  is the distance from central apertures to lateral apertures (in our case 5 cm is a maximum since we use 100 mm wafers)
- $X$  is the displacement of the deposited structure

The blurring extension on each side can be quantified by equation (IV.1) [28]:

$$\Delta W = \frac{B - W}{2} \approx \frac{1}{2} \frac{S * G}{D} \quad (\text{IV.1})$$

This extension is proportional to the gap. With the aim of recovering nominal dimensions, the correction of this loss of resolution has been the purpose of the work exposed in this section. As an example, a gap value of  $G = 10 \mu\text{m}$  results in a 100 nm blurring extension  $\Delta W$ .

All experiments were made with a deposition system with long source-target distance (1 m). This provides two advantages: blurring is reduced [refer to eq.(IV.1), as  $D$  increases] and lateral offsets ( $X$  value) can be neglected since  $D$  is much bigger than any other dimension.

In initial experiments, several Si wafers were patterned with  $\text{SiO}_2$  pillars (on which stencils lean on), whose thickness varies in the 1-10  $\mu\text{m}$  range from one wafer to another.

Subsequent experimental tests with predefined gaps show a resulting pattern that is a combination of:

- a well-defined *main pattern* whose flanks are abrupt (see Figure 13) and which size can be determined by eq. (IV.1).
- a surrounding thin metal layer or halo caused by surface migration, whose extension is material dependent.

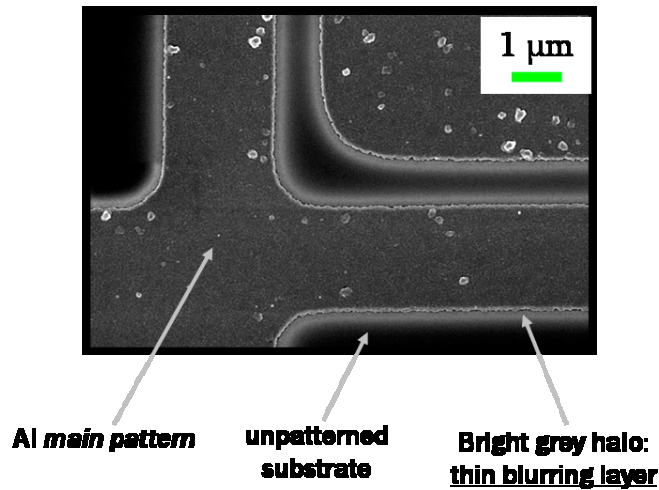


Figure 13. Scanning Electron Microscope (SEM) image of a main pattern with well defined contours and surrounding halo

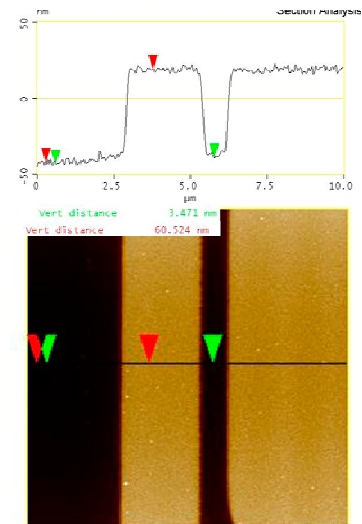


Figure 14. Atomic Force Microscope (AFM) picture: pattern profile with abrupt flanks

The thin Al halo is less than 5 nm thick, i.e. much thinner than the *main pattern* thickness (more than 50 nm). However, it is strong enough to sustain subsequent reactive ion etchings of SiO<sub>2</sub> and Si. This fact represents a major problem when a pattern contains features like small gaps because a proper trench formation is impeded (see Figure 15).

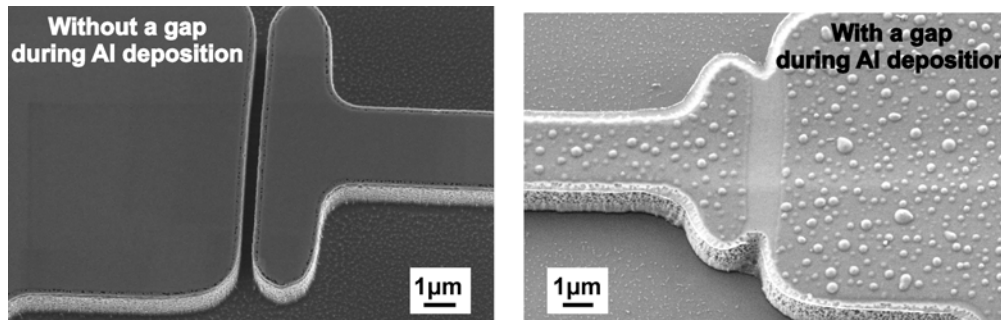


Figure 15. SEM pictures of nanostencil-deposited Al patterns transferred by RIE to silicon.

The *main pattern* exhibits several characteristics. First, we confirm that its thickness corresponds to the nominal deposited thickness (in our case from 50 nm up to 80 nm). Second, it has well-defined contours with abrupt flanks surrounded by a thin layer (a halo). This is a very relevant point that differs much from other materials, like Cu, that exhibit a progressive profile [5] in which there is no clear distinction between the blurring and the *main pattern*. Third, a good correspondence has been observed between its dimensions and the stencil aperture size: if the halo extension is disregarded, its dimensions are in agreement with eq.(IV.1).

As an additional remark, it is important to emphasize the major influence of the nanostencil structure on the blurring extension and its profile. All the previous observations are valid for lithography steps carried out with clean unstabilized nanostencils or stabilized nanostencils (with corrugated membranes) that do not deflect when material is deposited on them [33]. On the contrary, reused (already metal-coated) unstabilized stencils bend and therefore another model is required. In this case, the membrane progressively deflects locally around the apertures during

metal deposition because of an increasing stress (depending on the aperture shape, it is more or less sensitive). This means that the membrane aperture size and the gap are constantly increasing and varying, and consequently the pattern profile will be different.

CORRECTIVE ETCHING PRINCIPLE AND PROCESS DETAILS [31]

To overcome the loss of nominal dimensions due to blurring effect, in particular for the case of patterns with small gaps (i.e. trench definition), a corrective etching has been developed to recover nominal pattern dimensions. We have found that by performing a uniform controlled etching of a few nanometers of the deposited layer, its thickness is uniformly decreased all over the sample. Then, the characteristic thin blurring layer is eliminated (see Figure 16) because the blurring layer is much thinner than the *main pattern*.

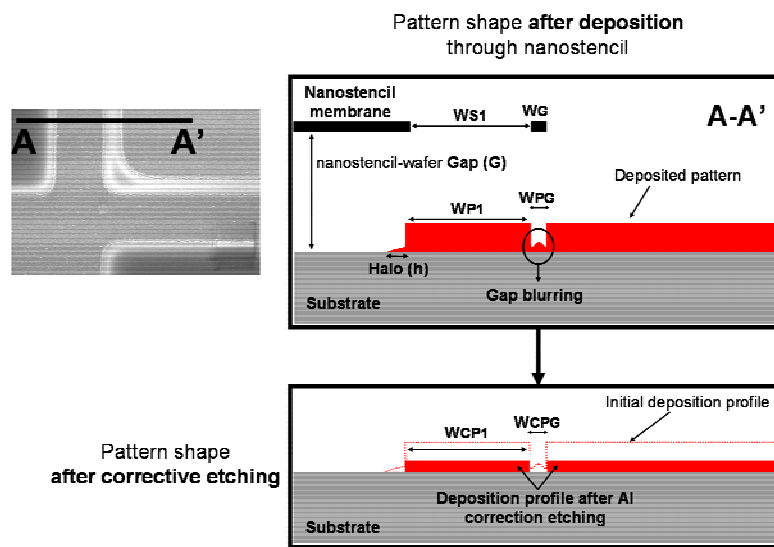


Figure 16. Sequential scheme for blurring correction

Two processes of controlled dry etching of Al were successfully developed: one recipe has been adapted to QUAD DRYTEK systems (LAM RESEARCH CORP., Fremont, CA) (anti-blurring recipe n°1, *ABI*), in order to be applied at CNM. The other has been adapted to STS MULTIPLEX ICP systems (*AB2*) in order to be applied at EPFL. Some initial unsuccessful tests of wet etching made us turn to dry etching processes for reasons of uniformity, repeatability and controllability.

Initial experiments were performed on chip-sized samples (silicon substrate with 100 nm thick thermal oxide grown on top) on which 70 nm thick Al patterns were deposited by nSL. Chip-sized nanostencils were used for testing in the QUAD DRYTEK system and therefore the *ABI* recipe was optimized for chip-sized samples (a recipe for whole wafer would also be feasible on this equipment). A special carrier wafer with equal Al/resist distribution is required to ensure etching uniformity over the chip. *ABI* is based on two steps: first, the thin native Al oxide layer ( $Al_2O_3$ ) [38], which is resistant to many wet etchers, is removed under the following conditions:  $BCl_3$  flow of 50 sccm, chamber pressure 325 mT, radio frequency (RF) power 125 W, chamber temperature 55°C. Then, chlorine chemistry is used to etch the precleaned thin Al layer. Assuming a 25 nm thick Al etching as a minimal target, we use a mixture of  $Cl_2$  (as Al etcher):

$\text{BCl}_3$  (to reduce the etch rate by neutralizing  $\text{H}_2\text{O}$ ):  $\text{N}_2$  (for better uniformity and low etch rate) with respective flows of 3:12:80 sccm (rest of conditions: 325 mTorr, 125 W, 55°C). The resulting etch rate is approximately 100 nm/min.

In the STS MULTIPLEX system (Inductive Coupling Plasma), a recipe (*AB2*) was specifically tuned for wafer-sized samples. Due to different characteristics between both systems, another type of recipe was optimized, based on a single step of  $\text{BCl}_3$  with a 10 sccm flow at 3 mTorr. Plate power and RF power are respectively 30 W and 600 W. Just like in the recipe for QUAD DRYTEK systems,  $\text{BCl}_3$  first removes native Al oxide but then its own action does not require any additional gas to etch Al itself. With this configuration, a sufficiently low etch rate around 100 nm/min is obtained and *AB2* provides excellent reproducibility and uniformity at wafer scale.

Using any of these recipes, the pattern widening is corrected as illustrated in the SEM images of Figure 17.

On left images, the bright halo surrounding the Al *main pattern* corresponds to the blurring. In the top row, blurring was not corrected and consequently trench definition is failed after RIE of silicon. In the second (chip-sized samples with a well-known step and corrected with *ABI*) and third row (whole 100 mm CMOS wafer corrected with *AB2*), a successful implementation of the recipes is demonstrated. In both kinds of samples, the bright halo disappears after the corrective etching of Al, and therefore a trench is successfully fabricated after the subsequent RIE of Si.

In Table IV - 2, we summarize the evolution of the pattern dimensions along the process sequence (in annex A7.4, more data are provided on pattern transfer and blurring extension): from the initial aperture size into the nanostencil until the final dimension of the pattern after the corrective etching. Deviation of final pattern dimensions with respect to the dimensions in the stencil is less than 10% in most of the cases. A perfect uniformity of the etching is verified at chip and wafer level.

Device location		Dimensions in stencil (nm)	Dimensions on patterned sample (nm)			
			Deposited pattern	Blurring (2- <i>h</i> )	Corrected pattern	Blurring (2- <i>h</i> )
Location 1	Beam	310 ( <i>WSI</i> )	236 ( <i>WPI</i> )	280	267 ( <i>WCPI</i> )	0
	Space between two patterns	775 ( <i>WG</i> )	856 ( <i>WPG</i> )	Unformed trench	813 ( <i>WCPG</i> )	Opened trench
Location 2	Beam	295 ( <i>WSI</i> )	291 ( <i>WPI</i> )	500	323 ( <i>WCPI</i> )	0
	Space between two patterns	750 ( <i>WG</i> )	788 ( <i>WPG</i> )	Unformed trench	769 ( <i>WCPG</i> )	Opened trench

**Table IV - 2. Patterns transfer data: patterns dimensions evolution along the process sequence. Refer to Figure 16 for the meaning of each dimension. Locations 1 and 2 are two different locations separated by several centimeters over a 100 mm wafer.**

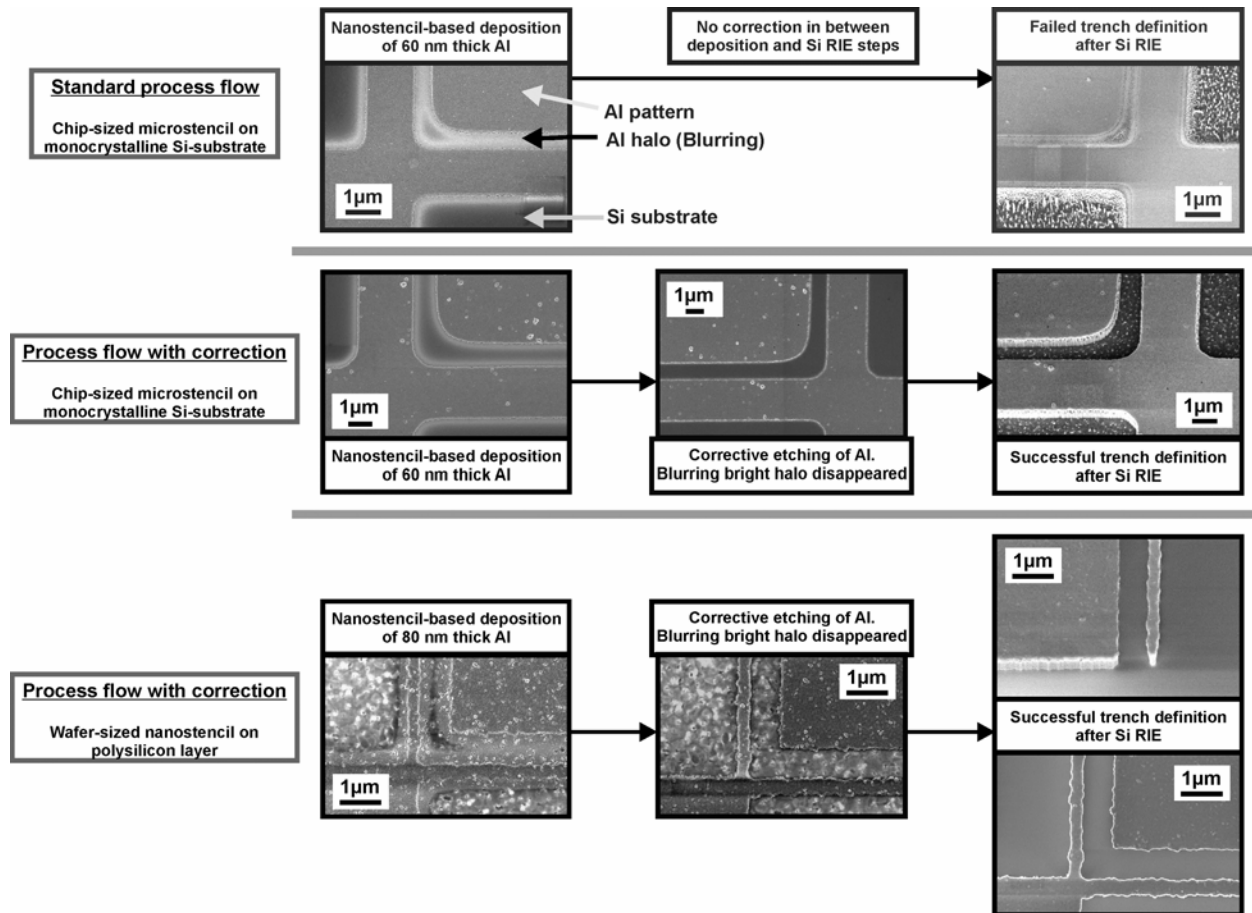


Figure 17. Visual comparison without/with blurring correction

II.2.c. Dummy wafers

It was not cost-effective to optimize the entire post-processing technology using CMOS wafers. This is why two kinds of dummy wafers were designed and fabricated in order to make various types of test: some for testing the successive post-processing steps, some others for the study and the correction of nSL related issues, like alignment or blurring.

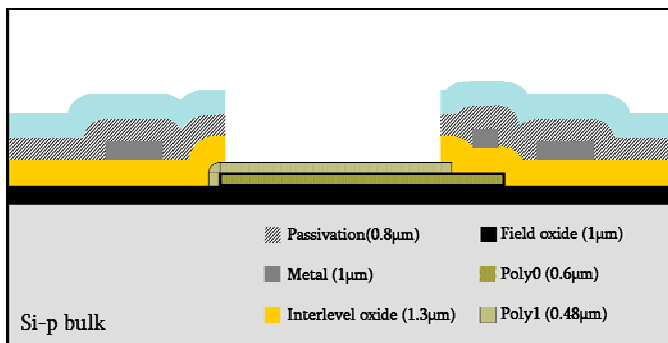
DUMMY WAFERS OF TYPE 1 (“DUMMIES 1”)

Their function is to help adjusting recipes of various dry etchings:

- dry etching in one step of two layers: *passivation* + *interlevel oxide*.  
This etch makes an aperture in those materials in order to give access to nanodevices integration areas.
- dry etching to remove *poly1* layer (that protects the structural layer *poly0*)
- dry etching to remove the *gate oxide* separating *poly1* and *poly0*, with Al patterns as etch masks (deposited by nSL).
- dry etching of *poly0* layer (resonators structural layer), also with Al patterns as etch masks.

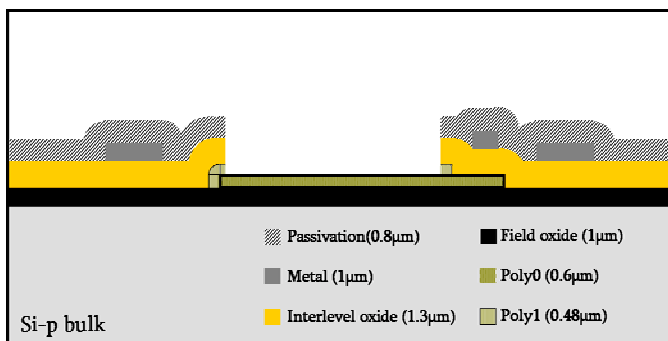
Moreover, they should help testing the alignment between CMOS and nanostencil wafers. In parallel, the blurring that will affect the CMOS wafers can initially be precisely estimated (because CMOS and dummy wafers have an identical topography so that their nanostencil-wafer gap is comparable). The fabrication process of dummies 1 in detailed in annex A7.2

LIST OF TESTS MADE WITH DUMMIES 1: their structural composition and their topography allow performing a series of optimization tests detailed hereafter:

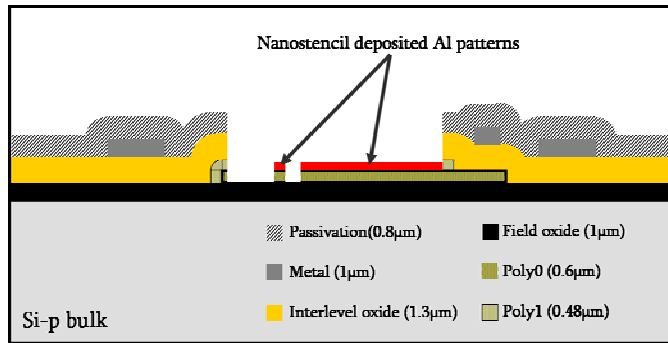


**Test n°1:** Successive dry etchings of *passivation* and *interlevel oxide* layers.

- photoresist as an etch mask
- succession of two recipes for both layers ( $\text{Si}_3\text{N}_4$  oriented, then  $\text{SiO}_2$  oriented recipes). Selectivity  $\text{SiO}_2/\text{Si}$  required.

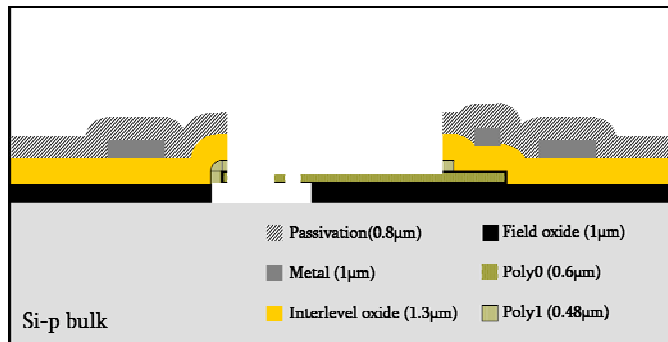


**Test n°2:** Dry etching of *poly1* with *passivation* and *interlevel oxide* layers as etch mask (no photoresist during this etch, selectivity  $\text{Si}/\text{SiO}_2$  required)



**Test n°3:** Dry etching of *gate oxide* with Al patterns deposited by nSL as etch mask. Selectivity SiO<sub>2</sub>/Si required.

**Test n°4:** Dry etching of *poly0* with Al patterns deposited by nSL as same etch mask. Selectivity Si/dielectrics required.



**Test n°5:** Development of the release process of wide and narrow nano/micromechanical resonators (etch time more or less long).

#### DUMMY WAFERS OF TYPE 2 (“DUMMIES 2”)

Their function is to study the blurring extension ( $\Delta W$ , see Figure 12) as a function of a known gap. For this purpose, SiO<sub>2</sub> steps of several well-controlled heights are made. By measuring  $\Delta W$  at several sites of the wafers (center, borders), information on clamping uniformity will be extracted as well. Their fabrication process in detailed in annex A7.2.

### II.3. Post-processing of pre-fabricated CMOS wafers based on nSL

Hereafter, we present a detailed description of the process flow that leads to the complete fabrication of nano/micromechanical resonators on CMOS. Our approach consists in post-processing prefabricated standard CMOS wafers using nanostencil lithography (nSL) as nanopatterning technique of the nanodevices.

#### II.3.a. *poly1* removal

After CMOS fabrication is completed, pads and integration areas are the single zones in which the passivation layer is opened. To access the structural layer (*poly0*), it is necessary to remove entirely the 480 nm thick *poly1* layer until arriving to the 70 nm thick thin oxide grown on *poly0*. (*poly1* had a function of protecting *poly0* during CMOS fabrication).

The removal is achieved by performing a RIE of *poly1* that must combine high selectivity with respect to Al (contact pads must not be damaged) and to dielectrics (SiO<sub>2</sub> and SiN, the passivation must not be damaged while the underlying thin oxide must remain intact, otherwise *poly0* may start to be etched). The uniformity at wafer scale is another key feature of the recipe.

For an easier detection of the etching end point, several extended test zones (400\*400 μm<sup>2</sup>) were included in the chip layout. They have such a profile: bulk silicon + gate oxide (70 nm) + *poly1* (480 nm). Their big size allows utilizing an ellipsometric technique, based on a large laser spot, that monitors the etching by measuring the remaining *poly1* thickness.

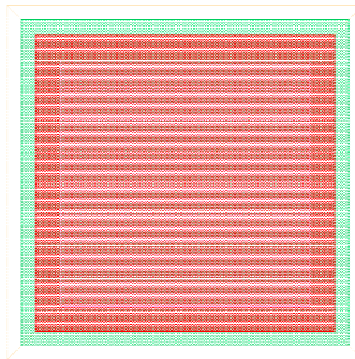


**Figure 18.** Layout of the test structure of *poly1* etching (400\*400 μm<sup>2</sup>)  
[green: bulk Si area; red: *poly1* area; violet: aperture in passivation]

#### PROCESS DETAILS:

System: ICP Alcatel A601E (recipe *Nano1 cont*) at CNM. The recipe is continuous and all gases are injected simultaneously.

t: 1min 20s

C<sub>4</sub>F<sub>8</sub>: 45 sccm

SF<sub>6</sub>: 35 sccm

Pressure: 2.10<sup>-2</sup> mbar

ICP Power: 1000 W

Plate power: 5 W

II.3.b. Alignment

It was performed at EPFL on a SÜSS MICROTEC MA/BA6 (mask aligner/bond aligner) system with a modified custom chuck developed by the same company in the framework of NaPa..

GENERAL ISSUES ALIGNMENT STENCIL TO CMOS

The microscope for topside alignment can be used in Bond Aligner-mode. In our experiments we have lowered the alignment gap to 20  $\mu\text{m}$  (15  $\mu\text{m}$  alignment gap shows a mechanical friction between stencil and substrate). The topography of the CMOS and the tolerances in the thickness and curvature of both stencil and substrate may make it difficult to align due to the depth of focus of the objectives.

ALIGNMENT RESULTS

Two CMOS substrates (CMOS11 and CMOS14) and one stencil (ST2-2182) were used for alignment experiments in which the misalignment was measured and analyzed based on Al patterns deposited by nSL. For both CMOS wafers, the obtained results were very similar. Therefore, we only present the results of CMOS wafer n°11.

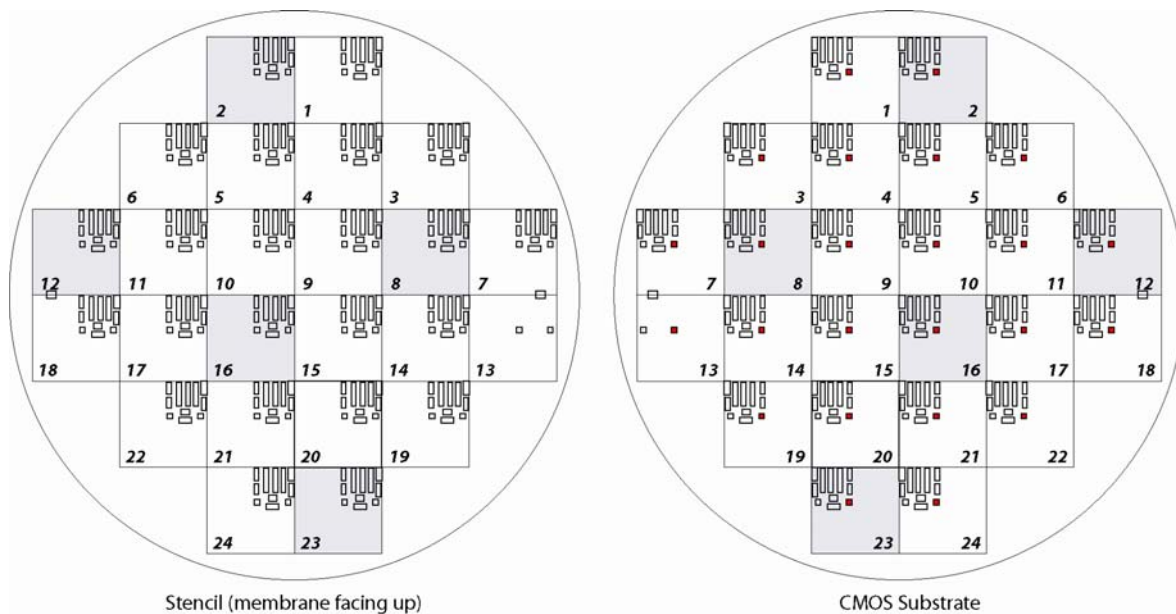


**Figure 19. Stencil and CMOS design showing exposure fields and structure areas. The alignment markers in the 24 chips were measured.**

In order to measure the misalignment between stencil and CMOS, the alignment marks on the stencil are considered accurate since they were patterned by DUV with a precision of 20 nm (ASML specifications). On the opposite, we have observed a scaling error between each CMOS chips, materialized by a linear increase of misalignment within a row or a column of chips..

The measurements of all 24 chips were performed on an optical microscope. Several of those fields were measured using a SEM. SEM measurements showed that optical microscope measurements are sufficiently accurate.

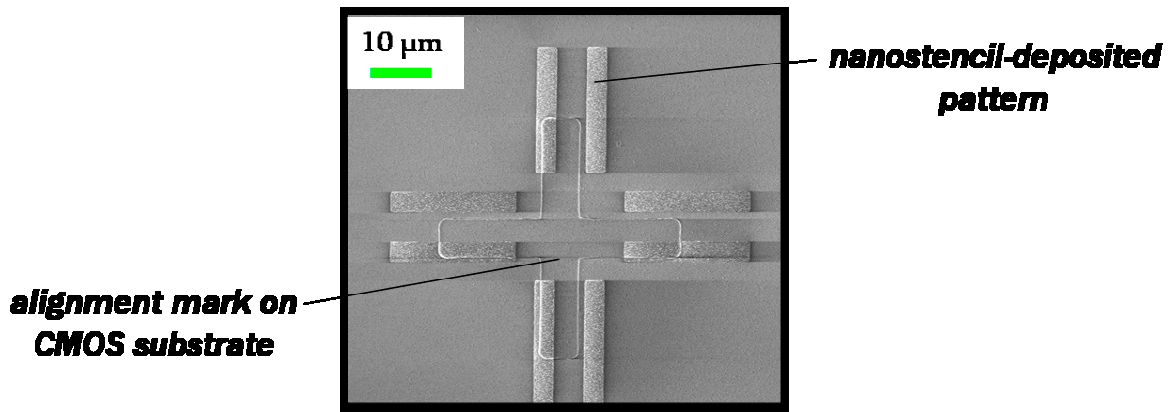


Figure 20. Example of an alignment mark used in stencil alignment. The cross marker is present on the CMOS substrate. The 8 lines are Al patterns deposited by nSL.

RESULTS OF ALIGNMENT OF ST2-2182 TO CMOS11

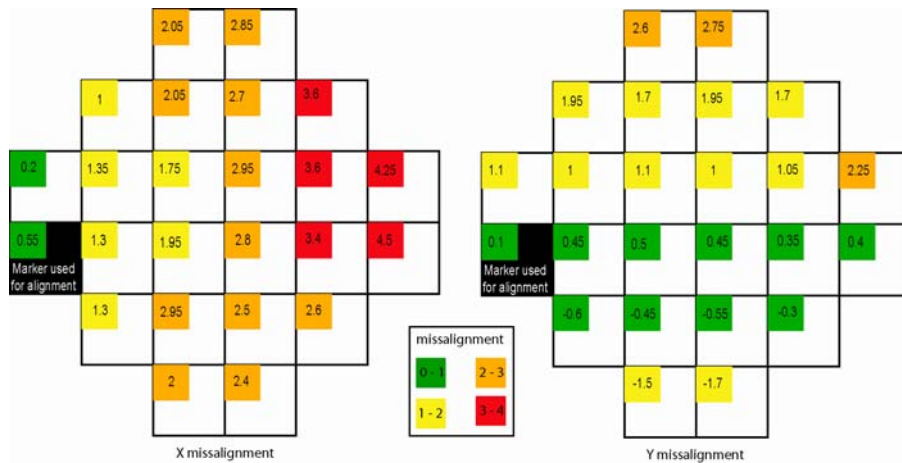


Figure 21. Misalignment results (in microns), measured with an optical microscope. The black field was used to align both X and Y, taken as a reference. The image shows an increase in misalignment radiating from the initial alignment marks.

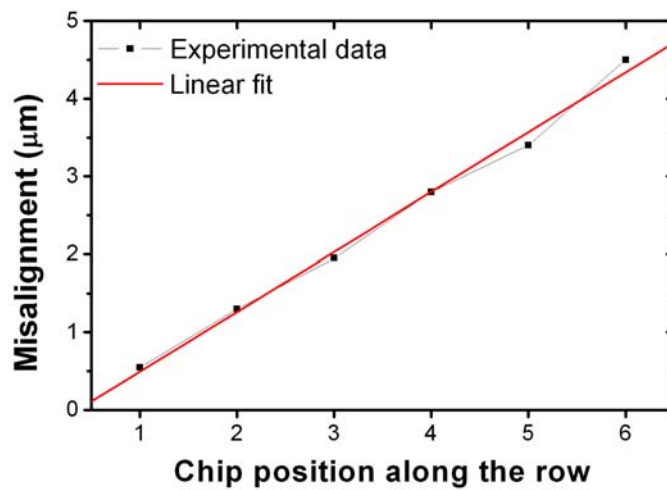


Figure 22. Graph showing a linear increase in misalignment in x direction for chips 13 through 18 (see Figure 19), second row.

From the linear fit of Figure 22 and the observed very linear trend of misalignment error measured along a row of chip (the same was observed along any other row and any column), we estimate around 0.8  $\mu\text{m}$  per chip the scaling error of CNM UV stepper. Further experiments for compensating this error are planned to be performed.

OVERALL ALIGNMENT RESULTS

Both alignments were successful and considering only the reference chip used for the first alignment, an accuracy below 1  $\mu\text{m}$  is obtained:

- for the first wafer, the misalignment was  $\Delta X=0.55 \mu\text{m}$  and  $\Delta Y=0.1 \mu\text{m}$  at the alignment site
- for the second wafer, the misalignment was  $\Delta X=0.1 \mu\text{m}$  and  $\Delta Y=-0.85 \mu\text{m}$  at the alignment site

These alignment results were achieved after evaporation what means that the alignment stays within the tolerance targets during transportation and fixing of the chuck inside the evaporator.

**II.3.c. Al deposition**

The stencil-substrate chuck must be transported to the deposition system (LEYBOLD-OPTICS LAB 600H at EPFL) for performing a deposition of Al through the apertures of the full-wafer nanostencil. The technique employed is electron beam evaporation. Around  $10^{-7}$  mbar, the Al crucible is bombarded by a high energy electron beam proceeding from a heated tungsten filament. Only the surface of the crucible is melt and evaporates; for this reason no cross contamination from the walls is generated and high purity Al is deposited. The high source-substrate distance (1 m) of the chamber contributed to minimize dispersive effects that lead to pattern widening [see eq.(IV.1)].

A 90 nm thick Al layer has been deposited on each wafer. The deposited thickness has been measured by in-situ quartz-crystal microbalances and subsequently by a mechanical profilometer indicating 80-85 nm.

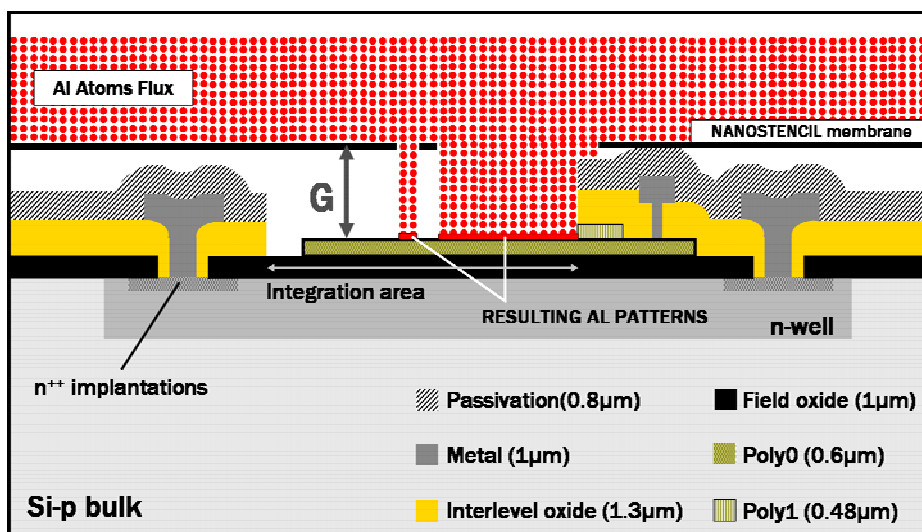


Figure 23. Al deposition through nanostencil onto a CMOS wafer

### II.3.d. Blurring correction

As explained in section II.2.b, because of the so-called *blurring effect*, Al patterns deposited by nSL are inherently more or less distorted and widened, with respect to the nominal dimensions defined by the dimensions of stencil apertures. They need to be corrected for improving their definition. This “correction” is based on a dry etching that uniformly decreases at wafer scale the thickness of the Al patterns and therefore removes the halo caused by the *blurring effect*. Hereafter are given the process details of the etching performed at EPFL.

#### PROCESS DETAILS OF AL ETCH:

System: ICP STS Multiplex (recipe *Al-slow*)  
 t: 20 s  
 BCl<sub>3</sub>: 10sccm  
 Pressure: 3 mTorr  
 ICP Power: 600 W  
 Plate power: 30 W  
 Nominal etching speed: 100 nm/min at RT

### II.3.e. Pattern transfer and release

As aforementioned, the Al patterns were deposited onto a thin oxide (70 nm) that initially separated *poly0* from *poly1*. Once deposition and correction are completed, the Al patterns must be transferred first to the thin oxide (70 nm thick) and second to *poly0* (600 nm thick). At this step, the polysilicon nanomechanical devices get their 3D shape. Hereafter are given the details of the two successive etching steps performed at EPFL.

#### PATTERN TRANSFER (TWO ETCHINGS) WITH CORRECTED AL MASK

##### (1) RIE OF THE THIN SiO<sub>2</sub> (70 NM THICK)

System: AMS 200 Adixen (recipe SiO<sub>2</sub> PR 1:1)  
 t: 25 s  
 C<sub>4</sub>F<sub>8</sub>: 15 sccm  
 Pressure: 8.10<sup>-3</sup> mbar  
 ICP Power: 1800 W  
 Plate power: 120 W (about 100V)  
 Nominal etching speed: 280 nm/min at RT

##### (2) RIE OF POLY0

System: AMS 200 Adixen (recipe Si opto)  
 t: 50 s  
 C<sub>4</sub>F<sub>8</sub>: 40 sccm  
 SF<sub>6</sub>: 50 sccm  
 Pressure: 3.10<sup>-2</sup> mbar  
 ICP Power: 1500 W  
 Plate power: 15 W  
 Nominal etching speed: 1200 nm/min at RT

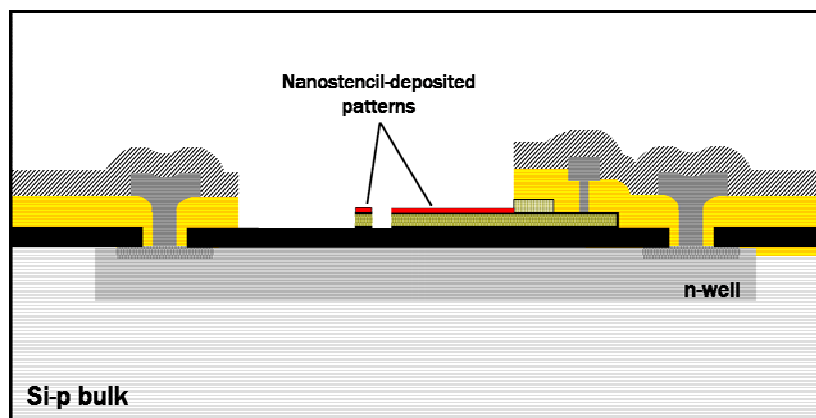


Figure 24. Pattern transfer to SiO<sub>2</sub> and polySi by successive RIE with corrected Al patterns as a mask

### WAFER DICING (PERFORMED AT CNM)

The wafers are diced into individual chips at this step of the process (before resonators release) because already released mechanical devices would be more susceptible to break during dicing. A standard photoresist is roughly coated over the wafer with a paintbrush before dicing. This operation protects the wafer surface from the particles arising from dicing (then the resist is simply removed in acetone).

### RELEASE PROCESS OF NANO/MICROMECHANICAL RESONATORS (PERFORMED AT CNM)

The last main step consists in releasing the nanomechanical devices relying on a photolithography process that makes apertures in the photoresist only around the resonators so that the rest of the chip (i.e. CMOS circuitry) remains protected. The apertures have a rectangular shape and are centered on each resonator. Their dimensions depend on each resonator: a minimum 10  $\mu\text{m}$  distance between every point of the resonator and the aperture border has been respected.

We have developed two different processes for the subsequent local wet etching (see Figure 25) according to the size of resonator. Both alternatives have demonstrated reproducibility and reliable release. It must be noticed that the wet etching step has two functions: (i) it releases the resonators and (ii) it removes the remaining layers, Al mask and thin gate oxide, that lean on the polysilicon structural layer.

For narrow devices (width in the micron/submicron range), like in-plane vibrating cantilevers, short etching times are sufficient and the resist withstands the aggressiveness of the solution.

### RELEASE PROCESS OF CANTILEVER (SHORT RELEASE ETCHING TIMES)

- **Step 1.** Standard photoresist (HPIR 6512) patterning  
Dehydration. 1h at 200°C  
Spinner. 3500 rpm, 1500 rpm/s, 45s  
Soft-bake. 15 min at 100°C  
Exposure: hard-contact, 15 s  
Development: 30s + rinsing in water  
Hard bake: 20 min at 100°C, ramp until 175°C, then 30 min at 175°C then soft descent until room temperature (~30 min)
- **Step 2.** Release wet etching  
SiOetch: 4 min (for 300 nm wide devices)  
Drying with a critical point dryer to avoid sticking
- **Step 3.** Resist stripping  
Resist stripping based on O<sub>2</sub> plasma in a TEPLA machine.

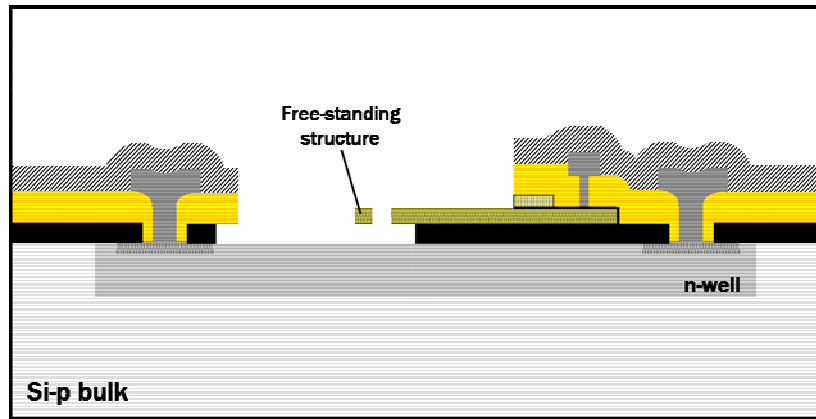


Figure 25. Released nanocantilever after photolithography and wet etching in BHF

For larger devices (width in the order of several microns), like quad-beams, long etching times are required but after a certain time the resist does not withstand anymore and strips.

Consequently, we use an alternative process whereby we first coat and pattern (with standard UV lithography) a SU8 layer (acting as negative resist) on top of the CMOS substrate. SU8 is very resistant to solutions based on HF. Then, to make this process even more reliable, we coat on top of this structured SU8 layer a standard photoresist and follow the same procedure as for cantilevers: as a consequence, the CMOS chip has a double protection during the HF etching.

#### RELEASE PROCESS OF QUAD-BEAMS RESONATORS (LONG RELEASE ETCHING TIMES)

- **Step 1.** SU8 deposition and patterning  
 Cleaning in acetone, IPA and water  
 Dehydration. 1h at 200°C  
 Spinner. 3000 rpm, 1500 rpm/s, 30s (to obtain a ~ 5µm thick SU8 layer)  
 Soft-bake. ramp from 65°C until 95°C, then 10 min at 95°C  
 Exposure: soft-contact, 12s  
 Post-exposure bake: ramp from 65°C until 95°C, then 20min at 95°C  
 Development: 1 day after, 6 min + IPA.
- **Step 2.** Standard photoresist (HPIR 6512) patterning on top of SU8  
 identical to step 1 for cantilevers
- **Step 3.** Release wet etching  
 Objective: wet etch locally, in a controllable way, the sacrificial field oxide layer in order to release the mechanical structures  
 Etchant: “SE34” solution. HF49% : NH4F [buffered] : CH3COOH [weak acid] (1:10:5 in volume)  
 Etching velocity: ~ 5 µm/hour. This value tends to decrease with time.
  - SE34 20 min + annealing 30 min 125-130°C + SE34 20 min (for 6.2 µm wide devices)
  - Drying with a critical point dryer to avoid sticking
- **Step 4.** Resists stripping  
 Resist stripping based on O<sub>2</sub> plasma in a TEPLA machine.  
 SU8 is partially stripped although the standard photoresist is completely removed

### II.3.f. Test of CMOS compatibility of nSL

After successfully demonstrating the potential of a CMOS post-processing technology based on nSL, it has been analyzed at CNM if specific processes related to nSL (evaporation and blurring correction) could eventually modify the performance of CMOS circuitry. It has been proven that electron beam lithography (EBL) degrades CMOS transistors performance [35] for acceleration voltages superior to 15 keV: in particular, threshold voltage and transconductance properties seem to be affected. In this context, it was important to demonstrate that nSL, beyond its great interest in terms of technology (clean, parallel, high-resolution, etc...), is a safe tool for CMOS circuitry post-processing in the sense that it does not modify its performance.

To carry out a comparison of the performances before and after CMOS post-processing, a simple CMOS-based voltage amplifier was electrically characterized: its static and dynamic response did not exhibit any relevant evolution.

In parallel, characteristic parameters of CNM CMOS technology, such as transistor threshold voltage, leakage current, square and contact resistances have been measured by means of specifically designed test structures: no substantial changes have been observed after post-processing, as it is shown in Figure 26:

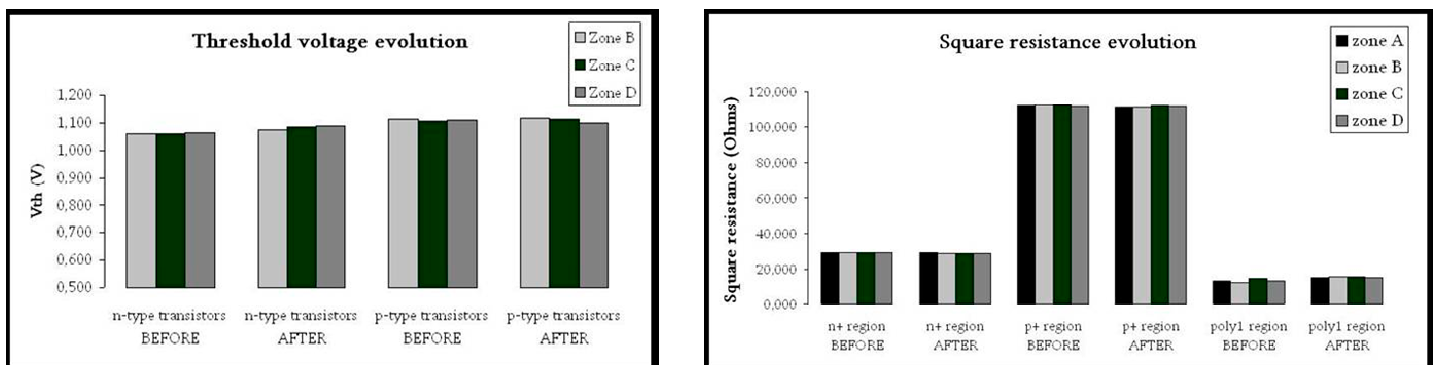


**Figure 26. Evolution of characteristic parameters before and after the entire nanostencil process (Al evaporation and subsequent corrective dry etching): measurements of threshold voltage (left) and square resistance (right) of MOS transistors (test structures)**

We have not found any relevant difference in the electrical performance of the circuits before and after nSL, neither for the test circuits located far from the integration areas nor for the readout circuits located besides the integration areas and connected to them. This means that any spatial proximity between nanomechanical device patterned by nSL and CMOS circuitry has no incidence on its performance and therefore a high density of integration is affordable with this nanopatterning technique.

FINAL RESULTS OF POST-PROCESSING

Full-wafer nanostencil lithography (nSL) has been applied to define 200 nm scale Si nanomechanical devices (resonators) monolithically integrated into CMOS circuits, using one single metal evaporation (nSL step), pattern transfer to Si by RIE and subsequent release etch of the sacrificial layer. In this way, we have achieved the simultaneous nanopatterning of ~2000 nanodevices on entire 100 mm pre-patterned standard CMOS substrates (see Figure 27). In each wafer (in total three wafers were patterned), there are 24 CMOS/NEMS chips (7.5\*7.5 mm<sup>2</sup>) containing each one 78 resonators.

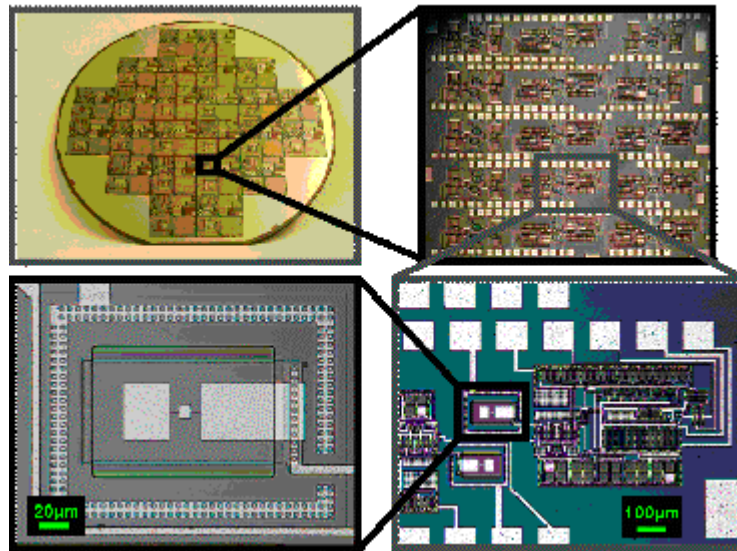


Figure 27. Full CMOS wafer (100 mm) with ~2000 nanomechanical resonators patterned by nanostencil lithography and monolithically integrated with CMOS readout circuits.

Several types of NEMS resonators fully integrated with readout CMOS circuitry were fabricated (see Figure 28): cantilevers, quad-beams and paddles.

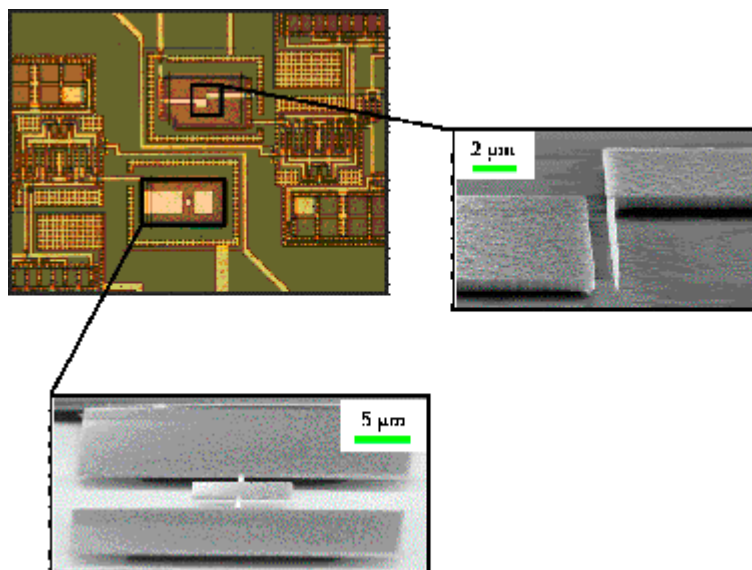


Figure 28. Examples of two types of 600 nm thick polysilicon resonators integrated with CMOS circuitry. A cantilever beam is depicted on the right: it has a width of 200 nm and the gap separating from its electrode is 800 nm wide. It is 14 μm long and 600 nm thick. The bottom resonator is a torsional paddle.

### III. Fabrication of nano/micromechanical resonators on CMOS by electron-beam lithography (eBL)

The approach we have followed to fabricate nanodevices on pre-fabricated standard CMOS wafers by eBL is absolutely similar to the nSL based process: it differs only about the lithography technique. This process can be entirely performed in CNM clean room.

Compared to nanostencil lithography eBL is slow and serial. However the development of such a technology is a great opportunity to be able to fabricate in-house new prototypes within a short timeframe. The lithography step is performed with a relatively low voltage in order not to degrade the performance of the circuitry.

All the process details of the entire post-processing based on eBL are given in annex A7.3.

## Conclusion of chapter 4

The potential of nanostencil lithography as a parallel, straightforward and CMOS compatible patterning technique to define devices on CMOS at the 200 nm scale has been demonstrated. Further decreasing the resolution below 50 nm is on progress.

Three 100 mm CMOS wafers (each one containing 24 chips) were post-processed according to this technique. This resulted in the complete fabrication of about 2000 resonators, per wafer, monolithically integrated with a CMOS readout circuitry.

In terms of technology, two critical issues have been solved: alignment full-wafer nanostencil/CMOS wafer at 100 mm wafer scale, and pattern blurring effect correction for enhanced resolution.

In terms of device operation, it has been demonstrated that a post-processing of CMOS wafers based on nanostencil lithography does not affect the circuitry performance. The work reported in this thesis represents the first time that an emerging nanolithography technique has been used to pattern multiple NEMS/MEMS devices on a whole CMOS wafer in a parallel and relatively low-cost approach.

The same strategy could be extended to other examples of nanodevices, such as single electron transistors (SETs) on CMOS [39], for which there is at present no affordable technological process that fulfill the requirements of high resolution processing at full wafer scale and CMOS compatibility.

Inspiring from this approach of integration, an almost identical post-processing technology based on electron beam lithography has also been developed to be able to fabricate new prototypes of nanodevices on CMOS within short timeframes.

## Bibliographical references

1. Arcamone, J., M.A.F.v.d. Boogaart, F. Serra-Graells, S. Hansen, J. Brugger, F. Torres, G. Abadal, N. Barniol, and F. Pérez-Murano  
**Full-wafer integration of NEMS on CMOS by nanostencil lithography**  
in the proceedings of the *IEEE IEDM*. 2006. San Francisco (USA).
2. Verd, J., G. Abadal, J. Teva, M.V. Gaudo, A. Uranga, X. Borriese, F. Campabadal, J. Esteve, E.F. Costa, F. Perez-Murano, Z.J. Davis, E. Forsen, A. Boisen, and N. Barniol  
**Design, fabrication, and characterization of a submicroelectromechanical resonator with monolithically integrated CMOS readout circuit**  
*IEEE Journal of Microelectromechanical Systems*, 2005. **14**(3): p. 508-519.
3. De Poortere, E.P., H.L. Stormer, L.M. Huang, S.J. Wind, S. O'Brien, M. Huang, and J. Hone  
**1-to 2-nm-wide nanogaps fabricated with single-walled carbon nanotube shadow masks**  
*Journal of Vacuum Science & Technology B*, 2006. **24**(6): p. 3213-3216.
4. De Poortere, E.P., H.L. Stormer, L.M. Huang, S.J. Wind, S. O'Brien, M. Huang, and J. Hone  
**Single-walled carbon nanotubes as shadow masks for nanogap fabrication**  
*Applied Physics Letters*, 2006. **88**(14).
5. van den Boogaart, M.A.F.  
**Stencil lithography: an ancient technique for advanced micro- and nanopatterning**  
Hartung-Gorre Verlag ed, Series in Microsystems, Vol. 20, 2006, Konstanz.
6. van den Boogaart, M.A.F., G.M. Kim, R. Pellens, J.P. van den Heuvel, and J. Brugger  
**Deep-ultraviolet-microelectromechanical systems stencils for high-throughput resistless. patterning of mesoscopic structures**  
*Journal of Vacuum Science & Technology B*, 2004. **22**(6): p. 3174-3177.
7. Ludwig, A., J. Cao, J. Brugger, and I. Takeuchi  
**MEMS tools for combinatorial materials processing and high-throughput characterization**  
*Measurement Science & Technology*, 2005. **16**(1): p. 111-118.
8. Takahashi, R., H. Kubota, M. Murakami, Y. Yamamoto, Y. Matsumoto, and H. Koinuma  
**Design of combinatorial shadow masks for complete ternary-phase diagramming of solid state materials**  
*Journal of Combinatorial Chemistry*, 2004. **6**(1): p. 50-53.
9. Zhou, Y.X. and A.T. Johnson  
**Simple fabrication of molecular circuits by shadow mask evaporation**  
*Nano Letters*, 2003. **3**(10): p. 1371-1374.
10. Tian, P.F., P.E. Burrows, and S.R. Forrest  
**Photolithographic patterning of vacuum-deposited organic light emitting devices**  
*Applied Physics Letters*, 1997. **71**(22): p. 3197-3199.
11. Egger, S., A. Ilie, Y.T. Fu, J. Chongsathien, D.J. Kang, and M.E. Welland  
**Dynamic shadow mask technique: A universal tool for nanoscience**  
*Nano Letters*, 2005. **5**(1): p. 15-20.
12. Guo, H.M., D. Martrou, T. Zambelli, J. Polesel-Maris, A. Piednoir, E. Dujardin, S. Gauthier, M.A.F. van den Boogaart, L.M. Doeswijk, and J. Brugger  
**Nanostenciling for fabrication and interconnection of nanopatterns and microelectrodes**  
*Applied Physics Letters*, 2007. **90**(9).

13. Gross, L., R.R. Schlittler, G. Meyer, A. Vanhaverbeke, and R. Allenspach  
**Fabrication of ultrathin magnetic structures by nanostencil lithography in dynamic mode**  
Applied Physics Letters, 2007. **90**(9).
14. Racz, Z., J.L. He, S. Srinivasan, W. Zhao, A. Seabaugh, K.P. Han, P. Ruchhoeft, and J. Wolfe  
**Nanofabrication using nanotranslated stencil masks and lift off**  
Journal of Vacuum Science & Technology B, 2004. **22**(1): p. 74-76.
15. Kolbel, M., R.W. Tjerkstra, J. Brugger, C.J.M. van Rijn, W. Nijdam, J. Huskens, and D.N. Reinhoudt  
**Shadow-mask evaporation through monolayer-modified nanostencils**  
Nano Letters, 2002. **2**(12): p. 1339-1343.
16. Brugger, J., J.W. Berenschot, S. Kuiper, W. Nijdam, B. Otter, and M. Elwenspoek  
**Resistless patterning of sub-micron structures by evaporation through nanostencils**  
Microelectronic Engineering, 2000. **53**(1-4): p. 403-405.
17. Kaminsky, G.  
**Noncontaminating Si-Based Shadow Masks for Mbe**  
Journal of Vacuum Science & Technology B, 1985. **3**(2): p. 741-742.
18. Kim, G.M., M.A.F. van den Boogaart, and J. Brugger  
**Fabrication and application of a full wafer size micro/nanostencil for multiple length-scale surface patterning**  
Microelectronic Engineering, 2003. **67-8**: p. 609-614.
19. Kim, G.M., S. Kawai, M. Nagashio, H. Kawakatsu, and J. Brugger  
**Nanomechanical structures with 91 MHz resonance frequency fabricated by local deposition and dry etching**  
Journal of Vacuum Science & Technology B, 2004. **22**(4): p. 1658-1661.
20. Bucher, V., J. Brugger, D. Kern, G.M. Kim, M. Schubert, and W. Nisch  
**Electrical properties of light-addressed sub- $\mu$  m electrodes fabricated by use of nanostencil-technology**  
Microelectronic Engineering, 2002. **61-2**: p. 971-980.
21. Vroegindewij, F., E.A. Speets, J.A.J. Steen, J. Brugger, and D.H.A. Blank  
**Exploring microstencils for sub-micron patterning using pulsed laser deposition**  
Applied Physics a-Materials Science & Processing, 2004. **79**(4-6): p. 743-745.
22. Cojocaru, C.V., C. Harnagea, A. Pignolet, and F. Rosei  
**Nanostenciling of functional materials by room temperature pulsed laser deposition**  
IEEE Transactions on Nanotechnology, 2006. **5**(5): p. 470-477.
23. Cojocaru, C.V., C. Harnagea, F. Rosei, A. Pignolet, M.A.F. van den Boogaart, and J. Brugger  
**Complex oxide nanostructures by pulsed laser deposition through nanostencils**  
Applied Physics Letters, 2005. **86**(18).
24. Fulton, T.A. and G.J. Dolan  
**Observation of Single-Electron Charging Effects in Small Tunnel-Junctions**  
Physical Review Letters, 1987. **59**(1): p. 109-112.
25. Schallenberg, T., C. Schumacher, and W. Faschinger  
**In situ structuring during MBE regrowth with shadow masks**  
Physica E-Low-Dimensional Systems & Nanostructures, 2002. **13**(2-4): p. 1212-1215.
26. Tsang, W.T. and M. Ilegems  
**Selective Area Growth of Gaas/Alxgal-Xas Multilayer Structures with Molecular-Beam Epitaxy Using Si Shadow Masks**  
Applied Physics Letters, 1977. **31**(4): p. 301-304.

27. Deshmukh, M.M., D.C. Ralph, M. Thomas, and J. Silcox  
**Nanofabrication using a stencil mask**  
Applied Physics Letters, 1999. **75**(11): p. 1631-1633.
28. Kohler, J., M. Albrecht, C.R. Musil, and E. Bucher  
**Direct growth of nanostructures by deposition through an Si<sub>3</sub>N<sub>4</sub> shadow mask**  
Physica E, 1999. **4**(3): p. 196-200.
29. Ono, K., H. Shimada, S.I. Kobayashi, and Y. Ootuka  
**A new fabrication method for ultra small tunnel junctions**  
Japanese Journal of Applied Physics Part 1-Regular Papers Short Notes & Review Papers, 1996. **35**(4A): p. 2369-2371.
30. Burger, G.J., E.J.T. Smulders, J.W. Berenschot, T.S.J. Lammerink, J.H.J. Fluitman, and S. Imai  
**High-resolution shadow-mask patterning in deep holes and its application to an electrical wafer feed-through**  
Sensors and Actuators a-Physical, 1996. **54**(1-3): p. 669-673.
31. Arcamone, J., A. Sanchez-Amores, J. Montserrat, M.A.F. van den Boogaart, J. Brugger, and F. Perez-Murano  
**Dry etching for the correction of gap-induced blurring and improved pattern resolution in nanostencil lithography**  
Journal of Micro/Nanolithography, MEMS and MOEMS, 2007. **6**(1): p. 013005-7.
32. van den Boogaart, M.A.F., L.M. Doeswijk, and J. Brugger  
**Silicon-supported membranes for improved large-area and high-density micro/nanostencil lithography**  
IEEE Journal of Microelectromechanical Systems, 2006. **15**(6): p. 1663-1670.
33. van den Boogaart, M.A.F., M. Lishchynska, L.M. Doeswijk, J.C. Greer, and J. Brugger  
**Corrugated membranes for improved pattern definition with micro/nanostencil lithography**  
Sensors and Actuators a-Physical, 2006. **130**: p. 568-574.
34. Rius, G.  
**Fabrication of NEMS structures by EBL**  
Master thesis, UAB (2005)
35. Campabadal, F., S. Ghatnekar-Nilsson, G. Rius, C. Fleta, J. Rafi, E. Figueras, and J. Esteve  
**CMOS degradation effects due to electron beam lithography in smart NEMS fabrication**  
in the proceedings of the *SPIE*. 2005.
36. Ghatnekar-Nilsson, S., E. Forsen, G. Abadal, J. Verd, F. Campabadal, F. Perez-Murano, J. Esteve, N. Barniol, A. Boisen, and L. Montelius  
**Resonators with integrated CMOS circuitry for mass sensing applications, fabricated by electron beam lithography**  
Nanotechnology, 2005. **16**(1): p. 98-102.
37. Forsen, E., S.G. Nilsson, P. Carlberg, G. Abadal, F. Perez-Murano, J. Esteve, J. Montserrat, E. Figueras, F. Campabadal, J. Verd, L. Montelius, N. Barniol, and A. Boisen  
**Fabrication of cantilever based mass sensors integrated with CMOS using direct write laser lithography on resist**  
Nanotechnology, 2004. **15**(10): p. S628-S633.
38. Bruce, R.H. and G.P. Malafsky  
**High-Rate Anisotropic Aluminum Etching**  
Journal of the Electrochemical Society, 1983. **130**(6): p. 1369-1373.
39. Likharev, K.K.  
**Nano and Giga Challenges in Microelectronics**  
Elsevier ed, 2003. 27-68.



# CHAPTER 5

## EXPERIMENTAL CHARACTERIZATION OF NEMS/CMOS DEVICES

I.	Experimental procedure and measurement set-up .....	156
II.	CCII circuit characterization .....	158
III.	Electrical measurements of the frequency response of integrated resonators.....	159
III.1.	Electrical measurement of in-plane vibrating cantilevers.....	159
III.1.a.	Samples characteristics.....	159
III.1.b.	Experimental results.....	161
III.1.b.i)	Measurements in air with set-up 1 .....	161
III.1.b.ii)	Measurements in vacuum with set-up 2.....	162
III.1.b.iii)	Estimation of the Young modulus of the structural layer.....	163
III.1.b.iv)	Electrical results summary .....	164
III.1.c.	Analysis of results.....	165
III.1.c.i)	Estimation of the fringing field parasitic capacitance $C_{PA}$ .....	165
III.1.c.ii)	Driving voltage effect: spring-softening .....	165
III.1.c.iii)	Q factor evolution as a function of the pressure .....	167
III.1.c.iv)	Estimation of critical deflection .....	168
III.1.c.v)	Noise considerations.....	169
III.2.	Electrical measurement of out-of-plane vibrating quad-beams.....	171
III.2.a.	Samples characteristics.....	171
III.2.b.	Experimental results.....	171
III.2.b.i)	Measurements in air with set-up 1 .....	172
III.2.b.ii)	Measurements in vacuum with set-up 2.....	172
III.2.b.iii)	Electrical Results Summary .....	173
III.2.c.	Analysis of results.....	174
III.2.c.i)	Estimation of the fringing field parasitic capacitance $C_{PA}$ .....	174
III.2.c.ii)	Q factor evolution as a function of the pressure .....	174
III.2.c.iii)	Driving voltage effects.....	175
	Conclusion of chapter 5 .....	177
	Bibliographical references .....	178

The scope of this chapter is the electrical characterization of our NEMS/CMOS system. The samples have been fabricated following technological processes described in chapter 4. The experimental set-up as well as the CCI circuit characterization will be briefly described.

This chapter is emphasized on electrical measurements of frequency spectra of two types of integrated resonators: in-plane vibrating cantilevers and out-of-plane vibrating quad-beams (QB). The main features of their magnitude and phase responses measured in air and in vacuum are analyzed. The accuracy of the RLC model is discussed.

## I. Experimental procedure and measurement set-up

We have performed all these measurements at the Electronic Circuit and Systems laboratory from the Escola Tècnica Superior de Enginyeria of Universitat Autònoma de Barcelona. Two different set-ups have been used: a probe station for measurements in air (set-up 1) and a vacuum chamber with electrical feed-through (set-up 2).

The electrical detection set-up comprising the probe station (SÜSS MICROTEC PA 200) is sketched in Figure 1. Its main elements are:

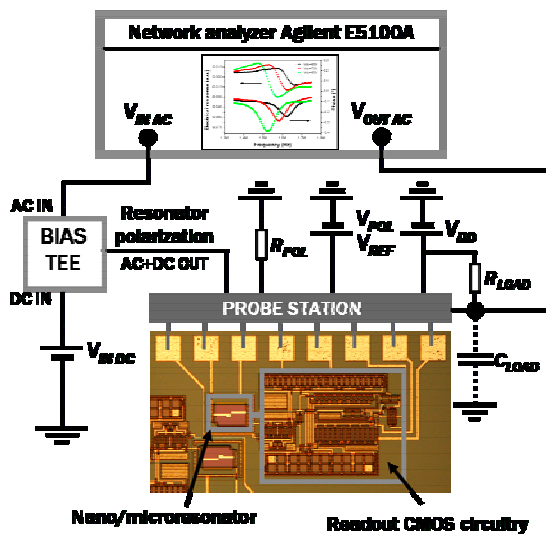


Figure 1. Experimental set-up based on a probe station

- a 16 probes card to access the contact pads
- a bias tee (MINI-CIRCUITS, ZFBT-4R2GW) to sum DC,  $V_{IN DC}$ , and AC,  $V_{IN AC}$ , voltages in order to drive the resonator.  $V_{IN AC}$  is supplied by a network analyzer
- the network analyzer (AGILENT E5100A) sweeps a programmable frequency range
- the amplified output current of the CMOS circuit is externally converted into a voltage,  $V_{OUT AC}$ , by flowing into the tunable resistor  $R_{LOAD}$
- $V_{OUT AC}$  is measured through the network analyzer whose adjustable input impedance is set to  $1 \text{ M}\Omega$

Samples pre-tested with the probe station can be measured with the second set-up that is adapted to vacuum measurements. This set-up is very similar to the other except that there is no probe station inside the vacuum chamber. Hence, NEMS/CMOS chips are mounted on a printed circuit board (PCB) (Cu lines), and wire bonded to it with Al wires by non-thermal welding based on ultrasounds. SMA connectors placed on the edge of the PCB are cabled to electrical feed-through mounted on the chamber wall. Following this procedure, air and vacuum measurements can be made; nevertheless it must be considered that the wire bonding of the samples requires an additional preparation step with respect to the direct characterization with set-up n°1, and only a limited number (one or two) of devices can be contacted per chip.

Using both set-ups,  $V_{POL}$  (see chapter 3) has been set to 2 V (although its optimum value is 1 V) so that the same DC source can simultaneously polarize  $V_{REF}$  and  $V_{POL}$ . In particular, this solution allowed reducing the number of connectors in the PCB for measurements in vacuum.

MEASUREMENT OF THE FREQUENCY RESPONSE OF A RESONATOR WITH A NETWORK ANALYZER

The network analyzer provides the frequency response in terms of magnitude and phase of the ratio  $V_{OUT\ AC}/V_{IN\ AC}$  (also named voltage gain in chapter 3, eq.III-13). A frequency span centered on a given value can be programmed. For any measurement, a trade-off must be found between the number of points of the scan and the narrowness of the band-pass filter applied around each frequency point, otherwise the scan can be very slow.

The magnitude response delivered by the network analyzer is  $\Re_{NA}$  given by:

$$\Re_{NA} (dB) = \text{voltage gain} = 20 \log \frac{V_{OUT\ AC}}{V_{IN\ AC}} \quad (V.1)$$

$I_{MEMS}$ , the total AC current originating from the resonator and given by  $I_{MEMS} = I_M + I_W + I_{PA}$ , can be estimated from  $\Re_{NA}$  in the following way:

$$\Re_{NA} (dB) = 20 \log \frac{V_{OUT\ AC}}{V_{IN\ AC}} = 20 \log \frac{MN R_{LOAD} I_{MEMS}}{V_{IN\ AC}} \quad (V.2)$$

where  $MN = 100$  according to the CCII design, what results in:

$$I_{MEMS} = \frac{V_{IN\ AC}}{100 R_{LOAD}} 10^{\frac{\Re_{NA}}{20}} \quad (V.3)$$

To estimate the motional current, the response out of resonance must be simply subtracted to the one in resonance:

$$I_M (f) = \frac{V_{IN\ AC}}{100 R_{LOAD}} \left( 10^{\frac{\Re_{NA\_IN\ RESONANCE}}{20}} - 10^{\frac{\Re_{NA\_OUT\ RESONANCE}}{20}} \right) \quad (V.4)$$

What we will further name the resonance current  $I_{RES}$  corresponds to the maximum motional current, i.e. at the resonance frequency:  $I_{RES} = I_M (f_{RES}) = I_{M\ MAX}$ .

An additional and very interesting capability of the network analyzer is the calibration of the background signal. As mentioned previously, this specific signal, originating from parasitic capacitances cross-talk, can be so high that the resonance peak is masked. The first step of the calibration procedure consists in measuring the background signal by normally polarizing the CCII and by polarizing the resonator with  $V_{IN\ AC} \neq 0$  and  $V_{IN\ DC} = 0$  so that the resonator is not excited but its capacitances (parasitic and static) already produce a current. Once the spectrum is recorded, the calibration option is activated and  $V_{IN\ DC}$  is applied to the device. In real time, the background signal is subtracted to the newly recorded signal containing the resonance peak: in this way, the resonance peak is highlighted. The response of the network analyzer becomes:

$$\text{calibrated signal (dB)} = 20 \log \frac{V_{OUT\ AC-RES}}{V_{OUT\ AC-BS}} \quad (V.5)$$

where  $V_{OUT\ AC-RES}$  is the output signal with resonance (with  $V_{IN\ DC} \neq 0$ ), i.e. of the  $R_M L_M C_M // C_W // C_{PA}$  element, while  $V_{OUT\ AC-BS}$  is the output signal without resonance, i.e. the background signal (with  $V_{IN\ DC} = 0$ ), that corresponds to the  $C_W // C_{PA}$  element.

Out of resonance, the magnitude should be 0. In practice, there is a slight offset with respect to 0 that is likely due to a perturbation caused by  $V_{IN\ DC}$ . Within the calibrated signal spectrum, the most interesting feature is  $\Delta dB$ , the amplitude of the resonance peak in dB with respect to the offset. At resonance, the value of  $I_{MEMS}$  is  $I_{MEMS\ MAX}$  which can be calculated in the following way

$$I_{MEMS\ MAX} = I_{MEMS\_BS} 10^{\Delta dB / 20} \quad (V.6)$$

where  $I_{MEMS\_BS}$  is the resonator current without the resonance contribution given by eq.(V.3):

$$I_{MEMS\_BS} = \frac{V_{IN\ AC}}{100 R_{LOAD}} 10^{\frac{\Re_{NA}}{20}} \quad (V.7)$$

here,  $\Re_{NA}$  is the network analyzer response without nor calibration neither resonance. Computing eq. (V.6) and (V.7),  $I_{MEMS\ MAX}$  at resonance is finally obtained:

$$I_{MEMS\ MAX} = \frac{V_{IN\ AC}}{100 R_{LOAD}} 10^{\frac{\Delta dB + \Re_{NA}}{20}} \quad (V.8)$$

and

$$I_{RES} = \frac{V_{IN\ AC}}{100 R_{LOAD}} \left( 10^{\frac{\Delta dB + \Re_{NA}}{20}} - 10^{\frac{\Re_{NA}}{20}} \right) \quad (V.9)$$

COMMENT ON SATURATION ISSUES:

In chapter 3, the condition of saturation of the output voltage was defined through eq.(III.11). Thus, it is possible to define the saturation threshold in the response of the network analyzer. Computing eq.(V.2) and (III.11), the maximum allowed response to avoid saturation is:

$$\Re_{NA\ MAX-SAT} (dB) = 20 \log \frac{100 R_{LOAD} V_{R_{POL}}}{V_{IN\ AC} R_{POL}} = 20 \log \frac{100 R_{LOAD} I_{BIAS}}{V_{IN\ AC}} \quad (V.10)$$

As it depends on well-known experimental parameters, this calculation is straightforward. Then, if during the measurements  $\Re_{NA}$  is smaller than this criteria, then one can be sure that the system is not operated in its saturation mode.

## II. CCII circuit characterization

The experimental response of the CCII circuit has been directly measured on a CCII containing an integration area. A serial resistor of value  $R_{IN}$  is inserted between the AC supply of the network analyzer and the bias tee. The resulting test current is approximately given by

$$I_{TEST} \approx \frac{V_{IN\ AC}}{R_{IN}} \quad (V.11)$$

To extract the corresponding transimpedance gain from  $\mathfrak{R}_{NA}$ , eq.(V.1) is computed with eq.(V.11):

$$20 \log \frac{V_{OUT AC}}{I_{TEST}} = G_{TRANSIMPEDANCE} = 20 \log R_{IN} + \mathfrak{R}_{NA} \quad (V.12)$$

For the experimental determination of the Bode diagram, a relatively high value for  $R_{LOAD}$  is chosen: in this way, the bandwidth is limited by the output  $R_{LOAD} // C_{LOAD}$  low-pass filter and not by the internal high impedance pole. Thus, the parasitic load  $C_{LOAD}$  capacitance can be estimated from the cut-off frequency (-3 dB) according to eq.III.7. The experimental spectrum of the transimpedance gain is shown in Figure 2:

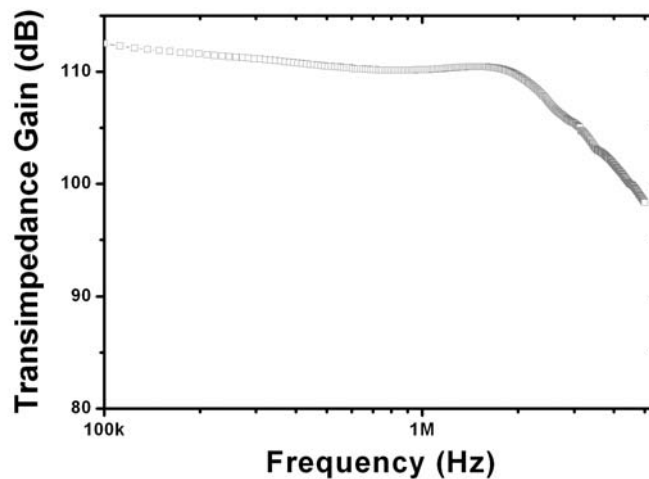


Figure 2. Experimental Bode diagram of the CCII circuit with  $R_{LOAD} = 2500 \Omega$  and  $R_{IN} = 1 M\Omega$

The response is not perfectly flat but the gain plateau is around 110 dB. This value is in good concordance with the theoretical value of 108 dB given by  $20 \log(100 R_{LOAD})$ . An approximate value of 30 pF for  $C_{LOAD}$  is extracted from the cut-off frequency.

### III. Electrical measurements of the frequency response of integrated resonators

Electrical measurements of resonance spectra of integrated cantilevers and QB are the topic of this section. Interesting features and signal level of the measured responses are discussed.

#### III.1. Electrical measurement of in-plane vibrating cantilevers

##### III.1.a. Samples characteristics

The cantilever beams are made of polysilicon and have been defined either by electron-beam (eBL) or by nanostencil lithography (nSL). As detailed in chapter 4, the fabrication process based on nSL provided a large amount of devices, about 500 in total. However, to be able to

introduce some changes in the design of the devices, some new prototypes have punctually been fabricated by eBL.

The devices are either single or double cantilevers (orthogonally oriented one to each other) operated in the fundamental in-plane flexural mode. Individually, single and each beam of the double cantilevers exhibit the same electrical behavior. However, double beams features some interesting properties regarding mass sensing and also in terms of electrical response if they can be successfully coupled. These aspects will be tackled in detail in chapter 6. Single and double cantilevers are depicted in Figure 3:

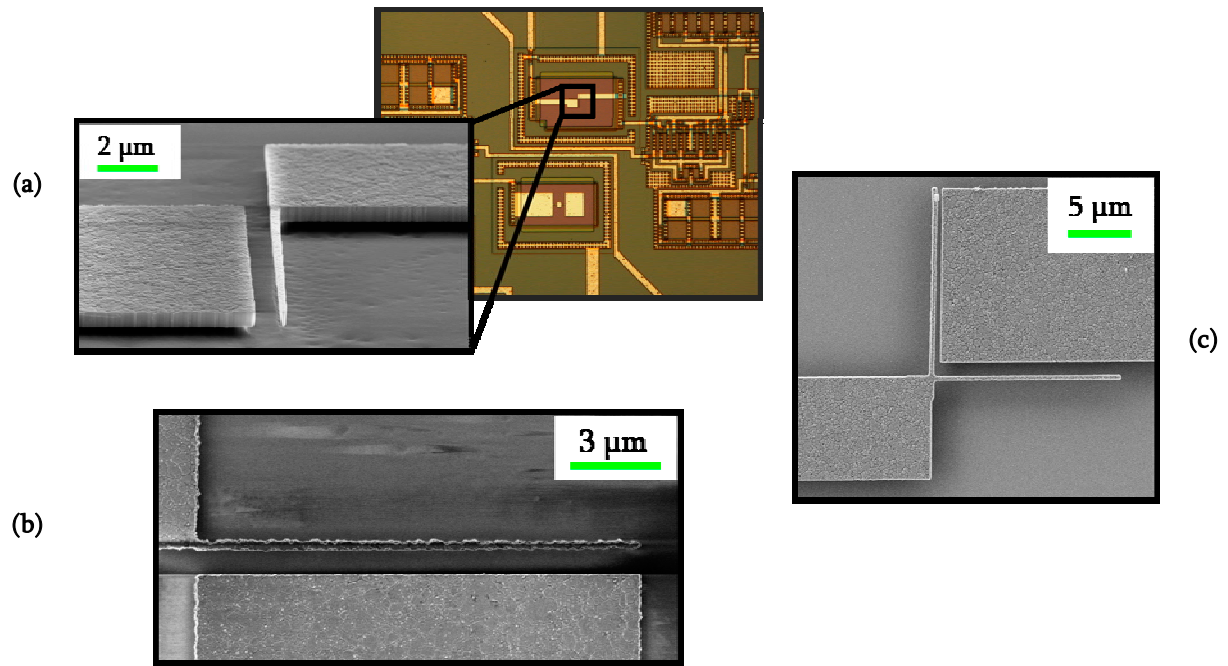


Figure 3. Images of fully fabricated CMOS integrated cantilevers. (a) Optical image of the CCII circuit and of the juxtaposed cantilever zoomed in the inset (tilted SEM image); (b) SEM image of a single cantilever whose edges are rough due to a defect in the patterning; (c) SEM image of a double cantilever

The geometrical dimensions measured by SEM of five characteristic cantilevers are reported in Table V - 1. The lithography technique employed for their patterning is specified.  $l$  is the cantilever length,  $b$  the width,  $h$  the thickness<sup>1</sup> and  $d$  the cantilever-driver gap.

Reference	Simplified Denomination	$l$ ( $\mu\text{m}$ )	$b$ (nm)	$h$ (nm)	$d$ (nm)	Lithography technique
3157-11-B5-c10	A	14.45	285	560	790	nSL
3157-13-c3 CD3	B	14.5	400	460	600	eBL
3157-13-c3 CD4	C	14.6	400	460	400	eBL
3157-13-c3 CD6	D	14.3	400	460	400	eBL
3157-11-F1 c3	E	14.5	260	570	820	nSL

Table V - 1. Cantilever samples characteristics. Geometrical dimensions measured by SEM

<sup>1</sup> some deviations are observable concerning the thickness of the devices. This difference is attributed to the fact that these samples come from different wafers that underwent process fluctuations. Actually, samples A and E are of the same wafer and  $h \approx 560$  nm, while B, C and D are from another wafer and  $h \approx 460$  nm.

### III.1.b. Experimental results

The correct operation of in-plane vibrating cantilevers has been demonstrated in air and in vacuum: the capacitive detection scheme including the CCII CMOS circuit successfully transduced mechanical oscillations into an electrical signal so that the mechanical frequency response, including the resonance peak, could be electrically detected. The obtained quality factors are around 15 in air, while they reach about 9700 in vacuum (at  $4 \cdot 10^{-3}$  mBar). This is a very high value despite the fact that polysilicon is a relatively disordered structural material.

#### III.1.b.i) Measurements in air with set-up 1

Figure 4 depicts characteristic responses of cantilevers (A and D) operated in air. In these measurements, the background signal has been pre-calibrated according to the aforementioned procedure. The resonance frequency of these cantilevers can be tuned by varying the applied DC voltage and a clear spring-softening effect is seen with increasing  $V_{IN\ DC}$ . The main structural difference between cantilevers A and D is the transducing gap: 800 and 400 nm respectively. This logically results in a better electrostatic coupling for D illustrated by a higher magnitude and a greater phase change: to reach a magnitude of 1 dB, A and D need 23 and 8 V respectively, corresponding to 17 and 20 ° of phase change. It is clear that future designs of low power NEMS/CMOS systems require taking advantage of the nanopatterning techniques to define narrow gaps in the deep submicron range.

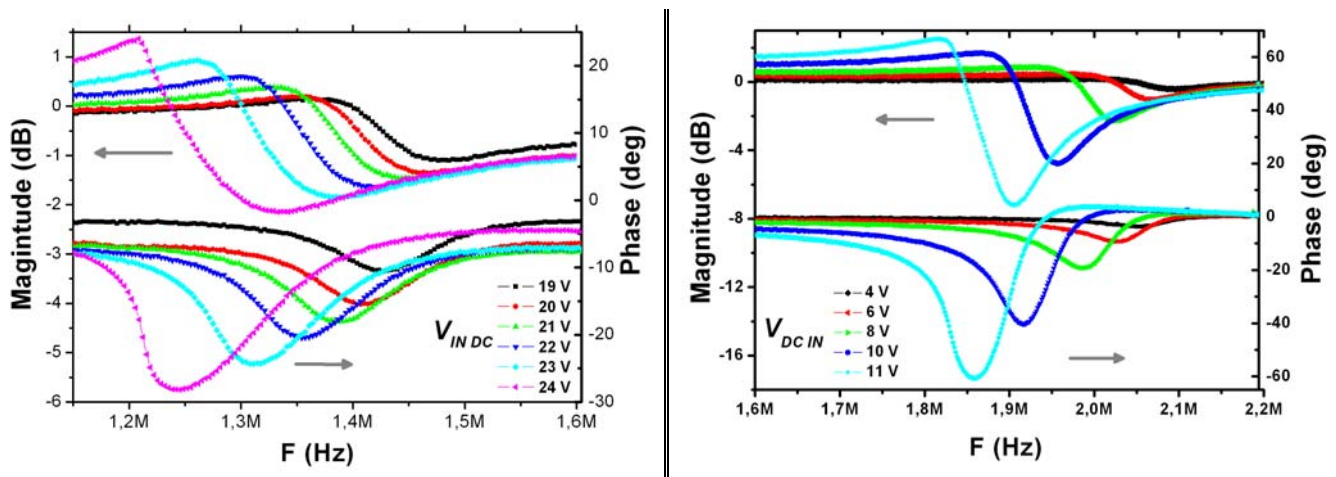


Figure 4. Calibrated resonance spectra in air of cantilever A (left) and D (right) for several  $V_{IN\ DC}$  voltages.  $V_{IN\ AC}$  is respectively 2.8 and 0.9 V peak-peak (pp) for A and D

Furthermore, after a certain threshold of  $V_{IN\ DC}$ , a very interesting nonlinear behavior is observable both cantilevers of Figure 4 and Figure 5. This means that the critical oscillation amplitude (see chapter 2) has been exceeded what leads to hysteretic frequency spectra that could provide novel applications like memory elements based on NEMS [1].

In this sense, the spectrum of Figure 5, recorded at  $V_{IN\ DC}=20$  V (non pre-calibrated curve), starts to exhibit a nonlinear behavior whereby the resonance peak takes the form of a spike and its related phase change is about to get an infinite vertical slope. Regarding the final objective of implementing nanoresonators as mass sensors, it is clear that being able to reach the nonlinear behavior of the cantilever with a low enough  $V_{IN\ DC}$  voltage (so that it remains inferior to the pull-

in voltage threshold) is a clear advantage in terms of mass sensitivity. Indeed, it is assumed [2] that the sensitivity is the highest at the onset of nonlinearity (because of the infinite slope).

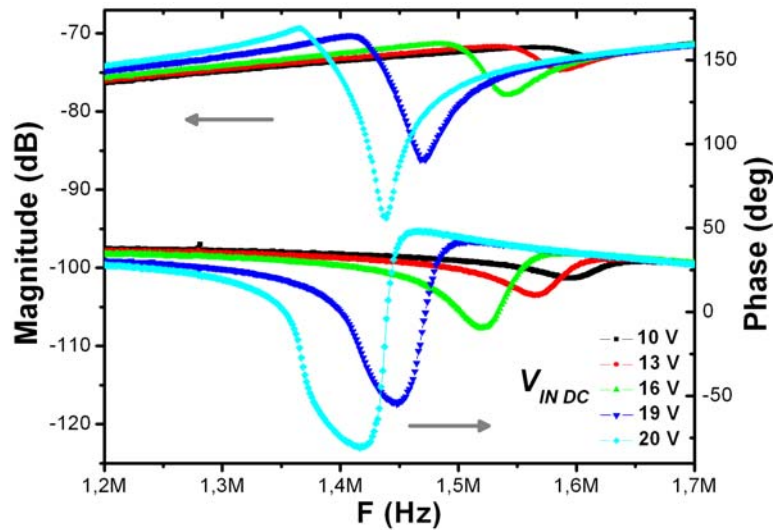


Figure 5. Non-calibrated resonance spectra in air of cantilever B for  $V_{IN AC}=0.9$  Vpp and several  $V_{IN DC}$

### III.1.b.ii) Measurements in vacuum with set-up 2

The chip containing cantilever E has been wire bonded and it has been measured in the vacuum chamber of set-up 2 whose minimum pressure is limited to about  $10^{-3}$  mBar.

Figure 6 depicts two spectra measured at  $P=10^{-2}$  mBar. Interestingly, very low driving voltages are enough for polarizing the device: 1 or 2 V DC (1 V is enough actually) added to a 0.092 V AC. A 2 V DC polarization is sufficient to provoke a strong nonlinear behavior yielding almost vertical slopes both in magnitude and in phase. A  $130^\circ$  phase change is obtained, not very far from the ideal case of  $180^\circ$ . The Q factors are respectively 9150 and 6650 for 1 and 2 V ( $V_{IN DC}$ ) while they are between 10 and 20 in air. This great enhancement is due to the lower level of pressure what drastically reduces the viscous damping.

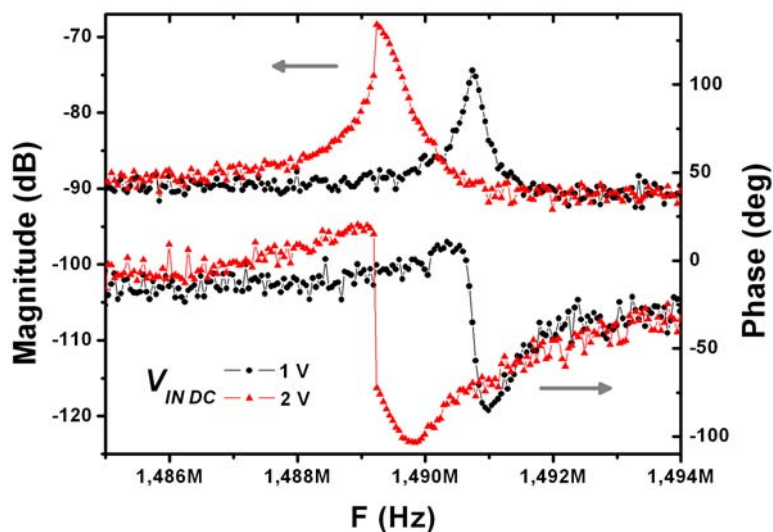


Figure 6. Non-calibrated resonance spectra in vacuum of cantilever E measured at  $P=10^{-2}$  mBar for  $V_{IN DC}=1$  and 2 V and  $V_{IN AC}=92$  mV pp.

It has to be noticed that these spectra feature a strange shape in the sense that the magnitude almost does not exhibit any anti-resonance peak. To understand this phenomenon, an electrical simulation (see chapter 3, section II.2.c.i) based on experimental parameters is performed and depicted in Figure 7:

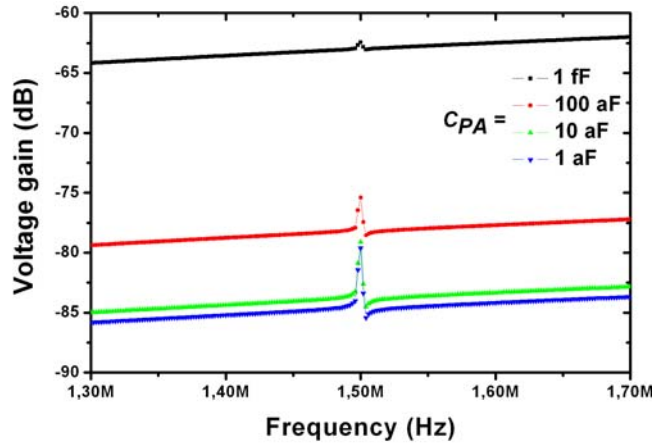


Figure 7. HSPICE simulation of cantilever E. All variable parameters are calculated basing on real geometrical dimensions and on the measured Q factor (=9150) for  $V_{IN\ DC}=1\text{ V}$ ,  $C_{PA2}=50\text{ fF}$ ,  $C_{DC}\approx C_O=89\text{ aF}$

The information provided by the simulation is coherent with the quasi-absence of anti-peak in the experimental curve (in fact, in Figure 6 it seems that there is a small anti-peak but it can not be well visualized because of the too narrow frequency span compared to Figure 7). In fact, the quasi-absence of anti-peak can only be explained if  $C_{PA}$  is very low.

According to the simulation, a background signal of -90 dB (see figure Figure 6) results from values of  $C_{PA}$  below 10 aF, e.g. much smaller than  $C_{DC}$  (normally,  $C_{PA}$  is in the order of  $C_{DC}$ ). Consequently, the absence of anti-peak seems to be related to a reduced  $C_{PA}$  but there is no apparent reason to explain this phenomenon.

### III.1.b.iii) Estimation of the Young modulus of the structural layer

Statistics on experimental and theoretical resonance frequency have been done. For samples fabricated by nSL, a very good matching is achieved setting a Young modulus of 130 GPa for the structural polysilicon layer. For samples defined by eBL, a non-explained slight distortion is found between theory and experiment. This may be attributed to the fact that these samples underwent a longer wet etch to release the structures what also partially released their anchor. This probably makes the ensemble less stiff and thereby they resonate at a lower frequency. These results are summarized in Table V - 2:

Cantilever	$f_{TH}$ (MHz)	$^1f_{EXP}$ (MHz)
A	1.65	1.63
E	1.49	1.49
B	2.3	1.93
C	2.26	1.86
D	2.36	2.15

Table V - 2. Theoretical resonance frequency calculated with  $E=130\text{ GPa}$  compared to the experimental value.

<sup>1</sup> the experimental resonance frequency is extrapolated at  $V_{IN\ DC}=0$  from a linear fit of spring-softening curve

## III.1.b.iv) Electrical results summary

The electrical results of cantilevers A, B, C, D and E are summarized in Table V - 3 and Table V - 4. The pull-in voltage  $V_{PI}$  (see chapter 2) is calculated with a spring constant of  $\alpha_2=2/3$ .

Table V - 3 reports data with calibrated measurements.  $\mathfrak{R}(\text{dB})$  means the background signal level and  $\Delta G(\text{dB})$  the relative amplitude of the resonance peak of the calibrated signal.  $I_{RES\_EXP}$  is calculated according to eq.(V.9) and  $I_{RES\_TH}$  is calculated as  $V_{IN\ AC}/R_M$  (see chapter 2) where  $R_M$  is the theoretical motional resistance.

Cant.	$R_{LOAD}$ $R_{POL}$	$V_{PI}$ (V)	$V_{IN\ DC}$ (V)	$V_{IN\ AC}$ (V <sub>PP</sub> )	Q	$\mathfrak{R}(\text{dB})$ BS	$\Delta G(\text{dB})$	$I_{RES\_EXP}$ (nA)	$I_{RES\_TH}$ (nA)
A	800 $\Omega$	28	19	2.8	15	-60	0.26	1	5
	180k $\Omega$		23		20		1,03	4,4	8
C	800 $\Omega$ 184k $\Omega$	48	8	0.9	14	-66	0.75	0.5	1.7
			10		15		1.43	1	2.9
			11		18.5		2.06	1.5	4.2
D	800 $\Omega$ 184k $\Omega$	49	10	0.9	13	-68	1.69	1	2.4
			11		17		2.51	1.5	3.7

Table V - 3. Electrical measurements results obtained with background signal calibration.

Table V - 4 reports data without background signal calibration.  $G(\text{dB})BS$  means the background signal level and  $G(\text{dB})Res$  the amplitude of the resonance peak.  $I_{RES\_XP}$  and  $I_{RES\_TH}$  are obtained following the method exposed for Table V - 3.

Cant.	$R_{LOAD}$ $R_{POL}$	$V_{PI}$ (V)	$V_{IN\ AC}$ (mV pp)	$V_{IN\ DC}$ (V)	Q	P (mBar)	$G(\text{dB})$ BS	$G(\text{dB})$ Res	$I_{RES\_EXP}$ (nA)	$I_{RES\_TH}$ (nA)
E	700 $\Omega$ 180k $\Omega$	25	92	1	9150	10 <sup>-2</sup>	-89.5	-74.4	0.21	0.29
				2	6650			-68.4	0.46	0.86
E	700 $\Omega$ 180k $\Omega$	25	92	1	9650	4.10 <sup>-3</sup>	-90	-75.75	0.17	0.31
					9150	10 <sup>-2</sup>		-76	0.17	0.29
					7640	10 <sup>-1</sup>		-77.2	0.14	0.25
					3880	0.9		-83.44	0.05	0.12
B	800 $\Omega$ 184k $\Omega$	48	900	16	8	1000	-73.3	-71.34	0.6	0.8
				19	10		-74.1	-70.25	1.24	1.35
				21	15		-75.3	-68.9	2.1	2.5

Table V - 4. Electrical measurements results obtained without background signal calibration.

The first statement to do is the accuracy of the pull-in voltage calculated with  $\alpha_2=2/3$ . It has been observed a good correspondence between the theoretical value and the experimental value of pull-in.

Concerning the RLC model accuracy for cantilevers, the experimental value of  $I_{RES\_EXP}$  is systematically smaller than  $I_{RES\_TH}$  by a factor two or three. Taking into account all the measurement uncertainties regarding the geometrical dimensions and the Q factor whose precise estimation is difficult ( $I_{RES\_TH}$  is directly linked to Q, as Q determines  $R_M$  through eq.III.15), this model can be considered relatively precise. It is more qualitative than quantitative, however to roughly predict the order of magnitude of the resonance signal, it constitutes an interesting tool.

This model is valid only in the mechanical linear regime of the cantilever. Since the model relies on a constant stiffness, its precision degrades when nonlinear resonance behavior appears.

### III.1.c. Analysis of results

Different features of the experimental behavior of cantilevers are analyzed in this section.

#### III.1.c.i) Estimation of the fringing field parasitic capacitance $C_{PA}$

In order to estimate  $C_{PA}$ , a comparison is carried out between experimental curves and simulated resonance spectra obtained with real parameters. The simulation value of  $C_{PA}$  is obtained by fitting the level of background signal.

We mainly attribute the parallel parasitic capacitance  $C_{PA}$  to the existence of a fringing electrostatic field in the cantilever/driver 'lateral' (in-plane) capacitor. This extra-field cannot be neglected since gap and height of the capacitor plates are of comparable dimensions (the height is not infinite unlike in the ideal parallel-plates approximation). In our case, gap ( $d$ ) and thickness ( $h$ ) are effectively comparable. Thereby, the theoretical expression of the total capacitance can be approximated as:

$$C_{TOT} \approx C_{DC} \left[ 1 + \frac{2d}{\pi h} \ln \frac{\pi h}{d} + \frac{2d}{\pi h} \ln \left( 1 + \frac{2b}{d} + 2\sqrt{\frac{b}{d} + \frac{b^2}{d^2}} \right) \right] = C_{DC} + C_{PA} \quad (V.13)$$

hence,

$$C_{PA} \approx C_{DC} \left[ \frac{2d}{\pi h} \ln \frac{\pi h}{d} + \frac{2d}{\pi h} \ln \left( 1 + \frac{2b}{d} + 2\sqrt{\frac{b}{d} + \frac{b^2}{d^2}} \right) \right] \quad (V.14)$$

These results are reported in Table V - 5:  $C_{PA}$  is compared to the (theoretical) static capacitance  $C_{DC}$  for a given  $V_{IN DC}$  voltage:

Cantilever	$V_{IN DC}$ (V)	$C_{DC TH}$ (fF)	$C_{PA SIMUL}$ (fF)	$C_{PA TH}$ (fF)
B	16	0.10	0.175	0.20
D	10	0.15	0.275	0.25

Table V - 5. Estimations of  $C_{PA}$  comparing experimental data (fitted with simulations) and analytical results

There is a good concordance between experimental results (fitted to simulation data) and analytical values: for this reason, the magnitude of  $C_{PA}$  can be mainly attributed to the fringing field.

#### III.1.c.ii) Driving voltage effect: spring-softening

As mentioned in chapter 2, the driving voltage ( $V_{IN AC} + V_{IN DC}$ ) has an incidence on the resonance frequency value and may tune it up or down. In all these experiments, a decrease of the resonance frequency with increasing driving voltage has been observed what corresponds to the so-called spring-softening effect. This means that for cantilevers, the electrostatic behavior dominates over mechanical stiffening (see chapter 2, section II.3.c).

In practice, the resonance frequency can be tuned down by varying only the applied DC voltage (assuming  $V_{IN DC} \gg V_{IN AC}$ ): in this case, it linearly decreases as a function of  $V_{IN DC}^2$  (eq. II-81). In Figure 8, a typical spring-softening curve obtained with cantilever A is shown:

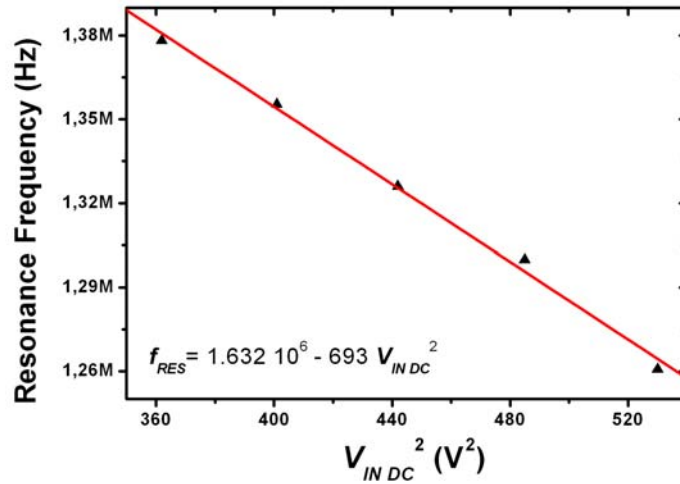


Figure 8. Resonance frequency dependence upon  $V_{IN DC}$  of cantilever A  
The linear fit is plotted in red and the fitted linear equation is indicated

$K$ , defined as the electromechanical coupling factor, can be extracted from experimental curves by putting the equation of the linear fit under the form  $f_{RES} = f_0(1 - KV_{IN DC}^2)$  (eq.II-81), where  $f_0$  is the natural resonance frequency.

$K$  can be expressed theoretically as a function of material and geometrical parameters eq.(II-81):

$$K = \frac{3\varepsilon_0 l^4}{4Eb^3 d^3} \quad (V.15)$$

The results of the comparison between theory and experiment are reported in Table V - 6:

Cant.	$K_{TH}$	$K_{EXP}$
A	$1.9 \cdot 10^{-4}$	$4.2 \cdot 10^{-4}$
B	$2 \cdot 10^{-4}$	$4.3 \cdot 10^{-4}$
C	$5 \cdot 10^{-4}$	$9 \cdot 10^{-4}$
D	$6 \cdot 10^{-4}$	$9 \cdot 10^{-4}$
E	$2.3 \cdot 10^{-4}$	$3.3 \cdot 10^{-4}$

Table V - 6. Comparison of theoretical and experimental electromechanical coupling factors

The experimental value is systematically higher than the theoretical one. This can be partially explained by the fact that the gap is overestimated in eq.(V.15) as it is considered in a non-polarized configuration. When the cantilever is polarized with  $V_{IN DC}$ , the cantilever bends towards its driving electrode and therefore the gap is reduced what contributes to increase  $K$ .

#### CANTILEVER BEHAVIOR AT HIGH DRIVING LEVELS

In continuity with chapter 2, the calculation of the transfer function of two parallel branches  $R_M L_M C_M // C_{PA}$  leads to two peaks in the amplitude-frequency domain:

- the proper resonance peak whose frequency is given by  $f_{RES} = \frac{1}{2\pi\sqrt{L_M C_M}}$
- the so-called anti-resonance peak whose frequency is given by  $f_{A-RES} = \frac{1}{2\pi\sqrt{L_M C}}$

$$\text{with } C = \frac{C_{PA} C_M}{C_{PA} + C_M}$$

If  $C_{PA} \gg C_M$ ,  $C \approx C_M$  i.e.  $f_{RES}$  is very close to  $f_{A-RES}$  and the anti-peak tends to cancel the resonance peak. If  $C_M$  becomes comparable to  $C_{PA}$ , then  $C$  is no more approximately equal to  $C_M$  and the anti-resonance peak gets farther from the resonance frequency towards higher frequencies. In terms of phase, this improvement materializes in the shape of the peak: it takes a 'U-shape' with flat bottom between  $f_{RES}$  and  $f_{A-RES}$ .

In Figure 9, cantilever B is driven in air at two relatively high DC voltages. Both resonance spectra exhibit very interesting behaviors combining two features: high phase changes and high nonlinearity due to the high driving level.

The observation of the curve recorded at 20 V is consistent with the aforementioned case whereby  $C_M$  gets closer to  $C_{PA}$ : the phase change is no more a spiky peak but U-shaped. Additionally, a nonlinear behavior starts to appear.

The observation of the curve recorded at 21 V is the continuation of the 20 V curve.  $f_{RES}$  and  $f_{A-RES}$  are far from each other (100 kHz) and the nonlinear behavior is much more pronounced: both phase changes are vertical and very important (100 and 180° for  $f_{RES}$  and  $f_{A-RES}$  respectively). The phase change related to the anti-peak gets downward by 180°: the analytical calculation of the transfer function always predicts that it should get upwards. This phase decrease is probably a measurement artifact of the network analyzer.

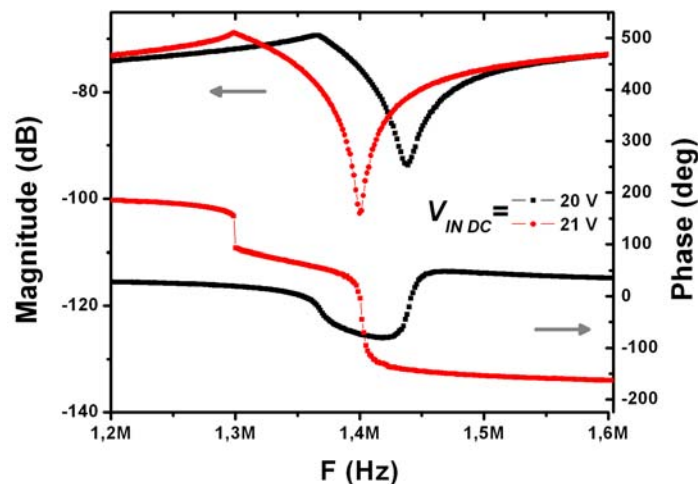


Figure 9. Strongly nonlinear behavior of cantilever B in air (non-calibrated signal).  
Resonance spectra for  $V_{IN DC}=20$  and 21 V.  $V_{IN AC}=0.9$  V pp.

### III.1.c.iii) Q factor evolution as a function of the pressure

In Figure 10 and Figure 11, the Q factor is extracted from resonance spectra measured at different levels of pressure and maintaining constant all the other parameters. These graphs must help in further assessing the sources of dissipation affecting the resonator.

Between other interests, information on the Q factor is also important to know if portable vacuum sealed systems are aimed to be developed (the complexity of the packaging would depend much on the required vacuum level).

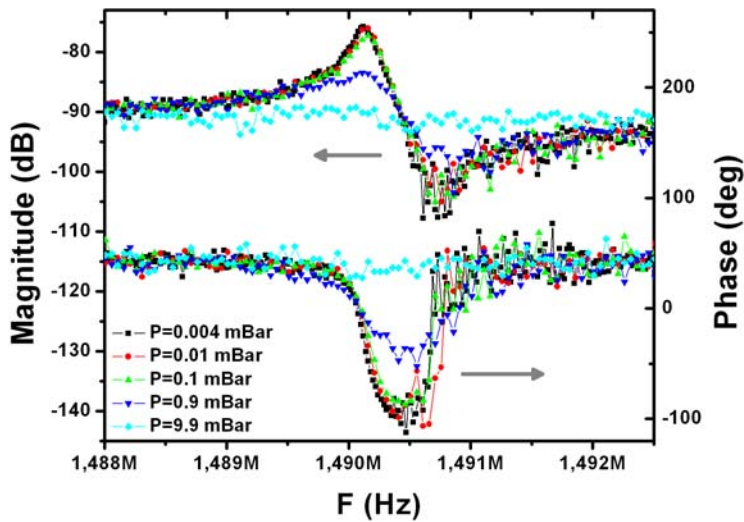


Figure 10. Resonance spectra in vacuum of cantilever E for  $V_{IN DC}=1$  V and  $V_{IN AC}=92$  mV pp Spectra recorded at several pressures (non-calibrated signal)

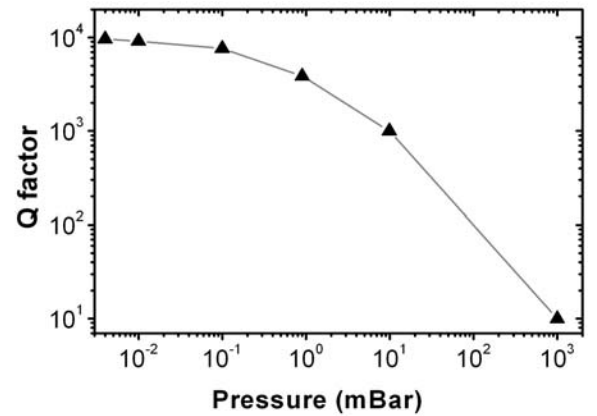


Figure 11. Based on data of Figure 10, the Q factor is plotted as a function of the chamber pressure

From Figure 11, it seems that the most pronounced evolution occurs between 1 Bar and 0.1 mBar: in this range, the Q factor can be enhanced by three orders of magnitude. Below 0.1 mBar the improvement saturates what is in agreement with reported experiments [3, 4]. These results confirm that viscous damping plays a key role regarding the value of the quality factor of nano/microresonators whereas at low pressure intrinsic mechanisms dominate.

These curves seem quite noisy but this is only due to the remarkably low DC driving voltage (1 V): this makes that the signal magnitude is low (according to eq.III-14 and -15, the motional resistance  $R_M$  effectively depends on  $V_{IN DC}$  and the higher  $V_{IN DC}$ , the lower  $R_M$ ). Thereby, the signal-to-noise ratio is lowered.

### III.1.c.iv) Estimation of critical deflection

It is well-known that a mechanical nonlinear behavior appears in the oscillations of a resonator when its deflection (static or dynamic) exceeds a certain value, named critical amplitude (or deflection) (of which the calculation was detailed in chapter 2). In this section, we propose to study the correlation between the apparition of nonlinear oscillations (visible in almost all the previous experimental curves) and the level of driving voltage. Indeed, the force that mechanically deflects the cantilever is precisely the electrostatic force generated by the driving voltage.

In Table V - 7, the critical deflection  $x_C$  is calculated for the samples B and E as a function of characteristic Q-factors: for B (in air), Q between 10 and 100 like in Figure 5 and for E (in vacuum), Q between 1000 and 10000 like in Figure 6. The calculation is based on eq.II-78 for  $\beta=1.58$  and  $\nu=0.22$  [5].

In Table V - 8, the theoretical displacement  $x$  of the cantilever tip is calculated for samples B and E as a function of characteristic driving DC voltages (we neglect the time-varying part of the displacement since it is about two orders of magnitude smaller according to our estimations). The calculation is based on eq.II-75 (the spring constant is considered with  $\alpha_2=0.25$  as the displacement is considered in one single point at the cantilever extremity).

Cant.	$b$ (nm)	Q	$x_C$ (nm)
B	400	10	146
		100	46
E	260	1000	9
		10000	3

Table V - 7. Theoretical critical amplitude as a function of the Q-factor.  $b$  is the cantilever width

Cant.	Conditions	$V_{INDC}$	$x$ (nm)
B	air	10	29
		15	78
		20	192
E	vacuum	1	0.5
		2	2

Table V - 8. Theoretical deflection of the cantilever extremity for samples B and E as a function of  $V_{INDC}$

The Q-factor of cantilever B is around 10 (see Table V - 4) what results in a critical amplitude of 146 nm according to Table V - 7. It is clear from Figure 5 that the nonlinear behavior of B starts at 20 V whose equivalent calculated deflection is 192 nm: both values are in quite good concordance. The same happens with cantilever E whose Q factor and critical amplitude are about 10 000 and 3 nm respectively according to Table V - 4 and Table V - 7. The calculated deflection for 2 V, whereby a strong nonlinear behavior is already visible (see Figure 6), is 2 nm in good concordance with the calculated  $x_C$  value (about 3 nm).

These results confirm that a sufficiently high voltage can result in a high enough static deflection so that the cantilever bends too much and comes out of its linear regime (it exceeds  $x_C$ ).

### III.1.c.v) Noise considerations

In this section, theoretically calculated noise levels are compared to experimental signal levels. Mainly three categories of noise may affect the electrical output response: (i) the noise generated by the nanomechanical device, (ii) the one generated by the CMOS circuitry, and (iii) an (external) noise related to the measurement set-up.

First, let us estimate the magnitude of the intrinsic noise of the nanoresonator: we make the assumption that it is exclusively of thermomechanical origin (see chapter 1). Following this approach, the current noise arising from thermomechanical motion [6] is estimated hereafter. According to the equipartition theorem, the thermal energy in the cantilever generates a motion of the cantilever:

$$\frac{1}{2}k_B T = \frac{1}{2}m_{EFF} \omega_0^2 \langle x_{TH}^2 \rangle \quad (V.16)$$

where  $k_B$  is the Boltzmann constant,  $T$  the temperature,  $m_{EFF}$  the efficient mass of the resonator,  $\omega_0$  the angular resonance frequency and  $\langle x_{TH}^2 \rangle$  the mean-square resulting displacement of the end of the cantilever.

To simplify the calculation of this term, we consider that the density of displacement noise  $\overline{x^2(\omega)}$  is constant over the resonator bandwidth ( $\omega_0/Q$ ). In this way, we calculate the effective noise displacement  $x_{THN}$  over the considered measurement bandwidth  $B$ :

$$\langle x_{TH}^2 \rangle = \int_0^\infty \frac{\overline{x^2(\omega)}}{B} d\omega \approx \int_{\omega_0 - \frac{\omega_0}{2Q}}^{\omega_0 + \frac{\omega_0}{2Q}} \frac{\overline{x^2(\omega)}}{B} d\omega \approx x_{THN}^2 \frac{\omega_0}{BQ} \quad (V.17)$$

Computing now eq.(V.16) with eq.(V.17), the oscillation amplitude due to thermomechanical noise is estimated as:

$$x_{THN} \approx \sqrt{\frac{k_B T Q B}{m_{EFF} \omega_0^3}} \quad (V.18)$$

then, computing eq.(V.18) with eq.(II.68), the resulting current noise of these oscillations is:

$$i_{NOISE} \approx \eta \omega_0 \langle x_{TH} \rangle = \frac{\varepsilon A}{d^2} V_{INDC} \sqrt{\frac{k_B T Q B}{m_{EFF} \omega_0}} \quad (V.19)$$

Calculating this noise for several samples measured either in air or vacuum with a measurement bandwidth  $B=10$  Hz (corresponding to the band-pass filter of the network analyzer), we find that  $i_{NOISE}$  is systematically in the order of 10-20 fA RMS.

Let us compare now this value with the equivalent noise current at CCII circuit input (ENCCI). The density of this noise, called  $D_{ENCCI}$ , can be calculated dividing the density of the output voltage noise  $D_{OVN}$  (obtained by simulation and reported in table III-8) by the transimpedance gain:

$$D_{ENCCI} = \frac{D_{OVN}}{100 R_{LOAD}} \quad (V.20)$$

For  $R_{POL}=200$  k $\Omega$  (see table III-8),  $D_{ENCCI} \approx 0.7$  pA/ $\sqrt{\text{Hz}}$  (RMS). Let us numerically estimate the noise levels for two characteristic samples (cantilevers B and E). The resonator bandwidth  $BW$  is calculated according to eq.III-12, then the equivalent noise current at circuit input (ENCCI) is evaluated. From this value, the resonance signal to noise ratio (SNR) is calculated considering the data of Table V - 4. Then, the equivalent voltage gain (see eq.III.13) is calculated:

$$\text{voltage gain} = 20 \log \left( \frac{ENCCI * 100 * R_{LOAD}}{V_{INAC}} \right) \quad (V.21)$$

As an indication, the background signal level is mentioned as well. The results are reported in Table V - 9.:

Cantilever	Q $V_{INDC}$ (V)	BW (Hz)	ENCCI (A)	SNR (dB)	Voltage gain (dB)	Experimental background signal level (dB)
B	10 (air) 19	140 k	0.26 n	14	-94 for $V_{INAC}=1$ V	-75
E	9150 (vac.) 1	160	9 p	27	-103 for $V_{INAC}=0.09$ V	-90

**Table V - 9. Theoretical estimates of the noise generated by the CMOS circuitry based on experimental data**

This table reveals that the noise generated by the CMOS circuitry dominates over the thermomechanical noise by at least three orders of magnitude and that the average SNR is around 20 dB. This table also confirms the previous assumption that the background signal results mostly from the parallel stray capacitance  $C_{PA}$  and not from the noise level. These data also indicate that the external noise does not seem to play any key role here.

## III.2. Electrical measurement of out-of-plane vibrating quad-beams

### III.2.a. Samples characteristics

The quad-beams are made of polysilicon and have been defined by electron-beam (eBL) lithography on pre-fabricated CMOS substrates. In this way, it has been possible to create new prototypes in order to optimize the design for an operation in out-of-plane flexion.

Geometrical dimensions measured by SEM of two characteristic QB are reported in Table V - 10. The lithography technique employed for their patterning is specified.  $L_1$  is the plate width,  $l$  the beam length,  $b$  the beam width,  $h$  the thickness and  $d$  the QB plate - bottom electrode (substrate) gap.

Reference	Simplified Denomination	$L_1$ ( $\mu\text{m}$ )	$l$ ( $\mu\text{m}$ )	$b$ (nm)	$h$ (nm)	$d$ ( $\mu\text{m}$ )	Patterning technique	$^1f_{EXP}$ (MHz)	$^2f_{TH}$ (MHz)
3157-13-c 19 A6	A	6.25	13.45	765	450	1	eBL	1.50	1.47
3157-13-c 16 A4	B	6	13.3	420	450	1	eBL	1.43	1.17

Table V - 10. QB samples characteristics. Geometrical dimensions measured by SEM

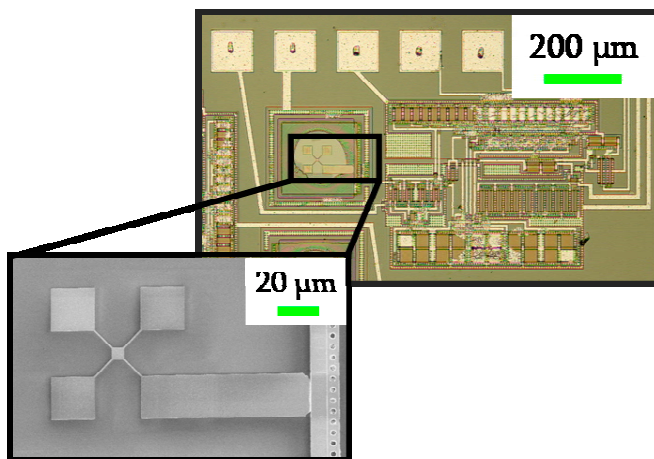


Figure 12. Images of a fully fabricated CMOS integrated quad-beam. Optical image of the CCII circuit and its juxtaposed QB; Inset (SEM image): zoom inside the integration area

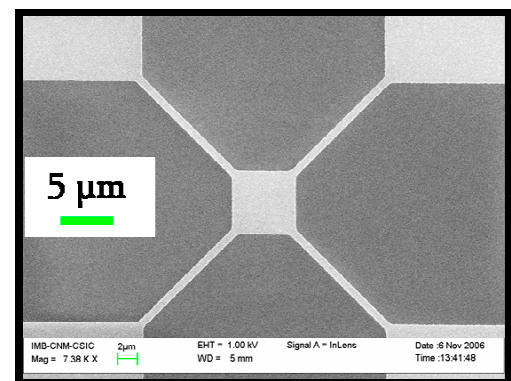


Figure 13. SEM image of a typical QB: central plate and four diagonal beams

### III.2.b. Experimental results

The correct operation of out-of-plane vibrating QB has been demonstrated in air and in vacuum: the capacitive detection scheme including the CCII CMOS circuit also successfully transduced mechanical oscillations into an electrical signal so that the mechanical frequency response of the QB, including the resonance peak, could be electrically detected. The obtained quality factors are around 30 in air, while they reach 6500 in vacuum (at  $1.1 \cdot 10^{-2}$  mBar).

<sup>1</sup> the experimental resonance frequency is extrapolated at  $V_{IN,DC}=0$  from a linear fit of spring-softening effect

<sup>2</sup> the theoretical resonance frequency is calculated with method 2 (see chapter 2)

### III.2.b.i) Measurements in air with set-up 1

Figure 14 depicts characteristic magnitude and phase responses of a QB (QB B) operated in air. In these measurements, the background signal has been pre-calibrated according to the aforementioned procedure. The resonance frequency can be tuned by varying the applied DC voltage and a clear spring-softening effect is seen in Figure 14 with increasing  $V_{INDC}$ .

As expected, this QB features much weaker phase and amplitude peaks than cantilevers, first, because of the much higher parasitic feed-through capacitance (related to the anchors), and second, because the transducing gap is as high as high  $1\ \mu\text{m}$ . Moreover, it is difficult to reduce this gap as it is determined by the thickness of the sacrificial  $\text{SiO}_2$ , the CMOS field oxide in this case. At 20 V, typical values of amplitude and phase peaks are 0.03 dB and  $0.25^\circ$  with respect to the background signal, to be compared to typical 1 dB and  $30^\circ$  for an in-plane vibrating cantilever.

Actually, these QB were initially designed to be operated at higher DC driving voltages than the presented 20 V, since they have high pull-in voltages ( $>50\ \text{V}$ ) and a big plate area to enhance the capacitive coupling. But an unexpected problem appeared in experimental tests: for voltages superior to 30-35 V the CMOS circuit operation was perturbed. This phenomenon is likely due to the depletion zone that forms at the border of the underlying n-well which serves as driving electrode. This n-well is relatively close to the p-type substrate where n-type transistors are implanted and the extension of the depletion zone probably arrives until the n-type transistors area and perturbs their operation.

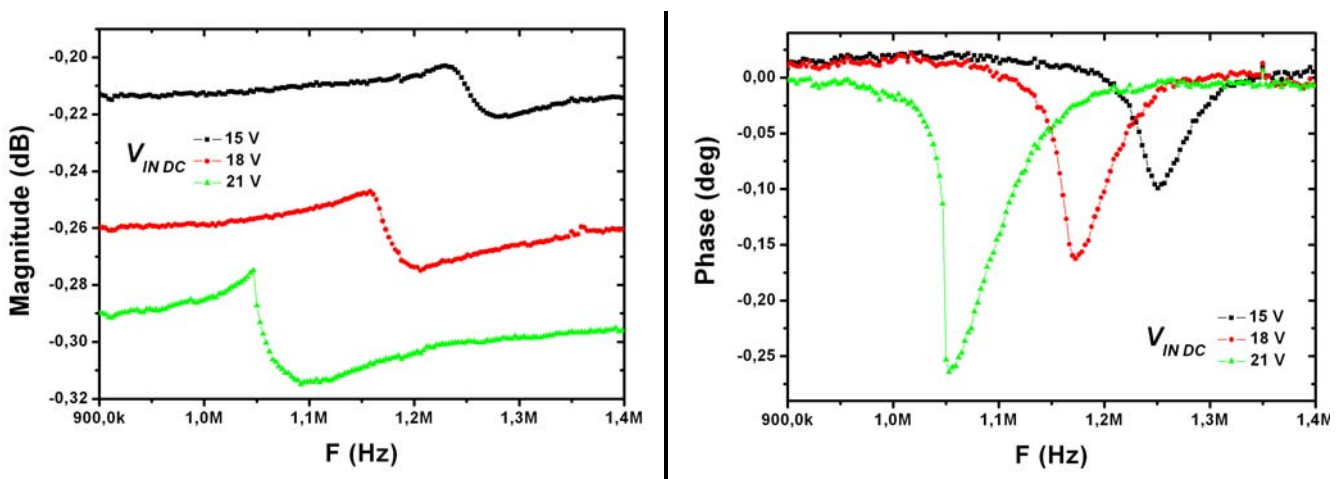


Figure 14. Calibrated resonance spectra in air of QB B for several  $V_{INDC}$  voltages, and  $V_{INAC}=0.9\ \text{V pp}$

Their thinness (about 450 nm) makes that from about  $V_{INDC}=20\ \text{V}$  on, they exhibit a nonlinear behavior (the critical oscillation amplitude mostly depends upon the thickness in the direction of vibration) what intrinsically limits the possibility to polarize QB at high voltages.

### III.2.b.ii) Measurements in vacuum with set-up 2

The chip containing QB A has been wire bonded and has been measured in the vacuum chamber of set-up 2. Figure 15 depicts spectra measured at  $P=1.1\ 10^{-2}\ \text{mBar}$  without calibrating the background signal. Lower driving voltages than in air are enough for polarizing the devices: 4 V DC added to a 0.032 V AC. All spectra exhibit a strong nonlinear behavior yielding almost vertical slopes both in magnitude and in phase. However phase changes are still smaller than  $1^\circ$ , what makes almost impossible a future implementation in close loop. The Q factors are in the order of 5000-6500.

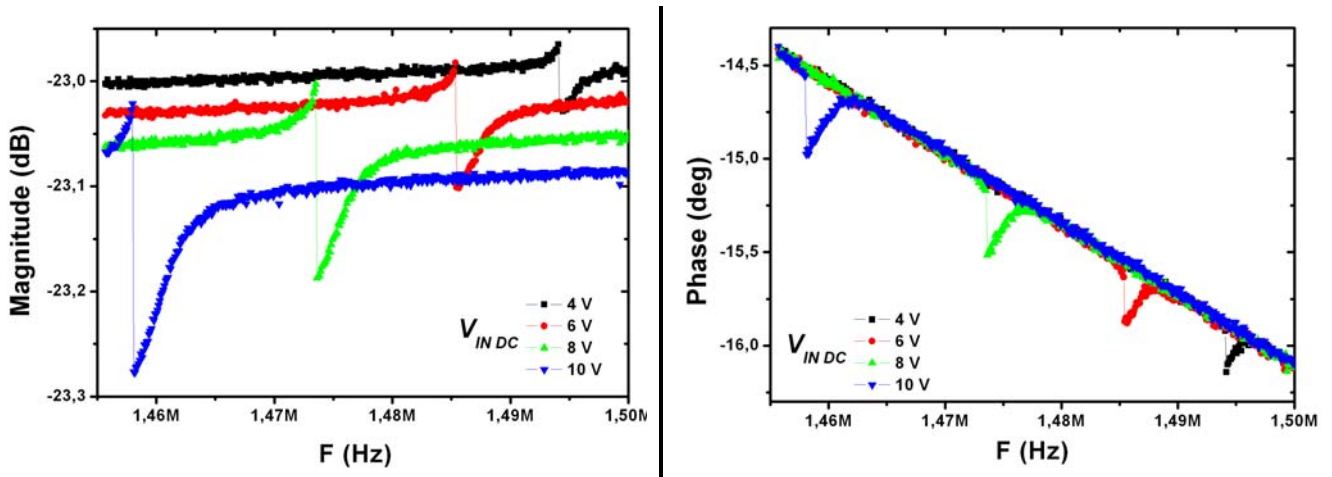


Figure 15. Non-calibrated resonance spectra in vacuum ( $P= 0.011$  mBar) of QB A for several  $V_{IN DC}$  voltages and  $V_{IN AC}=32$  mV pp.

### III.2.b.iii) Electrical Results Summary

The electrical results of QB A and B are summarized in Table V - 11 and Table V - 12.

Table V - 11 reports data of calibrated measurements.  $\mathfrak{R}(\text{dB})$  means the background signal level and  $\Delta G(\text{dB})$  the relative amplitude of the resonance peak of the calibrated signal.  $I_{RES\_EXP}$  and  $I_{RES\_TH}$  are obtained following the method exposed for Table V - 3.

QB	$R_{LOAD}$ $R_{POL}$	$V_{PI}$ (V)	$V_{IN DC}$ (V)	$V_{IN AC}$ (Vpp)	Q	$\mathfrak{R}(\text{dB})$ BS	$\Delta G(\text{dB})$	$I_{RES\_EXP}$ (nA)	$I_{RES\_TH}$ (nA)
A	$932\Omega$ $187\text{k}\Omega$	60	20	0.7	32	-24	0.0115	<b>0.63</b>	<b>1.76</b>
B	$923\Omega$ $183\text{k}\Omega$	52	15 18	0.9	32	-24	0.0108 0.0129	<b>0.77</b> <b>0.91</b>	<b>1.88</b> <b>2.71</b>

Table V - 11. Results of electrical measurements obtained with background signal calibration.

Table V - 12 reports data without background signal calibration.  $G(\text{dB})_{BS}$  means the background signal level and  $G(\text{dB})_{Res}$  the amplitude of the resonance peak.  $I_{RES\_EXP}$  and  $I_{RES\_TH}$  are obtained following the method exposed for Table V - 3.

QB	$R_{LOAD}$ $R_{POL}$	$V_{PI}$ (V)	$V_{IN AC}$ (mV pp)	$V_{IN DC}$ (V)	Q	P (mBar)	$G(\text{dB})$ BS	$G(\text{dB})$ Res	$I_{RES\_EXP}$ (nA)	$I_{RES\_TH}$ (nA)
A	$932\Omega$ $187\text{k}\Omega$	60	32	6	6440		-23.025	-22.98	0.13	1.41
				8	5500	0.011	-23.055	-23	0.15	2.1
				10	4300		-23.082	-23.02	0.17	2.6
				4	6700	0.011	-22.995	-22.969	0.073	0.65
				7000	0.12	-22.995	-22.972	0.064	0.68	
				2600	1	-22.995	-22.974	0.059	0.25	
				561	10	-22.989	-22.981	0.022	0.055	

Table V - 12. Electrical measurements results obtained without background signal calibration.

The pull-in voltage is interestingly high but as explained before it has not been possible to polarize higher than 25-30 V.

Concerning the accuracy of the RLC model for QB, the experimental value of  $I_{RES\_EXP}$  is systematically smaller than  $I_{RES\_TH}$  by a factor comprised between three and ten. This is probably due the conjugation of two factors. First, the Q factor is difficult to extract because of the low signal levels, and the method used here probably slightly overestimates the Q, what contributes to calculate too high values of  $I_{RES\_EXP}$ . Second, the RLC model depends on a linear restoring force and the problem here is to accurately estimate  $k_{QB}$ , the QB spring constant. The anchor underetching makes very difficult the determination of simple expression for  $k_{QB}$ . Moreover, as it will be explained later, these structures are stressed (what is consistent with the polycrystalline nature of the material) what puts in question the use of a linear RLC model based on an elastic constant  $k_{QB}$ . Even so, the RLC model remains a good qualitative model to predict within one order of magnitude the signal levels generated by a polysilicon QB.

### III.2.c. Analysis of results

Different features of the experimental behavior of quad-beams are analyzed in this section.

#### III.2.c.i) Estimation of the fringing field parasitic capacitance $C_{PA}$

In order to estimate  $C_{PA}$ , a comparison is made between experimental curves and simulated resonance spectra obtained with real parameters. The extracted value, obtained by fitting the level of background signal, is compared to the value of the capacitance related to the four anchors area.

For QB A and B, the capacitance related to the anchors is calculated around 80 fF. This value is in good concordance with the results provided by the simulations that fit the experimental curves of QB A and B. This confirms the assumption that  $C_{PA}$  is generated by the anchor capacitor.

#### III.2.c.ii) Q factor evolution as a function of the pressure

In Figure 16 and Figure 17, the Q factor is extracted from resonance spectra measured at different levels of pressure and maintaining all the other parameters constant.

From Figure 17, it seems that the most pronounced evolution occurs above 0.1 mBar like for cantilevers: this pressure level seems to represent a threshold below which no major improvement is achieved.

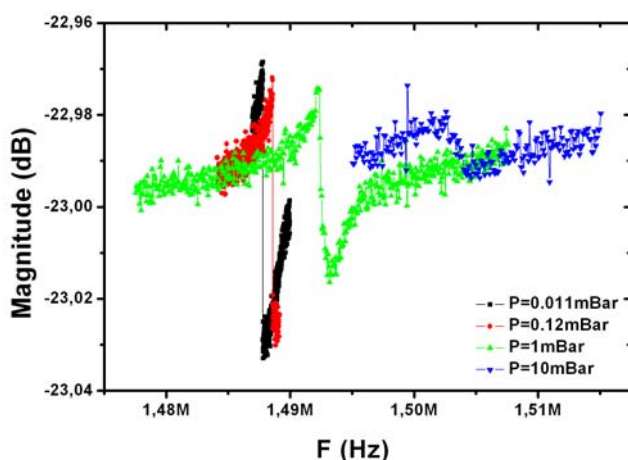


Figure 16. Non-calibrated resonance spectra of QBA recorded at different levels of vacuum for  $V_{INDC}=4$  V and  $V_{INAC}=32$  mV pp.

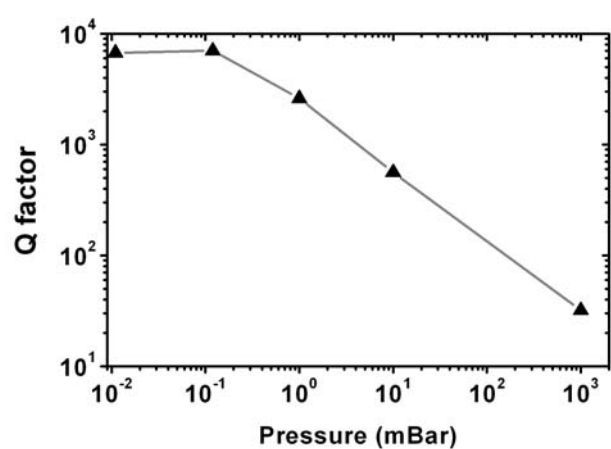


Figure 17. Corresponding dependence of the Q factor upon the level of vacuum

One can notice from Figure 11 and Figure 17 that cantilevers and quad-beams exhibit similar dependences of their Q factor upon the level of vacuum (qualitatively and quantitatively). This means that both resonators are affected in a similar way by viscous damping at ambient pressure and that they have similar mechanisms of intrinsic dissipation (clamping losses, etc... see chapter 1).

### III.2.c.iii) Driving voltage effects

In the case of cantilevers, it has been systematically observed that the driving voltage ( $V_{IN AC} + V_{IN DC}$ ) has a spring-softening effect on the resonance frequency and that it tunes it down. In the case of QB, this statement is not always true and in our samples every sample has exhibited its own behavior depending upon one critical parameter: its upwards or downwards curvature.

Indeed, the key parameter that seems to determine the effect of the driving voltage is the initial curvature caused by the stress of the structural polysilicon layer (deposited on top of a  $\text{SiO}_2$  layer). Just after their release, several QB located on the same chip have been inspected with a CONFOCAL microscope.

In almost all the QB, the central plate is curved upwards of between 150 and 300 nm with respect to the anchor. However, one (let us call it QB C) was curved downwards by 300 nm (on other chips the same was observed in the same proportion: less than 10 % in number of devices). It seems that there is a correlation between the initial curvature and the effect of the driving voltage.

QB with initial upward curvature tend to feature spring-softening effect like in Figure 18 while QB with initial downward curvature tend to feature the contrary, in other words what could be called 'spring-stiffening' effect like in Figure 19 and Figure 20 (curves of QB C).

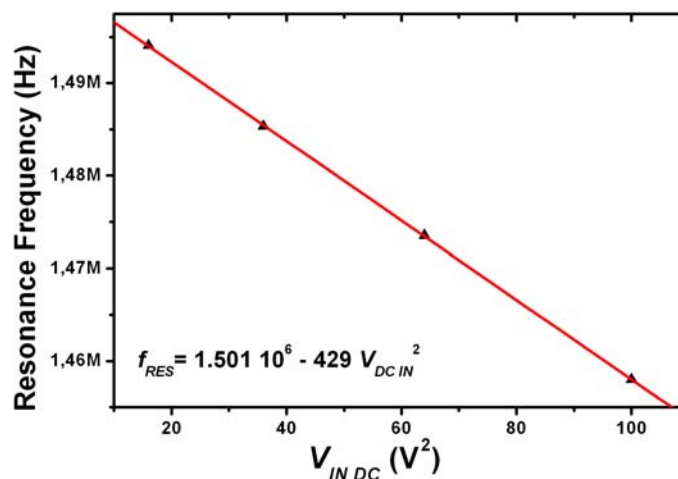


Figure 18. Based on data of Figure 15, resonance frequency dependence upon  $V_{IN DC}$

Based on the study done in chapter 2, qualitative explanations can be proposed. Concerning QB initially curved upwards, the electrostatic force created by the driving voltage attracts them downwards, therefore the mechanical strain tends to decrease as they go towards their relaxed flat position. In these conditions, the electrostatic force dominates and spring softening effect occurs.

Concerning QB initially curved downwards, the electrostatic force created by the driving voltage also attracts them downwards, but in this case the strain tends to increase as they are more

pulled away from the equilibrium position. This creates a situation similar to the case of a stretched guitar string: the QB is mechanically stiffened. This behavior dominates over electrostatic attraction and ‘spring stiffening’ effect occurs (also named ‘hard-spring’ effect). This probably remains true while the gap is not too narrow otherwise electrostatic force would probably dominate again.

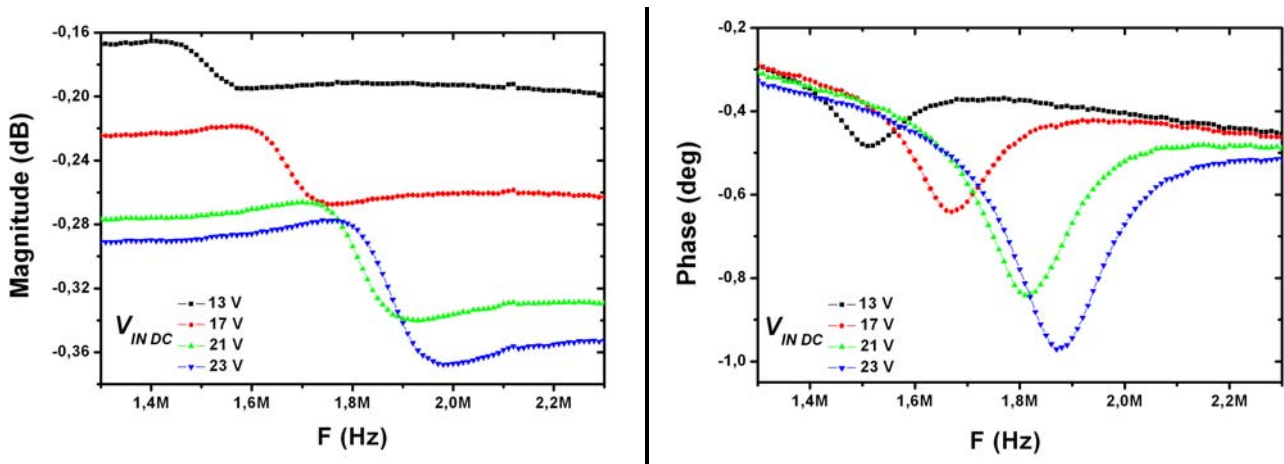


Figure 19. QB C frequency response as a function of DC driving voltage: magnitude (left) and phase (right)

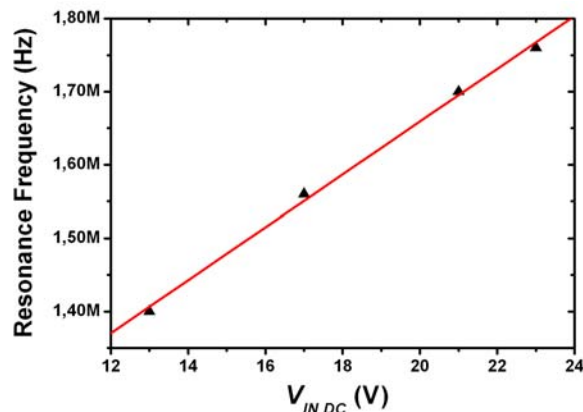


Figure 20. Resonance frequency dependence of QB upon the driving voltage

## Conclusion of chapter 5

Following a capacitive detection scheme, the mechanical resonance of fully integrated nanomechanical resonators, cantilevers and quad-beams, has been successfully sensed by the CMOS circuitry. Cantilevers and quad-beams have exhibited quality factors in vacuum up to 9500 and 7000 respectively. The resonance frequency could be tuned by varying the driving voltage and interesting hysteretic nonlinear behaviors have been observed either in air or in vacuum.

These results also demonstrate that the correct operations of both the CMOS circuit and the general system are not degraded by post-processing technologies based on nSL or eBL.

The RLC electromechanical model is found to be more qualitative than quantitative but the high number of uncertainties regarding the resonators parameters (Young modulus, exact dimensions, underetching, etc...) impedes to conclude more definitively on the model accuracy. At least, this model is precise enough to predict resonance signal levels within one order of magnitude what is actually sufficient to define the specifications of a CMOS readout circuit.

As future prospects, several improvements regarding the design of the resonator could allow obtaining better electrical responses with the same circuit topology. In the case of quad-beams, the integration area should be placed farther from the circuit area so that it can be polarized at much higher voltages without perturbing the operation of closely located MOS transistors. In order to reduce 'vertical' (out-of-plane) stray capacitances, the pads area should be minimized. This could be achieved by incorporating holes in the central plate so that the etching time would be reduced and smaller anchors would be enough to support the structure. Concerning the cantilevers, optimizing the design of the readout and driving electrodes could lead to an important reduction of the fringing field parasitic capacitance.

After demonstrating the successful fabrication and the correct operation of CMOS integrated nano/micromechanical resonators, these devices have been implemented as ultra-sensitive mass sensors: this is the topic of next chapter (6).

## Bibliographical references

1. Badzey, R.L. and P. Mohanty  
**Coherent signal amplification in bistable nanomechanical oscillators by stochastic resonance**  
Nature, 2005. **437**(7061): p. 995-998.
2. Buks, E. and B. Yurke  
**Mass detection with a nonlinear nanomechanical resonator**  
Physical Review E, 2006. **74**(4).
3. Mohanty, P., D.A. Harrington, K.L. Ekinici, Y.T. Yang, M.J. Murphy, and M.L. Roukes  
**Intrinsic dissipation in high-frequency micromechanical resonators**  
Physical Review B, 2002. **66**(8).
4. Xu, Y., J.T. Lin, B.W. Alphenaar, and R.S. Keynton  
**Viscous damping of microresonators for gas composition analysis**  
Applied Physics Letters, 2006. **88**(14).
5. Sharpe, W.N.  
**Measurement of Young's modulus, Poisson's ratio, and tensile strength of polysilicon**  
in the proceedings of the *IEEE MEMS*. 1997.
6. Albrecht, T.R., P. Grutter, D. Horne, and D. Rugar  
**Frequency-Modulation Detection Using High-Q Cantilevers for Enhanced Force Microscope Sensitivity**  
Journal of Applied Physics, 1991. **69**(2): p. 668-673.

# CHAPTER 6

## FUNCTIONAL CHARACTERIZATION

### IMPLEMENTATION OF N-MEMS/CMOS AS MASS SENSORS

I.	Punctual mass sensing.....	181
I.1.	Monitoring the evaporation of femtoliter droplets (exp. I).....	181
I.1.a.	Experimental set-up.....	182
I.1.b.	Results and analysis.....	186
I.2.	Double cantilever resonators (exp. II).....	189
I.2.a.	Features of double cantilever devices.....	189
I.2.b.	Results of mass sensing.....	195
II.	Distributed mass sensing experiments.....	200
II.1.	Monitoring the deposition of ultra-thin gold layers (exp. III).....	202
II.1.a.	Experimental set-up.....	202
II.1.b.	Nanomechanical sensor.....	206
II.1.c.	Results and analysis.....	207
II.2.	Application of NEMS/CMOS mass sensors as positioning sensors (exp. IV).....	216
II.2.a.	Quasi-dynamic approach.....	216
II.2.b.	System description.....	216
II.2.b.i)	Alignment procedure.....	218
II.2.b.ii)	Mass sensor requirements.....	220
	Conclusion of chapter 6.....	223
	Bibliographical references.....	224

Chapter 1 established a state-of-the-art of existing nano/micromechanical resonators implemented as highly sensitive mass sensors. Compared to quartz-crystal microbalances (QCM), they offer advantages in terms of sensitivity and system integration. In addition, if they are small enough, they can provide mass sensing with spatial resolution.

These two features, unprecedented sensitivity and spatial resolution, offer new opportunities both for nanoscience and engineering purposes. Concerning the scientific aspect,

such sensors can help in studying previously unexplored chemical, physical or biological new mechanisms. Concerning engineering and industrial techniques, they could replace QCM in a near future for the monitoring of the deposition of thin layers in semiconductor processing systems, as well as serve as positioning sensors for nanostencil lithography systems of as it will subsequently explained.

Chapters 3, 4 and 5 have given a detailed description of the modeling, design, fabrication and characterization of Si nano and micromechanical resonators monolithically integrated with CMOS circuitry for on-chip resonance signal detection and amplification. These monolithic integrated microsystems that could contain very large scale integration of arrays of resonators can potentially be fabricated in batch using standard silicon technology processes. They represent compact and portable systems getting closer to the category of system-on-chip (SoC).

Taking advantage of the large number of fabricated N-MEMS/CMOS chips, four different experiments have been designed and carried out. Experiments I and II are oriented towards punctual mass sensing and experiments III and IV towards distributed mass sensing.

Experiment I is related to the development of nanofluidics and nanodispensing. The emergence of these two techniques is actually linked to a better understanding of wetting mechanisms at these scales. Within this field, the work presented here represents a breakthrough: the capability of NEMS/CMOS mass sensors is used to monitor the evaporation of femtoliter droplets, i.e. volumes that are nine orders of magnitude smaller than published data.

In experiment II, it has been tested a new functionality in the operation of nanomechanical mass sensors. A new device based on a double cantilever is proposed, allowing differential mass measurements in air with a self-reference, thus directly providing the measurement uncertainty. In parallel, other interesting features of this device are introduced. Among them, the reasons why such a device could allow measuring the mass change in function of amplitude changes and not of frequency shifts, as usually done, will be exposed.

Experiments III and IV are linked together. Actually, experiment IV consists of implementing a NEMS/CMOS mass sensor as position sensitive device, concretely as an alignment sensor. CNM and EPFL are currently developing a demonstrator of quasi-dynamic nanostencil lithography system (QDS). This system is an automated step-and-repeat nanopatterning apparatus that perform successive depositions of various materials with various patterns through a movable full-wafer stencil shadow mask. In-between each deposition step, the vacuum is not broken so that high-purity deposits are obtainable. In this context, the mass sensor will help in aligning in-situ the full-wafer nanostencil with respect to the substrate to be patterned. The first sketch of this system is presented. As a first step towards the realization of this objective, experiment III has been carried out in order to demonstrate the functionality of NEMS/CMOS mass sensors and to characterize their performance as ultra-sensitive devices for the monitoring of the deposition of ultra-thin layers.

All four experiments will be successively described and their main results will be exposed. The variety of applications presented hereafter is a real proof of the versatility of NEMS-based mass sensors.

## I. Punctual mass sensing.

In this section, two experiments of punctual mass sensing are described detailing the initial motivation and their potential interest as well as their practical implementation. Then, the main significant obtained results are discussed.

### I.1. Monitoring the evaporation of femtoliter droplets (exp. I)

This experiment has been carried out in collaboration with Thierry Ondarçuhu and Erik Dujardin from CEMES-CNRS, Toulouse (France), whose activity is centered on the study of wetting phenomena, nanodispensing and focused ion beam (FIB)-based nano/micromachining techniques.

Manipulation and deposition of nano/micrometer scale liquid sessile (i.e. attached) droplets on surfaces is a relatively recent topic facing a major development for about ten years. Diverse techniques like microcontact printing [1], microfluidics [2, 3], inkjet printing [4], or microlever plotting [5] routinely perform micrometer scale surface patterning, then dip-pen (DPN) lithography [6] pushed the resolution limit to the deep submicron scale. These methods constitute new tools to perform very local surface patterning or functionalization: they have a great potential for instance for biological sampling, micro/nanofluidics refilling and could eventually serve as a way to correct layout or pattern defects in IC.

In this context, CEMES has developed a novel nanoscale dispensing system (NADIS [7, 8]) that combines the high resolution potentials of DPN with the flexibility of manipulating liquids. It is based on the transfer of liquid by direct contact with the substrate of a hollow commercial AFM tip whose apex has been milled by FIB to make a small aperture. When the cantilever is loaded on its top side with a liquid, a large number of droplets with volumes in the femtoliter to subattoliter range can be deposited on a substrate with high spatial density. The parameters influencing the size of the spots are discussed in [7]: basically the spot size is determined (i) by the hole diameter but also (ii) by the wetting properties of the solvent on the tip and on the substrate surface (hydrophobic/philic character) and (iii) by the contact time.

The need of methods to manipulate very small liquid quantities has recently emerged, leading to the development of nanofluidics or nanodispensing techniques. The point is that at these scales, evaporation processes become important. However, previous comprehensive studies have only given precise descriptions of the evaporation mechanisms for microliter droplets [9] (diameter in the millimetre range). The question of the validity of the macroscopic model for droplets with diameters in the micro and nano-scale (sub-femtoliter range) still has to be addressed.

In this context, we present a time-resolved study of the evaporation in air of sessile droplets with diameters in the  $\mu\text{m}$  range, what corresponds to volumes of femtoliters and smaller, i.e. nine orders of magnitude smaller than presently published data. The droplets have been deposited by NADIS and nanomechanical resonators have been used to determine with high precision the change in mass of liquid droplets with time.

### I.1.a. Experimental set-up

The experiment has been based on employing CMOS integrated QB resonators as mass sensors for the monitoring of the droplet mass decrease along the evaporation process.

#### SENSOR DESIGN AND FABRICATION

The nanomechanical device used as mass sensor is a quad-beam resonator (QB). These QB (Figure 1) have been defined by electron-beam lithography on pre-fabricated CMOS substrates according to the process described in chapter 4 and with the CCII circuitry presented in chapters 3 and 5. Consequently, these resonators must have a resonance frequency limited to 2-3 MHz (because of the CMOS technology). Thus, devices have been adequately designed in order to have such resonance frequencies and a punctual mass sensitivity in the order of 100 attogram ( $10^{-16}$  g). Typically, they have the following dimensions (like QB A of table V.10): plate width and beam length around  $10\ \mu\text{m}$ , thickness and beam width in the submicron scale.

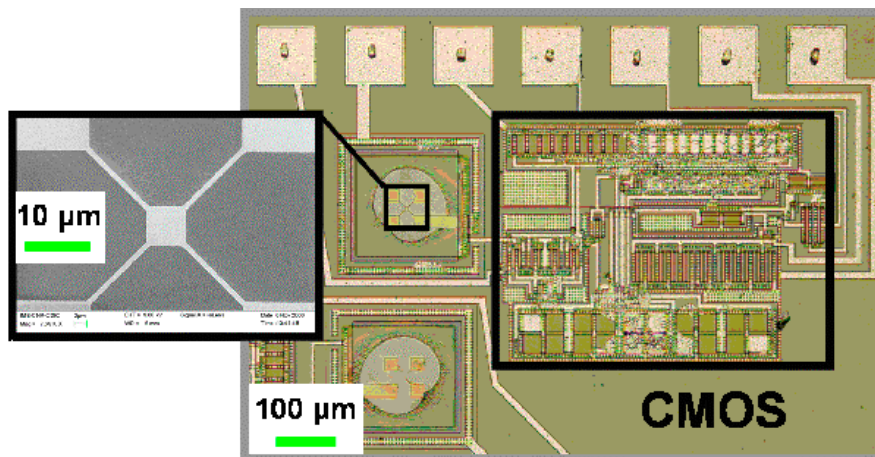


**Figure 1. Optical image of a CMOS integrated QB. The device has the following dimensions: central plate  $6 \times 6\ \mu\text{m}^2$ , beams width and length:  $600\ \text{nm}$  and  $13.5\ \mu\text{m}$ , thickness:  $450\ \text{nm}$ .**

The QB is particularly adapted to mass measurements in air of any solid (particles, molecular aggregate) or liquid (sessile droplets of any nature) compounds. In addition to its high mass sensitivity, the QBR operated in its out-of-plane flexion fundamental mode provides a large active area for convenient droplet depositions: the alignment of the dispensing probe with the QB sensor is considerably easier than for example with narrow cantilevers.

In the QB design, the central plate is located at the extremity of the four beams what ensures that it undergoes the maximum deflection (i.e. the point where the mass sensitivity is the highest [10]). Also, when depositing a punctual mass only on the central plate and operating it in the out-of-plane fundamental mode, the QB should remain relatively insensitive to the adsorbate stiffness [11] and to the induced surface stress [12]: these assumptions ensure that the mass loading effect is mechanically dominant over stiffness (i.e. spring constant) variations. In the same perspective, the position of the adsorbate on the plate should not have any effect [10, 13] as it is assumed that the plate remains flat and uniformly undergoes the same (maximized) deflection.

The electrical detection (capacitive) scheme is non-invasive with respect to evaporation processes as it does not interfere with the specie to measure. On the contrary, laser-based optical detection techniques would have likely perturbed the measurement: the heat dissipated by the

laser spot onto the plate surface would have artificially accelerated the evaporation and diminish its duration.

In comparison, the electrical detection is not optimal neither since relatively low resonance signal levels are obtained because of the high feed-through capacitances inherent to QB. But at least the detection technique does not interfere with the evaporation process.

#### SENSOR CALIBRATION

Prior to the evaporation experiments, QB were calibrated (Figure 2) by successively loading, using a micro-manipulator, 1, 2, 3, and 4 silica beads whose mass is well-known (diameter of 1.57  $\mu\text{m}$  and density of 2.18  $\text{g}\cdot\text{cm}^{-3}$ ). The resulting resonance frequency shifts are measured and reported in Figure 2. The calibration curve (CC) constitutes a very useful and accurate reference for subsequent droplets mass measurements.

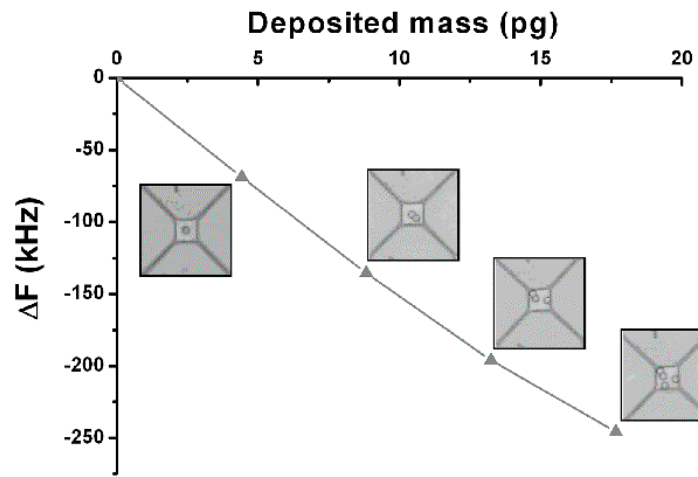


Figure 2. Calibration curve of the QB mass sensor obtained by successive loading of 1, 2, 3 and 4 silica beads, 4.4 pg each, using a micro-manipulator. The resulting resonance frequency shift is plotted as a function of the deposited mass.

For a deposited mass smaller than 5 pg, the CC follows a linear trend whose slope is the punctual mass sensitivity  $S$ . For small variations around the resonance frequency  $f$ ,  $S$  is given by eq. (VI.1) (see eq.II-46):

$$S \cong 2 \frac{m_{EFF\_P}}{f} \quad (\text{VI.1})$$

where  $m_{EFF\_P}$  is the efficient mass of the resonator for a punctual mass loading. From Figure 2, and for small variations around the unloaded resonance frequency,  $S$  is estimated around  $6.4 \cdot 10^{-17} \text{ g}\cdot\text{Hz}^{-1}$ .

This value is not the intrinsic mass sensitivity of the resonator but the one valid only for a given  $V_{IN\ DC}$  voltage. Indeed, the QB sensors used here are subject to spring-softening effect and according to eq.(VI.1) spring-softening tends to artificially decrease  $f$  what slightly degrades  $S$ . Therefore, it is important to emphasize that this calibration curve is valid only at the  $V_{IN\ DC}$  voltage whereby it was obtained (22 V in this case) and that all mass experiments done with the QB of Figure 2 must be performed precisely at this voltage.

However, for a **larger** deposited mass, the CC does not follow any more a linear trend as shows Figure 2, not because of a loss of linearity (see chapter 2) but simply because eq.(VI.1) cannot be considered constant anymore as  $f$  decreases according as some mass is deposited. For large variations, the quotient of eq.(VI.1) tends to increase as  $f$  decreases: this is why in Figure 2 the slope tends to get flatter. In that case, the resonance frequency variation can be generalized by eq.(II-53):

$$f_{RES} = f_U \sqrt{\frac{m_{EFF\_P}}{m_{EFF\_P} + m_{DEPOSITED\_PUNCTUAL}}} \quad (VI.2)$$

where  $f_U$  is the initial unloaded resonance frequency (actually determined by the level of  $V_{INDC}$ ),  $m_{EFF\_P}$  is the efficient mass of the resonator for a punctual mass loading, and  $m_{DEPOSITED\_PUNCTUAL}$  is the quantity of deposited mass.

$m_{EFF\_P}$  is calculated based on eq.(II-36):

$$m_{EFF\_P} = m_{PLATE} + \frac{33}{140} m_{BEAM} \quad (VI.3)$$

The frequency shift is plotted in Figure 3 as a function of the deposited mass, comparing the theoretical expression provided by eq.(VI.2) and the experimental data of Figure 2, and indicating the line with constant sensitivity given by eq.(VI.1). The theoretical curve is fitted adjusting the efficient mass of the resonator  $m_{EFF\_P}$  to 38 pg, very close to the nominal value of 42 pg calculated from the dimensions measured by SEM. Both theoretical and experimental curves are in good agreement:

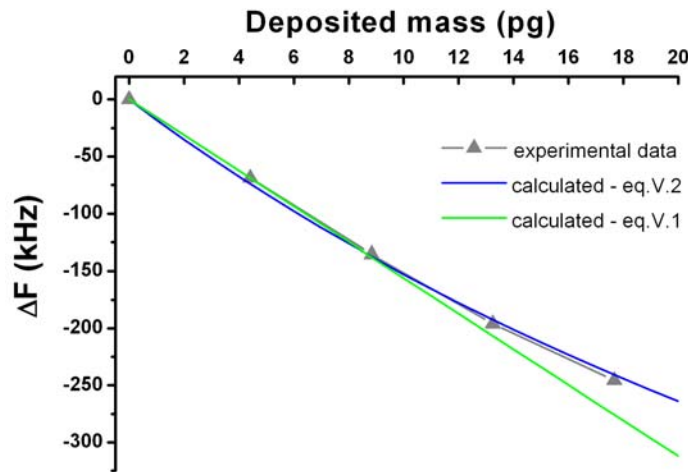


Figure 3. Comparison between the experimental data of Figure 2 and the theoretical curves given by eq.(VI.2) and (VI.1)

With the information provided by the calibration and considering small mass accretions, the performance of the QB mass sensor is compared to the one of commercially available quartz-crystal microbalances (QCM). Given the low Q-factors of QB in air (approx. 35), a minimum detectable frequency shift  $\Delta f_{MIN}$  of 1000 Hz is arbitrarily fixed while for QCM a value of 0.005 Hz is proposed, corresponding to the best commercially available device operated in the optimum conditions. The resulting minimum detectable mass  $\Delta m_{MIN}$ , given by  $\Delta m_{MIN} = \Delta f_{MIN} \times S_{PUNCTUAL}$ , is reported in Table VI - 1:

Device	$S_{AREAL}$ (g.cm <sup>-2</sup> .Hz <sup>-1</sup> )	$S_{PUNCTUAL}$ (g.Hz <sup>-1</sup> )	$\Delta f_{MIN}$ (Hz)	$\Delta m_{MIN}$ (pg)
QCM	$1.23 \cdot 10^{-8}$	$1.84 \cdot 10^{-8}$	0.005	92
Si QB	$1.8 \cdot 10^{-10}$	$6.4 \cdot 10^{-17}$	1000	0.064

Table VI - 1. Comparison between commercial QCM and silicon QB in terms of distributed and punctual mass sensitivity, frequency resolution in air and resulting mass resolution in air.

The obtained mass resolution of Si QB is three orders of magnitude better than the commercial QCM one. Although QCM have an outstanding frequency resolution, they suffer from a poor mass sensitivity. On the contrary, Si QB have a poor frequency resolution (furthermore this value is arbitrary and could be optimized) but a very high mass sensitivity.

The silica beads used for QB calibration have a mass in the order of the mass of the droplets to measure, i.e. few pg. In this context, the QCM would not have been able to measure them as its resolution is 92 pg. This explains why already published evaporation studies [14, 15] are limited to microliter droplets: it is because they are carried out with QCM.

In this experiment, the objective is to monitor the mass decrease from its initial value  $m_0$  until about  $m_0/10$ . If  $m_0/10 = 0.064$  pg (i.e. the detection limit  $\Delta m_{MIN}$  in Table VI - 1), the corresponding minimum initial diameter of the droplet is in the order of  $1.5/2 \mu\text{m}$ , also depending on the hydrophilic character of the QB surface (hydrophobic surfaces result in bigger volumes for a fixed diameter). This size fixes the aperture size of the NADIS probes.

#### NADIS PROBES AND DROPLETS DEPOSITION PROCEDURE

Nanodispensing of droplets is performed using the technique described in [7], based on a modified AFM set-up. NADIS tips are fabricated by modification of commercially available AFM Si<sub>3</sub>N<sub>4</sub> cantilevers (Olympus OMCL-RC800RP) by FIB milling. They allow dispensing droplets through a small hole milled at the tip apex (these tips are hollow pyramidal square-shaped). Whereas droplets as small as 75 nm in diameter can be obtained [7], tips with an aperture of 300 nm in diameter (see Figure 4) and hydrophilic outer walls were prepared in order to deposit micron-sized droplets, according to the QB resolution.

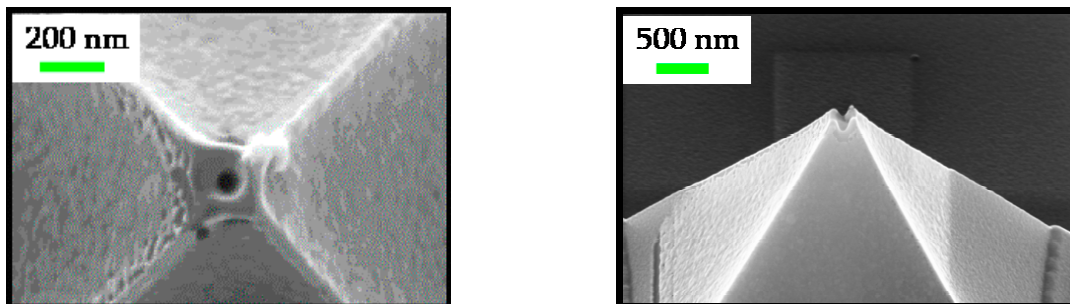


Figure 4. SEM images of modified AFM cantilever tip apex milled by FIB to form an aperture for liquid nanodispensing. (left) common NADIS probe with an aperture of 35 nm in diameter for nanoscale droplets; (right) custom NADIS probe made for this experiment with a bigger aperture of 100 nm in diameter

All the experiments were performed with glycerol-based solutions. The liquid is loaded on the modified cantilever tip with a micropipette connected to a microinjector (NARISHIGE) and controlled by a micromanipulator (THE MICROMANIPULATOR Inc.). Due to its very low volatility (boiling point, 290 °C, vapor pressure, 25 °C), the evaporation of the glycerol big accretion on top of the cantilever can take several hours.

For depositing, the tip is approached a few micrometers from the surface. Alignment with the resonator is then performed using a nanopositioning table (Figure 5) incorporated in the sample holder of the AFM set-up [16]:

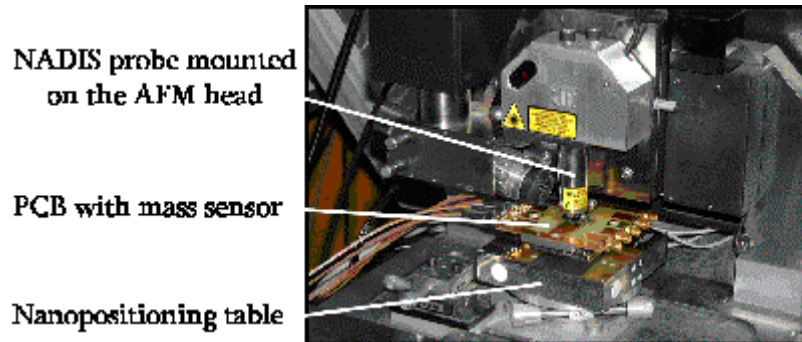


Figure 5. Experimental set-up

Droplets with diameters ranging from 1 to 5  $\mu\text{m}$  were reproducibly deposited on the resonators (Figure 6) by engaging the tip on the QB surface: the droplet size can actually be modulated by adjusting the contact time. This method was soft enough to keep the resonator properties intact (the same resonance frequency before and after tip contact is maintained).

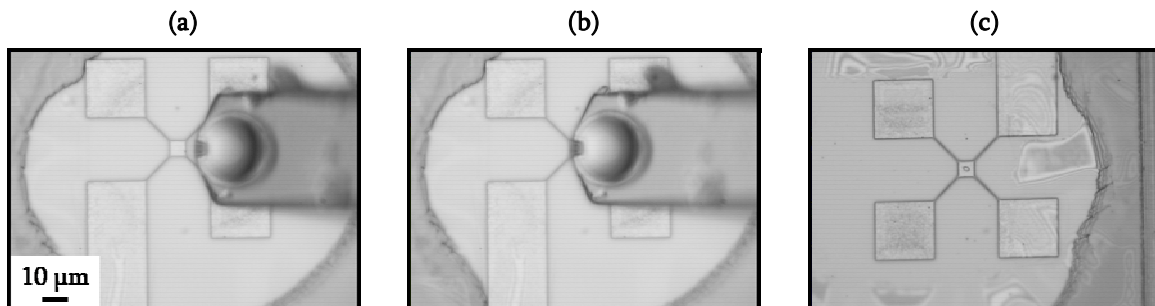


Figure 6. Top view of a nanodispensing probe (NADIS). (a) the tip, pre-loaded with a liquid, is approached; (b) it is aligned with a QB adjusting its position with the control table; (c) final image of the deposited droplet on the QB central plate.

### I.1.b. Results and analysis

During evaporation, the resonance frequency of the QB (Figure 7) is monitored. Using the calibration curve, the evolving frequency shifts are converted into mass variations so that the temporal evolution of the droplets mass is determined down to around 10 fg (10 attoliters volume) resolution. The curves are rather noisy due to limitations in the experimental set-up.

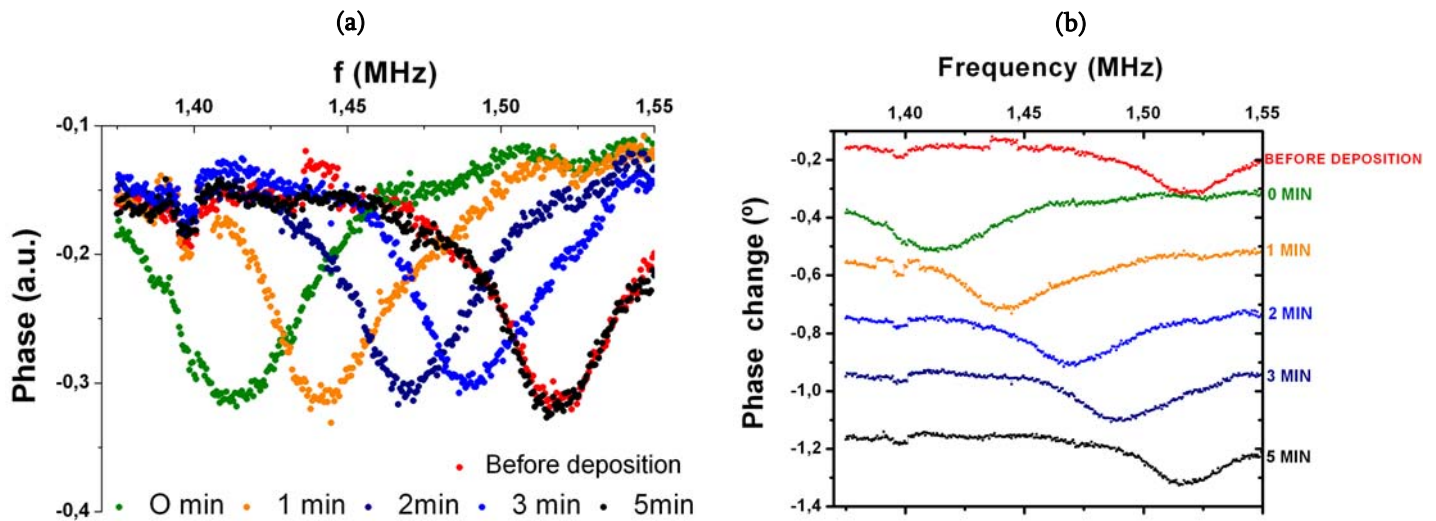


Figure 7. Evolution of the resonance frequency of a QB as a function of the evaporation time (unloaded resonance frequency  $\approx 1.5$  MHz) during the evaporation of a  $\mu\text{m}$ -sized droplet deposited by NADIS. (a) Standard curves with the same phase scale. (b) An offset is introduced between each curve in order to visualize the displacement of the phase peaks

The fact that the resonance frequency turns back to its initial value at the end of the evaporation process demonstrates that no extra particle is brought by the tip onto the surface and that the tip does not deform the QB above its elastic limit when depositing the droplet.

Time evolutions of the evaporation of glycerol droplets with initial volumes ranging from 0.2 fL to 20 fL are shown on Figure 8. The droplet mass decreases nonlinearly, with a slowing down of the evaporation rate along the process.

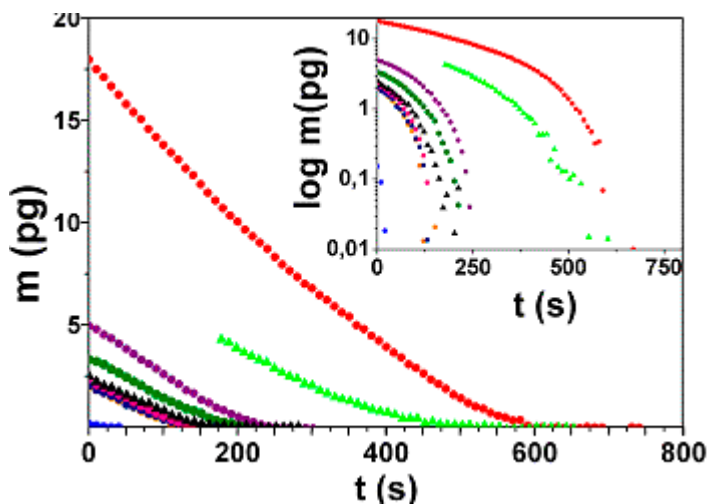


Figure 8. Temporal evolution of the mass of droplets of different initial sizes (initial volumes ranging from 0.2 fL to 20 fL). The inset plots the same data with logarithmic scale for the mass.

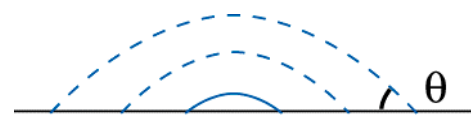


Figure 9. Constant contact angle evaporation mode on hydrophobic surfaces

It has been optically observed along the evaporation process that the droplets diameter decreases as a function of the time. This is actually characteristic of an evaporation mode taking place on hydrophobic surfaces with a constant contact angle between droplet and surface (see Figure 9). In this regime, at macroscopic scale, the droplet mass  $m$  is expected to decrease along the evaporation time with a power law  $2/3$  [9]:

$$m^{2/3} = m_0^{2/3} - \frac{2}{3}\alpha t \tag{VI.4}$$

where  $\alpha$  is a coefficient depending only on the diffusion coefficient and not on the mass, and  $m_0$  is the initial mass.

This equation has two implications: (i) first,  $m^{2/3}$  is linear with respect to the evaporation time and (ii) second, the total evaporation time  $t_E$  (at  $m=0$ ) must be proportional to the initial size at power 2/3 ( $m_0^{2/3}$ ).

To check if this macroscopic model is still valid at these scales,  $m^{2/3}$  is plotted in Figure 10 (same data as in Figure 8) as a function of time: a linear decrease with the same slope is observed for every droplet. The inset also shows that the total evaporation time  $t_E$  effectively depends on the initial mass  $m_0$  at power 2/3 (the slope of the logarithmic plot is 2/3). Both assumptions are confirmed.

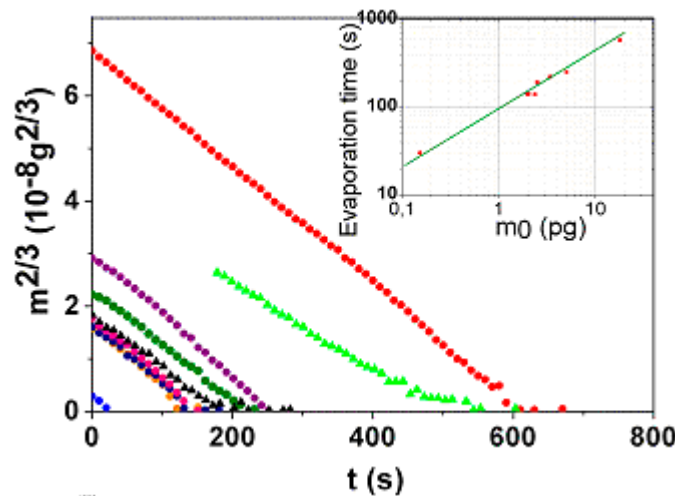


Figure 10. Temporal evolution of the droplet mass at a power 2/3 for the same data as in Figure 8. The inset is a logarithmic plot of the total evaporation time as a function of the initial mass.

Furthermore, according to eq.(VI.4), the term  $m_0^{2/3} - m^{2/3}$  should be identical for every droplet since it depends only on the time and on  $\alpha$  which is independent of the mass. This term is plotted as a function of the time for six different droplets in Figure 11:

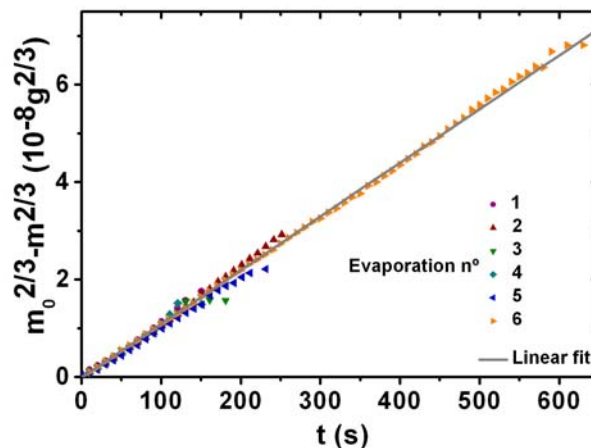


Figure 11. Plot of the term  $m_0^{2/3} - m^{2/3}$  as a function of the time, for six different droplets

The curve is almost identical for six droplets which have different initial sizes. The results of Figure 10 and Figure 11 indicate that the macroscopic laws are still valid at these scales. Values of diffusion coefficients or vaporization heat extracted from these data are presently being compared with macroscopic values.

## CONCLUSION

This experiment made in collaboration with CEMES provides a new knowledge of wetting mechanisms until the femtoliter range (micron scale droplet diameters) confirming the validity of macroscopic models down to these scales. Furthermore, it confirms the high potential in terms of mass sensing of CMOS integrated nano/micromechanical devices.

In order to explore the behavior of deep submicron scale droplets, and even below (100 nm scale), the resonator should be operated at higher frequencies to improve its sensitivity and selecting another design, for example cantilevers, more sensitive regarding the punctual mass sensitivity. In this experiment, cantilevers were not utilized due to their too reduced width compared to the droplet size but for depositions of droplets with diameters in the range of 100-500 nm, the cantilever narrowness would not be a limitation anymore.

Another parameter to take into account is that the evaporation time will be much shorter with nanometer scale droplets. This will oblige the mass sensor to have a much faster response time. To circumvent this issue, a closed-loop implementation of the resonator is being studied.

## I.2. Double cantilever resonators (exp. II)

Chapter 1 established a state-of-the-art of existing implementations of nano/micro mechanical devices as mass sensors illustrating the recent strong interest on this topic. In this type of experiment, an important question to address is to know up to what extent the observed frequency shift is exclusively due to the mass accretion.

Towards the objective of designing a compact and portable mass sensing platform operable in ambient conditions, a reliable sensing procedure has to be defined to evaluate the measurement uncertainties which mostly arise from the formation of water thin films and from the random deposition of extra particles in suspension in air.

In order to address this issue, an innovative design that allows the direct determination of the measurement uncertainty is presented. Two closely located and almost identical (in terms of material and dimensions) nanomechanical resonators are simultaneously operated: one serves as sensor and the other as reference. In this way, rapid and reliable measurements in air are made possible.

The nanomechanical device is a polysilicon double cantilever (DBC). The DBC also features other promising properties that are detailed hereafter. Finally, the self-reference application will be emphasized describing the experimental procedure and the obtained results.

### I.2.a. Features of double cantilever devices

The DBC consists of two cantilevers with the same anchor (i.e. same readout electrode) orthogonally orientated one to each other. They have been defined by electron-beam lithography on prefabricated CMOS substrates according to the process detailed in chapter 4. These DBC are

operated in their in-plane flexural fundamental mode and their oscillations are detected through the CCII circuit following the same capacitive scheme as for the single cantilevers described in chapter 3.

Both cantilevers are designated according to the nomenclature depicted in Figure 12: so-called vertical (VC) and horizontal (HC) cantilevers. Typically, these cantilevers are 14  $\mu\text{m}$  long, 300/400 nm wide, 450 nm thick and have a gap comprised between 400 nm and 1  $\mu\text{m}$  with respect to the driving electrode:

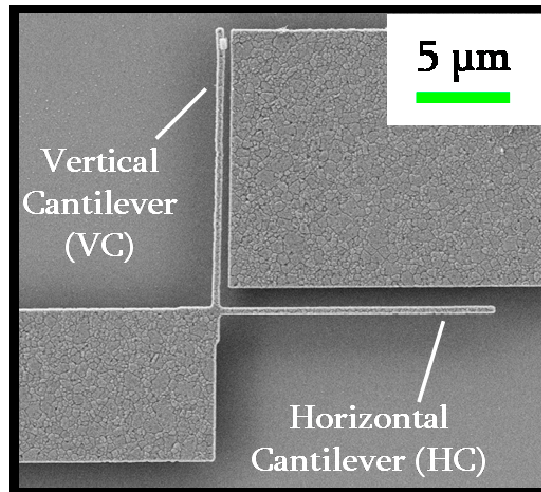


Figure 12. SEM image of a characteristic polysilicon DBC with the designation of each cantilever

In Figure 13, an overview of the integration of DBC on CMOS substrates is proposed. The inferior tilted SEM image illustrates the release.

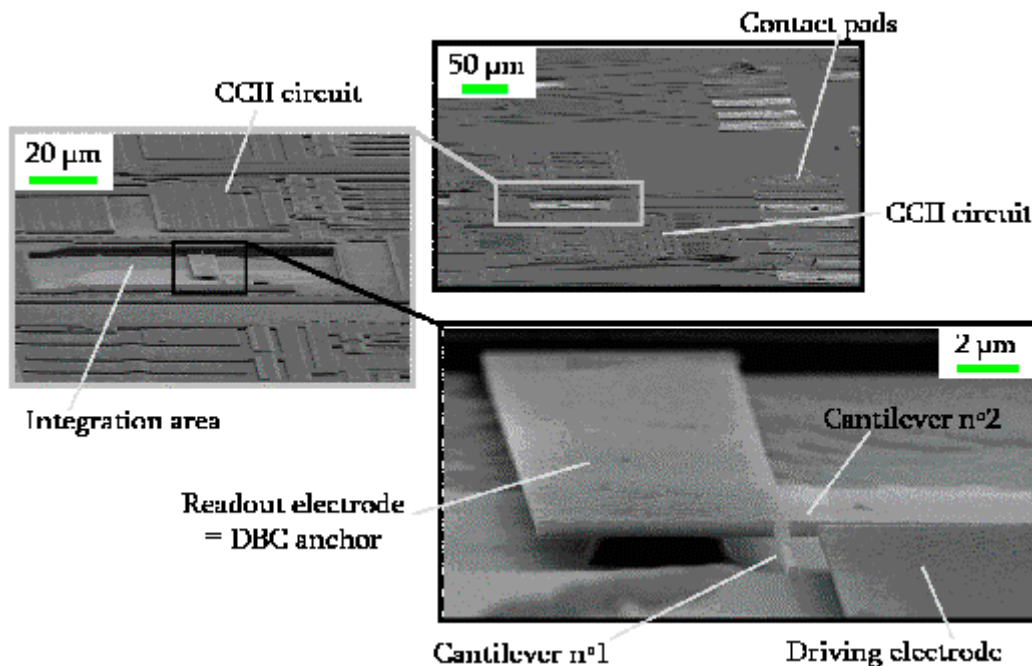


Figure 13. Tilted SEM images, with increasing magnification, of a DBC monolithically integrated into CMOS circuitry. Anchor underetching is well visible.

RESONANCE PEAKS SUPERPOSITION

The electrical frequency response of a DBC is the addition of the individual response of each cantilever. Individually, each one exhibits spring-softening effect (see chapter 3) and thereby its resonance frequency can be tuned down when increasing the driving voltage. Adjusting the voltage allows superposing both resonance peaks. In the example of Figure 14, each cantilever is independently polarized and the frequency response of each one is approximated by a Lorentzian function. The single condition is that one has a natural bigger resonance frequency than the other.

This superposition implies at least two interesting applications. First, a tunable electromechanical band-pass frequency filter could be formed through the control of the difference of resonance frequency between both. Its position and sharpness could be adjusted through the driving voltage of each one. Moreover, this concept could be extended to more than two cantilevers provided they all have the same readout electrode.

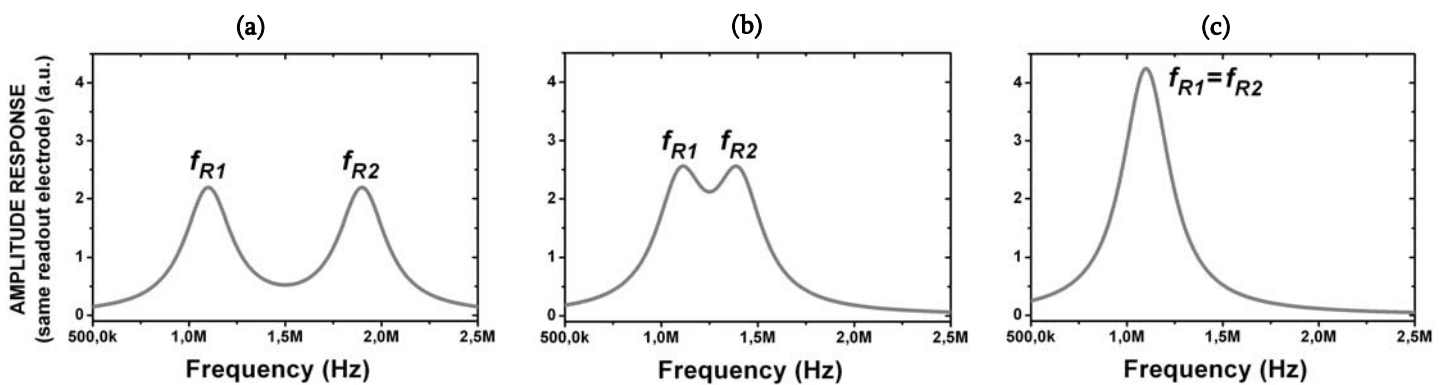


Figure 14. Conceptual representation of the global frequency response of a DBC device with common readout electrode. The cantilever with higher resonance frequency ( $f_{R2}$ ) is driven from (a) to (c) with increasing driving voltage while the other ( $f_{R1}$ ) is driven at a constant voltage

A second application to explore, which has not been experimentally tested yet, would consist in detecting a mass deposition through a change in amplitude of the superposed peaks instead of the classical approach relying on the measurement of resonance frequency shifts. If in the moment of starting the mass deposition, both cantilevers are driven in a way that both resonance peaks are superposed, and if only one cantilever is loaded, the combined frequency response exhibit important changes in terms of amplitude (see Figure 15) that can proportionally be much more important than changes of resonance frequency. Such an approach has already been tested but relying on mechanically coupled cantilevers [17].

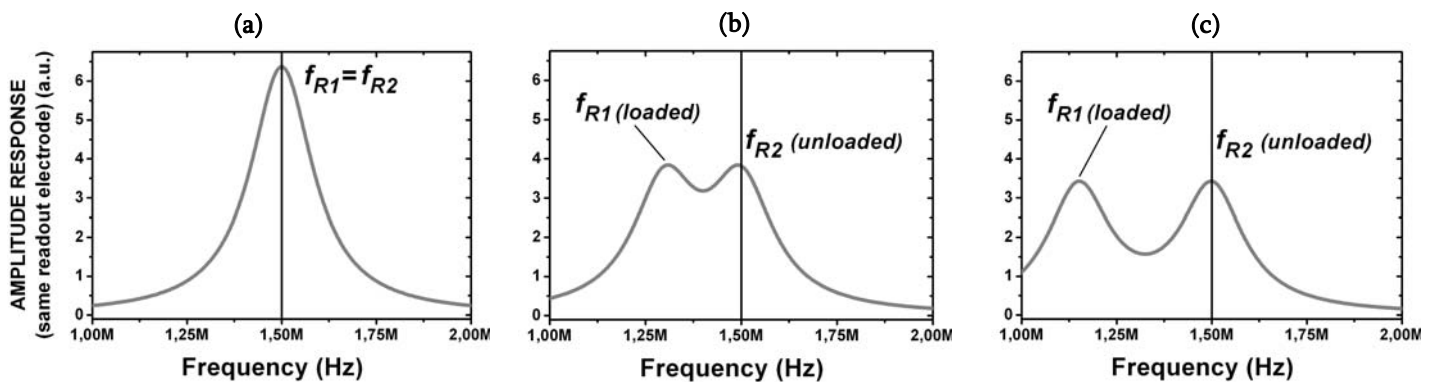


Figure 15. Conceptual representation of the global frequency response of a DBC initially operated so that both resonance peaks are superposed (a). In (b) and (c), 1 of the 2 cantilevers is progressively loaded with mass while the other remains unloaded.

In practice, superposing the two peaks is not straightforward especially if the driving electrode is common. It implies a series of requirements regarding the cantilevers design. First, one cantilever must have a higher natural resonance frequency than the other. For in-plane vibrating cantilevers, the resonance frequency  $f_0$  and the punctual mass sensitivity  $S$  are related to the geometrical dimensions in the following way:

$$f_0 \propto \frac{b}{l^2} \quad S \propto hl^3 \quad (VI.5)$$

where  $l$ ,  $b$  and  $h$  are the cantilever length, width and thickness respectively

To make higher the resonance frequency of the vertical cantilever than the horizontal one, it is defined wider:  $f_{0V} > f_{0H}$  with  $b_V > b_H$  and  $l_V = l_H$ .

The resonance frequency is tuned by the DC driving voltage (assuming  $V_{IN\ DC} \gg V_{IN\ AC}$ ) in the following way (see chapter 2):

$$f = f_0 (1 - K V_{IN\ DC}^2) \quad (VI.6)$$

where  $K$ , the electromechanical coupling factor, is given by eq.II-81:

$$K = \frac{\epsilon_0 l h}{d^3} \frac{1}{2k} = \frac{3 \epsilon_0 l^4}{4 E b^3 d^3} \quad (VI.7)$$

this means in practice that with  $l_V = l_H$  and  $d_V = d_H$ , then

$$K_V < K_H \quad (VI.8)$$

From eq.(VI.5) and (VI.7), it is clear that at same length and gap, the driving voltage dependence of the cantilever with higher resonance frequency has intrinsically a lower slope than the other. In these conditions it is impossible to superpose both resonance peaks as the curves cannot intersect (see Figure 16).

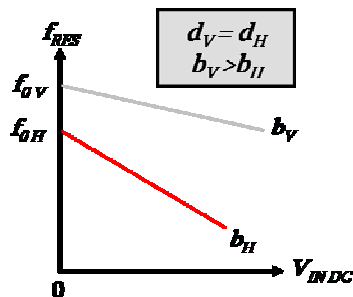


Figure 16. Dependence of the resonance frequency of the vertical and horizontal cantilevers for identical length and gap but  $b_V > b_H$

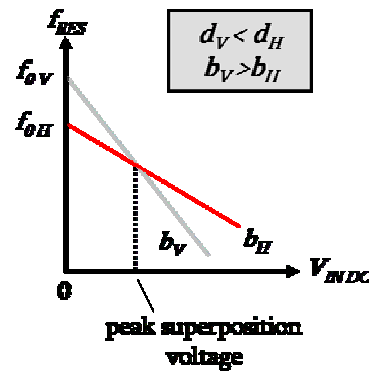


Figure 17. Dependence of the resonance frequency of the vertical and horizontal cantilevers for identical length but  $b_V > b_H$  and  $d_V < d_H$

The only way to intersect them is to decrease the gap of the vertical cantilever with respect to the other in order to compensate the larger width (see eq.(VI.7)).

First prototypes of double cantilevers with different gaps and widths, and identical lengths have been fabricated. However, due to deviations in the definition of dimensions by e-beam lithography and RIE, the nominal design could not be reproduced in these first tries. As a consequence, both peaks could not be superposed but the curves of Figure 18 constitute a first step towards a proof of concept:

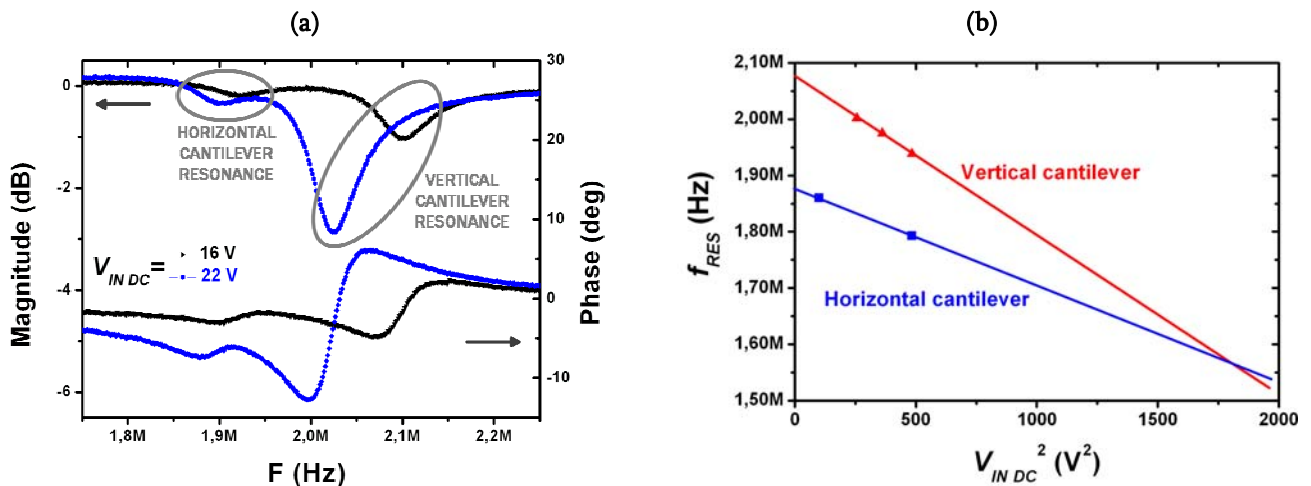


Figure 18. First experimental prototype of DBC. Both peaks are tried to be superposed adjusting the DC driving voltage. (a) resonance spectra; (b) corresponding dependence of the resonance frequency upon the driving voltage  $V_{IN DC}$

The vertical and horizontal cantilevers (VC and HC) (see Figure 12) have a gap of 600 and 1000 nm respectively. This explains two things: first, this is why the vertical one exhibits a higher slope that would intersect the other curve at about  $(42 V)^2$  ( $\equiv 1800 V^2$ ) [see Figure 18(b)]. Second, this is why the resonance peak of the horizontal cantilever is so weak, the capacitive coupling is lessened owing to the wide gap. Furthermore as it can be seen in Figure 12, its readout electrode is not optimized as it is wider than the cantilever what creates a higher parasitic fringing field capacitance.

In future devices, redesigning the readout electrode and optimizing the patterning, DBC with not too different gaps could allow obtaining peak magnitudes of the same order and superposing them in a reasonable range of driving voltage (15-25 V).

#### MASS MEASUREMENT BASED ON AMPLITUDE CHANGE OF THE COMBINED PEAKS

Mass measurements are usually based on monitoring resonance frequency shifts. Yet, as Figure 15 illustrates it, operating the DBC so that its resonance peaks are superposed and loading mass only on one cantilever, the peak of the loaded cantilever should shift down to lower frequencies while the other remains stationary. As a consequence, the combined electrical response is modified also in terms of maximum amplitude.

Hereafter, a short demonstration is given of the interest of measuring the amplitude change as a more sensitive method than the tracking of resonance frequency shift. This is just a presentation of the concept, its experimental implementation could not be done and it must be

admitted that relying on the amplitude may not be optimum in the sense that it can experience some external fluctuations (arising from the instrumentation in general) independently of any mass loading.

Considering that the DBC is capacitively detected and that both cantilevers have a common readout electrode, let us approximate the electrical amplitude response as the sum of two frequency dependent Lorentzian functions of same magnitude, corresponding to the contribution of each cantilever centered on their respective resonance frequency  $f_{RESH}$  or  $f_{RESV}$ . Although the Lorentz function is not the most accurate representation of a RLC//C response (that has resonance and anti-resonance peaks), it can be used as an adequate mathematical support for the demonstration:

$$A = L(f_{RESH}) + L(f_{RESV}) \quad \text{with} \quad L(f_{RES}, f) = \frac{1}{\pi} \frac{\left(\frac{\Gamma}{2}\right)}{(f - f_{RES})^2 + \left(\frac{\Gamma}{2}\right)^2} \quad (\text{VI.9})$$

where  $\Gamma$  is considered identical for both and equal to  $\Gamma = \frac{f_{RES}}{Q\sqrt{\sqrt{2}-1}}$ ,  $Q$  is the Q-factor and  $f$  is the frequency. The amplitude maximum of this Lorentz function is  $\frac{2}{\pi\Gamma}$  and  $\Gamma$  is the width at half-maximum. At the superposition frequency ( $f_{RESV} = f_{RESH} = f_{SP}$ , accessible with the adequate driving voltage), the combined magnitude response is maximum ( $A_{MAX}$ ).

Staying in the same driving conditions, let us assume that a small mass is deposited on top of the VC, and let us compare now the ratio  $\frac{\delta A}{A_{MAX}}$  and  $\frac{\delta f}{f_{SP}}$ .  $\delta f$  is the resulting frequency deviation of the VC from  $f_{SP}$  the superposition resonance frequency, and  $\delta A$  is the change in magnitude at the frequency  $f_T = \left(\frac{f_{RESH} + f_{RESV}}{2}\right)$ .

Tracking the signal at  $f_T$  is interesting since at this frequency the response offers the widest possible range: from  $A_{MAX}$  at the superposition frequency ( $f_{RESV} = f_{RESH} = f_{SP} = f_T$ ) down to 0 when both peaks are far from each other. The magnitude corresponding to this frequency is globally given by:

$$A\left(\frac{f_{RESH} + f_{RESV}}{2}\right) = \frac{4\Gamma}{\pi \left[ (f_{RESH} - f_{RESV})^2 + \Gamma^2 \right]} \quad (\text{VI.10})$$

To compare the ratio  $\frac{\delta A}{A_{MAX}}$  and  $\frac{\delta f}{f}$ , the following calculations are undertaken:

$$\delta A \approx \frac{\partial A}{\partial f} \delta f \quad (\text{VI.11})$$

what results in: 
$$\frac{\delta A}{A_{MAX}} = U \frac{\delta f}{f_T} \quad (\text{VI.12})$$

where:

$$U = \frac{1}{(A/f)} \frac{\partial A}{\partial f} \approx \frac{f_{RESH} (f_{RESH} - f_{RESV})}{(f_{RESH} - f_{RESV})^2 + \Gamma^2} \quad (VI.13)$$

Studying the function  $U(f_{RESV})$ , we determine that  $U$  becomes superior to 1 (i.e. when the method of mass measurement based on amplitude changes becomes better) provided a minimum frequency shift  $\delta f_{MIN}$  is caused by mass loading:

$$\delta f_{MIN} \geq \left( f_{RESH} - \sqrt{f_{RESH}^2 \left( 1 - \frac{4(1+\sqrt{2})}{Q^2} \right)} \right) \quad (VI.14)$$

For  $f_{RES}$  in the MHz range,  $\delta f_{MIN}$  is around 25 kHz for  $Q=10$ , around 250 Hz for  $Q=100$ , and around 2.5 Hz for  $Q=1000$ . The higher the  $Q$ , the wider is the improvement range in which the magnitude-based mass measurement becomes better.

Different interesting features of the DBC device have been emphasized. However, up to now our practical experimentation of the DBC has been focused only, for a matter of time, on the application of self-reference mass measurements. Hereafter, this experiment is detailed in terms of implementation and results.

### I.2.b. Results of mass sensing

The objective is to establish a new method for robust and rapid mass measurements in ambient conditions. In this case, the resonator-based sensor faces two issues: (i) high air damping resulting in low  $Q$ -factors and therefore less precise measurements, and (ii) parasitic mass depositions under the form of water thin film arising from the ambient humidity and extra adsorbed particles, which introduce additional fake frequency shifts. In this context, the DBC represents an interesting approach.

The idea is to use one of the two cantilevers, on which a punctual mass accretion is deposited, to determine with high precision the amount of deposited mass by measuring its resonance frequency shift. The other cantilever also exhibits a shift, whether positive or negative, but much smaller: this deviation provides a straightforward value of the measurement uncertainty.

In terms of device design, a series of specifications can be defined. First, both cantilevers should be spatially separated enough in order to ensure that only one cantilever undergoes an addition of mass during material dispensing. However they must be closely located so that it can be considered they face the same environmental perturbations (humidity, temperature changes, particles in suspension in air, etc...). The third point is the required similarity in the dimensions: in this way, they have the same punctual mass sensitivity and any resonance frequency shift exhibited by one cantilever or the other can be quantitatively compared with respect to the other. The orthogonal design of Figure 12 is proposed but different implementations are also possible.

This auto-reference principle has been experimentally tested by very locally depositing mass accretions by FIB only at the free extremity of the vertical cantilever (i.e. where the mass sensitivity is maximum [10]).

Several tests have been carried out following an experimental procedure based on three steps:

- first, the DBC is measured in ambient conditions (not in clean room atmosphere) with the measurement set-up n°1 referenced in chapter 5. Its resonance spectrum exhibits two different peaks related to each cantilever (like in Figure 18.a). Several spectra are recorded at different driving voltages, so that the spring-softening curve  $f_{RES} = f(V_{IN\ DC}^2)$  (like the curve of Figure 18.b) is characterized for both cantilevers.
- then, the chip is placed into the vacuum chamber of a focused ion beam (ZEISS 1560XB, GEMINI column) and a certain amount of material (a Ga/Pt/C alloy with a density of 12.5 g/cm<sup>3</sup>) is locally deposited<sup>1</sup> at the tip of the vertical cantilever only (see Figure 19 and Figure 20). A typical rectangular-shape deposit is 600 nm long, 300 nm wide and 120 nm thick what represents approximately 250 fg. This operation has been realized by Gemma Rius, Jordi Llobet and Xavier Borrise at CNM.

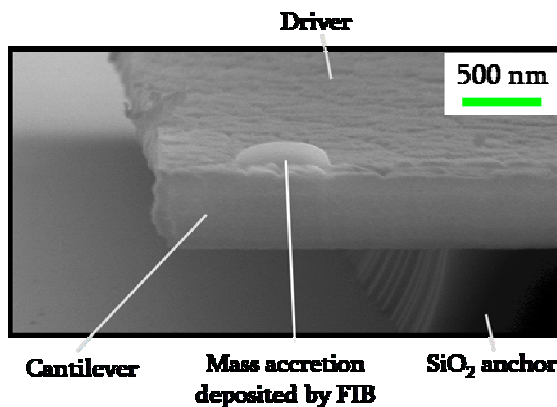


Figure 19. Tilted SEM image of the vertical cantilever tip where a mass accretion has been deposited by FIB

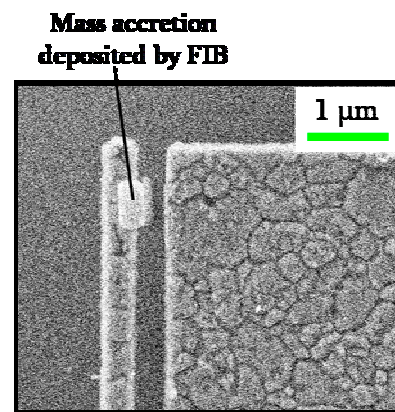


Figure 20. SEM image in top view of the vertical cantilever tip with a deposited mass accretion

- the third step consists in taking the sample off the FIB chamber and measuring it again in ambient conditions with the same electrical set-up.

Following this procedure, seven experiments have been carried out on five cantilevers. Their dimensions and their experimental (initial) natural resonance frequency are reported in Table VI - 2. The natural resonance frequency is estimated from the value extrapolated at  $V_{IN\ DC} = 0$  in the spring-softening curves. The subsequent mass deposition is not supposed to modify the slope of the driving voltage dependence (given by eq.(VI.7)) as, in theory, the stiffness is not modified during the loading, especially if the mass is deposited at the end [11, 13]. The theoretical mass sensitivity of all these DBC is in the order of  $1.2 \cdot 10^{-18} \text{ g}\cdot\text{Hz}^{-1}$ .

<sup>1</sup> Deposition parameters: ion current 1 pA, nominal deposit area: 250\*500 nm<sup>2</sup>, exposure time 20s

DBC	Vertical cantilever				Horizontal cantilever			
	$l_V$ ( $\mu\text{m}$ )	$b_V$ (nm)	$d_V$ ( $\mu\text{m}$ )	$f_{EXP\_V}$ (MHz)	$l_H$ ( $\mu\text{m}$ )	$b_H$ (nm)	$d_H$ (nm)	$f_{EXP\_H}$ (MHz)
CD1	14.4	0.4	0.6	2.07	14.5	0.42	1	1.88
CD2	14.5	0.4	0.4	1.90	14.2	0.42	0.93	2.09
CD3	14.5	0.4	0.6	1.93	14.5	0.42	1	1.89
CD4	14.6	0.4	0.4	1.86	14.2	0.42	0.93	2.07
CD6	14.3	0.4	0.4	2.15	14.2	0.42	0.93	2.27

Table VI - 2. Initial characteristics of the five DBC used in mass sensing experiments. The thickness is around 460 nm for all of them

On each DBC, small mass accretions have been deposited only on the vertical cantilever. The sizes of the resulting deposits have been subsequently estimated by imaging them with SEM and AFM. The frequency shifts are calculated from the changes of natural resonance frequencies (that are extrapolated at  $V_{INDC}=0$ ). All the results are reported in Table VI - 3:

Test nº (DBC nº)	$f_i$ (MHz)	$f_f$ (MHz)	$\Delta f$ (kHz)	deposit shape	dimensions of accretion ( $\text{nm}^3$ )	$m_{TH}$ (fg)
1 (CD1)	2.07	1.89	-182	cylindrical	$\pi(200)^2/2*300$	240
2 (CD3)	1.93	1.75	-174	parallelepiped	$l,w,h$ 700, 390, 120	410
3 (CD6)	2.15	2.06	-89	cylindrical	$2\pi(120)^2/3*300$	45
4 (CD2)	1.90	1.77	-137	parallelepiped	$l,w,h$ 580, 310, 130	290
5 (CD3)	1.74	1.63	-110	parallelepiped	$l,w,h$ 620, 390, 100	300
6 (CD4)	1.86	1.71	-149	parallelepiped	$l,w,h$ 600, 320, 120	290
7 (CD6)	2.06	1.95	-108	parallelepiped	$l,w,h$ 590, 270, 120	240

Table VI - 3. Results of seven depositions on five vertical cantilevers. The initial  $f_i$  and final  $f_f$  resonance frequency as well as the resulting shift are provided. The dimensions of the deposits are given

It can be noticed from Table VI - 3 that the devices CD3 and CD6 were used in two sets of experiments (separated by two weeks) and the initial frequencies of the second set (nº5 and 7) are in perfect concordance with the final frequencies of the first set (nº2 and 3).

In Figure 21, an example of resonance spectra recorded before and after FIB depositions is proposed. The reason why the peak of the HC is much weaker than for the VC is that its gap is much larger than the VC one. In future samples, simply setting an equal gap for both the VC and the HC will result in two similar peaks in terms of magnitude.

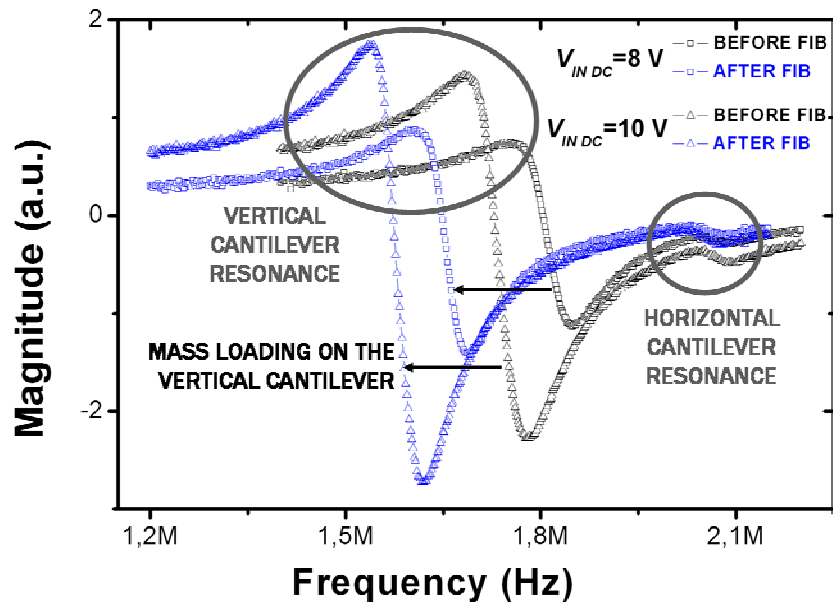


Figure 21. Resonance spectra of CD4 for two DC driving voltages before and after FIB depositions

This graph clearly illustrates the resonance frequency shift of the VC while the one of the HC remains stationary. The corresponding spring-softening curve of this device is shown in Figure 22:

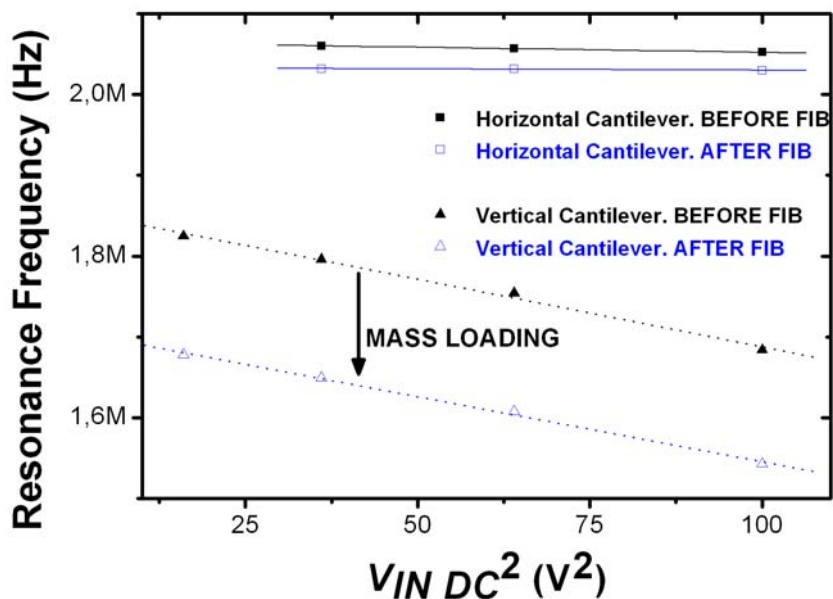


Figure 22. Spring-softening curves of CD4 (experiment n°6).  
The mass is deposited only on the vertical one.

Coherently, the slope of the spring-softening curves is not affected by the deposition and the VC exhibits a clear shift downward while the HC exhibits a small shift determining the uncertainty of the measurement. The results of the seven experiments are reported in Table VI - 4. The measured frequency shifts as well as the deposits sizes are listed: the corresponding experimental sensitivity  $S_{EXP}$  is obtained making the ratio  $\Delta m_{EXP} / \Delta f$  ( $\Delta m_{EXP}$  is the value estimated

from AFM and SEM images). The theoretical deposited mass is calculated as a function of the initial and final resonance frequency through eq.II-47:

$$\Delta m = \frac{k_{EFF\_P}}{4\pi^2} \left( \frac{1}{f_F^2} - \frac{1}{f_I^2} \right)$$

where  $k_{EFF\_P}$  is the effective spring constant for a punctual mass deposition at the free end.

From the frequency shifts of the HC, an uncertainty for the theoretical value is calculated.

DBC	Vertical cantilever with FIB deposition				Horizontal cant. with no FIB deposition
	$\Delta f$ (kHz)	$\Delta m_{EXP}$ (fg)	$S_{EXP}$ (g/Hz)	$\Delta m_{TH}$ (fg)	$\Delta f$ (kHz)
1 (CD1)	-180	240	$1.3 \cdot 10^{-18}$	$405 \pm 73$ (18%)	+57
2 (CD3)	-174	410	$2.4 \cdot 10^{-18}$	$436 \pm 61$ (14%)	-48
3 (CD6)	-89	45	$5 \cdot 10^{-19}$	$166 \pm 12$ (7%)	-9
4 (CD2)	-137	290	$2.2 \cdot 10^{-18}$	$345 \pm 8$ (2%)	-6
5 (CD3)	-110	300	$2.3 \cdot 10^{-18}$	$357 \pm 18$ (5%)	-14
6 (CD4)	-149	290	$1.9 \cdot 10^{-18}$	$412 \pm 40$ (10%)	-31
7 (CD6)	-108	240	$2.2 \cdot 10^{-18}$	$209 \pm 26$ (12%)	-20

Table VI - 4. Results of seven depositions successively performed on five cantilevers

Masses in the range of 250-400 fg have been deposited and successfully measured with an average uncertainty of 10 % provided by the measurement of the HC shift. The experimental and theoretical values of the mass are in good concordance taking into account all the measurement uncertainties: the one arising from estimations of deposits size based on SEM/AFM images, and the other coming from environmental perturbations which are estimated from the HC shift.

In further experiments, it will be necessary to refine the spring-softening curves for a finer extraction of resonance frequency. This should be obtainable (i) optimizing the readout electrode design (to reduce the fringing field capacitance affecting the HC), (ii) assigning the same value for both gaps and (iii) recording the resonance spectra with a finer sweep of the DC driving voltage.

Present measurements have been performed in non-optimal conditions, in fact the electrical test and the FIB depositions did not even take place in the same building. Taking into account these non-optimal conditions, the DBC can provide the measurement uncertainty through the ‘error shift’ measured with the HC. It can be noticed that the deviation does not exceed an average of 10% and the theoretical and experimental values of the deposited mass match quite well.

## II. Distributed mass sensing experiments

The starting motivation behind the realization of distributed mass sensing experiments has been the development of a ‘quasi-dynamic stencil’ system (QDS) in partnership with EPFL. Such a system is supposed to achieve a relative motion between a full-wafer stencil and a substrate, so that multiple-layer nanostructures can be formed in-situ by shifting the stencil patterns in a step-and-repeat mode. In this way, high purity multi-material deposits can be structured and thereby very specific devices like tunnel junctions can be fabricated.

Within this context, the incorporation of a mass sensor below the stencil presents two interests. First, the material transport through confined geometries, i.e. nanostencil apertures, can be characterized in order to determine the local mass deposition rate on the substrate. Second, the sensor can be used for in-situ alignment of the stencil with respect to the substrate. The principle of operation is simple (see Figure 23): when the sensor is located below a dedicated stencil aperture, it detects a signal corresponding to a mass loading thus providing simultaneously the spatial position and the deposition rate:

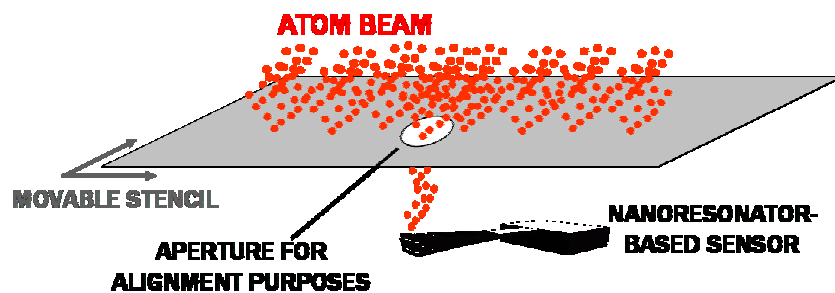


Figure 23. Schematic representation of a nanomechanical mass sensor implemented as position-sensitive sensor for nanostencil lithography systems

Resonating NEMS, like the previously presented ones, and quartz-crystal microbalances (QCM) are basically the two types of devices which are adequate for distributed mass sensing purposes (e.g. having the ability to detect the deposition of uniform thin layers). However, nano/micromechanical resonators should represent an important progress with respect to QCM as they feature a potentially higher mass sensitivity and an intrinsic higher spatial resolution due to their small size (in comparison, a QCM has a 1 cm<sup>2</sup> area).

Furthermore, QCM achieve their best performance when they are uniformly loaded over their entire surface. However in the QDS system, the beam is expected to have a diameter of few microns after passing through the apertures: in this case the QCM would be operated like in punctual mode (compared to its whole area). In these conditions, its performance is very poor as it has been demonstrated in Table VI-1.

On the contrary, the nanomechanical resonator is operated in a distributed mass sensing configuration since the material beam is larger than it and uniformly coats it.

With the aim of implementing nano/microresonators as positioning sensors in the QDS system, their performance has been assessed in experiment III, whereby the in-situ monitoring of the deposition of ultra-thin gold layers has been realized. Meanwhile, a QCM, placed in the

vicinity of the NEMS has allowed (i) comparing NEMS and QCM performance and (ii) having a reference to estimate quantitatively the deposited mass.

For the purpose of the final application (in situ detection of ultra-thin layer deposition, in a high vacuum chamber), the target is the ability to measure a frequency shift corresponding to a 1 s shutter aperture time at a typical deposition rate of 0.3 nm/s for gold, silver and aluminum. The minimum detectable frequency shift is assumed to be around 100 Hz, what is voluntarily overestimated. First, the frequency shift as a function of the sensitivity is calculated in order to determine the NEMS mass sensitivity required in those conditions of operation. The deposited mass is given by:

$$\Delta m = \rho \Delta e A = S_D \Delta f A \quad (\text{VI.15})$$

where  $\Delta m$  is the mass of the on-top deposited layer,  $S_D$  the distributed mass sensitivity ( $\text{g}\cdot\text{cm}^{-2}\cdot\text{Hz}^{-1}$ ),  $\Delta f$  the resulting frequency shift,  $A$  the resonator area, and  $\rho$  the density of the deposited material.  $\Delta e$  is the deposited thickness and can be expressed as:

$$\Delta e = \frac{S_D \Delta f}{\rho} \quad (\text{VI.16})$$

Defining  $\Delta e$  as  $\Delta e = R t$  ( $R$  is the evaporation rate (nm/s) and  $t$  the evaporation time), one can also express the resulting frequency shift as:

$$\Delta f = \frac{\rho R t}{S_D} \quad (\text{VI.17})$$

In Table VI - 5, the frequency shift resulting from a 1 s deposition at a rate of 0.3 nm/s is reported as a function of the deposited material and of the distributed mass sensitivity:

Distributed mass sensitivity ( $\text{g}\cdot\text{cm}^{-2}\cdot\text{Hz}^{-1}$ )	$1 \cdot 10^{-9}$	$1 \cdot 10^{-10}$	$1 \cdot 10^{-11}$
$\Delta f$ (Hz) for <b>Au</b> deposition ( $\rho=19.3 \text{ g}\cdot\text{cm}^{-3}$ )	580	5800	58000
$\Delta f$ (Hz) for <b>Ag</b> deposition ( $\rho=10.5 \text{ g}\cdot\text{cm}^{-3}$ )	320	3200	32000
$\Delta f$ (Hz) for <b>Al</b> deposition ( $\rho=2.7 \text{ g}\cdot\text{cm}^{-3}$ )	80	800	8000

**Table VI - 5. Frequency shifts associated to a given distributed mass sensitivity for a 1s deposition at a rate of 0.3 nm/s for gold, silver and aluminum**

In order to exceed the frequency resolution of 100 Hz for any deposition material, an appropriate range for the distributed mass sensitivity is  $10^{-10}$  -  $10^{-11} \text{ g}\cdot\text{cm}^{-2}\cdot\text{Hz}^{-1}$ , i.e. more sensitive than state of the art quartz microbalances ( $1.23\cdot 10^{-8} \text{ g}\cdot\text{cm}^{-2}\cdot\text{Hz}^{-1}$ ).

This section will be structured in the following way: first, the high performance in terms of distributed mass sensing of CMOS integrated nano/micromechanical structures will be demonstrated in experiment III. Second, the design of the QDS system will be described, focusing on the implementation of the mass sensor to achieve in-situ full-wafer alignment between stencil and substrate.

## II.1. Monitoring the deposition of ultra-thin gold layers (exp. III)

This experiment has been carried out using a deposition chamber designed and assembled by Dr. Jordi Fraxedas from ICMAB-CSIC (Barcelona, Spain). Experiment III has consisted in placing inside the vacuum chamber a QCM and a CMOS chip containing integrated nanomechanical resonators (whose fabrication has been described in chapter 4) mounted on a PCB. Both have been simultaneously operated in order to monitor in-situ and in real time the deposition of ultra-thin gold layers (less than 0.1 nm thick).

Hereafter, the main components of the experimental set-up are described, the choice and mode of operation of the nanomechanical sensor are discussed and finally an analysis of the main results is proposed.

### II.1.a. Experimental set-up

#### DEPOSITION CHAMBER CHARACTERISTICS

The deposition chamber has been designed in order to be able to evaporate gold at low rates. In Figure 24, the vacuum chamber and its main components are depicted:

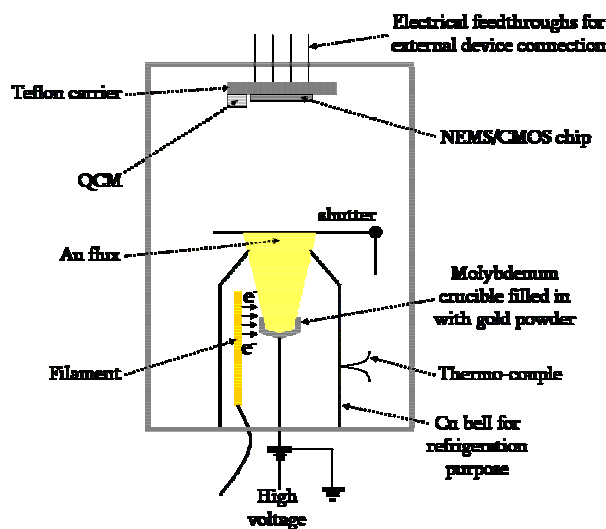


Figure 24. Scheme of the high vacuum evaporation chamber with its different components and the electrical feedthroughs. The configuration with closed shutter is depicted.

This is a hybrid deposition chamber: this is not an electron beam neither a thermal evaporator but rather a combination of both. Under high vacuum conditions (around  $10^{-7}$  mBar), a tungsten (W) filament is heated by a current flow so that it starts emitting electrons that impact on a closely located molybdenum crucible in which gold powder is stored. This crucible is polarized at a high voltage to attract the electrons and becomes heated by their bombardment. In this way, some Au is melt and evaporates isotropically. The surrounding bell is made of copper (Cu) and its temperature can be controlled by a thermo-couple. The Au beam can be confined to the bell by means of a shutter manually controllable from outside.

Operated at a pressure of  $7 \cdot 10^{-7}$  mBar, typical deposition parameters are a filament current of 1.83 A, an emission current of 25 mA (corresponding to the electron flux created by the filament, it flows into the crucible and the high voltage electrode), a flux current of 1.5  $\mu$ A (corresponding

to ionized gold atoms, and measured by a probe in the vicinity of the crucible) and a polarization voltage of the crucible of 750 V.

The NEMS/CMOS chip is stuck on a PCB and wire bonded. This PCB is placed on a Teflon<sup>®</sup> carrier (see the white part in Figure 25) on which some metallic clips ensure both mechanical clamping and electrical contacts with the pads of the PCB. These clips are soldered in the lower side of the Teflon carrier to a series of wires connected to electrical feedthroughs that allow electrically connecting the device from outside the chamber:

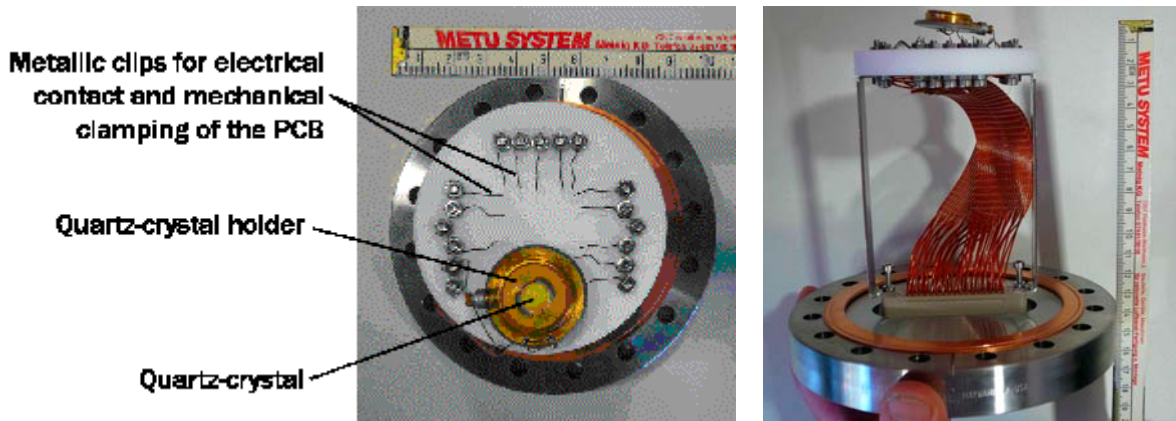


Figure 25. Pictures in top (left) and side (right) views of the sample holder (the PCB containing the chip is not present here)

#### OPERATION OF THE QUARTZ-CRYSTAL MICROBALANCE (QCM):

In the vicinity of the NEMS/CMOS chip, an AT-cut quartz-crystal (INFICON 008-010-G10, [www.inficon.com](http://www.inficon.com)) and its specific holder are placed just above the Teflon carrier so that the crystal is implemented as a microbalance. Actually, the holder is the genuine INFICON one but without the refrigeration network. Therefore the QCM cannot be controlled in temperature what can represent a major problem assuming that the quartz crystal temperature coefficient (in Hz/°C) is in the order of few ppm (part per million), in other words of few Hz (since its resonance frequency is the MHz range). The problem is that few Hz are precisely the expected range of frequency shifts caused by a mass loading of thin gold layers. The resonance frequency (around 6 MHz) is electrically measured in real time by a network analyzer (AGILENT E5100A).

To translate the resonance frequency shift related to mass loading into a value of deposited material thickness, mostly three methods exist: the ‘Sauerbrey’ [18] one, the ‘period measurement’ one and the ‘Z-match’ one [19]. These last two methods are more modern and are more accurate for already loaded quartz devices having experienced large frequency shifts. In our case, the ‘Sauerbrey’ [18] approach is followed since the devices are only used for ultra-small depositions (the maximum frequency shift to maintain the accuracy of the calculation is limited to 2% of the initial resonance frequency, here it would correspond to 120 kHz). This equation is only strictly applicable to uniform, rigid, thin-film deposits on the QCM active area that is restricted by the area of the rear contact electrode (0.6 mm in diameter). Assuming that this is the case, the deposited thickness  $\Delta e$  is given by [18]:

$$\Delta e = \frac{\rho_{QCM} e_{QCM}}{\rho_D f_1} (f_I - f_F) \quad (VI.18)$$

where  $\rho_{QCM}$  is the density of quartz crystals (about  $2.65 \text{ g.cm}^{-3}$ ),  $e_{QCM}$  its thickness,  $\rho_D$  the density of the deposited material, and  $f_i$  and  $f_f$  the resonance frequency of the QCM before and after the deposition.

Assuming that the crystal vibrates longitudinally, the crystal thickness can be calculated by the following equation [20]:

$$e_{QCM} = \frac{N_{AT}}{f_i} \quad (\text{VI.19})$$

where  $N_{AT}$  is equal to half the wavespeed for transverse waves:  $1661 \text{ m.s}^{-1}$  and  $f_i$  is the initial resonance frequency. For a 6 MHz QCM, eq.(VI.19) gives around  $280 \mu\text{m}$ .

#### CHARACTERIZATION OF THE INTERNAL CONDITIONS OF THE DEPOSITION CHAMBER

The operation of the tungsten filament has likely an incidence on the internal temperature of the chamber what is problematic regarding the lack of temperature control for the QCM. In parallel, it emits radiations (in particular at X-ray, infra-red [IR] and visible wavelengths) which may perturb the CMOS circuitry.

The effect of the progressive aperture of the shutter until full illumination has been investigated placing in the vacuum chamber and very close a QCM and a temperature sensor (a wire bonded cross-bridge resistance (CBR) polysilicon structure).

This CBR has helped in assessing the internal temperature to know if during posterior mass experiments the QCM may exhibit frequency shifts related to temperature changes. A CBR structure (chip ref. 3157-13-6) made of n-type *poly1* (see chapter 4) has been wire bonded to the pads indicated in Figure 26:

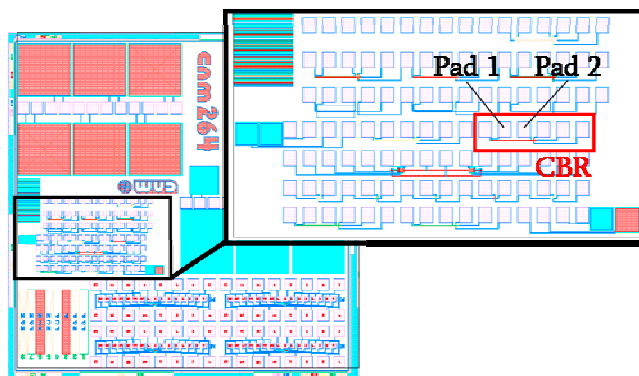
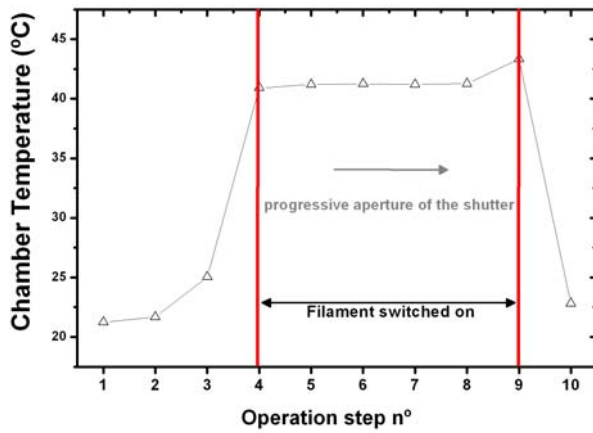


Figure 26. Position of the *poly1* CBR inside the chip, indicating the two bonded pads

The CBR is a simple polysilicon structure acting as a resistor of known dimensions that can serve to calculate the polysilicon resistivity. The sample has first been placed into an oven with controllable temperature. Sweeping from  $25 \text{ }^\circ\text{C}$  to  $80 \text{ }^\circ\text{C}$ , the temperature dependence has been measured: it exhibits a law of the type  $R_T = R_0(1 + \alpha T)$  where  $T$  is the temperature (in  $^\circ\text{C}$ ),  $R$  the resistance from pad 1 to pad 2 (in  $\Omega$ ) and  $\alpha$  the temperature coefficient:  $R_0=1734 \Omega$  and  $\alpha= 0.7 \cdot 10^{-3} /^\circ\text{C}$  are deduced.

Then, the CBR has been placed in the vacuum chamber and the internal temperature has been monitored switching on the filament but without evaporating and progressively opening the shutter in four intermediate grades. The entire timeframe here is around two and a half hours.



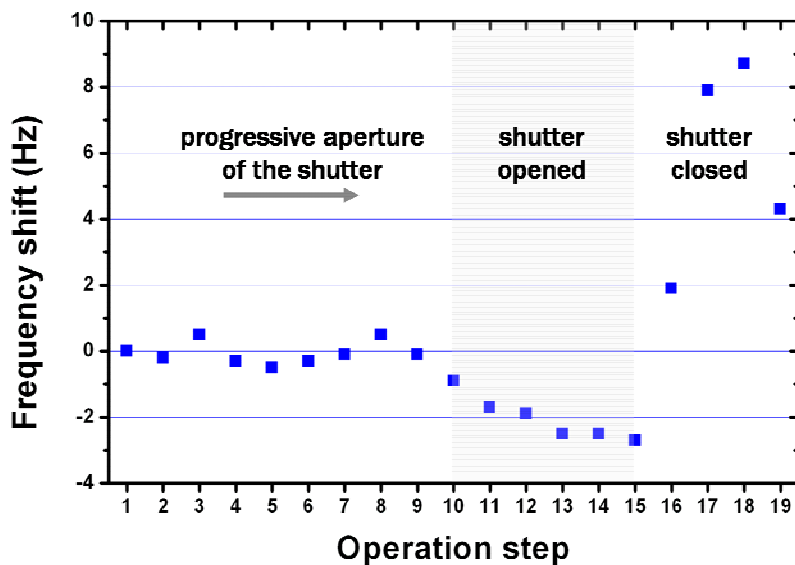
**Operation steps:**

- 1: ambient conditions
- 2: in vacuum
- 3: in vacuum, one day later
- 4: filament switched on (t=0)
- 5: aperture grade 1 (t=1 min)
- 6: aperture grade 2 (t=1h02 min)
- 7: aperture grade 3 (t=1h12 min)
- 8: aperture grade 4 (t=1h18 min)
- 9: shutter completely opened (t=1h44 min)
- 10: shutter closed (t=2h30 min)

Figure 27. Internal temperature of the chamber as a function of the filament state and the grade of shutter aperture

More than the grade of aperture itself, it seems that mostly the state of the filament (switched off or on) determines the internal temperature. It reaches 43.3°C after twenty minutes (maybe it would have increased even more after a longer time), i.e. more than twenty degrees above the room temperature.

Simultaneously, both a CCH circuit and a QCM have been monitored. Within one hour, the resonance frequency of the QCM increased of 2.8 Hz with the switched off filament. Then it was switched on and the resonance frequency evolution (normalized to 5.963544 MHz) has been recorded: it is reported in Figure 28 as function of the grade of shutter aperture:



**Operation steps:**

- 1: initial (t=0)
- 2: aperture grade 1 (t=1 min)
- 3: aperture grade 1 (t=13 min)
- 4: aperture grade 1 (t=59 min)
- 5: aperture grade 2 (t=1h04 min)
- 6: aperture grade 2 (t=1h08 min)
- 7: aperture grade 3 (t=1h15 min)
- 8: aperture grade 4 (t=1h20 min)
- 9: aperture grade 4 (t=1h41 min)
- 10: shutter opened (t=1h46 min)
- 11: shutter opened (t=1h53 min)
- 12: shutter opened (t=1h55 min)
- 13: shutter opened (t=1h59 min)
- 14: shutter opened (t=2h07 min)
- 15: shutter opened (t=2h13 min)
- 16: shutter closed (t=2h30 min)
- 17: shutter closed (t=2h45 min)
- 18: shutter closed (t=2h50 min)
- 19: shutter closed (t=4h28 min)

Figure 28. Variation of the QCM resonance frequency as a function of the aperture of the shutter and constantly switched on filament

It seems that when the filament is switched on, the frequency fluctuates around a constant value independently of the grade of shutter aperture. When it is completely opened, the resonance frequency starts falling down slowly (about -2.5 Hz in 30 minutes) while the internal temperature increases of 2°C (see Figure 27). Recapitulating previous data, it can be stated that:

- the temperature increases of about 20 °C when switching on the filament
- when switching on the filament, we have observed a decrease of about 18 Hz in the QCM resonance frequency

As a conclusion, it seems that an increasing internal temperature makes decrease the QCM resonance frequency of about 1 Hz per Kelvin. Concerning the CMOS circuitry, its performance degrades drastically and rapidly when the shutter is totally opened, supposedly because of X-ray and IR radiations.

However, these results have to be considered with caution as in these proofs the relative orientation between the circuitry and the QCM with respect to the shutter has not been checked. In this context, one element may have been exposed before or after the other to the filament radiation. The CCII is maybe degraded even before a total exposure to the filament.

### II.1.b. Nanomechanical sensor

The nano/micromechanical resonators used in experiment III are CMOS integrated in-plane vibrating cantilevers like the ones characterized in chapter 5. They have been defined by nanostencil lithography.

For measurements in vacuum, the associated high Q factor makes attractive CMOS integrated cantilevers compared to QB for three reasons. (i) thanks to the high Q, low driving voltages are enough to offer good electrical performance (in terms of magnitude and phase changes) (ii) Technologically speaking, CMOS cantilevers require less process steps as no protective SU8 layer needs to be coated and patterned. (iii) Regarding the distributed mass sensitivity, cantilevers and QB (with dimensions like the ones presented in chapter 5) have similar characteristics in the range of  $10^{-10}$  g.cm<sup>-2</sup>.Hz<sup>-1</sup> (see also chap.2, Figure 18), what is better than state-of-the-art QCM (typically  $10^{-8}$  g.cm<sup>-2</sup>.Hz<sup>-1</sup>). The distributed mass sensitivity of in-plane vibrating cantilevers is:

$$S_D = \frac{4\pi}{1.015} \frac{\rho^{3/2} h l^2}{E^{1/2} b} \quad (\text{VI.20})$$

where  $l$ ,  $b$  and  $h$  are its length, width and thickness respectively

These CMOS cantilevers have been wire bonded to a PCB fixed to the Teflon holder by means of metallic clips which assume two functions. They mechanically clamp the PCB to the holder by leaning on the contact pads of the PCB (connected to the bonded wires): in this way they also electrically contact the resonator. This pre-existing solution is actually not optimal and should be improved in the future since the electrical contact is not very good. Measurements done with this set-up have generally been noisier than with measurement set-up n° 1 or 2 (see chapter

5). Moreover, the manual manipulation of the clips to place the PCB under them has several times induced electrostatic discharges which have stuck the cantilever to its in-front electrode.

### II.1.c. Results and analysis

In the following experiments of gold deposition, the relative orientation of the QCM and the NEMS/CMOS chip has been carefully adjusted to ensure that both devices are equally exposed to the crucible so that they undergo the same temperature and radiation effect as well as they receive the same quantity of mass.

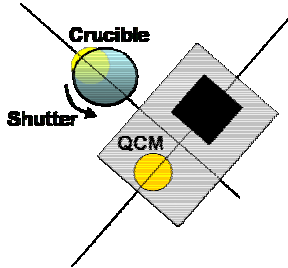


Figure 29. Top view of the orientation of the devices with respect to the atom beam

Initial tests have shown that the shutter can be only partially opened otherwise the signal of the NEMS/CMOS chip degrades rapidly until complete extinction. With regard to this matter, it has been observed that the deposition rate depends upon each grade of aperture. Furthermore this grade is not very precise as it relies on visual marks and the shutter screw was rather loose.

The measurement set-up is similar to the set-up n°2 described in chapter 5 except that the AC output of the network analyzer is commonly connected both to NEMS and QCM input ports while two separate input ports are used to get the output signals (the NEMS one with an input impedance of 1 MΩ, the QCM one with 50 Ω).

Two wire bonded CMOS cantilevers, very similar, have been used in the following experiments. Their characteristics are reported in Table VI - 6: geometrical dimensions, theoretical resonance frequencies  $f_{0 TH}$  and theoretical distributed mass sensitivity  $S_{D TH}$ .

device	$l$ (μm)	$b$ (nm)	$h$ (nm)	$f_{0 TH}$ (MHz)	$S_{D TH}$ (g.cm <sup>-2</sup> .Hz <sup>-1</sup> )
WB-A	14.4	0.5	0.58	2.91	9.0 10 <sup>-11</sup>
WB-D	14.6	0.5	0.58	2.83	9.3 10 <sup>-11</sup>

Table VI - 6. Samples characteristics

Three sets of experiments performing several depositions have been carried out: two sets (n°1 and 2) with WB-D and one (n°3) with WB-A. The frequency shifts related to mass loading are monitored through the phase peak.

The QCM and the cantilevers have been excited with  $V_{IN AC} = 32$  mV. The parameters of the CCII circuit are  $R_{LOAD} \approx 800$  Ω and  $R_{POL} \approx 180$  kΩ. In the first and second set with WB-D,  $V_{IN DC}$  is set to 8 and 8.4 V respectively, and in the third with WB-A to 8.5 V.

To simultaneously monitor the deposition of gold atoms onto the resonator surface and onto the quartz surface, three approaches have been followed.

Being the objective the demonstration of the NEMS high mass sensitivity and taking into account that the low deposition rate of the evaporator is reduced by only partially opening the shutter, ultra-small deposits have successfully been formed but they have been impossible to

image neither with AFM nor with SEM. Furthermore, the circuitry could not be exposed a long time to the atoms beam owing to its sensitivity to the radiations emitted by the filament.

In practice, within the permitted short timeframe (because of the circuit sensitivity to the radiation), we have been able to observe frequency shifts of the cantilever in the order of hundreds of Hz.

As aforementioned, these CMOS cantilevers are nominally around 100 times more sensitive than QCM. As a result, the QCM has always been operated in its detection limit if one considers that the expected resulting shifts were in the order of few Hz and the opening/closure of the shutter has typically brought about few Hz shifts because of the lack of temperature control. Consequently, in all the results presented hereafter, the QCM shifts have been difficult to separate between temperature- and mass loading related shifts.

A first approach, that constitutes a proof of the successful operation of the resonator as mass sensor, has consisted in recording in real time the cantilever resonance spectra during the deposition, while the QCM was measured just before and just after this deposition.

This means that the quartz crystal does not experience any vibration while the cantilever is permanently excited during the evaporation and constantly vibrates in the plane. With regard to this matter, it is assumed that this motion, in the order of 1-10 nm according to chapter 5, Table V.7 and V.8, does not perturb the binding of atoms onto the surface and that it collects the same amount of mass as if it were static. In Figure 30, resonance spectra are recorded before, during and after a 3 minutes long deposition. In this example, the resonance frequency showed a good stability within a timeframe of 10 minutes after the end of the deposition.

This stability combined to the fact that the frequency shifted down to lower frequencies in a relatively linear dependence upon the deposition time indicate that these shifts are surely caused by mass loading. The total frequency shift is of minus 745 Hz approximately.

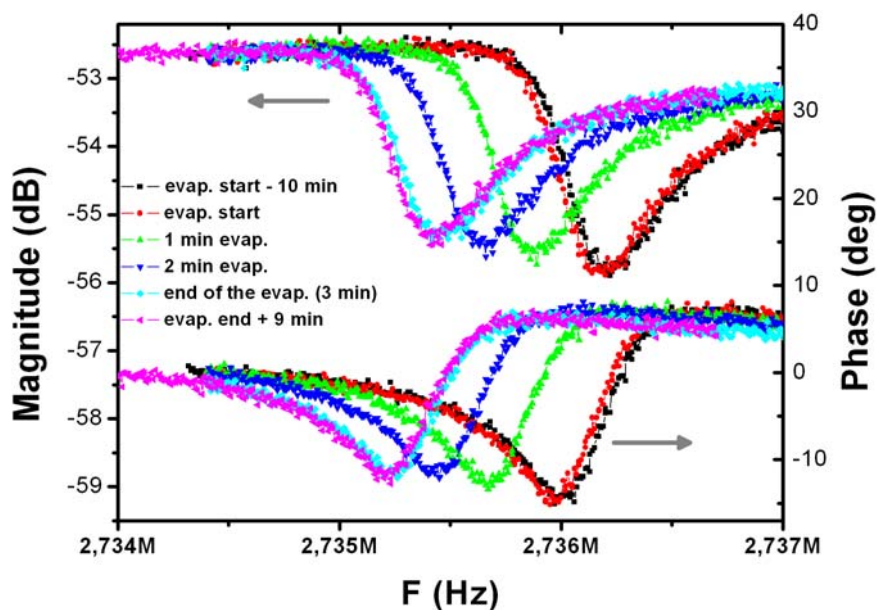


Figure 30. Set 1, WB-D device. Constant monitoring of the cantilever resonance signal during a 3 minutes long gold deposition by evaporation (span around 3 kHz)

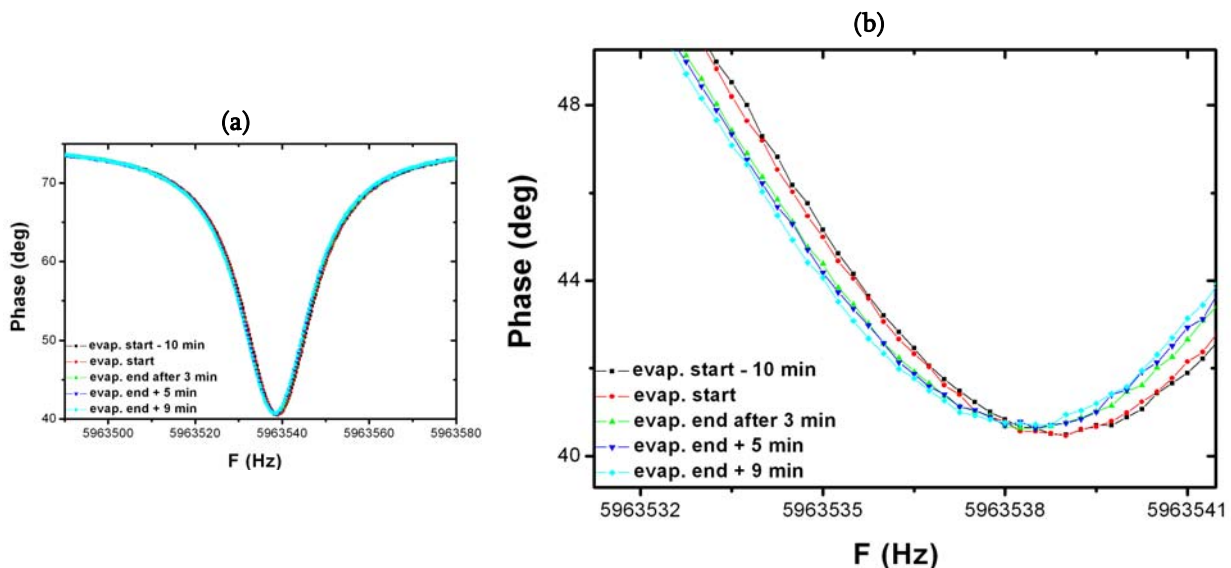


Figure 31. QCM resonance spectra (phase) measured before and after a 3 minutes long gold deposition by evaporation. In (a) span of 90 Hz, in (b) span of about 10 Hz [zoom of (a)]

In Figure 31(a), the resonance spectra of the QCM before and after the 3 minutes long deposition are reported inside a span of 90 Hz (the Q-factor is much higher). However, the corresponding shifts are so small that a zoom depicted in Figure 31(b) is needed to visualize any change. Before and after the deposition, the QCM resonance frequency seems relatively stable. The deposition resulted in a frequency shift of approximately minus 0.5/0.75 Hz, i.e. three orders of magnitude less than the cantilever.

Complementarily with the first one, the second approach has consisted in recording in real time the QCM resonance spectra during the deposition, while the cantilever was measured just before and after this deposition.

This means that the quartz crystal is permanently excited during the evaporation. In Figure 32, resonance spectra of the QCM are again recorded inside a span of 90 Hz for a 3 minutes long evaporation while in Figure 33 the cantilever resonance spectra are recorded before and after the deposition.

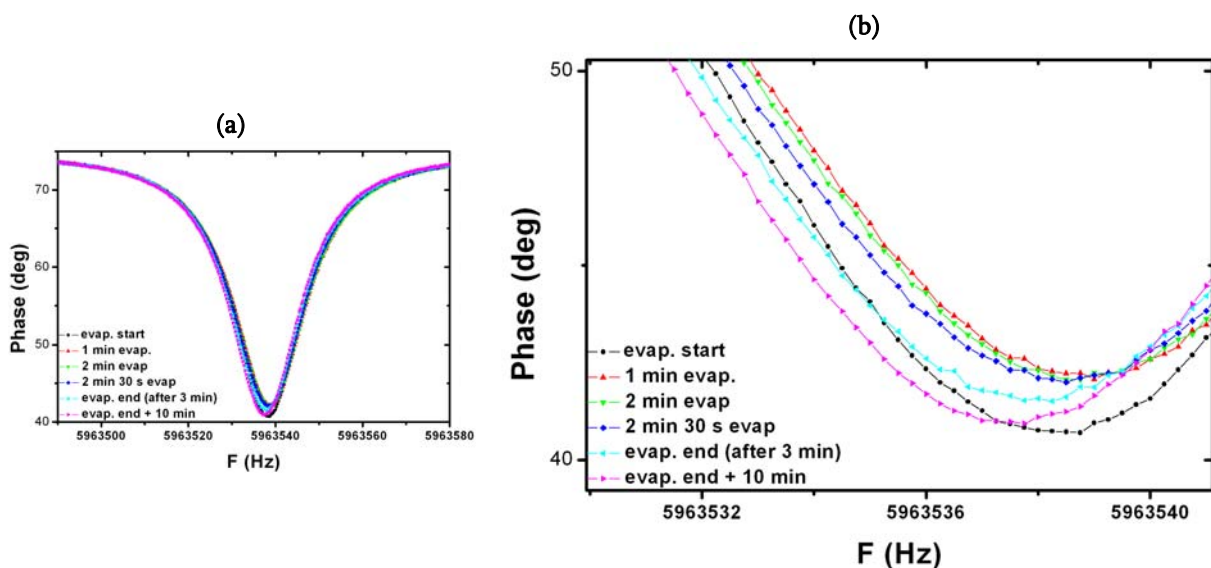


Figure 32. Constant monitoring of the QCM resonance spectrum (phase) during a 3 minutes long evaporation with a span of (a) 90 Hz, (b) about 10 Hz [zoom of (a)]

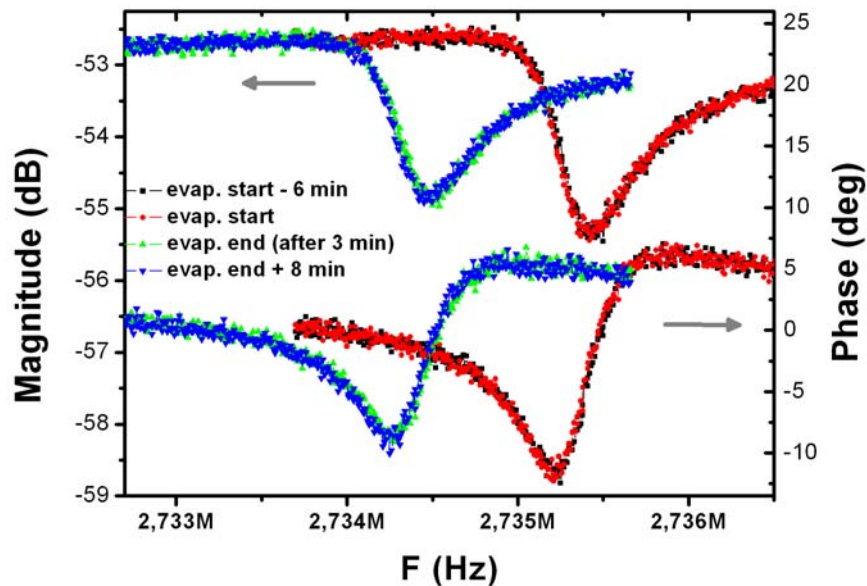


Figure 33. Set 1, WB-D device. Cantilever resonance spectra measured before and after a 3 minutes long evaporation with a span of about 3500 Hz

In Figure 32(a), the 90 Hz span has again been too large for the resulting small frequency shifts. A zoom is depicted in Figure 32(b) where a more complex pattern appears compared to Figure 31(b). Between the black curve (deposition start) and the red one (after 1 minute of deposition), the resonance shifts upwards and then decreases in posterior curves. This matter is not coherent with the observed negative shift of Figure 28 when opening the shutter. This indicates that without temperature control, a QCM operated in its resolution limit is not reliable enough to assess the deposited thickness.

However to try to extract any quantitative information, which shift could be considered? Between the black and the light blue curves (deposition start and end) of Figure 32(b), there is approximately a minus 0.5/0.75 Hz deviation. But if one considers the difference between the red and the light blue curves (respectively after 1 and 3 minutes of deposition), a larger deviation is observed (approximately minus 1.25 Hz). This value is maybe underestimated since in the first minute of evaporation, no spectrum has been recorded and the positive shift may still have been larger. In comparison, the cantilever resonance shift is much more significant as it exhibits a total deviation of minus 920 Hz.

The third approach has consisted in monitoring at a fixed frequency  $f_{SPAN 0}$  the evolution of the cantilever signal during the deposition.

In this case, a resonance spectrum has to be recorded before the deposition (red curve in Figure 34) in order to determine the value of frequency where the phase peak is at its steepest transition. Then, the phase is scanned at this fixed frequency (by setting the span to 0). In the example of Figure 34, the grey straight line indicates that the oscillations of the cantilever are set to 2.92462 MHz.

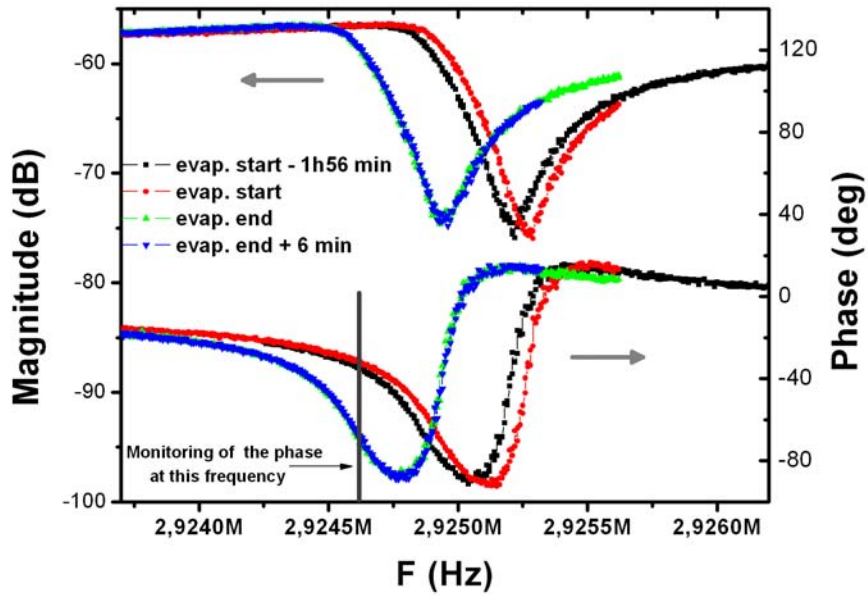


Figure 34. Set 3, WB-A device. Cantilever resonance spectra measured before and after several depositions (2 min 40 s in total) with a span of about 2500 Hz

While continuously monitoring the cantilever signal at the fixed frequency (here  $f_{SPAN\ 0}$ ), four sequential evaporations of 40 seconds each have been performed. The resulting evolution of the phase signal is depicted in Figure 35(a): the grey bars indicate when the shutter is partially opened, i.e. when some gold is deposited. The final phase level is about  $70^\circ$ , what is confirmed by the spectra recorded just after the end of the depositions: see blue and green curves in Figure 34.

With a mathematical treatment, it is possible to convert the phase evolution of Figure 35(a) into a real-time evolution of the resonance frequency. Although the phase peak is not symmetrical, its left part (expressed as  $\varphi$ ) can be fitted very accurately by a Lorentz function  $L(f_{RES})$  centered on the phase peak (considered as the resonance frequency  $f_{RES}$ ):

$$\varphi = L(f_{RES}) = \varphi_0 + \frac{2a}{\pi} \frac{b}{4(f - f_{RES})^2 + b^2} \quad (\text{VI.21})$$

where  $a$  and  $b$ , and  $\varphi_0$  are fitting parameters related to the curve width and to the phase offset respectively. Assuming that the initial and the final phase spectra conserve the same characteristics (offset and width), the left part of the curve is fitted so that  $a$ ,  $b$  and  $\varphi_0$  are determined. Then, setting the frequency at  $f_{SPAN\ 0}$ ,  $f_{RES}$  can be obtained from  $\varphi$  applying the inverse function  $f_{RES} = L^{-1}(\varphi)$ :

$$f_{RES} = L^{-1}(\varphi) = f_{SPAN\ 0} \pm \frac{1}{2} \sqrt{\frac{2ab}{\pi(\varphi - \varphi_0)} - b^2} \quad (\text{VI.22})$$

In this specific case, the sign is (+) since  $f_{SPAN\ 0}$  is always inferior to  $f_{RES}$ . (see Figure 34). In this way, the curve of Figure 35(b) is obtained:

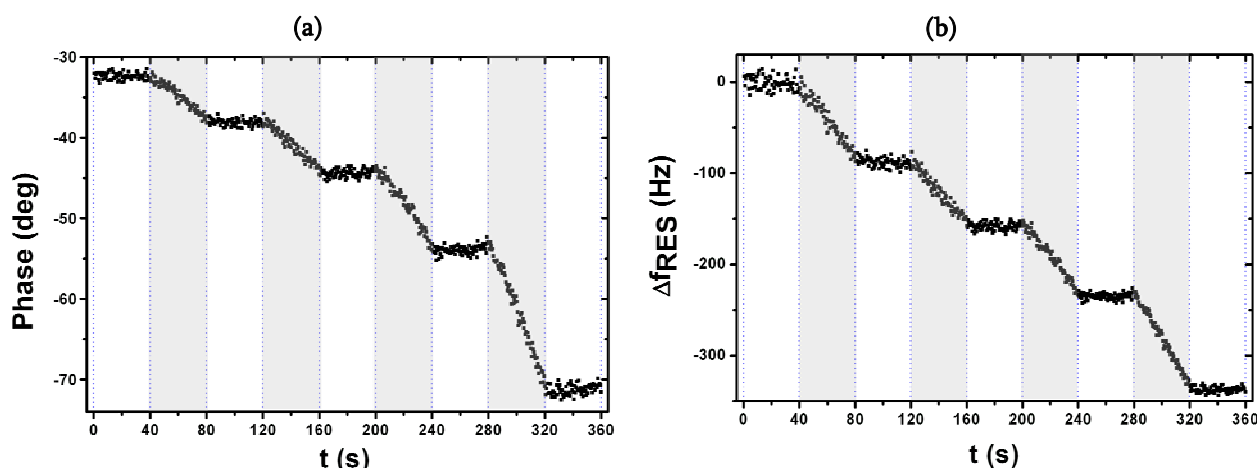


Figure 35. (a) Monitoring of the phase evolution in a 6 minutes time span during which 4 depositions of 40 s each are performed (illustrated by the grey bars). (b) Corresponding curve of resonance frequency shift evolution obtained by the transformation of the phase curve applying the inverse Lorentz function

This curve of Figure 35(b) coherently features (i) flat plateaus when the shutter is closed and (ii) linear shifts towards lower frequencies when the shutter is partially opened. The differences of slope between the successive evaporations are likely related to different deposition rates because the shutter has not been opened each time exactly in the same way, rather than to artifact of the mathematical method.

The example of Figure 35(b) shows that the presented mathematical strategy is effective, provided the phase signal presents significant derivatives. It is a straightforward and convenient method to track the evolution of the resonance frequency just by measuring the phase.

#### STABILITY AND NOISE CONSIDERATIONS

Both the QCM and the cantilever have exhibited a drift of resonance frequency when the filament was switched on. Over large timeframes, the cantilever seems to stabilize and the drift is much attenuated. This means that during a gold deposition of few minutes the contribution of the thermal drift to the resulting frequency shift can be neglected.

To estimate the noise featured by the CMOS cantilever, the cantilever phase signal has been recorded at a fixed frequency where the phase presents a steep evolution (like where the grey line is located in the blue curve of Figure 34). Figure 36 plots the phase signal as function of the time. The signal shows a drift of about  $5.5^\circ$  over 10 min and exhibits a permanent fluctuation.

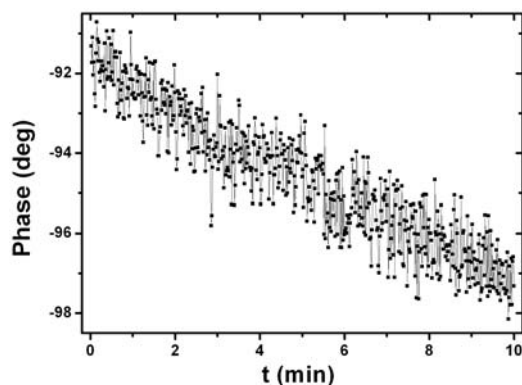


Figure 36. Phase noise measured during 10 minutes at a fixed frequency of 2.926286 MHz (in the pre-recorded spectrum, it is where the steepest point of the phase signal is located)

The phase noise is in the order of 2° peak to peak, i.e. 1.4° RMS. Taking into account the local slope of the variation of phase versus frequency, the resulting frequency noise has been estimated around 8 Hz RMS. (in chapter 5, we analyzed the different sources of noise that affect the output signal of the NEMS/CMOS system and the CMOS circuit was found to be the dominant source).

This value of frequency noise  $\Delta f_{NOISE}$  directly determines the minimum detectable mass  $\Delta m_{MIN}$  through the relation:

$$\Delta m_{MIN} = S \Delta f_{NOISE} \quad (VI.23)$$

where  $S$  is the mass sensitivity (in g.Hz<sup>-1</sup>)

### SUMMARY OF THE RESULTS

In the three sets of experiments, multiple depositions have been carried out. In Figure 37, Figure 38 and Figure 39, the resonance frequency shifts of QCM and cantilevers are plotted as a function of the deposition steps.

In Figure 37, the QCM exhibits at the beginning a large negative shift although no gold seems to have been deposited until gold evaporation n°5 if one relies on the cantilever behavior (previous ‘evaporations’ were operation tests only to calibrate the shutter aperture). This peak must be likely neglected as the large timeframe indicates a long stabilization time because of thermal drift. Afterwards, both curves do not follow perfectly parallel evolutions but in order to try to extract any quantitative information, the shifts resulting of evaporations 5 to 9 are considered and reported in Table VI - 7. The same in Figure 38, only the shifts resulting of evaporations 11 to 13 are considered, and in Figure 39 the shifts of evaporations 5 to 8.

From the QCM resonance frequency shift, an equivalent thickness  $\Delta e$  is calculated with eq.(VI.18). Using this value and the measured frequency shift of the cantilever  $\Delta f_{RES}$ , the experimental distributed mass sensitivity  $S_{D EXP}$  can be obtained in this way (see eq.(VI.15)):

$$S_{D EXP} = \frac{\rho_{Au} \Delta e}{\Delta f_{RES}} \quad (VI.24)$$

All the results are reported in next table. It also provides the values of deposited thickness theoretically calculated using the mass sensitivities of Table VI - 6 and eq.(VI.16):

Set	Device	$\Delta f_{RES}$ QCM (Hz)	$\Delta e$ (nm)	$\Delta f_{RES}$ Cant. (Hz)	$\Delta e_{TH}$ (nm)	$S_{D EXP}$ (g.cm <sup>-2</sup> .s <sup>-1</sup> )
1	WB-D	2.5	0.016	2550	0.123	1.2 10 <sup>-11</sup>
2	WB-D	3.25	0.021	1220	0.059	3.3 10 <sup>-11</sup>
3	WB-A	2.5	0.016	2000	0.093	1.5 10 <sup>-11</sup>

Table VI - 7. Experimental results of the three sets of experiments and resulting experimental distributed mass sensitivity

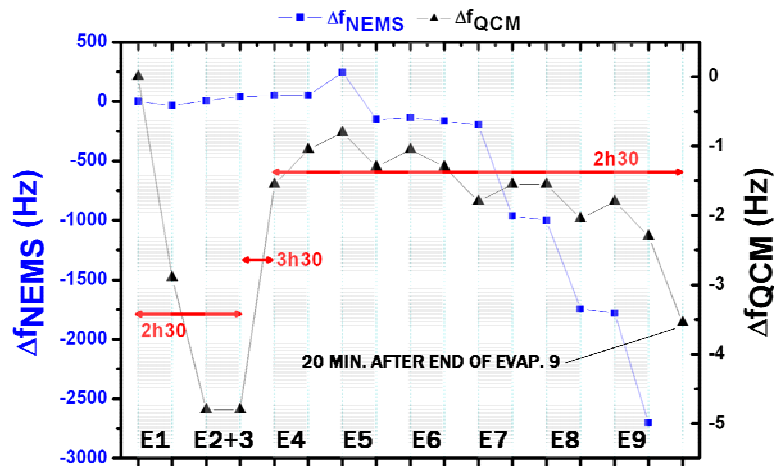


Figure 37. Set 1, WB-D. Resonance frequency shifts of cantilever and QCM as a function of successive depositions of gold by evaporation (represented by a grey bar and named E#)

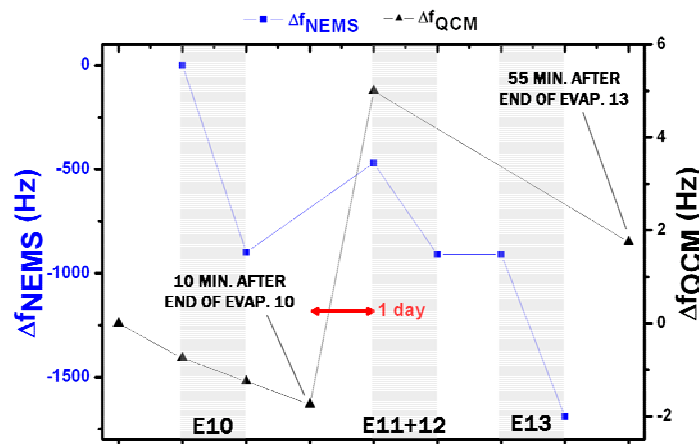


Figure 38. Set 2, WB-D. Resonance frequency shifts of cantilever and QCM as a function of successive depositions of gold by evaporation (represented by a grey bar and named E#)

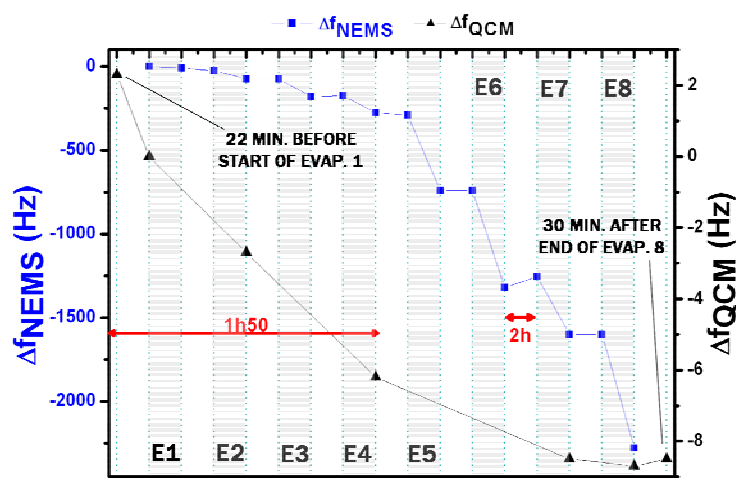


Figure 39. Set 3, WB-A. Resonance frequency shifts of cantilever and QCM as a function of successive depositions of gold by evaporation (represented by a grey bar and named E#)

The apparent total thickness deposited during each set is inferior to the tenth of nanometer (0.1 nm), what indicates that not even a monolayer has been formed on the cantilever surface after each set. Probably, the deposits are under the form of localized clusters which remain too small to be imaged. This would have helped in having another reference than the QCM which did not provide reliable quantitative information on the amount of deposited mass. Indeed, the QCM has been operated without temperature control and in its detection limit. For example, there is no reason to find a difference of mass sensitivity by a factor 3 between sets 1 and 2 although both sets were realized with the same cantilever. Apart from the uncertainty in the QCM shift, other sources of error arise from data not provided by the QCM fabricant like its precise thickness and active area, which have been roughly estimated.

The apparent distributed mass sensitivity of the cantilevers is between 2.8 and 7.8 times better than the theoretical value (see Table VI - 6). In this sense, experiment III qualitatively confirms the high mass sensitivity of cantilever resonators. The theoretical calculation of sensitivity seems to provide the correct order of magnitude (but from those results it cannot be concluded if accurately or not). Furthermore, curves like the one of Figure 35(b) confirm the linearity of the mass sensor (this type of curve has been repeated several times).

#### ADDITIONAL REMARKS

A first remark concerns the specific behavior of CMOS cantilevers within this set-up. From Figure 30 and Figure 33, it is clear that both magnitude and phase degrade along the depositions. Observing that it did not occur in experiments I and II, we make the assumption that this progressive decrease is not related to a mass loading but to the successive irradiations which degrade the CMOS circuitry according to complex physical processes. In this sense, experiment IV is going to provide additional information on this topic assuming that the circuitry will not be exposed to any irradiation as it will be covered by a nanostencil membrane.

The second remark concerns the validity of attributing the entire frequency shift to mass loading. When some material is adsorbed on a nano/micromechanical resonator, the produced shift is the combination of three contributions: one related to adsorption-induced surface stress [12, 21], another to the adsorbate stiffness that modify the effective Young modulus [11], and the third related to the proper mass loading. The two first contribute to shift the resonance upwards while the third downwards. It has been reported [22, 23] that metal deposits under the form of a single monolayer can result in a dominant stress effect and thereby in a shift upwards. In the example of experiment III, the gold thickness is so thin that the negative shift is probably entirely related to mass loading. However, a further study would be to perform theoretical calculations combining the three effects in order to predict the cantilever behavior for larger deposited thicknesses.

## II.2. Application of NEMS/CMOS mass sensors as positioning sensors (exp. IV)

In experiment III, CMOS cantilevers have exhibited a linear behavior during mass depositions and have fulfilled the requirements in terms of distributed mass sensitivity listed in Table VI-5. These specifications have been defined to further implement NEMS-based mass sensors as alignment sensors within a quasi-dynamic stencil lithography system (QDS). This system is presently being developed with EPFL. The first deposition experiments are scheduled for October 2007.

Hereafter, first progresses towards the realization of a demonstrator of the QDS concept are detailed: the QDS approach is introduced and the system is described focusing on the requirements that the alignment sensor has to fulfill.

### II.2.a. Quasi-dynamic approach

The goal is to use full-wafer sized stencil and substrate in combination with a large range, highly accurate XY nanopositioning stage to perform stencil lithography in a quasi-dynamic approach. The patterning procedure consists in (i) aligning stencil and substrate within the vacuum chamber, (ii) putting them in contact, (iii) evaporating a material through the nanostencil apertures, (iv) stopping the deposition and separating them again, (v) performing a controlled motion, (vi) putting them in contact and evaporating again, eventually with another material.

Repeating  $n$ -times this step-an-repeat approach, multiple ( $n$ ) nanometer-sized patterns of multiple ( $n$ ) materials can potentially be obtained. A decisive advantage of this technique is the opportunity to form high purity deposits since the vacuum is not broken in-between each deposition step. In this way, specific devices like tunnel junctions can potentially be fabricated. Racz et al.[24] made a first attempt of realization of QDS but using a different approach.

Thus, a system for full-wafer (100 mm) evaporation needs to be developed. The idea is to externally roughly pre-align the stencil to the substrate, to place the holder containing the two pieces into an evaporation chamber and to perform inside a finer alignment relying on the mass sensor. Once both elements are correctly positioned one with respect to the other (a 2-3  $\mu\text{m}$  accuracy is aimed), the evaporation step starts. In between each subsequent evaporation step, the stencil is translated by two independent nanopositioning stages which have a 25 mm range and an encoder resolution of 20 nm. In the first demonstrator, the necessary motion between each deposition step is realized relying on the high resolution of the stage what conveniently avoids any posterior alignment step with the mass sensor.

### II.2.b. System description

The guidelines of the QDS system are presented hereafter. The development is still on going and is not complete. The idea is to maintain fixed substrate and mass sensor while the stencil is linked to the translation stages. Like in static Stencil Lithography (SL), the gap between stencil and substrate needs to be controlled during the deposition in order to improve the patterning resolution. The gap must also be controlled during the stencil motion because of wafer curvatures that may cause frictions. The first version of the system is sketched in Figure 40: the substrate is located above the stencil and below the mass sensor.

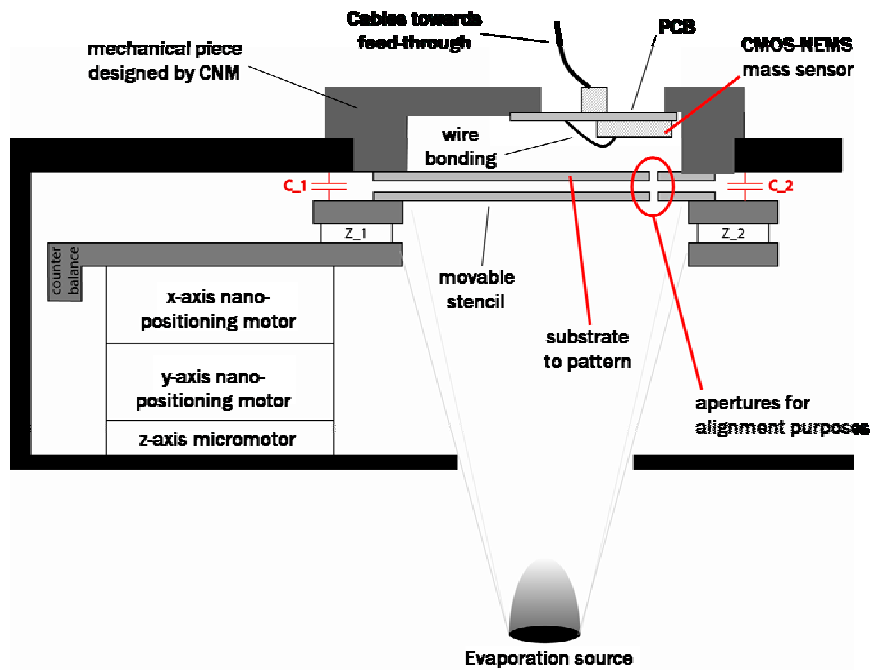


Figure 40. Schematic representation of the QDS system.

The gap between stencil and substrate is measured using three capacitive sensors ( $C_1$ ,  $C_2$  and,  $C_3$  [not visible in the 2D scheme of Figure 40]) and controlled using three piezo-actuators ( $Z_1$ ,  $Z_2$  and,  $Z_3$ ). During the phase of approximation of the stencil towards the substrate, the capacitive sensors indicate a progressively decreasing distance. When the measurement of distance becomes constant while the actuators are still pushing the stencil against the substrate, it means that both elements are effectively in contact (at least, in the three points of measurement).

This ‘contact detection’ can be performed over all three actuators in order to determine the correct position of the stencil with respect to the substrate. Actuation and sensor feedback signals have to be controlled by software. This software must simultaneously control and coordinate the following elements:

- XY actuation of the nanopositioning table
- active gap control. This consists in monitoring in real time the gap between substrate and stencil and therefore to actuate the stencil adequately through the three piezo. When touching, the procedure must be interrupted and the position must be memorized for further steps.
- stencil/substrate alignment procedure. A special scanning motion of the stencil must be carefully defined in order to provide a rapid and accurate alignment. The software must be connected to the network analyzer that measures in real time the frequency spectrum of the sensor. The phase change is monitored at a fixed frequency: the RMS value is continuously calculated and when it changes by twice the measured RMS noise, it means that the aperture is above the sensor and the position is memorized by the software.

The critical issue that determined the first guidelines of the system design has arisen from the need to be able to electrically connect the NEMS/CMOS chip. To simplify the packaging, a classical solution has been adopted based on bonding wires from the contact pads of the circuitry to a PCB. The height of these wires, given by their vertical curvature, implies an important gap in

the order of few mm between substrate and mass sensor. This has important consequences upon the sensor specifications.

The mechanical part on which the PCB is fixed has been already designed according to all these requirements: its schematic can be found in annex A.8. Another critical issue has arisen from the difficulty to find a straightforward and reliable method to fix substrate and stencil to their respective holder. This issue is circumvented through the use of stiff clips (see fig.4 in annex A.8).

### II.2.b.i) Alignment procedure

The first operation consists in roughly pre-aligning the substrate above the mass sensor. In order to make it easier, a matrix of relatively large apertures (tenths of microns) is fabricated onto the substrate according to the standard microstencil fabrication process of EPFL. This operation is illustrated in Figure 41: the mass sensor is roughly positioned within one of those large apertures.

In order to obtain a spatial reference of the stencil aperture with respect to the substrate, our idea is to rely on the borders of one of the rectangular-shape apertures made in the substrate. Basically, when the stencil hole dedicated to alignment purposes is on top of the substrate, no flux passes [see Figure 41(a)], but whenever the hole arrives at one border, the mass sensor starts detecting it [see Figure 41(b)].

Figure 41 illustrates the alignment procedure in the X-direction (in the Y-direction the procedure is equivalent): the point here is that the flux is much enlarged when impacting on the surface because of the large gap between substrate and sensor. This feature is numerically described in next section [II.2.b.ii). Mass sensor requirements].

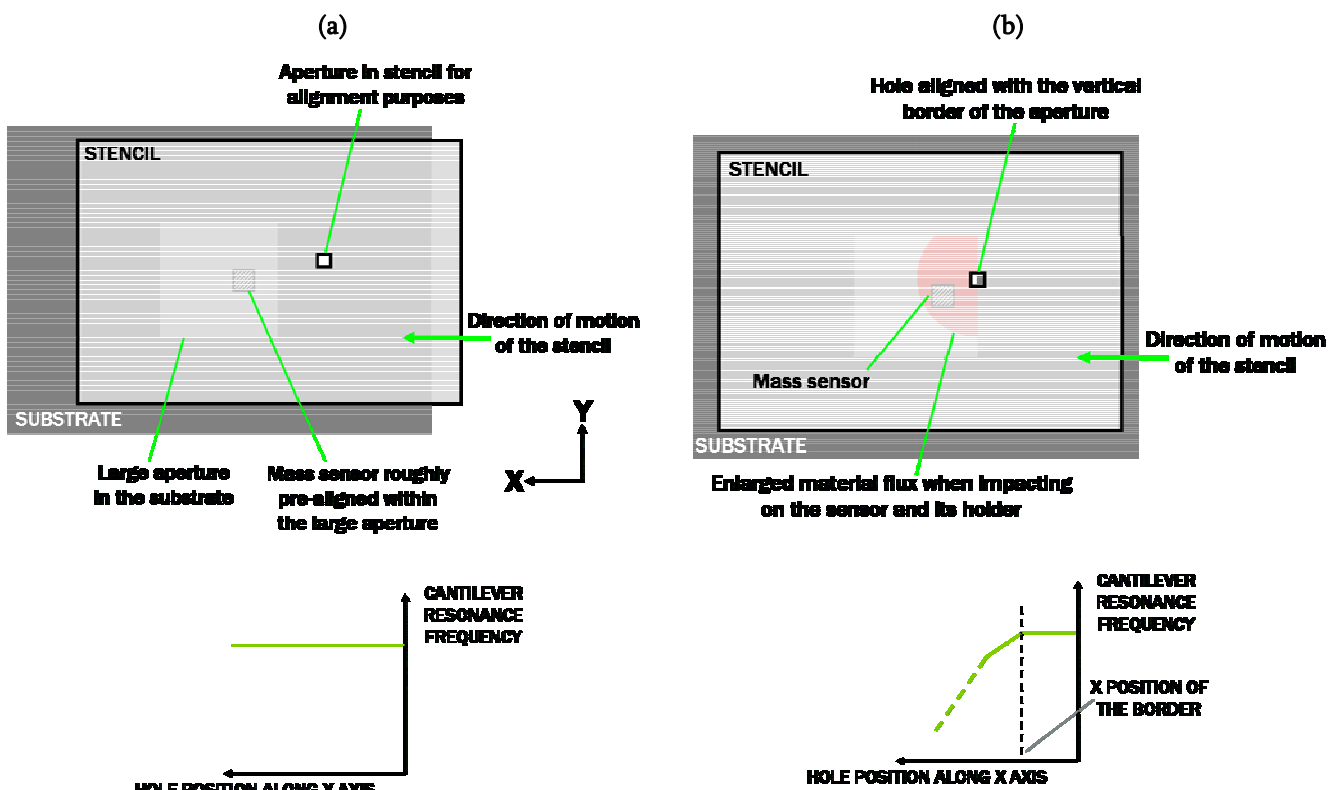


Figure 41. Alignment principle in the X direction. The stencil is schematically drawn transparent in order to make visible the underneath elements. (a) the stencil hole is above the substrate and no material impacts on the sensor. (b) the stencil hole arrives at the border of a substrate aperture and some material starts impacting on the cantilever sensor so that its resonance frequency starts decreasing

In fact, the precision of the system is determined by the ability to detect a fast and steep deviation of cantilever resonance frequency. The faster and the more pronounced is the transition between the plateau and the decreasing slope [see Figure 41(b)], the most precise is the determination of the X-axis spatial reference provided by the X-coordinate of the border. Actually, the faster and the more sensitive is the mass sensor, the most accurate will be the alignment.

To schematically illustrate alignment and deposition sequences, all the operation steps are sketched from Figure 42 to Figure 46:

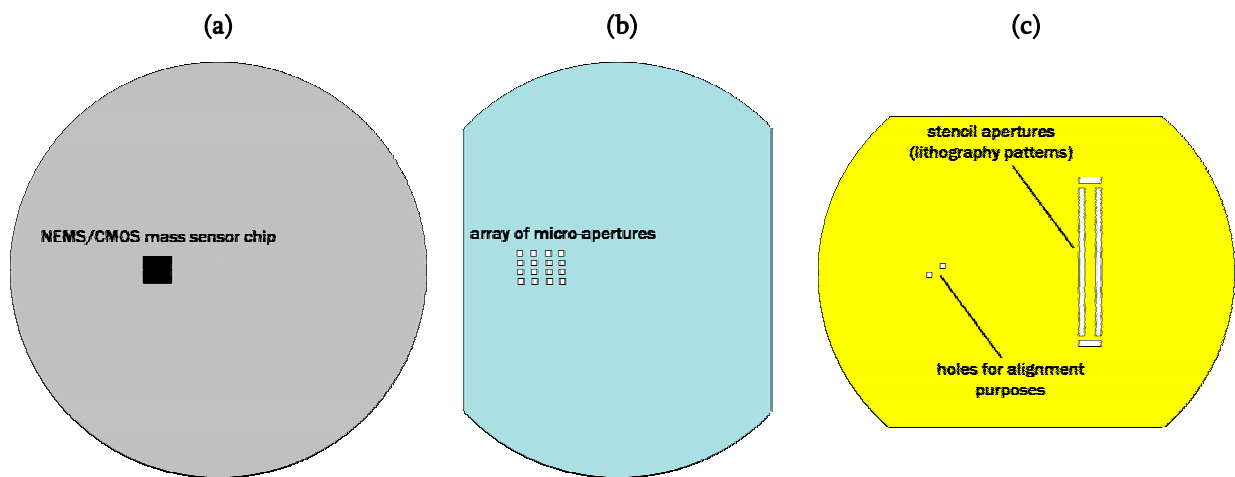


Figure 42. Schematic representation of the three elements involved in the alignment procedure. (a) NEMS/CMOS mass sensor chip. (b) substrate with an array of micro-apertures. (c) stencil containing holes for alignment purposes and other holes for patterning purposes.

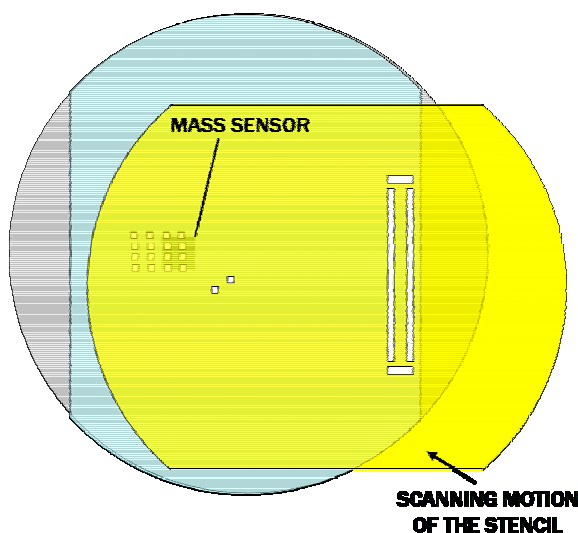


Figure 43.

STEP 1: substrate and sensor roughly pre-aligned externally. Start of the alignment procedure by moving the stencil while some material starts to be deposited

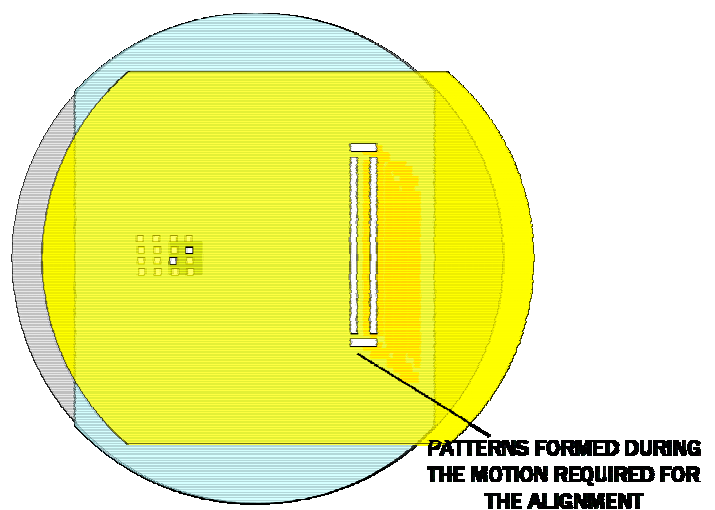


Figure 44.

STEP 2: stencil moved above the substrate. The scan lasts until a signal is detected by the mass sensor, corresponding to an alignment between stencil aperture and one of the substrate apertures. During this procedure, the substrate is already "drawn" due to the motion.

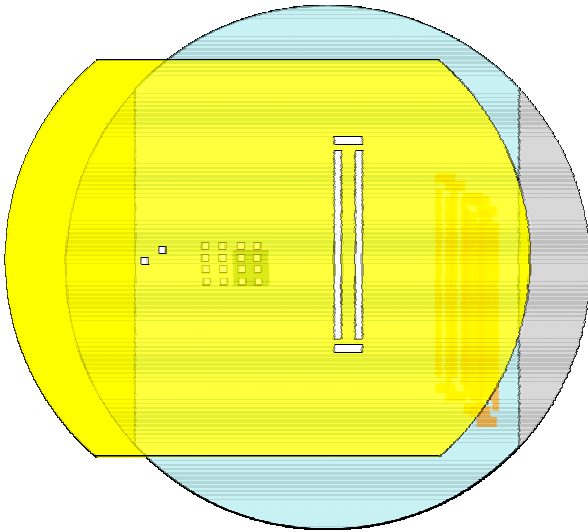


Figure 45.

STEP 3: Now the position is known, the deposition is stopped. The stencil is displaced until a given position.

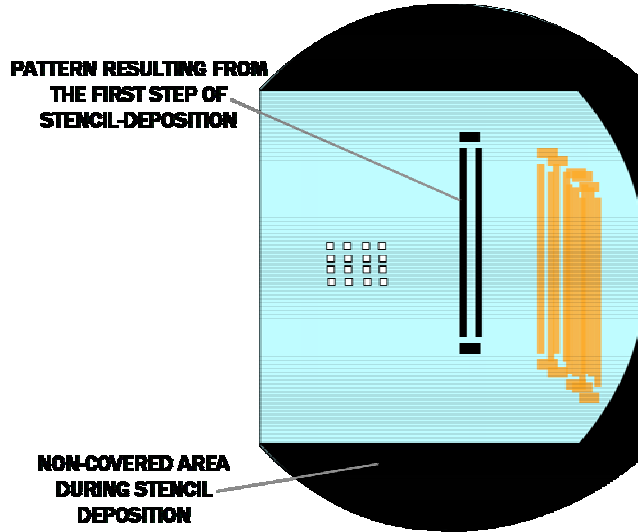


Figure 46.

STEP 4: Metal deposition. This scheme depicts the substrate after the alignment procedure and after a single metal deposition.

### II.2.b.ii) Mass sensor requirements

Owing to the large gap between substrate and mass sensor (because of the height of the bonding wires), the atom flux is dispersed over a large area when impacting on the sensor chip. For this reason, the quantity of material potentially received by the mass sensor is much attenuated and will actually depend on the size of the stencil aperture. In the following section, these considerations are numerically assessed, in particular to estimate the time response of the sensor. Figure 47 sketches the critical dimensions of the system:

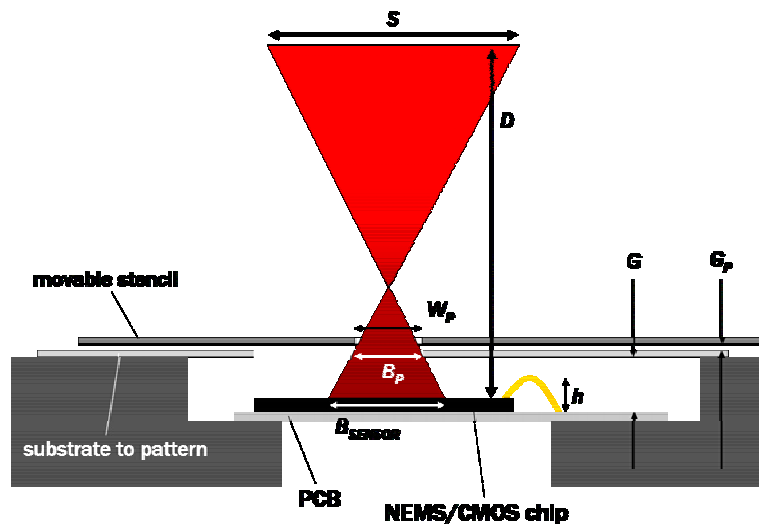


Figure 47. Schematic representation of the broadening of the flux when impacting on the sensor surface

$D$  is the source-sample distance ( $\approx 50$  cm);  $S$  the source diameter ( $\approx 1$  cm);  $h$  the height of the wires (i.e. curvature,  $\approx 1.5$  mm);  $G$  the substrate-sensor gap ( $G \approx 1.5$  mm, 1 mm margin respect to  $h$ );  $G_p$  the substrate-stencil gap ( $G_p \approx 10$   $\mu\text{m}$ , but nominally substrate and stencil are supposed to be in

contact);  $W_P$  the pattern size in the stencil (the specific pattern devoted to aligning),  $B_P$  the resulting pattern size on the substrate, and  $B_{SENSOR}$  the resulting pattern size on the surface of the sensor chip.

Let us quantify now the resulting frequency shift as a function of the deposition flux and of  $W_P$ . According to eq.IV-1,  $B_P$  is given by:

$$B_P = W_P + \frac{S G_P}{D} \quad (VI.25)$$

with  $G_P = 10 \mu\text{m}$ ,  $B_P = W_P + 200 \text{ nm}$ . Assuming  $W_P$  in the micron range,  $B_P \approx W_P$ , what means that the beam is not widened when impacting after the stencil onto the substrate.

Now the lateral extension of the flux when impacting on the chip surface must be estimated. Assuming  $G$  equal to 1.5 mm:

$$B_{SENSOR} = W_P + \frac{S G}{D} \approx W_P + 30 \mu\text{m} \approx 30 \mu\text{m} \quad (VI.26)$$

As a conclusion, the flux size on the NEMS chip surface is constant around 30  $\mu\text{m}$  and is independent of  $W_P$ . This implies that the resonator receives much less flux. For a device with a given distributed mass sensitivity, this will convert into higher times before detecting anything.

To quantify this issue, a short study is carried out. First, it is assumed that the stencil is fully in front of the substrate aperture exposing it to the ‘collimated’ atoms beam.

The nominal flux of the deposition chamber that impacts and passes through stencil and substrate is called  $F_{SOURCE}$  (in nm/s). The resulting flux  $F_{SENSOR}$  impacting on the sensor chip surface can be expressed as:

$$F_{SENSOR} = F_{SOURCE} \frac{A_{STENCIL}}{A_{SENSOR}} \quad (VI.27)$$

where  $A_{STENCIL}$  is the area of the stencil aperture ( $W_P$ ) and  $A_{SENSOR}$  the area related to  $B_{SENSOR}$ .

$A_{STENCIL}$  is approximately given for a circular hole shape by:

$$A_{STENCIL} = \pi \left( \frac{W_P}{2} \right)^2 \quad (VI.28)$$

$A_{SENSOR}$ , the area related to  $B_{SENSOR}$ , is approximately given for a circular shape by:

$$A_{SENSOR} = \pi \left( \frac{30 \mu\text{m}}{2} \right)^2 \quad (VI.29)$$

Now, the minimum time ( $t_{MIN}$ ) of aperture of the shutter, in order to be able to detect a minimum resonance frequency variation, can be evaluated from eq.(VI.15). So:

$$\frac{S_D \Delta f_{MIN}}{\rho} = \Delta e_{MIN} = F_{SENSOR} t_{MIN} \quad (VI.30)$$

where  $S_D$  is the distributed mass sensitivity ( $\text{g.cm}^{-2}.\text{Hz}^{-1}$ ),  $\Delta f_{MIN}$  the minimum detectable frequency shift produced by mass loading,  $\rho$  the density of the deposition material and  $\Delta e_{MIN}$  the corresponding minimum detectable thickness.

Computing eq.(VI.27) and (VI.30), the minimum time to detect a mass change is expressed:

$$t_{MIN} = \frac{S_D \Delta f_{MIN} A_{SENSOR}}{\rho F_{SOURCE} A_{STENCIL}} \quad (VI.31)$$

In Table VI - 8,  $t_{MIN}$  is reported in function of the stencil aperture size and the distributed mass sensitivity of the sensor (in the order of the ones of experiment III) with the example of silver as deposition material ( $\rho=10.5 \text{ g.cm}^{-3}$ ),  $\Delta f_{MIN}=10 \text{ Hz}$  (noise level estimated from experiment III), and  $F_{SOURCE}=0.4 \text{ nm/s}$  (standard value provided by the fabricant):

Stencil aperture size ( $\mu\text{m}$ )		1	5	10
$t_{MIN}$ (s) for	$S= 5.10^{-11}\text{g.cm}^{-2}.\text{Hz}^{-1}$	1.1	0.04	0.01
	$S= 10^{-10}\text{g.cm}^{-2}.\text{Hz}^{-1}$	2.1	0.09	0.02

**Table VI - 8. Minimum time to detect any mass-related resonance frequency variation in function of the stencil aperture size and of two distributed mass sensitivities**

This table shows that the bigger is the stencil hole, the faster is the time response of the mass sensor. It may seem paradoxical but this means that the larger is the stencil hole dedicated to alignment, the better will be the alignment, i.e. the borders of substrate apertures will be easier and faster detected.

The alignment accuracy is difficult to quantify since it depends on the scanning speed, the precision of the XY actuators and on the mass sensors sensitivity (in the sense that the inflexion point of the resonance frequency evolution can be more or less precisely determined). Provided that the scanning speed is not too fast, the accuracy should be at least in the range of few microns.

## Conclusion of chapter 6

In this chapter, the versatility of NEMS-based mass sensors has been illustrated through four different examples of applications.

For scientific purposes, these ultra-sensitive nanosensors open up new possibilities of exploring new physical or chemical phenomena previously unattainable with any other tools. In this thesis, the study of wetting mechanisms at very small scales (femtoliter droplets) has been made possible thanks to the use of NEMS/CMOS as nano/microbalances. Such phenomena could have not been analyzed with traditional quartz microbalances whose mass resolution is more limited.

Through the in-situ monitoring of the deposition of ultra-thin gold layers, experiment III has confirmed the very high distributed mass sensitivity of NEMS-based mass sensors.

The fact that such sensors provide an unprecedented mass sensitivity and a very high spatial resolution inherent to their small size makes them interesting devices for industrial applications as well. In this sense, applying a mass sensor like a positioning sensor has allowed developing a quasi-dynamic stencil lithography system.

## Bibliographical references

1. Xia, Y.N. and G.M. Whitesides  
**Soft lithography**  
Annual Review of Materials Science, 1998. **28**: p. 153-184.
2. Thorsen, T., S.J. Maerkl, and S.R. Quake  
**Microfluidic large-scale integration**  
Science, 2002. **298**(5593): p. 580-584.
3. Delamarche, E., A. Bernard, H. Schmid, B. Michel, and H. Biebuyck  
**Patterned delivery of immunoglobulins to surfaces using microfluidic networks**  
Science, 1997. **276**(5313): p. 779-781.
4. Calvert, P.  
**Inkjet printing for materials and devices**  
Chemistry of Materials, 2001. **13**(10): p. 3299-3305.
5. Belaubre, P., M. Guirardel, G. Garcia, J.B. Pourciel, V. Leberre, A. Dagkessamanskaia, E. Trevisiol, J.M. Francois, and C. Bergaud  
**Fabrication of biological microarrays using microcantilevers**  
Applied Physics Letters, 2003. **82**(18): p. 3122-3124.
6. Piner, R.D., J. Zhu, F. Xu, S.H. Hong, and C.A. Mirkin  
**"Dip-pen" nanolithography**  
Science, 1999. **283**(5402): p. 661-663.
7. Fang, A.P., E. Dujardin, and T. Ondarcuhu  
**Control of droplet size in liquid nanodispensing**  
Nano Letters, 2006. **6**(10): p. 2368-2374.
8. Meister, A., M. Liley, J. Brugger, R. Pugin, and H. Heinzelmann  
**Nanodispenser for attoliter volume deposition using atomic force microscopy probes modified by focused-ion-beam milling**  
Applied Physics Letters, 2004. **85**(25): p. 6260-6262.
9. Picknett, R.G. and R. Bexon  
**Evaporation of Sessile or Pendant Drops in Still Air**  
Journal of Colloid and Interface Science, 1977. **61**(2): p. 336-350.
10. Dohn, S., R. Sandberg, W. Svendsen, and A. Boisen  
**Enhanced functionality of cantilever based mass sensors using higher modes**  
Applied Physics Letters, 2005. **86**(23).
11. Tamayo, J., D. Ramos, J. Mertens, and M. Calleja  
**Effect of the adsorbate stiffness on the resonance response of microcantilever sensors**  
Applied Physics Letters, 2006. **89**(22).
12. Chen, G.Y., T. Thundat, E.A. Wachter, and R.J. Warmack  
**Adsorption-Induced Surface Stress and Its Effects on Resonance Frequency of Microcantilevers**  
Journal of Applied Physics, 1995. **77**(8): p. 3618-3622.
13. Ramos, D., J. Tamayo, J. Mertens, M. Calleja, and A. Zaballos  
**Origin of the response of nanomechanical resonators to bacteria adsorption**  
Journal of Applied Physics, 2006. **100**(10).

14. Pham, N.T., G. McHale, M.I. Newton, B.J. Carroll, and S.M. Rowan  
**Application of the quartz crystal microbalance to the evaporation of colloidal suspension droplets**  
Langmuir, 2004. **20**(3): p. 841-847.
15. Joyce, M.J., P. Todaro, R. Penfold, S.N. Port, J.A.W. May, C. Barnes, and A.J. Peyton  
**Evaporation of sessile drops: Application of the quartz crystal microbalance**  
Langmuir, 2000. **16**(8): p. 4024-4033.
16. Ondarcuhu, T., L. Nicu, S. Cholet, C. Bergaud, S. Gerdes, and C. Joachim  
**A metallic microcantilever electric contact probe array incorporated in an atomic force microscope**  
Review of Scientific Instruments, 2000. **71**(5): p. 2087-2093.
17. Spletzer, M., A. Raman, A.Q. Wu, X.F. Xu, and R. Reifenberger  
**Ultrasensitive mass sensing using mode localization in coupled microcantilevers**  
Applied Physics Letters, 2006. **88**(25).
18. Sauerbrey, G.  
**Verwendung Von Schwingquarzen Zur Wagung Dunner Schichten Und Zur Mikrowagung**  
Zeitschrift Fur Physik, 1959. **155**(2): p. 206-222.
19. Miller, J.G. and D.I. Bolef  
**Sensitivity Enhancement by Use of Acoustic Resonators in Cw Ultrasonic Spectroscopy**  
Journal of Applied Physics, 1968. **39**(10): p. 4589-&.
20. Cumpson, P.J. and M.P. Seah  
**The Quartz Crystal Microbalance - Radial Polar Dependence of Mass Sensitivity Both on and Off the Electrodes**  
Measurement Science & Technology, 1990. **1**(7): p. 544-555.
21. Lu, P., H.P. Lee, C. Lu, and S.J. O'Shea  
**Surface stress effects on the resonance properties of cantilever sensors**  
Physical Review B, 2005. **72**(8).
22. Haiss, W.  
**Surface stress of clean and adsorbate-covered solids**  
Reports on Progress in Physics, 2001. **64**(5): p. 591-648.
23. Friesen, C., N. Dimitrov, R.C. Cammarata, and K. Sieradzki  
**Surface stress and electrocapillarity of solid electrodes**  
Langmuir, 2001. **17**(3): p. 807-815.
24. Racz, Z., J.L. He, S. Srinivasan, W. Zhao, A. Seabaugh, K.P. Han, P. Ruchhoeft, and J. Wolfe  
**Nanofabrication using nanotranslated stencil masks and lift off**  
Journal of Vacuum Science & Technology B, 2004. **22**(1): p. 74-76.



## General Conclusion

This PhD thesis features specific results in three different directions.

First, it demonstrates through a specific application the applicability of nanostencil lithography as a novel, clean (resistless), parallel and straightforward nanopatterning technique for the full-wafer scale integration of silicon NEMS on CMOS.

With regard to this matter, this work shows that CMOS-NEMS are systems that combine two interesting features:

- they have unprecedented sensing attributes originated by the mechanical part
- they also offer the possibility to detect the sensing signal in enhanced conditions as the on-chip CMOS circuitry reduces parasitic loads and can complementarily amplify and condition the sensing signal.

Finally, several examples of applications of CMOS-NEMS as ultra-sensitive nanomechanical mass sensors have been detailed. Their results reveal the high versatility of such sensors that can be utilized both for scientific research purposes, as they allow exploring new physical, chemical or biological mechanisms at previously unexplored scales; and in industrial applications, in particular in the semiconductor industry, to control depositions of thin film or as alignment sensors in lithography systems.

In the following paragraphs, the main results are summarized.

As a first step, the mechanical and electrical behavior of electrostatically actuated nano/microresonators (cantilevers, bridges and quad-beams) embedded in a capacitive detection scheme have been analyzed. A comparative electrical study of resonators vibrating in in-plane and out-of-plane flexion has been carried out. The main issue in a capacitive detection scheme comes from parasitic stray capacitances that can drastically degrade the performance of the transduction. In this configuration, in-plane vibrating devices are much less affected than the out-of-plane ones as much higher amplitude and phase relative changes can be obtained with respect to the background signal. However in practice, in-plane vibrating resonators present reduced capacitive coupling areas what results in low absolute signal levels. Additionally, output parasitic capacitances arising from the measurement instrumentation can further reduce the available signal levels.

In this sense, the opportunity to integrate monolithically nano/micromechanical resonators on CMOS in order to detect the signal through a specific circuitry has been studied. Such

integration provides two major advantages: (i) reducing all the parasitic loads at the resonator output, and (ii) amplifying and conditioning ‘on-chip’ the resonance signal. Hence, a specific low-power CMOS readout circuit, whose function is to read out the capacitive current generated by a resonating nano/micromechanical device, has been designed. It is basically a transimpedance amplifier whose architecture is based on a second generation current conveyor.

Its topology and the corresponding layout have been described and the circuit behavior (intrinsic and coupled to the NEMS) has been fully simulated. According to simulation results, the detection of the resonance of a nano/microcantilever is greatly enhanced through the CMOS integration. In the case of in-plane vibrating cantilevers, this integration reduces much the signal attenuation at the resonator output, nevertheless, in the case of quad-beams resonators, the integration provides the same advantage but does not solve the issue of ‘vertical’ (out-of-plane) stray capacitances.

In terms of processing, combining the technology for the fabrication of nanomechanical resonators with a standard CMOS technology is challenging. In this thesis, this issue has been addressed by developing jointly with EPFL (École Polytechnique Fédérale de Lausanne) a novel post-processing technology based on nanostencil lithography. Our works demonstrate the potential of nanostencil lithography (nSL) as a parallel, straightforward and CMOS compatible patterning technique to define devices on CMOS at the 200 nm scale.

To achieve this, two critical issues have been solved: (i) the full-wafer alignment between nanostencil and CMOS substrate at 100 mm wafer scale, and (ii) the correction of pattern blurring effect to obtain an enhanced resolution. Regarding the aspect of device operation, it has been shown that post-processing CMOS wafers with nanostencil lithography does not affect the circuitry performance on the contrary to e-beam lithography, for example.

These results represent the first time that an emerging nanolithography technique has been used to pattern multiple N-MEMS devices on a whole CMOS wafer in a parallel, potentially low-cost approach. The same strategy could be extended to other examples of nanodevices, such as single electron transistors on CMOS, for which there is at present no affordable technological process that fulfill the requirements of high resolution processing at wafer scale and CMOS compatibility.

To finish with the fabrication aspects, it must be pointed out that an alternative post-processing technology of pre-fabricated CMOS wafers has also been developed. Using electron beam lithography at low electron energy, new prototypes of NEMS/CMOS have been rapidly processed with a high flexibility.

After their fabrication, fully integrated nanomechanical resonators (either cantilevers or quad-beams) have been extensively characterized electrically. Their mechanical resonance has been successfully sensed by the CMOS circuitry. Cantilevers and quad-beams have exhibited quality factors in vacuum up to 9500 and 7000 respectively. The resonance frequency could be tuned by varying the driving voltage and interesting hysteretic non-linear behaviors have been observed either in air or in vacuum

The RLC electromechanical model, which predicts the level of electrical signal produced during mechanical resonance, is found to be rather qualitative. Yet, the large number of

uncertainties regarding the resonators parameters (Young modulus, exact dimensions, underetching extension, etc...) impedes to conclude more definitively on the accuracy of the model. Taking into account all the possible errors, this model can be considered precise within one order of magnitude what is actually sufficient to define the specifications of a CMOS readout circuit. A characterization technique based on atomic force microscopy is currently being developed to determine intrinsic mechanical parameters of those resonators (such as stiffness, mode shape, etc...).

As future prospects, several improvements regarding the design of the resonator could allow obtaining better electrical responses with the same circuit topology. In the case of the quad-beams, the integration area should be placed farther from the circuit area so that it can be polarized at much higher voltages without perturbing the juxtaposed MOS transistors. In order to reduce stray capacitances, the anchors area should be minimized, for example incorporating holes in the central plate: in this way the etching time would be reduced. Concerning cantilevers, optimizing the design of the readout and driving electrodes could lead to an important reduction of the fringing field parasitic capacitance.

Finally, the versatility of NEMS-based mass sensors (all integrated on CMOS) has been illustrated through four different examples of applications.

Indeed, such ultra-sensitive nanosensors open up new possibilities of exploring new physical or chemical phenomena previously unattainable with any other tools. In the first experiment, wetting mechanisms of sessile droplets have been explored at very small scales (volumes in the femtoliter range) implementing the resonators as nano/microbalances. Such phenomena could not have been analyzed with traditional quartz microbalances whose mass resolution is more limited.

In the second experiment, a new architecture of resonator based on a double nano/microcantilever has been designed and tested: this new device allows making reliable measurements under ambient conditions by providing a direct estimation of the measurement uncertainty. Other interesting features of these double cantilevers have been described like the possibility to measure a mass loading relying on amplitude instead of frequency changes.

The fact that NEMS-based mass sensors provide an unprecedented mass sensitivity and a very high spatial resolution inherent to their small size makes of them interesting devices for industrial applications as well.

With regard to this matter, another experiment has consisted in monitoring in-situ the deposition of ultra-thin gold layers both with NEMS/CMOS and quartz-crystal microbalances. When measuring in real time the mass of these uniform deposits of thicknesses inferior to sub-monolayer, silicon nano/microresonators have exhibited a mass sensitivity better than QCM by between two and three orders of magnitude. This is very promising with regard to the possibility of replacing QCM in the semiconductor industry as a tool to monitor the deposition of thin layers.

These outstanding mass sensing attributes have led us to apply such sensors as positioning sensors according to an innovative concept. In fact, CNM and EPFL are presently developing a 'quasi-dynamic' stencil lithography system and there was initially a need to find an adequate technique to align in-situ (within the vacuum deposition chamber) the stencil with the substrate to be patterned. Nanomechanical mass sensors will accomplish this function thanks to their mass sensitivity and spatial resolution attributes.



# Annex

A1.	Resum en català .....	232
A2.	Resumen en castellano .....	234
A3.	Résumé en français .....	236
A4.	Zusammenfassung auf Deutsch .....	238
A5.	Glossary .....	239
A6.	Complete diagram of the CCII CMOS circuit .....	240
A7.	Technological processes .....	241
A7.1.	CNM CMOS process .....	241
A7.2.	Dummy wafers process .....	247
A7.3.	Post-processing based on eBL .....	250
A7.4.	Experimental results of pattern transfer of nanostencil lithography .....	251
A8.	QSD system: schematic of the mechanical holder of the sensor .....	253
A9.	AFM characterization of resonators: preliminary work .....	254
A10.	List of publications .....	257

## A1. Resum en català

Aquest treball de tesi ha estat realitzat principalment en el Centre Nacional de Microelectrònica – Institut de Microelectrònica de Barcelona (CNM-IMB), que pertany al Consell Superior d'Investigacions Científiques (CSIC) i, en part també a l' Institut de Nanotecnologia de Lyon (França) que pertany al Centre Nacional d' Investigacions Científiques (CNRS, França). El doctor Francesc Pérez-Murano ha co-dirigit la tesi al CNM, i el professor Georges Brémond al INL.

El marc d'aquest treball ha estat el projecte europeu NaPa ('Emerging Nanopatterning Methods') l'objectiu del qual és desenvolupar tècniques emergents de litografia a nivell nanomètric que es puguin industrialitzar a mig termini, i les seves possibles aplicacions. En aquest sentit, els objectius principals de la tesi han estat desenvolupar (i) sistemes nanoelectromecànics (NEMS) integrats amb CMOS, i (ii) processos de fabricació basats en una tècnica avançada de nanolitografia que es diu 'nanostencil' per poder fabricar aquests sistemes monolítics.

Aquesta tesi comporta dos aspectes principals: un està relacionat amb el disseny i la operació d'un nanodispositiu mecànic i l'altre amb les tecnologies de nanofabricació. Concretament, s'ha modelat i dissenyat un ressonador nano/micromecànic de silici, després s'ha estudiat les venteges i la viabilitat d'una integració monolítica amb un circuit CMOS. De fet, els NEMS/CMOS són sistemes atractius que combinen extraordinàries propietats del sensat, proporcionades per la part mòbil mecànica, amb la possibilitat de detectar el senyal de sortida en condicions molt més favorables ja que les capacitats paràsites són reduïdes dràsticament en tractar aquesta senyal a través d'una circuiteria CMOS 'on-chip' que addicionalment pot amplificar-la i acondicionar-la.

Posteriorment, aquests dispositius han estat fabricats combinant una tecnologia CMOS estandar amb mètodes emergents de nanolitografia, en particular mitjançant litografia 'nanostencil', la qual s'ha hagut de optimitzar en terminis d'aplicabilitat i resolució.

Ha estat possible després demostrar el funcionament correcte del dispositiu NEMS/CMOS fabricat: caracteritzant la resposta freqüencial de l'estructura nano/micromecànica on el senyal de sortida ha estat obtingut sota la forma d'un senyal elèctric alternatiu tractat per un circuit CMOS específic de detecció. Finalment, s'ha implementat aquest ressonador NEMS/CMOS com un sensor de massa ultra-sensible en quatre experiments diferents orientats a objectius tècnics o científics.

A continuació, es resumeix amb més detalls el treball realitzat. Com a primer pas, dos tipus de ressonadors nano/micromecànics ('cantilevers' i 'quad-beams') s'han modelat analíticament per poder estudiar la seva resposta freqüencial mecànica. Amb l'objectiu d'excitar-los i detectar-los elèctricament, s'ha optat per una tècnica capacitiva. Per tant s'ha implementat un model mixt electromecànic per poder calcular el seu comportament elèctric.

Per millorar la resposta elèctrica, s'ha dissenyat específicament un circuit CMOS de lectura i de baix consum. Funciona com amplificador de transimpedància per convertir el corrent creat per la ressonància mecànica en un voltatge suficientment alt. A partir de simulacions, s'ha analitzat exhaustivament (i) el comportament intrínsec d'aquest circuit i (ii) quan està acoblat el ressonador mecànic.

Tot i això, la fabricació d'aquests nanodispositius integrats en CMOS constituïa un repte ja que la integració a nivell d'òbvia sencera de NEMS sobre CMOS mitjançant processos no excessivament cars no havia estat demostrada encara a l' inici d'aquesta tesi. Partint d'aquesta observació, s'ha posat en marxa una col·laboració amb l'EPFL (École Polytechnique Fédérale de Lausanne, Suïssa) per desenvolupar la litografia 'nanostencil' amb l'objectiu d'integrar a escala d'òbvia estructures mesoscòpiques (micro i nano) sobre circuits CMOS pre-fabricats. Després d'identificar els principals problemes inicials, s'ha pogut desenvolupar amb èxit una tecnologia de post-procés que permet integrar NEMS en CMOS mitjançant una única etapa de litografia 'nanostencil'. En paral·lel, un altre post-procés basat en una etapa de litografia per feix d'electrons ('e-beam lithography') s'ha posat a punt de manera que es poden fabricar dins de períodes breus nous prototips de nanodispositius sobre CMOS.

Aquests NEMS/CMOS han estat extensament caracteritzats elèctricament a l' aire i al buit. Les característiques principals dels espectres de ressonància, els nivells de senyal obtinguts experimentalment així com l'efecte de la tensió aplicada han estat analitzats.

Finalment, com ja ha sigut mencionat, aquests dispositius NEMS/CMOS han estat implementats com sensors de massa. Actualment, aquesta aplicació dels NEMS és una de les més explorades ja que els ressonadors nano/micromecànics ofereixen grans avantatges en termes de sensibilitat i integració de sistemes comparats amb les tradicionals microbalances de quars. Cal destacar que degut a les seves reduïdes dimensions, no tan sols garanteixen una sensibilitat en massa molt bona sinó també una resolució espacial infinitament millor que en els dispositius de quars.

En relació a aquesta última aplicació, quatre experiments diferents s'han portat a terme amb els ressonadors NEMS/CMOS: (i) en col·laboració amb un grup d'investigació en química física s'ha estudiat mitjançant un ressonador nano/micromecànic aplicat com nano/microbalança l' evaporació de gotes de volums extremadament reduïts, de l'ordre del femtolitre ( $10^{-15}$ ), per aprofundir els coneixements necessaris per al desenvolupament de dispositius nano/microfluídics; (ii) una nova arquitectura de ressonador, basada en una palanca doble ('doble cantilever'), s'ha dissenyat i testejat. Aquest nou dispositiu permet fer mesures de massa en condicions ambientals amb una auto-referència proporcionant la incertesa de la mesura; (iii) s'han fet proves de deposició en ultra buit de capes ultra-fines d'or (d'espessor inferior al d'una mono-capa) sobre ressonadors. D'aquesta manera, s'ha demostrat la gran sensibilitat en massa distribuïda d'aquests dispositius NEMS/CMOS, en particular al comparar la seva resposta amb la d'una microbalança de quars a la que superen per entre dos i tres ordres de magnitud en termes de sensibilitat; (iv) basant-se en els resultats de l'experiment previ de deposició d'or, s'està dissenyant un sistema 'quasi-dinàmic' de litografia nanostencil junt amb l'EPFL. Aquest sistema consisteix en efectuar deposicions successives de diferents materials a través d'un nanostencil (plantilla) desplaçat entre cada deposició: d'aquesta manera s'obtenen nanoestructures multi-materials i ultra-pures. De manera innovadora, el sensor de massa NEMS/CMOS s'ha fet servir aquí com a sensor d'alineament entre la membrana nanostencil i el substrat per litografiar.

## A2. Resumen en castellano

La presente tesis ha sido realizada principalmente en el Centro Nacional de Microelectrónica – Instituto de Microelectrónica de Barcelona (CNM-IMB), que pertenece al Consejo Superior de Investigaciones Científicas (CSIC), y en parte también en el Instituto de Nanotecnología de Lyon (Francia) que pertenece al Centro Nacional de Investigaciones Científicas (CNRS, Francia). El doctor Francesc Pérez-Murano ha codirigido la tesis en el CNM, y el profesor Georges Brémond en el INL.

Este trabajo se enmarca en el proyecto europeo NaPa ('Emerging Nanopatterning Methods') cuyo objetivo es desarrollar técnicas emergentes, industrializables a medio plazo, de litografía a nivel nanométrico, y sus posibles aplicaciones. Así pues, los objetivos principales de la tesis han sido los desarrollos simultáneos (i) de sistemas nanoelectromecánicos (NEMS) integrados en CMOS, i (ii) de procesos de fabricación basados en una técnica avanzada de nanolitografía llamada 'nanostencil lithography' para poder fabricar tales sistemas monolíticos.

Esta tesis comporta dos aspectos principales: uno relacionado con el diseño y la operación de un nanodispositivo mecánico, el otro con las tecnologías de nanofabricación. En concreto, primero se ha modelado y diseñado un resonador nano/micromecánico de silicio, luego se han estudiado las ventajas y la viabilidad de una integración monolítica con circuitería CMOS. En efecto, los NEMS/CMOS son sistemas atractivos ya que combinan extraordinarias propiedades de sensado, proporcionadas por la parte móvil mecánica, con la posibilidad de detectar la señal de salida en condiciones mucho más favorables. Las capacidades parásitas son reducidas drásticamente al tratar dicha señal a través de una circuitería CMOS 'on-chip' que adicionalmente puede amplificarla y acondicionarla.

Posteriormente, estos dispositivos se han fabricado combinando una tecnología CMOS estándar con métodos emergentes de nanolitografía, en particular con la litografía 'nanostencil', que se ha tenido que optimizar en términos de resolución y aplicabilidad.

Ha sido posible luego demostrar el correcto funcionamiento del dispositivo NEMS/CMOS fabricado, caracterizando la respuesta frecuencial de la estructura nano/micromecánica cuya señal de salida está obtenida bajo la forma de una señal eléctrica alterna tratada por una circuitería CMOS específica de detección. Finalmente, se ha implementado dicho resonador NEMS/CMOS como sensor de masa ultra-sensible en cuatro experimentos distintos orientados hacia objetivos técnicos o científicos.

A continuación, se resume con más detalles el trabajo efectuado. Como primer paso, dos tipos de resonadores nano/micromecánicos ('cantilevers' y 'quad-beams') se han modelado analíticamente para poder estudiar su respuesta frecuencial mecánica. Con el objetivo de excitarlos y detectarlos eléctricamente, se ha optado por una técnica capacitiva. Por lo tanto se ha implementado un modelo mixto electromecánico para poder calcular su comportamiento eléctrico.

Para mejorar la respuesta eléctrica, se ha diseñado específicamente un circuito CMOS de lectura y de bajo consumo. Funciona como amplificador de transimpedancia para convertir la corriente creada por la resonancia mecánica en un voltaje suficientemente alto. A partir de simulaciones, se ha analizado exhaustivamente (i) el comportamiento intrínseco de este circuito y (ii) cuando está acoplado al resonador mecánico.

Sin embargo, la fabricación de tales nanodispositivos integrados en CMOS constituía un reto ya que la integración a nivel de oblea entera de NEMS sobre CMOS mediante procesos no excesivamente costosos no había sido demostrada aún al inicio de esta tesis. Debido a esto, se puso en marcha una colaboración con el EPFL (École Polytechnique Fédérale de Lausanne, Suiza) para desarrollar la litografía ‘nanostencil’ con el objetivo de integrar a escala de oblea estructuras mesoscópicas (micro y nano) sobre circuitos CMOS pre-fabricados. Después de identificar los principales problemas iniciales, se ha podido desarrollar con éxito una tecnología de post-proceso que permite integrar NEMS en CMOS mediante una única etapa de litografía nanostencil. En paralelo, otro post-proceso basado en una etapa de litografía por haz de electrones (‘e-beam lithography’) se ha puesto a punto de manera que se pueden fabricar nuevos prototipos de nanodispositivos sobre CMOS en cortos plazos de tiempo.

La caracterización eléctrica de estos NEMS/CMOS se ha llevado a cabo intensamente tanto en aire como en vacío. Han sido analizados los niveles de señal obtenidos experimentalmente, las características principales de los espectros de resonancia y el efecto de la tensión aplicada.

Finalmente, como ya ha sido mencionado, estos dispositivos NEMS/CMOS han sido implementados como sensores de masa. Actualmente, esta aplicación de los NEMS es una de las más exploradas ya que los resonadores nano/micromecánicos ofrecen grandes ventajas en términos de sensibilidad e integración de sistemas comparados con las tradicionales microbalanzas de cuarzo. Cabe destacar que debido a sus reducidas dimensiones, no tan solo garantizan una alta sensibilidad en masa sino también una resolución espacial infinitamente mayor que los dispositivos de cuarzo.

En relación a esta última aplicación, se han llevado a cabo cuatro experimentos diferentes con resonadores NEMS/CMOS: (i) en colaboración con un grupo de investigación en química física se ha estudiado mediante un resonador nano/micromecánico utilizado como nano/microbalanza la evaporación de gotas de volúmenes extremadamente reducidos, del orden del femtolitro ( $10^{-15}$ ), para profundizar en los conocimientos necesarios para el desarrollo de dispositivos de nano/microfluídica; (ii) una arquitectura nueva de resonador, basada en una palanca doble (‘doble cantilever’), se ha diseñado y testeado. Este dispositivo novedoso permite hacer medidas de masa en condiciones ambientales con una auto-referencia proporcionando la incertidumbre de la medida; (iii) se han hecho pruebas de deposición en alto vacío de capas ultra-finas de oro (de espesor equivalente inferior a una mono-capa) sobre resonadores. De esa manera, se ha demostrado la gran sensibilidad en masa distribuida de estos dispositivos, en particular al comparar su respuesta con la de una microbalanza de cuarzo a la que superan por entre dos y tres ordenes de magnitud a nivel de sensibilidad; (iv) basándose en los resultados del experimento previo de deposición de oro, se está diseñando, y sigue en curso, un sistema ‘quasi-dinámico’ de litografía nanostencil junto con el EPFL. Este sistema consiste en efectuar deposiciones sucesivas de distintos materiales a través de un nanostencil desplazado entre cada deposición: de esa manera se obtienen multi-depósitos estructurados y ultra-puros. De manera muy novedosa, el sensor de masa NEMS/CMOS se utiliza aquí como sensor de alineamiento entre la membrana nanostencil y el substrato a litografiar.

### A3. Résumé en français

Cette thèse a été réalisée principalement au Centre National de Microélectronique - Institut de Microélectronique de Barcelone (CNM-IMB), qui est un organisme du Conseil Supérieur (espagnol) de la Recherche Scientifique (CSIC), et en partie à l'Institut de Nanotechnologie de Lyon, sur le site de l'INSA Lyon, qui est lui un organisme du Centre National de la Recherche Scientifique (CNRS). Le docteur Francesc Pérez-Murano a co-dirigé la thèse au CNM, et le professeur Georges Brémond à l'INL.

Le travail a été mené dans le cadre du projet de recherche européen NaPa ('Emerging Nanopatterning Methods') dont le double objectif est de développer des techniques émergentes de nanolithographie industrialisables à moyen terme, et d'en promouvoir leurs applications potentielles. Les objectifs principaux de cette thèse ont donc été les développements simultanés (i) de systèmes nanoélectromécaniques (NEMS) intégrés sur CMOS, et (ii) de procédés de fabrication basés sur une technique avancée de nanolithographie, nommée 'nanostencil' ('nanopochoir'), pour pouvoir fabriquer de tels systèmes monolithiques.

Ce travail de thèse comporte ainsi deux aspects principaux: l'un porte sur la conception et l'actionnement d'un nanodispositif mécanique, et l'autre sur les technologies de nanofabrication. Concrètement, il a tout d'abord fallu modéliser et concevoir un résonateur nano/micromécanique de silicium, puis étudier les avantages et la faisabilité d'une intégration monolithique avec circuiterie CMOS. Les NEMS/CMOS sont en effet des systèmes très attractifs qui combinent des propriétés de transduction extraordinaires, grâce à la partie mécanique mobile, avec la possibilité de détecter le signal de sortie dans des conditions beaucoup plus favorables puisque les capacités parasites sont réduites drastiquement en traitant ce signal au travers d'une circuiterie CMOS 'on-chip' qui peut en complément l'amplifier et le conditionner.

Ces dispositifs ont ensuite été fabriqués en combinant une technologie CMOS standard avec des méthodes émergentes de nanolithographie, en particulier avec la lithographie nanostencil dont il a fallu optimiser les conditions d'application et la résolution.

Il a ensuite été possible de démontrer le bon fonctionnement des dispositifs NEMS/CMOS ainsi fabriqués en caractérisant la réponse fréquentielle des structures nano/micromécaniques, le signal de sortie étant obtenu sous la forme d'un signal électrique traité par une circuiterie CMOS spécifique pour la détection. Finalement, les résonateurs NEMS/CMOS ont été implémentés comme capteurs de masse ultra-sensibles dans quatre applications distinctes orientées vers des objectifs techniques ou scientifiques.

Dans les paragraphes suivants, le contenu du travail est explicité avec plus de détails. La première étape a donc été de modéliser analytiquement trois types de résonateurs nano/micromécaniques ('cantilevers', 'ponts' et 'quad-beams') afin de pouvoir étudier leur réponse fréquentielle mécanique. Avec l'objectif de les exciter et de les détecter électriquement, un mode de détection capacitif a été sélectionné. Par conséquent, un modèle mixte électromécanique a été appliqué de manière à pouvoir calculer la réponse électrique des dispositifs mécaniques vibrants.

Afin d'améliorer cette réponse électrique, un circuit CMOS de détection de faible consommation a été conçu spécialement. Son principe de fonctionnement est celui d'un

amplificateur de transimpédance qui convertit le courant créé par la résonance mécanique en une tension de sortie suffisamment élevée. À partir de simulations, les comportements (i) intrinsèque du circuit et (ii) lorsqu'il est couplé au résonateur mécanique ont été analysés exhaustivement.

Cependant, la fabrication de tels dispositifs intégrés sur CMOS constituait au départ un défi si l'on considère que l'intégration à échelle de 'wafer' de NEMS sur CMOS selon des procédés à relativement bas coût, incluant des étapes de nanolithographie, n'avait pas encore été démontrée lorsque cette thèse a débuté. En partant de ce constat, une collaboration avec l'EPFL (École Polytechnique Fédérale de Lausanne, Suisse) a été mise en place afin de développer la lithographie 'nanostencil' avec pour objectif d'intégrer à échelle de 'wafer' entier des structures mésoscopiques (micro et nano) sur substrat CMOS pré-fabriqués. Après en avoir identifié les principaux challenges, une technologie de post-procédé permettant d'intégrer des NEMS sur CMOS au moyen d'une unique étape de lithographie nanostencil a été développée avec succès. En parallèle, un autre post-procédé, basé lui sur une étape de lithographie par jet d'électrons ('e-beam lithography'), a été mis au point de manière à pouvoir fabriquer en un temps court de nouveaux prototypes de nanodispositifs sur CMOS.

Ces NEMS/CMOS ont ensuite été caractérisés électriquement de manière exhaustive dans l'air et sous vide poussé. Les caractéristiques principales des spectres de résonance, les niveaux de signal obtenus expérimentalement ainsi que l'effet de la tension d'excitation sur la forme du spectre ont été analysés.

Finalement, ces dispositifs NEMS/CMOS ont été implémentés comme capteurs de masse. De nos jours, cette application des NEMS est l'une des plus explorées car les résonateurs nano/micromécaniques offrent d'énormes avantages comparés aux traditionnelles microbalances à quartz en termes de sensibilité et de possibilités d'intégration de système. Leur taille extrêmement réduite leur garantit non seulement une très haute sensibilité en masse mais aussi une résolution spatiale infiniment meilleure que les macro-dispositifs à quartz.

Dans ce contexte, quatre expériences différentes ont été menées à bien avec des résonateurs NEMS/CMOS: (i) en collaboration avec un groupe de recherche en chimie physique, l'évaporation de gouttes de volumes extrêmement réduits, de l'ordre du femtolitre ( $10^{-15}$  L), a été étudiée en utilisant les résonateurs comme des nano/microbalances avec l'objectif d'approfondir les connaissances des mécanismes de mouillage à ces échelles. Cet apport devrait aider à la conception de dispositifs nano/micro-fluidiques; (ii) une nouvelle architecture de résonateur basée sur une double nano/micropoutre a été conçue et testée. Ce nouveau dispositif permet de réaliser des mesures de masse fiables sous conditions ambiantes dont l'auto-référence fournit une estimation de l'incertitude de la mesure; (iii) des expériences de dépôt sous vide poussé de couches ultra-fines (d'épaisseurs équivalentes inférieures à une monocouche) d'or sur des résonateurs ont été entreprises. De cette manière, la grande sensibilité en masse distribuée de ces dispositifs a été clairement démontrée, en particulier en comparant leur réponse avec celle d'une microbalance de quartz. Il s'avère que la sensibilité des NEMS/CMOS est meilleure par entre deux et trois ordres de grandeur; (iv) en se basant sur les résultats de l'expérience précédente de dépôt d'or, un système 'quasi-dynamique' de lithographie 'stencil' a commencé à être conçu en partenariat avec l'EPFL. À terme, ce système doit pouvoir effectuer des dépôts successifs de divers matériaux à travers un nanostencil déplacé entre chaque dépôt: de cette manière des nanostructures multi-matériaux et ultra-pures seront fabricables. Selon un concept novateur, le capteur de masse NEMS/CMOS est utilisé ici comme capteur d'alignement entre la membrane nanostencil et le substrat à lithographier.

## A4. Zusammenfassung auf Deutsch

Diese Doktorarbeit wurde hauptsächlich am CNM-IMB-CSIC (Centro Nacional de Microelectronica - Instituto de Microelectronica Barcelona) und am INL (Institut für Nanotechnologie von Lyon der französische Vorstand von wissenschaftliche Forschung) realisiert. Die Arbeit wurde im Rahmen des europäischen Forschungsprojekts NaPa (Emerging Nanopatterning Methods) durchgeführt. Dieses Projekt verfolgt die Zwecke, aufstrebende Nanolithografie Techniken zu entwickeln und Anwendungen dieser Techniken zu fördern.

Die zwei grundsätzlichen Ziele dieser Doktorarbeit waren es, nano-elektro-mechanische Systeme (NEMS) in CMOS zu integrieren(i), und ihre Fabrikationsprozesse, die auf der "Nanostencil"-Technologie basieren, zu entwickeln (ii).

Zuerst wurden drei Typen von nano-/mikromechanischen Resonatoren (cantilevers', bridges' und quad-beams') aus Silizium mechanisch modelliert und entworfen, dann wurden die Vorteile und die Machbarkeit einer monolithischen Integration mit CMOS Schaltkreisen studiert. NEMS/CMOS sind Systeme, die aussergewöhnliche Transduktionseigenschaften haben dank dem mechanisch beweglichen Teil. Das Ausgangssignal kann unter viel günstigeren Bedingungen detektiert werden, da die parasitären Kapazitäten auf Grund der CMOS Integration stark reduziert sind. Außerdem erlaubt diese Integration das Signal 'on-chip' zu verstärken und zu verpacken. Deshalb wurde ein Low-Power CMOS-Schaltkreis für die kapazitive Detektion des Resonanz-Signals entwickelt um die elektrischen Eigenschaften weiter zu verbessern. Dieser funktioniert wie ein Transimpedanz-Verstärker, der den bei mechanischer Resonanz entstehenden geringeren Strom in eine messbare Ausgangsspannung umwandelt. Das Verhalten des Schaltkreises unter idealen Bedingungen sowie sein Verhalten mit gekoppeltem Resonator wurden simuliert und analysiert. Dafür wurde ein elektro-mechanisches Modell verwendet, um den elektrischen Verlauf der mechanischen Bauelemente zu berechnen.

Um diese Bauelemente herzustellen, wurden zwei Verfahren kombiniert: eine Standard CMOS Technologie und die Nanostencil-Lithografie, bei der die Auflösung und die Betriebsart optimiert wurden. Damit wurde die Möglichkeit der 'full-wafer'-Integration von NEMS in CMOS nachgewiesen.

Danach, wurde das Frequenzverhalten der hergestellten NEMS/CMOS in Luft und Vakuum analysiert. Qualitäts-Faktoren bis zu 9000 wurden erreicht. Der Schaltkreis der im Rahmen dieser Doktorarbeit entwickelt wurde, erfüllte alle geforderten Spezifikationen.

Zum Schluss wurden die NEMS/CMOS Resonatoren als ultra-empfindliche Masse-Sensoren in vier verschiedenen technischen und wissenschaftlichen Anwendungen implementiert. Im Besonderen haben wir die Verdunstung von Femtoliter-Tropfen studiert. Das NEMS wurde verwendet um die Masseveränderung pro Zeit zu bestimmen. Die Ablagerung von ultra-dünnen Gold-Schichten in Vakuum wurde mit den NEMS/CMOS charakterisiert. Dies sind Anwendungsbeispiele, die die Möglichkeiten dieser viel versprechenden Bauelementen aufzeigen.

## A5. Glossary

MEMS: MicroElectroMechanical Systems

NEMS: NanoElectroMechanical Systems

CMOS: complementary metal oxide semiconductor

IC: integrated circuit

RF: radio frequency

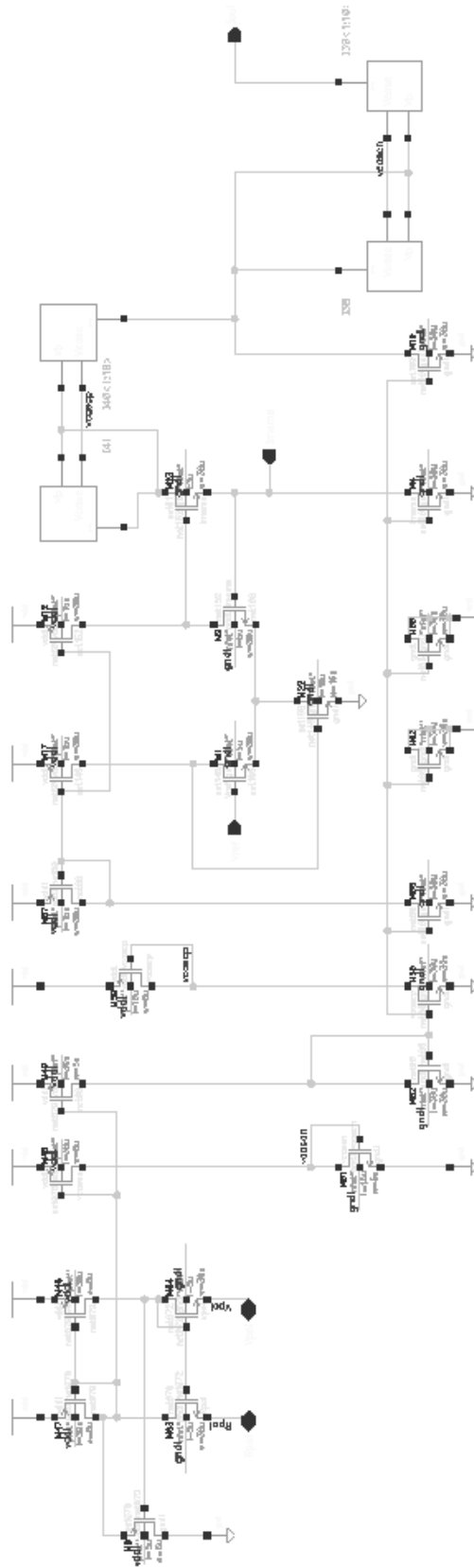
nSL: nanostencil lithography

eBL: electron-beam lithography

NIL: Nanoimprint lithography

DUV: deep ultra-violet

## A6. Complete diagram of the CCII CMOS circuit



## A7. Technological processes

### A7.1. CNM CMOS process

In the present work, eight photolithography levels (set of reticules *CNM 264*) are required for the entire definition of the IC before its post-processing for nanomechanical structures integration. All lithographic steps are carried out with positive photoresists patterned with a NIKON stepper designed for standard UV (ultra-violet) lithography. All alignment marks are inserted inside the dicing tracks located in between chips.

#### **N- AND P-TYPE WELLS DEFINITION (see Figure 1):**

The first stage is the definition of n- and p-type wells at the surface of a p-type epitaxial Si wafer. It starts with the growth of a thin thermal 40 nm thick silicon oxide ( $\text{SiO}_2$ ) on top of an ultra-clean Si surface. Then, a 120 nm thick silicon nitride ( $\text{Si}_3\text{N}_4$ ) layer is deposited by Low Pressure Chemical Vapor Deposition (LPCVD) at high temperature. This  $\text{Si}_3\text{N}_4$  layer is patterned by dry etching in a QUAD DRY TEK system using a photosensitive resist as a mask after its photolithography with dark field reticule n°1 (NTUB).

The  $\text{Si}_3\text{N}_4$  layer acts as an implantation barrier so that n-wells can be defined by implantation of phosphorous only through its patterned apertures. After removing the resist, a thermal process leads to a growth of 400 nm of  $\text{SiO}_2$  onto the n-wells and of a mixed nitride/oxide layer on the rest. This layer is then selectively wet etched, and the wafer surface remains covered by an oxide layer only above n-wells acting as an implantation barrier. Thus the p-wells are defined by boron implantation and the thermal oxide of the n-wells is then removed by wet etching. As a remark, this operation generates a topographical step (about 200 nm high) between p- and n-wells (located below), that creates a sufficient visual contrast allowing the posterior alignment of the second lithography reticule with the patterns of the first one.

It can be noticed also that doping implantations into silicon are generally made with a screening 20 nm thick  $\text{SiO}_2$  layer. This implies two advantages: it avoids ion channeling into silicon bulk (what would provoke a decrease in the superficial dose) and it eliminates any risk of surface contamination possibly due to the deposition of particles arising from chamber walls after their ion bombardment due an eventual beam deflection.

Doping species are then activated by a thermal annealing (at very high temperature) under dry atmosphere. The resulting silicon oxide is immediately wet etched.

#### **FIELD OXIDE GROWTH AND ACTIVE AREAS DEFINITION (see Figure 1):**

Now both types of wells are defined, active areas (where transistors have to be integrated) must be opened into a grown field  $\text{SiO}_2$  that ensures lateral electrical isolation between transistors. So, a 20 nm thick silicon oxide is grown and a 120 nm thick silicon nitride ( $\text{Si}_3\text{N}_4$ ) layer is deposited on top by LPCVD at high temperature. The second photolithography is performed with

the so-called GASAD bright field reticule (n°2) so that it remains resist patterns only where active areas will be located.

Their definition is based on LOCOS (Localized oxidation of silicon) process. First, a nitride dry etching leaves patterns only where resist is masking, that is to say only above active areas. This nitride layer will locally act as an implantation and thermal barrier. After photoresist removal, some boron is implanted and a 1  $\mu\text{m}$  thick field silicon oxide is subsequently thermally grown except where nitride patterns remain. The boron doping is used since it increases  $\text{SiO}_2$  growth rate. The remaining oxide-nitride layer above active areas and its underneath nitride layer are wet etched. At this stage, active areas are now defined and ready for transistors integration.

A sacrificial 100 nm thick  $\text{SiO}_2$  layer is thermally grown and a maskless boron implantation all over the wafer is performed to adjust the doping level of the future channel of the transistors: this operation adjusts precisely the threshold voltage.

#### **POLY0STRUCTURING, GATE OXIDE GROWTH (see Figure 1):**

The *poly0* (polysilicon) layer is normally implemented as a highly doped layer to be structured as capacitor electrode for the monolithic integration of capacitors into CMOS circuits. In our case, the IC schematic does not include any capacitor but *poly0* has a fundamental importance in the process as it is implemented as structural material of the micro/nanomechanical resonators. The mechanical Q-factor of a resonating device is directly related to the internal losses and a polycrystalline structure intrinsically provides a lower Q-factor than monocristalline Si. With the aim of improving the grain structure and decreasing the surface roughness, the deposition parameters were modified with respect to a normal utilization as capacitor electrode. The thickness is adjusted to 600 nm.

So, *poly0* is deposited by LPCVD with a  $\text{SiH}_4$  (silane) basis. Then, it was doped with  $\text{POCl}_3$  by diffusion of phosphorous (n-type) at high temperature. An unwanted PSG (phosphor-silicon-glass) grows meanwhile but is removed by wet etching just after. Then, a photoresist is patterned by performing a third lithography with so-called *poly0* bright field reticule (n°3). It is hardened by a special bake so that it endures better the subsequent dry etching (APPLIED MATERIALS 5000) of polysilicon, based on chlorine chemistry. Resist is stripped and the remaining sacrificial oxide that also acted as diffusion barrier during boron doping, for threshold voltage adjustment, is removed by wet etching.

Then the gate oxide is thermally grown. Different doping levels induce different growth rates and consequently this gate oxide is 38 nm thick above active areas and 70nm thick above *poly0*. Figure 1 depicts a cross-section of the wafer at this point of the fabrication.

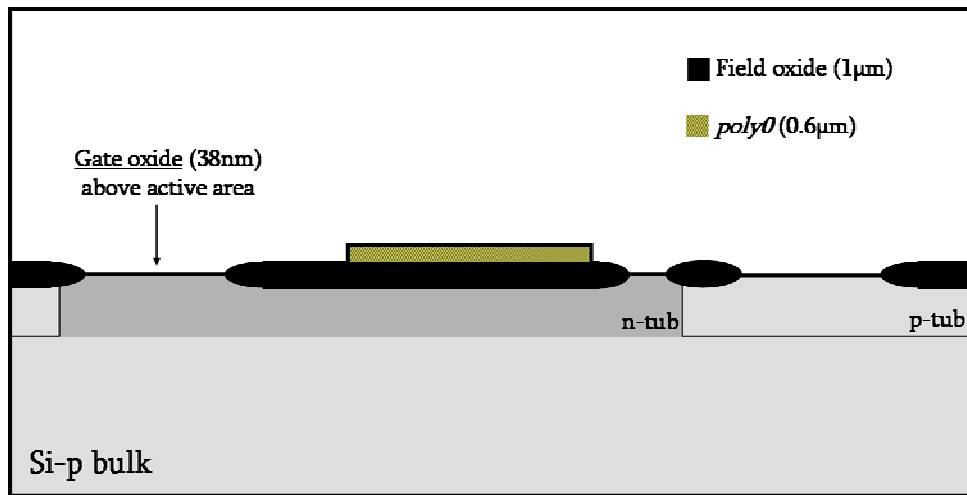


Figure 1. Part I of CMOS fabrication. Wells implantations and field oxide definition. *poly0* deposition and patterning. Gate oxide growth. NB: the topographic step between n- and p-tubs is not depicted

#### *POLY1* STRUCTURING (see Figure 2):

Immediately after gate oxide formation, a second 480 nm thick polysilicon layer, so-called *poly1*, is deposited by LPCVD. In addition to its normal implementation as transistor gate material, it coats *poly0* within the integration areas in order to protect it during the rest of the process flow. Then a doping process based on diffusion of  $\text{POCl}_3$  follows, similar to that of *poly0*.

Subsequent steps (PSG removal, photolithography with bright field *poly1* reticule [n<sup>4</sup>], resist hardening, dry etching and resist removal) are identical to that of *poly0*.

#### SOURCE AND DRAIN STRUCTURING (see Figure 2):

At this stage, the transistors are almost structured: within active areas, the doping of the future channel was adjusted, a thin oxide (gate oxide) was grown and on top of it the gate was patterned. The remaining step is the functionalization of source and drain.

A photolithography with *n-plus* dark field reticule (n<sup>5</sup>) is performed: photoresist is opened only above n-type transistors and a special bake is made in order to harden it. The subsequent implantation of P (with a dose of  $4.2 \cdot 10^{15}$  at.cm<sup>-2</sup>) must define highly doped n<sup>++</sup> wells so that source and drain are formed. Subsequent resist stripping requires two successive steps because of its hardness: oxygen plasma etching and wet etching.

For the definition of source and drain of p-type transistors, no photolithography is needed. This operation is realized through a maskless p-type implantation of boron (with a dose of  $1 \cdot 10^{15}$  at.cm<sup>-2</sup>) that does not degrade the unmasked n-type transistors. Indeed, the level of the previous n<sup>++</sup> doping is voluntarily exceeded so that this boron implantation subsequent decreases its level to reach the target value.

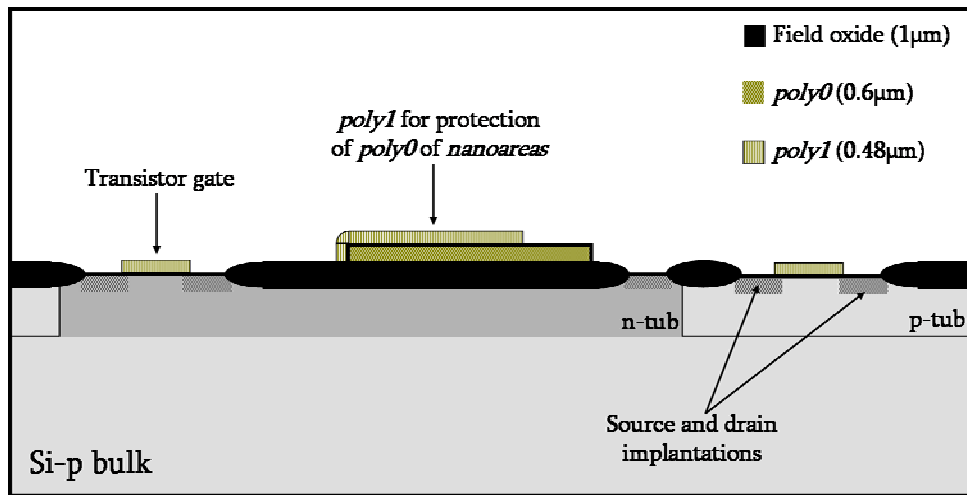


Figure 2. Part II of CMOS fabrication.  
Transistor definition with gate structuring (*poly1*); source and drain doping

#### INTERLEVEL OXIDE STRUCTURING (see Figure 3):

CNM CMOS technology involves one single metal level and at this stage back-end operations start. The so-called *interlevel oxide* must be structured to isolate future metal interconnections from underlying layers. It is deposited by LPCVD in an AMI-DEP (APPLIED MATERIALS) with a BPTEOS (Boron-Phosphorous-Tetra-Ethyl-Ortho-Silicate) basis for a 1.3 µm target thickness. TEOS is a classical gas for the deposition of SiO<sub>2</sub> according to the chemical reaction:



where  $x$ ,  $y$ ,  $z$ ,  $a$  and  $b$  are stoichiometric coefficients

Addition of boron and phosphorus in gaseous phase (B<sub>2</sub>O<sub>3</sub> and P<sub>2</sub>O<sub>5</sub>) significantly improves the conformation of the deposited layer (BPSG): subsequent annealing for fluidification purposes can be made at a much lower temperature than with a standard only TEOS based oxide layer.

A photolithography with the dark field *Windows* reticule (n°6) is performed. Then with this resist masking, a dry etching is made in a DRY TEK QUAD in order to open windows accessing the underlying layers. In this way, transistors are interconnected afterwards with the metal layer. In addition, this oxide anisotropic etching must remove the gate oxide in the access windows for accessing source and drain. After this, resist is stripped and a special cleaning is made to prepare the surface to posterior metallization.

As mentioned in chapter 3, a change in the *window* reticule layout led to a drastic improvement of fabrication throughput with respect to anterior runs performed at CNM during previous research projects. In this CMOS layout, no aperture is drawn on top of the integration areas so that they remain protected by this *interlevel oxide* during posterior metal etching. Indeed,

this etch is known to be non uniform and from one point of the wafer to another removal of metal is not realized at the same speed: while in some integration areas some metal still needs to be etched, in others the process has already started to overetch and to damage the underlying non-dielectric layers, as for example the protective *poly1*.

Now, within all integration areas, apertures into *interlevel oxide* are made immediately after aperture into *passivation* layer (c.f. next paragraphs) with the same masking corresponding to the final reticule (*passivation*, n°8).

#### **METAL LAYER STRUCTURING**

The metal used in back-end for interconnections is an alloy Al / 0.5% Cu. The incorporation of Cu into Al prevents from electromigration of Al atoms during device polarization. Usually, Si-based alloys of Al are employed to prevent from the formation of spikes at aluminum/silicon interface in the contact region. Here, the doping depth in the contact region is high enough to avoid this phenomenon so that no such alloy has to be employed. A 1 µm thick layer is deposited by sputtering in a VARIAN 3180 system.

A photolithography (with bright field *Metal1* reticule, n°7) is performed with anti-reflexive photoresist. The metal layer is structured by dry etching in a DRY-TEK QUAD and the resist is removed in water. This etch is not uniform but is very selective with respect to dielectric layers, consequently as no silicon-based layer is still accessible, an eventual overetch has no consequence. This Al layer is annealed at 350°C under forming gas for improving the quality of its interface with Si in source and drain.

#### **PASSIVATION LAYER STRUCTURING (see Figure 3):**

Let us turn to the final steps of CMOS circuit fabrication. The surface needs to be protected for packaging purposes, and has to be coated by a passivation layer that will be opened only above Al contact pads and above integration areas.

This passivation is a bi-layer of Si<sub>3</sub>N<sub>4</sub> (400 nm thick) on top of SiO<sub>2</sub> (400 nm thick) deposited on both wafers sides by PECVD (Plasma Enhanced Chemical Vapor Deposition). This technique provides quite high deposition rates and well conformal layers but it is mainly interesting because it allows depositing at low temperature (below Al fusion point). With respect to previous CMOS runs, the thickness of Si<sub>3</sub>N<sub>4</sub> was reduced thereby a too high curvature of the wafers due to silicon nitride internal stress could be avoided.

The front side of the wafer is coated with a resist and the back side is dry etched (ALCATEL GIR 160) in order to remove this bi-layer. After dielectrics removal on backside, the front side resist is stripped.

The last photolithography (CAPS dark field reticule, n°8) is performed using a non-standard resist thickness of 2 µm. This resist is hardened with a special bake so that this thermal treatment together with a bigger thickness makes it more resistant to a longer dry etching.

First, a dry etching of  $\text{Si}_3\text{N}_4$  in DRY-TEK QUAD removes entirely the 400 nm thick layer inside the resist apertures. Once this is completed, a dry etching of oxide in DRY-TEK QUAD starts. After a penetration of 400 nm into the oxide layer, the PECVD deposited oxide is entirely removed and consequently the Al contact pads are accessed. Without being stopped, the dry etch carries on in order to remove the *interlevel oxide* on top of the integration areas while the Al contact pads are not damaged thanks to etching selectivity. A special recipe is used to obtain vertical sidewalls for a total etching depth of 1.7  $\mu\text{m}$  (400 nm PECVD + 1200 nm BPSG + 130 nm thermal oxide). For easier end point detection, we included several extended test zones ( $400 \times 400 \mu\text{m}^2$ ) in the chip layout with such a profile: bulk silicon + gate oxide (30 nm) + *interlevel oxide* + *passivation* layers. Their big size allows monitoring the remaining  $\text{SiO}_2$  thickness with an ellipsometric technique of large laser spot.

At this point, CMOS fabrication is completed and the wafers are now ready for post-processing with the purpose of integrating nanomechanical devices inside the integration areas:

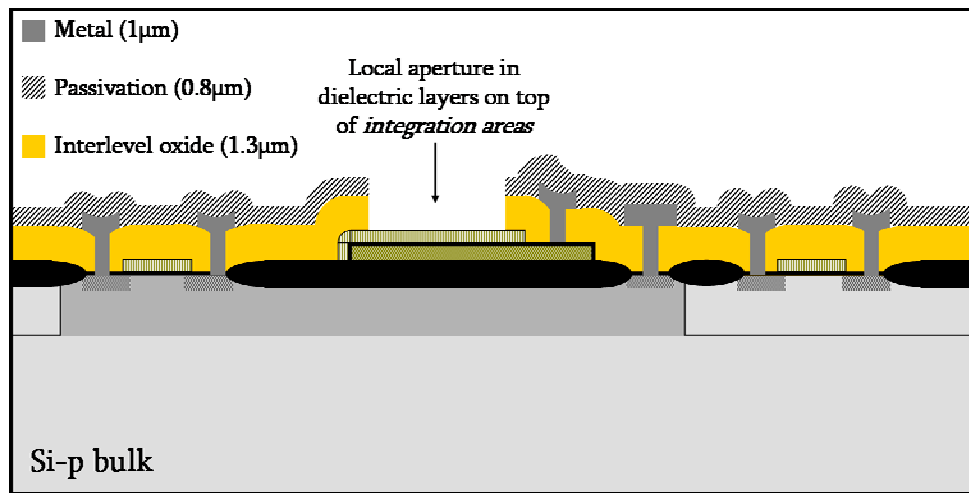
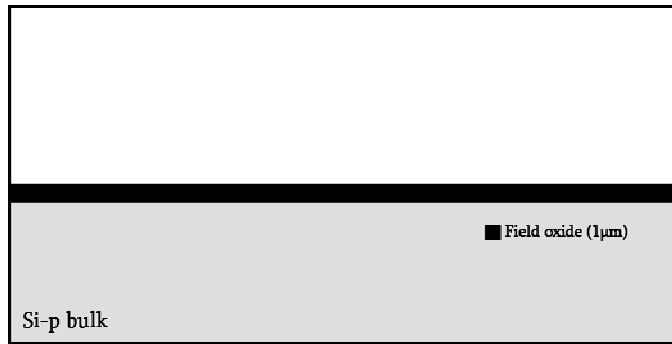


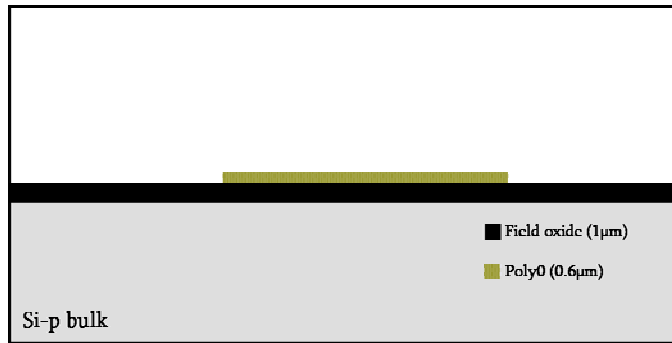
Figure 3. Final aspect at the end of the CMOS fabrication. Wafer ready for post-processing after realizing apertures in dielectric layers above the integration areas to enable posterior integration of nanodevices

## A7.2. Dummy wafers process

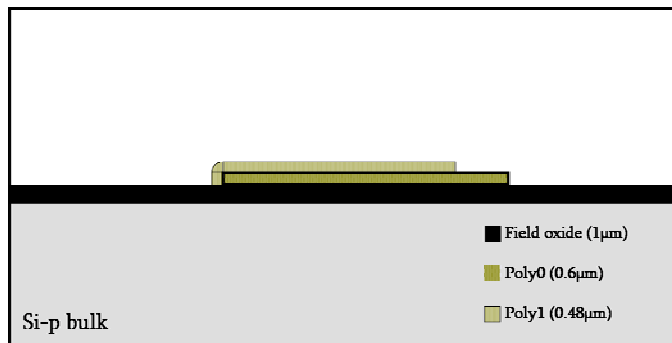
STRUCTURE AND FABRICATION PROCESS OF DUMMIES 1: Since dummy wafers have no electrical function, they consequently have a more simple fabrication process in which all implantations and connections through *interlevel oxide* were skipped. Eight wafers were fabricated.



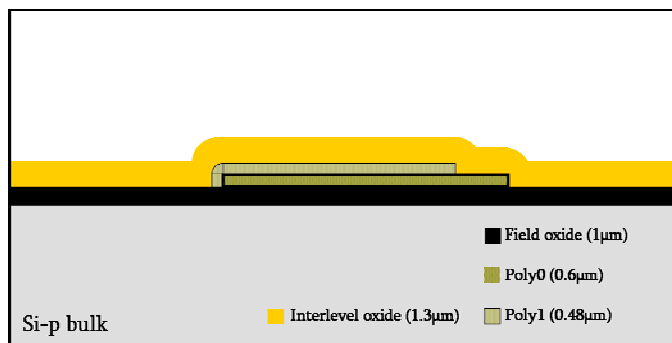
1. Growth of a 800 nm thick field SiO<sub>2</sub> layer



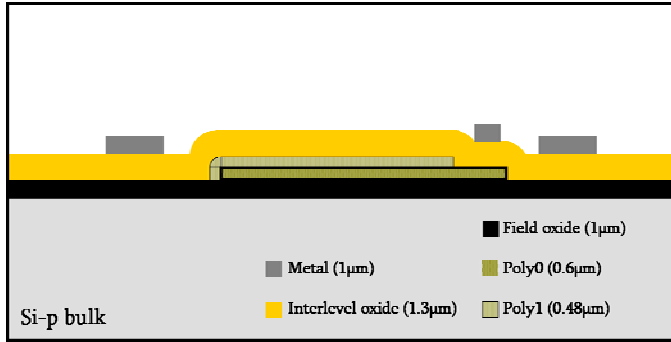
2. Deposition of a 600 nm thick *poly0* layer, POCl<sub>3</sub> doping and PSG (Phospho-silicon glass forming during doping) removal. Then, a standard UV lithography with *poly0* CMOS reticule is performed. With this resist mask, *poly0* is selectively dry etched respect to SiO<sub>2</sub>.



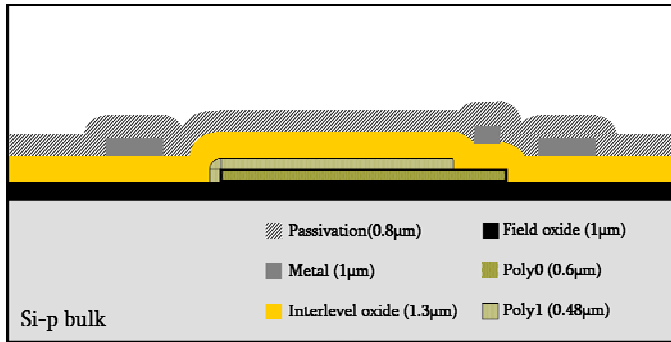
3. Pseudo "gate oxidation", deposition of a 480 nm thick *poly1* layer, POCl<sub>3</sub> doping and PSG removal. Then, a standard UV lithography with *poly1* CMOS reticule is performed. With this resist mask, *poly1* is selectively dry etched respect to SiO<sub>2</sub>.



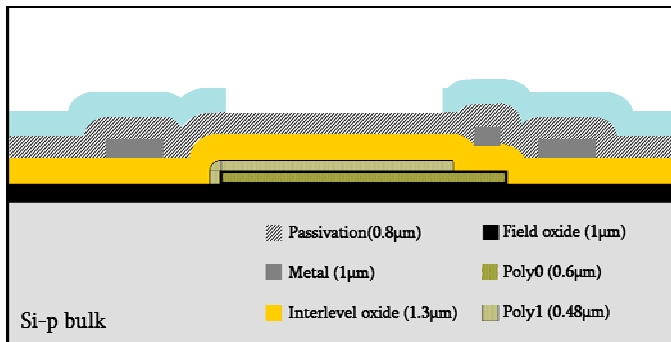
4. Deposition of a 1.1 µm thick BPSG (boro-phospho-silicon-glass, so-called *interlevel oxide*) and subsequent heat treatment for conformation to underlying topography. This layer is not patterned.



5. Metal deposition (Al, 1 µm thick) and subsequent standard UV photolithography and dry etching. As the *interlevel oxide* was not structured, the Al layer is not interconnected to underlying layers but this is not the purpose of dummies 1.

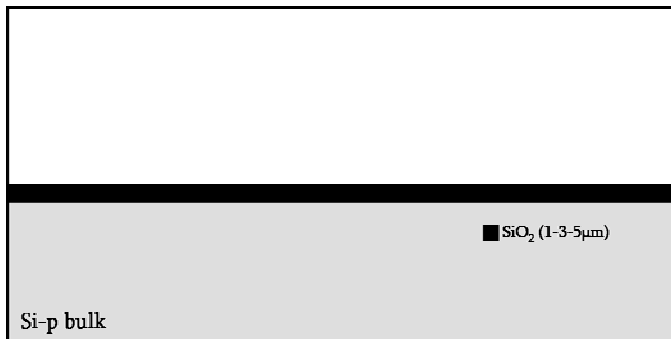


6. Deposition of a 0.8 µm thick passivation layer by PECVD (plasma enhanced chemical vapor deposition) technique.

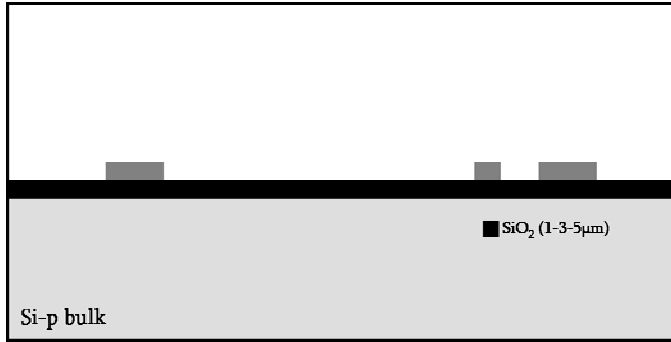


7. Standard UV lithography with CMOS *passivation layer* reticule. Given that the following step, and the first issue to be tested, is the dry etching in one single step of both *interlevel oxide* and *passivation* layers, the resist thickness is doubled.

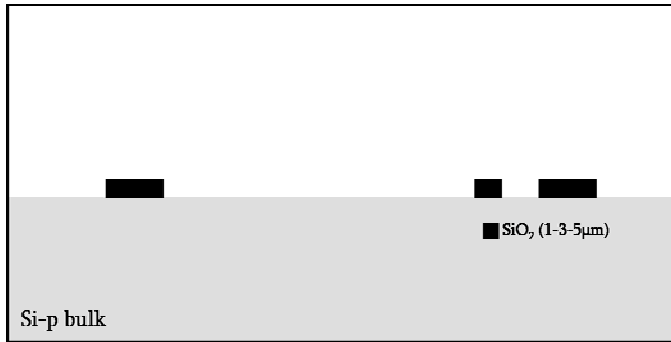
STRUCTURE AND FABRICATION PROCESS OF DUMMIES 2:



1. Deposition of a SiO<sub>2</sub> layer of variable thickness (1-3-5µm)



2. Deposition of a metal layer (Al, 500 nm thick) and photolithography with *metal* CMOS reticule. Al dry etching and resist removal.



3.  $\text{SiO}_2$  dry etching with Al as etch mask, then Al removal.

### A7.3. Post-processing based on eBL

#### PMMA DEPOSITION, E-BEAM EXPOSURE OF PMMA AND PMMA DEVELOPMENT

Same procedure as for discrete devices made by eBL (c.f. chapter 2), except the exposure made at 3 kV (dose  $\sim 30 \mu\text{C}/\text{cm}^2$ ). This lower voltage should not result in a degradation of the performance of the CMOS circuits

#### METALLIZATION

idem as for discrete devices made by eBL (c.f. chapter 2), but with a 32 nm thick Al layer

#### LIFT-OFF

like for discrete devices made by eBL (c.f. chapter 2), but without ultra-sounds to avoid that the metal strips in high-topography zones

#### PATTERN TRANSFER BY RIE

- RIE of the thin SiO<sub>2</sub> layer (70 nm thick) with Al mask structured by EBL and lift-off:

System: GIR 160 Alcatel (recipe PGIOXGUI)

t: 1 min 30 s

CHF<sub>3</sub>: 50 sccm

Pressure:  $5 \cdot 10^{-2}$  mbar

Power: 500 W

Nominal etching speed: 100 nm/min at RT

- RIE of the structural polySi layer ( $\sim 600$  nm thick) with the same Al mask

Same procedure as for discrete devices (c.f. chapter 2)

System: Alcatel A601-E (recipe *NanoI*)

t: 14 s + 14 s + 7 s (3 discontinued steps, one entire gas cycle corresponds to 3.5 s)

C<sub>4</sub>F<sub>8</sub>: 100 sccm (1 s)

SF<sub>6</sub>: 150 sccm (2.5 s)

Pressure:  $1.4 - 2.8 \cdot 10^{-2}$  mbar

ICP Power: 1500 W

Plate power: 15 W

Nominal etching speed: 1300 nm/min at 20°C

#### RESONATORS RELEASE

The same process is used as for devices defined by nSL (see chapter 4)

## A7.4. Experimental results of pattern transfer of nanostencil lithography

### ANNEX ON BLURRING DATA

Dummy wafer 1-2

Chip	$\Delta W$ (nm) for cantilevers	$\Delta W$ (nm) for paddles
2	100	225
8	100	245
12	110	230
16	110	245

CMOS wafer n°11

Chip	$\Delta W$ (nm) for cantilevers	$\Delta W$ (nm) for paddles
2	140	190
23	250	250

$\Delta W$  is the blurring extension and is given by eq.(IV.1). Experimental measurements based on SEM images are reported in those tables for dummies and true CMOS wafers. Unstabilized full-wafer stencils were used, this is why  $\Delta W$  is bigger for paddles since its design makes the membrane more sensible to stress during material loading.

### ANNEX ON PATTERN TRANSFER DATA

In this section, pattern transfer data based on SEM images measurements are reported. Clogging effect (reduction of stencil aperture size after deposition), membrane stress with Al loading (high  $\Delta W$  in the case of paddles), displacement effect (chips located in the border e.g. n°2, 8 or 12 exhibit a smaller pattern than the stencil aperture size) are well visible. When membrane is stable (in the present case membranes for cantilevers, in the future every corrugated membrane), an average deviation less than 10% is achieved.

#### Data measured on dummy wafers 1 and 2

(1) Data measured on cantilever patterns

Chip	Aperture size in stencil (nm)	Aperture size in stencil (nm) after evaporation	Deposited main pattern dimension (nm)	$\Delta$ stencil-deposited pattern (nm)		Deviation (%)	
				Left: initial; Right: final	Left: initial stencil size; Right: final stencil size		
2	304	223	248	-56	+25	-18%	+11%
	335	341	335	0	-6	Idem	-2%
8	434	403	409	-25	+6	-6%	-1%
	546	564	509	-37	-55	-7%	-10%
12	391	335	385	-6	+50	-1.5%	+15%
	478	490	465	-13	-25	-3%	-5%
16	471	422	490	19	+68	+4%	+16%
	571	546	602	31	+56	+5%	+10%

## (2) Data measured on paddle patterns

Chip	Aperture size in stencil (nm)	Aperture size in stencil (nm) after evaporation	Deposited main pattern dimension (nm)	$\Delta$ stencil-deposited pattern (nm)		Deviation (%)	
				<i>Left: initial; Right: final</i>		<i>Left: initial stencil size</i>	<i>Right: final stencil size</i>
2	459	682	471	+12	-211	+2.6%	-31%
8	515	757	633	118	-124	+23%	-16%
12	521	782	639	118	-143	+23%	-18%
16	552	602	633	81	+31	+18%	+5%

## Data measured on CMOS wafer n°11

## (1) Data measured on cantilever patterns

Chip	Aperture size in stencil (nm)	Aperture size in stencil (nm) after evaporation	Deposited main pattern dimension (nm)	$\Delta$ stencil-deposited pattern (nm)		Deviation (%)	
				<i>Left: initial; Right: final</i>		<i>Left: initial stencil size</i>	<i>Right: final stencil size</i>
2	310	223	236	-74	+13	-24%	+6%
	397	304	329	-68	+25	-17%	+8%
23	275	285	291	+16	+6	+6%	+2%
	409	366	378	-31	+12	+5%	-8%

## (2) Data measured on paddle patterns

Chip	Aperture size in stencil (nm)	Aperture size in stencil (nm) after evaporation	Deposited main pattern dimension (nm)	$\Delta$ stencil-deposited pattern (nm)		Deviation (%)	
				<i>Left: initial; Right: final</i>		<i>Left: initial stencil size</i>	<i>Right: final stencil size</i>
2	370	403	397	+27	-6	+7%	-1%
23	333	385	378	+45	-7	+13%	-2%



## A9. AFM characterization of resonators: preliminary work

The atomic force microscope (AFM) potentially constitutes an alternative tool to measure the mechanical response of a nanomechanical resonator [1, 2], in particular the detect its oscillations [1, 3, 4]. In the framework of this thesis, some preliminary work has been undertaken at INL (at INSA Lyon) to explore this method. Several possible applications have been identified:

- (1) applying a force with a relatively stiff tip and measuring its deflection should help in determining the spring constant of the resonant device
- (2) exciting electrostatically with a DC voltage and measuring the deflection of an appropriate low-stiffness AFM cantilever applied on the resonator should allow determining the static bending of the mechanical structure and thereby obtaining information on its electromechanical behavior
- (3) exciting electrostatically with an AC voltage, the frequency spectrum of the resonator could be measured and the vibration mode shapes could be ‘imaged’. For this purpose, a new technique needs to be developed. As a basis, we have inspired from the lock-in detection technique of A. San Paulo et al. [3, 4]
- (4) another interesting experiment would consist in approaching an AFM tip from a vibrating nanomechanical resonator and analyzing the perturbation of its frequency response generated by the interaction between both elements. For this purpose, the frequency response of a CMOS integrated nanomechanical resonator, like the ones presented in this thesis, could be electrically measured to observe any effect on the response when approaching the tip. This experiment can lead to a force calibration of the nanomechanical sensor.

Experiments of static bending of quad-beams have been performed. An excitation voltage was applied on the substrate to drive the resonator but the high voltage that was required likely perturbed the AFM cantilever. Either in contact or in tapping mode, the signal of the piezo-tube was measured while the excitation voltage was progressively increased: very large deflections of the central plate seemed to be produced but paradoxically the central plate apparently tended to get farther from the substrate (see Figure 6) what is not coherent since the plate should be electrostatically attracted. This apparent upwards bending is maybe caused by a bending downwards of the AFM cantilever due to the electrostatic attraction of the substrate: consequently the piezo-tube probably tries to compensate by retracting.

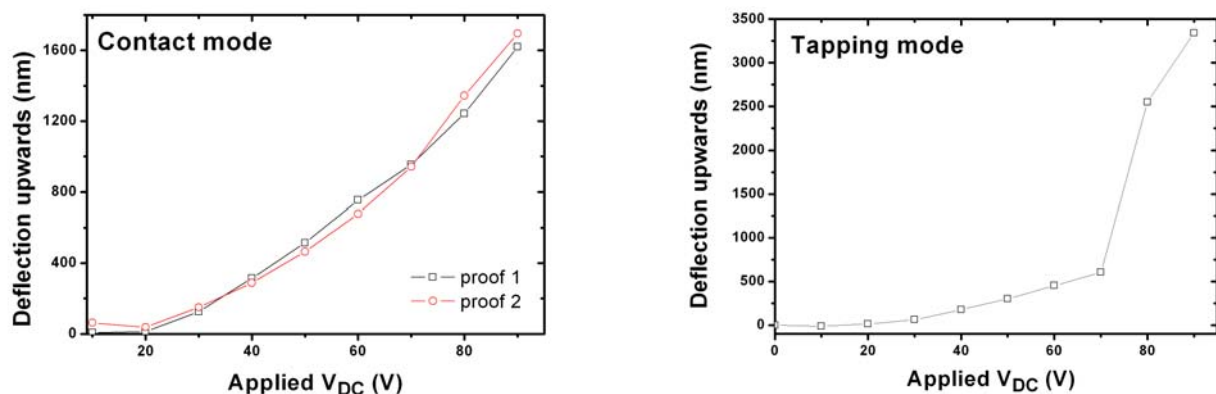


Figure 6. Measurements of the static deflection of the QB central plate by operating the AFM either in contact (left) or in tapping (right) modes [measurement of the signal of the AFM piezo-tube]

This issue should be circumvented working with undoped non-conductive AFM probes.

Dynamic electromechanical characterization has been carried out measuring the signal of the position sensitive photodiode of the AFM set-up but this signal was very noisy and difficult to stabilize. Furthermore, a very pronounced parasitic peak observed at 2.8 MHz, even when the tip was not in contact with the resonator, perturbed the measurement (this peak is attributed to the electronics of the AFM, DIMENSION 3100, VEECO INC.).

Then, the lock-in detection technique presented in [3, 4] has been adapted to the quad-beam device. In this method, the tip is placed in contact with the center of the QB plate: a sinusoidal amplitude-modulated high frequency signal (in the range of the resonance frequency of the QB), with a modulation frequency inferior to the resonance frequency of the AFM cantilever, is applied to the substrate to drive the resonator. The high frequency oscillation amplitude is measured using the modulation signal as a reference for the lock-in amplification of the photodiode signal of cantilever deflection.

The choice of an adequate frequency of modulation is important to ensure that the oscillation amplitude is only related to a mechanical resonance and not to any thermal expansion effect [3, 4]. For this purpose, we set the high frequency component at the expected resonance frequency while the vibration amplitude was measured with this technique as a function of the modulation frequency:

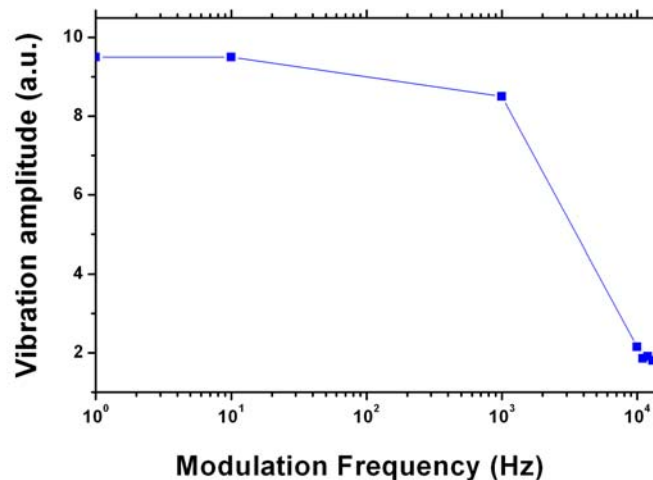


Figure 7. Vibration amplitude measured at the expected resonance frequency (2.5 MHz) as a function of the modulation frequency

This graph is consistent with what is observed in the papers [3, 4]: the system vibrates more for low modulation frequencies. Attributing this to a thermal effect, the modulation frequency is set at 5 kHz to ensure that the mechanical behavior is the dominant mechanism of vibration. Then, the frequency spectrum is measured for  $V_{IN DC} = 35$  V and  $V_{IN AC} = 5$  V peak-peak. The result is plotted in Figure 8. A peak is found around 2.35 MHz what is consistent with the expected range of resonance. However this experiment needs to be repeated and the device should also be measured with an alternative technique to corroborate the peak detected by AFM.

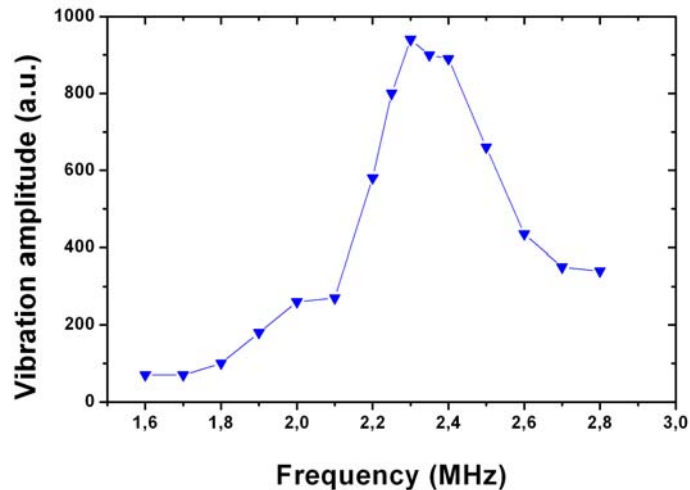


Figure 8. Frequency spectrum of a quad-beam measured by the lock-in detection technique with the AFM

Future experiments are scheduled for September 2007 with a double aim: (i) repeating the implementation of the lock-in detection technique to measure frequency spectra and (ii) analyzing the perturbation generated by the AFM tip on an oscillating CMOS nanomechanical resonator whose response is constantly detected electrically through the CMOS circuitry.

#### BIBLIOGRAPHICAL REFERENCES

1. Abadal, G., Z.J. Davis, X. Borrise, O. Hansen, A. Boisen, N. Barniol, F. Perez-Murano, and F. Serra  
**Atomic force microscope characterization of a resonating nanocantilever**  
*Ultramicroscopy*, 2003. **97**(1-4): p. 127-133.
2. Ollier, E., L. Duraffourg, M. Delaye, H. Grange, S. Deneuville, J. Bernos, R. Dianoux, F. Marchi, D. Renaud, T. Baron, P. Andreucci, and P. Robert  
**NEMS Devices for Accelerometers Compatible with Thin SOI Technology**  
 in the proceedings of the *2nd IEEE International Conference on Nano/Micro Engineered and Molecular Systems*. 2007. Bangkok, Thailand.
3. San Paulo, A., X. Liu, and J. Bokor  
**Atomic Force Microscopy characterization of electromechanical properties of RF acoustic bulk wave resonators**  
 in the proceedings of the *IEEE MEMS*. 2004.
4. San Paulo, A. and J. Bokor  
**Scanning acoustic force microscopy characterization of thermal expansion effects on the electromechanical properties of film bulk acoustic resonators**  
*Applied Physics Letters*, 2005. **86**(8).

## A10. List of publications

### ARTICLES ALREADY PUBLISHED

1. J. Arcamone, G. Rius, G. Abadal, J. Teva, N. Barniol, and F. Pérez-Murano  
**Mechanical resonator for distributed mass sensing and capacitive detection**  
Microelectronic Engineering 83, pp.1216-1220 (2006)
2. J. Arcamone, A. Sánchez-Amores, J. Montserrat, M.A.F. van den Boogaart, J. Brugger, and F. Pérez-Murano  
**Dry etching for the correction of gap-induced blurring and improved pattern resolution in nanostencil lithography**  
Journal of Micro/Nanolithography, MEMS and MOEMS 6 (1), 013005 (2007)
3. J. Arcamone, B. Misischi, F. Serra-Graells, M.A.F. van den Boogaart, J. Brugger, F. Torres, G. Abadal, N. Barniol, and F. Pérez-Murano  
**A compact and low-power CMOS circuit for fully integrated NEMS resonators**  
IEEE Transactions on Circuits and Systems II, 54 (5) pp 377-381 (2007)

### ARTICLES ALREADY SUBMITTED

4. J. Arcamone, B. Misischi, F. Serra-Graells, M.A.F. van den Boogaart, J. Brugger, F. Torres, G. Abadal, N. Barniol, and F. Pérez-Murano  
**A compact CMOS current conveyor for integrated NEMS resonators**  
SPRINGER Journal of Analog Integrated Circuits and Signal Processing

### ARTICLES IN PREPARATION

5. J. Arcamone, M.A.F. van den Boogaart, A. Sanchez-Amores, J. Montserrat, J. Fraxedas, F. Torres, G. Abadal, N. Barniol, J. Brugger and F. Pérez-Murano  
**Fabrication of attogram sensitivity micro-nanomechanical mass sensors based on a full wafer integration on CMOS by nanostencil lithography**  
to be submitted to the IEEE Journal of Microelectromechanical systems
6. J. Arcamone, G. Rius, J. Llobet, X. Borriase and F. Pérez-Murano  
**Mass measurements based on nanomechanical devices: differential measurements**  
to be submitted to the IEEE Transactions on Nanotechnology

7. J. Arcamone, E. Dujardin, G. Rius, F. Pérez-Murano and T. Ondarçuhu  
**Monitoring the evaporation of femtoliter sessile droplets with CMOS integrated nanomechanical mass sensors**  
to be submitted to the ACS Journal of Physical Chemistry B
- 

CONTRIBUTIONS AT NATIONAL AND INTERNATIONAL SCIENTIFIC CONFERENCES

1. J. Arcamone, G. Rius, X. Borrís and F. Pérez-Murano  
**Combination of e-beam and UV lithography for the prototyping of nano-mechanical devices**  
poster at the Nanospain conference, March 2005, Barcelona (Spain)
2. J. Arcamone, G. Rius, G. Abadal, J. Teva, N. Barniol and F. Pérez-Murano  
**Micro/nanomechanical resonators for distributed mass sensing with capacitive detection**  
poster at the MNE (Micro/NanoEngineering) conference, September 2005, Vienna (Austria)
3. J. Arcamone, A. Sánchez-Amores, L. Doeswijk, M.A.F. van den Boogaart, J. Brugger and F. Pérez-Murano  
**Pattern recovery by dry etching of gap-induced blurring in nanostencil lithography**  
poster at the MNE (Micro/NanoEngineering) conference, September 2005, Vienna (Austria)
4. F. Torres, J. Arcamone, J. Teva, J.L.L. Lopez, A. Uranga, G. Abadal, N. Barniol and F. Perez-Murano  
**Beam shape resonator made from EBL and RIE techniques**  
poster at the Nanospain conference, March 2006, Pamplona (Spain)
5. J. Arcamone, G. Rius, and F. Pérez-Murano  
**Micro/nanomechanical resonators for distributed mass sensing with capacitive detection**  
poster at the International Workshop on Nanomechanical Sensors, May 2006, Copenhagen (DK)
6. J. Arcamone, M.A.F. van den Boogaart, F. Serra-Graells, S. Hansen, J. Brugger, F. Torres, G. Abadal, N. Barniol, and F. Pérez-Murano  
**Full-wafer integration of NEMS on CMOS by nanostencil lithography**  
oral presentation at the IEEE IEDM 2006 (International Electron Devices Meeting), December 2006, San Francisco (USA)
7. J. Arcamone, T. Ondarçuhu, E. Dujardin, G. Rius, and F. Pérez-Murano  
**Characterization of femtoliter droplets with nanomechanical mass sensors**  
oral presentation at the International Workshop on Nanomechanical Sensors, May 2007, Montreal (Canada)

8. J. Arcamone, M.A.F. van den Boogaart, F. Serra-Graells, J. Fraxedas, J. Brugger, F. Torres, G. Abadal, N. Barniol, and F. Pérez-Murano  
**Nanomechanical mass sensors based on a full-wafer integration of NEMS on CMOS by nanostencil lithography**  
poster at the International Workshop on Nanomechanical Sensors, May 2007, Montreal (Canada)
  
9. F. Torres, G. Abadal, J. Arcamone, J. Teva, J. Verd, A. Uranga, J.Ll López, X. Borrisé, F. Pérez-Murano and N. Barniol  
**Coupling resonant micro and nanocantilevers to improve mass responsivity by detectability product**  
oral presentation at the IEEE Transducers conference, June 2007, Lyon (France)
  
10. J. Verd, A. Uranga, J. Teva, G. Abadal, F. Torres, J. Arcamone, J.Ll López, F. Pérez-Murano, J. Fraxedas, J. Esteve and N. Barniol  
**Monolithic 0.35  $\mu\text{m}$  CMOS cantilever for mass sensing in the attogram range with self-excitation**  
oral presentation at the IEEE Transducers conference, June 2007, Lyon (France)
  
11. J. Arcamone, T. Ondarçuhu, E. Dujardin, G. Rius, and F. Pérez-Murano  
**Monitoring the evaporation of femtoliter droplets with CMOS integrated nanomechanical mass sensors**  
oral presentation at the IEEE Sensors conference to be held in October 2007, Atlanta (USA)

